

**X-RAY SPECTROSCOPIC STUDIES OF PLASMA PRODUCED BY
INTENSE LASER BEAMS**

By
VIPUL ARORA
PHYS 03 2007 04 013

Raja Ramanna Centre for Advanced Technology, Indore

A thesis submitted to the
Board of Studies in Physical Sciences
In partial fulfilment of requirements
for the Degree of
DOCTOR OF PHILOSOPHY
of
HOMI BHABHA NATIONAL INSTITUTE



October, 2013

Homi Bhabha National Institute

Recommendations of the Viva Voce Board

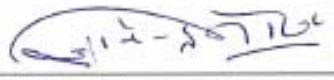
As members of the Viva Voce Board, we certify that we have read the dissertation prepared by *Shri Vipul Arora* entitled "*X-ray spectroscopic studies of plasma produced by intense laser beams*" and recommend that it may be accepted as fulfilling the dissertation requirement for the Degree of Doctor of Philosophy.

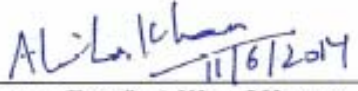

_____ Date: June 11, 2014
Chairman – Prof. L. M. Kukreja


_____ Date: June 11, 2014
Guide – Prof. P. D. Gupta


_____ Date: June 11, 2014
Co-Guide: Prof. P. A. Naik


_____ Date: June 11, 2014
Member – Prof. N. K. Gupta

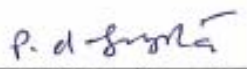

_____ Date: June 11, 2014
Member – Prof. G. S. Lodha


_____ Date: June 11, 2014
External Examiner - Prof. Alike Khare

Final approval and acceptance of this dissertation is contingent upon the candidate's submission of the final copies of the dissertation to HBNI.

I hereby certify that I have read this dissertation prepared under my direction and recommend that it may be accepted as fulfilling the dissertation requirement.

Date: June 11, 2014

Guide: 
(Prof. P. D. Gupta)

Place: Indore

STATEMENT BY THE AUTHOR

This dissertation has been submitted in partial fulfilment of requirements for an advanced degree at Homi Bhabha National Institute (HBNI) and is deposited in the Library to be made available to borrowers under rules of the HBNI.

Brief quotations from this dissertation are allowable without special permission, provided that accurate acknowledgement of source is made. Requests for permission for extended quotation from or reproduction of this manuscript in whole or in part may be granted by the Competent Authority of HBNI when in his or her judgment the proposed use of the material is in the interests of scholarship. In all other instances, however, permission must be obtained from the author.



Vipul Arora

DECLARATION

I, hereby, declare that the study presented in the thesis has been carried out by me. The work is original and has not been submitted earlier as a whole or in part for a degree / diploma at this or any other Institution / University.



Vipul Arora

List of Publications arising from the thesis

A. Papers in refereed Journals : (10)

- 1) Effect of gold on keV x-ray emission yield from laser produced plasma of gold copper mix-Z targets
V.Arora, J.A.Chakera, P.A.Naik, N.K.Gupta, S.R.Kumbhare, and P.D.Gupta
J. Appl. Phys. **100**, 033306 (2006)
- 2) Study of 2ω and $3/2\omega$ harmonics in ultra-short high-intensity laser plasma interaction
V.Arora, P.A. Naik, J.A. Chakera, R.A. Khan, and P.D. Gupta
Pramana J. Phys. **75**, 1175 (2010)
- 3) Conversion efficiency and spectral broadening of the K- α line emitted from planar titanium targets irradiated with ultra-short laser pulses of high intensity.
V.Arora, H. Singhal, P.A. Naik, and P.D. Gupta
J. Appl. Phys. **110**, 083305 (2011)
- 4) Strain and mosaic deformation in laser irradiated silicon.
M. Gupta, V.Arora, S. Bagchi, A. Gupta, J.A.Chakera, P.A.Naik, P.Chaddah, and P.D.Gupta.
Am. Inst. Phys. Conf. Proc. **1447**, 785 (2011)
- 5) A comparative study of the ionic keV x-ray line emission from plasma produced by femtosecond, picosecond, and nanosecond duration laser pulses.
V.Arora, P. A. Naik, B. S. Rao, and P. D. Gupta
Pramana J. Phys. **78**, 227 (2012)
- 6) Laser induced shock studies at RRCAT, Indore.
P.A. Naik, V.Arora, S. Bagchi, Y.B.S.R. Prasad, S. Barnwal, and P.D. Gupta.
J. Physics: Conference Series **377**, 012052 (2012)
- 7) Dispersion-less spectrograph for absolute measurement of multi keV x-ray flux from highintensity laser produced plasmas
V.Arora, H.S. Vora, J.A. Chakera, M. Tayyab, P.A. Naik and P.D. Gupta
J. Instrum. **8**, 01010 (2013)
- 8) Study of strain propagation in laser irradiated silicon crystal by time-resolved diffraction of K- α x-ray probe of different photon energies.
V.Arora, S. Bagchi, M. Gupta, J. A. Chakera, A. Gupta, P. A. Naik, P. Chaddah, and P.D. Gupta
J. Appl. Phys. **114**, 023302 (2013)
- 9) Bright 1-8 keV K- α x-ray source generated by high intensity femtosecond laser produced plasma for time resolved x-ray diffraction studies.
V.Arora, P.A. Naik, J.A. Chakera, S. Bagchi, M. Tayyab, and P.D. Gupta
AIP Advances **4**, 047106 (2014)

- 10) Spectral analysis of K-shell x-ray emission of magnesium plasma produced by ultra-short high intensity laser pulse irradiation.
V. Arora, U. Chakravarty, M. P. Singh, J.A. Chakera, P.A. Naik, and P.D. Gupta
Pramana J. Phys. 82, 365 (2014)

B. Publications in National Conferences/ Symposia: (9)

- 1) X-ray CCD camera based crystal spectrograph for x-ray spectroscopy of laser produced plasmas
V. Arora, H. Singhal, P.A. Naik, U. Chakravarty, R.A. Khan, J.A. Chakera, R. Jain, H.S. Vora, and P.D. Gupta.
DAE-BRNS National Laser Symposium, (NLS-2006) Indore, Dec. 2006.
- 2) Optimization of the K- α radiation produced by interaction of high intensity femtosecond laser pulses with thick titanium foils.
V. Arora, H. Singhal, P.A. Naik, S.R. Kumbhare, and P.D. Gupta
DAE-BRNS National Laser Symposium, (NLS-2007) Vadodara, Dec. 2007.
- 3) Optimization of the K- α radiation produced by interaction of high intensity femtosecond laser pulses with thick titanium foils.
V. Arora, H. Singhal, P.A. Naik, S.R. Kumbhare, and P.D. Gupta.
DAE-BRNS National Laser Symposium, (NLS-2007) Vadodara, Dec. 2007.
- 4) Spectral broadening of K- α x-ray line emission from high-intensity ultra-short laser pulse irradiation of planar titanium targets.
V. Arora, H. Singhal, P.A. Naik, S.R. Kumbhare, and P.D. Gupta.
23rd National Symposium on Plasma Science and Technology, Mumbai, Dec. 2008.
- 5) X-ray radiation from the rear side of foil targets irradiated by ultra-short high intensity laser pulses
V. Arora, P.A. Naik, J.A. Chakera, S.R. Kumbhare, M. Tayyab, and P.D. Gupta.
24th National Symposium on Plasma Science & Technology, Hamirpur, Dec. 2009
- 6) Correlation of the K- α x-ray line shape with the 2ω and $3/2 \omega$ emission in ultra-short high intensity laser plasma interaction.
V. Arora, P.A. Naik, J.A. Chakera, and P.D. Gupta.
International Symposium on Waves, Coherent Structures & Turbulence in Plasmas. Institute for Plasma Research, Gandhinagar. 12-15 January, 2010.
- 7) Spectroscopic study of laser light specularly reflected from solid targets irradiated by ultra-intense laser pulses.
V. Arora, P.A. Naik, J.A. Chakera, R.A. Ganeev, S.R. Kumbhare, and P.D. Gupta.
DAE-BRNS National Laser Symposium (NLS-19), Indore, Dec. 2010

- 8) Study of shock wave propagation in silicon crystal by picosecond time-resolved x-ray diffraction.
V.Arora, S. Bagchi, R.A. Khan, M. Gupta, J. A. Chakera, A. Gupta, P. A. Naik, P. Chaddah, and P. D. Gupta.
26th National Symposium on Plasma Science & Technology, Patna, Dec. 2011.
- 9) Study of strain propagation in laser irradiated silicon crystal by time-resolved diffraction of K- α x-ray probe of different photon energies.
V.Arora, S. Bagchi, M. Gupta, J. A. Chakera, A. Gupta, P. A. Naik, P. Chaddah, and P. D. Gupta.
DAE-BRNS National Laser Symposium (NLS-20), Chennai, Jan. 2012.
(Awarded best poster prize)



Vipul Arora

DEDICATION

*I dedicate this thesis to my daughters Navya and Yashi
who sacrificed their precious time of our togetherness for realization of my
dreams.*

ACKNOWLEDGEMENTS

The work presented in this thesis could not have been possible without the support and collaboration of many people. It is a pleasure for me to acknowledge the help they have provided me from time to time for this thesis work.

First and foremost, I would like to express my sincere gratitude to my thesis guide *Prof. P. D. Gupta* for his trust and confidence in me and introducing me to the field of laser produced plasma. He has taught me planning experiments, writing manuscripts and skills of communicating scientific discussion effectively. I am thankful for his valuable guidance and encouragement during the course of this work. I am extremely grateful to him for his keen interest in my professional growth and for his guidance for taking new challenges. Despite his ever-growing responsibilities as the Director, RRCAT, he took time to check that my research work progressed steadily and smoothly.

I am extremely grateful and indebted to my thesis co-guide *Prof. P. A. Naik* for his insightful guidance and continued supervision of various experiments, elaborate discussions of the results, and motivating for publishing the results. He has always inspired me with his extraordinary interpretations and explanations of physical phenomenon in simple and lucid manner. His welcoming approach to my queries and his contributions in creating a pleasant scientific environment made the work more enjoyable. Special thanks to him for teaching me the nuances of x-ray spectroscopy in particular.

I would like to thank my Doctoral Committee for reading the yearly reports and reviewing thesis work annually. Their suggestions helped to improve the quality of my work.

I am deeply indebted to *Dr. J.A. Chakera* for his valuable technical guidance throughout the course of my work.

Many thanks are due to my affectionate colleagues at Ti:Sapphire laser lab like *Dr. Himanshu Singhal*, *Shri B. S. Rao*, and *Shri Uday Chakravarty* who made the working environment scientifically charged and delightful. Our discussions motivated and helped me to enjoy the research work. *Rao* inspired with his exceptional clarity of concepts, *Uday* with his ability of mathematical formulation for physical phenomena, and *Himanshu* with his intellect and problem solving attitude.

Many thanks to my close colleagues who have shown immense confidence in my abilities and motivated me to complete the work despite the several odds during the course of the work. I should specially mention *Dr. A. Moorti*, *Shri M. P. Kamath*, and *Shri M. Raghuramaiah* for supporting me and being with me.

I sincerely thank *Prof. Ajay Gupta* and *Dr. Mukul Gupta*, UGC-DAE-CSR, Indore for collaborative experiments on time resolved x-ray diffraction.

I would like to thank *Dr. Suman Bagchi* for many constructive discussions and suggestions in preparation of the thesis.

I thank and appreciate *Shri Tayyab*, and *Shri Mukund Kumar* for their active participation in some of the experiments.

Thanks are due to *Shri S.R. Kumbhare* for helping me in setting up the experiments. I have learnt many technical skills from him, which have made me self-reliant on many aspects of working in laboratory

I thank *Shri H.S. Vora* for his ever enthusiastic support with image analysis software and in algorithms for dispersionless spectrograph.

I thank *Dr. M.P. Singh* for his help in setting up PrismSPECT software.

My sincere thanks to *Shri Riyaz Khan*, *Shri R. A. Joshi*, and *Shri R. K. Bhat* for providing the laser support. My thanks also go to *Shri R. P. Kushwaha* and *Shri S. Sebastin*, for the mechanical support in experiments.

I express my deepest regards to my late father for his love, care and motivation without which I wouldn't be where I am today. I would like to thank my sister for her unconditional love and backing. I am extremely thankful to my mother for her support and taking care of me and my daughters *Navya* and *Yashi*. Without her contribution, this thesis completion would not have been possible.

Finally, this work could not have been accomplished without the continuous persuasion of my beloved wife late *Poonam Arora*. It was her dream that I attain this academic milestone. It was her strength that showed me the light to overcome my apprehensions and accomplish this cherished goal.



(Vipul Arora)

CONTENTS

List of publications	v
Synopsis	xiv
List of figures	xxi
List of tables	xxvii
Chapter 1: Introduction	1 - 48
1.1 Plasma	4
1.2 Waves in plasma	7
1.3 Laser produced plasma	10
1.3.1 Long pulse laser - matter interaction	11
1.3.1.1 Inverse bremsstrahlung	13
1.3.1.2 Parametric decay processes	17
1.3.2 Short pulse laser – matter interaction	21
1.4 Equilibrium in plasma	25
1.4.1 Ionization and recombination processes	26
1.4.2 Ionization models	35
1.4.2.1 Complete thermal equilibrium	35
1.4.2.2 Local thermodynamic equilibrium model	37
1.4.2.3 Coronal equilibrium model	38
1.4.2.4 Collisional radiative model	39
1.5 X-ray emission processes.....	39
1.5.1 Bremsstrahlung emission.....	39
1.5.2 Free – bound radiation.....	40
1.5.3 Bound – bound radiation.....	41
1.6 Application of LPP x-ray source in time resolved x-ray diffraction.....	47
Chapter 2: Laser system and x-ray diagnostics	49 - 85
2.1 Nanosecond Nd:phosphate glass laser chain	49
2.2 Multi-picosecond 100 GW Nd: glass laser chain	51
2.3 Ti: Sapphire laser system	53
2.3.1 Characterization of laser parameters	54
2.4 Plasma chamber and target setup.....	61
2.5 X-ray CCD camera based crystal spectrograph	62
2.6 Dispersionless spectrograph	68
2.6.1 Description of the spectrograph	70
2.6.2 Reconstruction algorithms to identify the single pixel event	72

2.6.3 Characterization and performance of the spectrograph	76
2.7 X-ray p-i-n diode	82
Chapter 3: Dependence of the ionic x-ray line emission on laser pulse duration	86 - 102
3.1 Description of the experiment	89
3.2 Results and discussion	90
3.3 Analytical calculation of the ionization equilibrium time	96
Chapter 4: keV x-ray emission from gold-copper mix-z plasma	103 - 117
4.1 Effect of opacity on x-ray emission	104
4.2 Mix-Z target preparation	106
4.3 Description of the experiment	107
4.4 Results and discussion.....	108
Chapter 5: Inner-shell and the ionic line radiation from magnesium plasma.....	118 - 135
5.1 Description of the experiment	119
5.2 Main features of x-ray emission spectrum from Mg plasma	121
5.3 X-ray line intensity scaling with laser intensity	124
5.4 X-ray line emission intensity variation with focusing	126
5.5 Angular dependence of x-ray emission	128
5.6 Effect of laser pulse duration on x-ray emission	130
5.7 Discussion of the observed x-ray spectrum	131
Chapter 6: Bright ultra-short 4-8 keV k-α x-ray source	136 - 151
6.1 K- α source characteristics	137
6.1.1 X-ray photon yield	138
6.1.2 Pulse duration of the K- α radiation.....	138
6.1.3 Monochromatic line radiation	139
6.1.4 Source size	140
6.2 Experimental details	141
6.3 Experimental results and discussion.....	142
6.4 X-ray source size	150
CHAPTER 7: 2ω and $\frac{3}{2}\omega$ harmonics as diagnosticfor pre-formed plasma ...	152 - 172
7.1 General properties of optical emission spectrum	154
7.1.1 2ω generation	154
7.1.2 $\frac{3}{2}\omega$ generation	155
7.2 Description of the experiment	157

7.3 Experimental results and analysis	158
7.4 Conversion efficiency and spectral broadening of the K- α line emitted from planar titanium targets	164
Chapter 8: Time resolved x-ray diffraction studies using K-α radiation ...	173 - 194
8.1 X-ray diffraction from compressed sample	175
8.2 Description of the experiment	179
8.3 Measurement of shock-wave profiles	182
8.4 Probing of strain propagation in laser shocked crystal with K- α x-ray probe of different photon energies	184
8.5 Deformation in laser irradiated silicon crystal	192
Chapter 9: Conclusion	195 - 199
9.1 Summary of the research work	195
9.2 Outlook and future perspective	198
Bibliography.....	200 - 218

Synopsis

When a pulsed intense laser beam is focussed onto a solid target, a rapidly evolving hot dense plasma emitting intense x-ray radiation is created at the target surface. The spectrum of the x-ray emission is governed by the plasma parameters viz. electron temperature, electron density, target atomic number, degree of ionization of plasma etc. The above parameters depend on the various mechanisms through which laser energy is absorbed in the plasma, which in turn, are determined by the intensity and the temporal profile of the laser pulse. Under optimal conditions, up to $\sim 10\%$ of laser energy can be converted into x-rays in the >1 keV spectral range. This makes laser plasmas one of the most promising high brightness sources of x-ray radiation for many scientific and technological applications.

The study of intense x-ray emission in laser – plasma interaction has been a subject of considerable importance for research investigations, especially those related to the laser driven inertial confinement fusion (ICF) scheme. As a potentially viable mechanism of energy production, it is being pursued actively at several large scale laser facilities across the globe and the most notable among them is the National Ignition Facility, USA. Various x-ray diagnostic techniques are utilized to derive information on the ion temperature T_{ion} , the total areal density ρR_{total} , the core areal density ρR_{core} , ion temperature and the other plasma parameters which are critical for understanding and improving the ICF fuel pellet design parameters to achieve the *break-even* condition. Here ρ is the fuel density in the pellet and R is its radius. X-ray diagnostics complement the neutron diagnostics and can also be used for bench-marking hydrodynamics codes. The investigations in experiments relevant to ICF, such as probing of the high areal density targets, require x-ray diagnostics capabilities with sufficiently large photon flux to record the event in a single shot, with high contrast and resolution. The development of highly efficient sources of high energy (10 – 40 keV) x-rays suitable for high resolution radiography for large ρR targets, and of low photon energy (1–2 keV) sources which are more suitable for backlighting of low- Z material for optimal contrast, is the prime motivation to study the x-ray emission from plasma produced by the intense laser beams.

The plasma created with a high intensity, ultra-short laser pulse has attracted attention as a potential source for time-resolved x-ray probing. The narrow bandwidth and short duration of the characteristic K-shell line radiation ($K-\alpha$) has generated much interest to be used as a probe pulse. The heating mechanism of plasma generated by ultra-short laser pulses

predominantly creates hot electrons (i.e. electrons with energy much higher than the thermal distribution) through collective mechanisms of resonance absorption, vacuum heating, jxB heating, etc. The interaction of the hot electrons with the cold target material behind the plasma leads to the emission of characteristic line radiation and continuum hard x-ray bremsstrahlung. Under optimized conditions, the x-ray emission typically lasts only for the duration of the laser pulse used, since the hot electrons responsible for the x-ray emission are generated only during the laser pulse. The x-ray photon energy can be suitably selected by the choice of the target material and optimum parameters for conversion efficiency and source size. The x-ray pulse duration can be controlled through the laser irradiation parameters.

In the recent years, a number of studies have been reported on the ultra-fast dynamics performed using the laser plasma x-ray source. The ultra-short duration quasi-monochromatic x-ray pulses in the energy range of 1–10 keV, delivering sufficient photon numbers, from femtosecond laser produced plasma, allow investigation of materials with high temporal and spatial resolution. The experimental setup to probe a sample uses an optical pump to create disturbance, and the x-ray pulse to probe it. The pump pulse is a small fraction derived from the main laser pulse used to produce the x-ray source (probe). The main advantage offered by this scheme is that the x-ray probe pulse is exactly synchronized with the laser pulse and no jitter exists between the probe and pump pulses for the purpose of time resolved experiments. For practical applications in the ultra-fast x-ray diffraction or scattering experiments, there are three prime requirements. First, a large photon flux is required in single x-ray spectral line to record the diffracted x-ray spectrum from the sample in a single shot. Second, a smaller temporal pulse width of the x-ray pulse is required to resolve the rapidly changing conditions. Third, a narrow spectral bandwidth (small $\Delta E/E$) is required to resolve the changes of few eV to few tens of eV in the spectral feature usually observed in such experiments. Generally, fulfilling the above requirements simultaneously is often difficult. It is important to know the effect of improvement in one parameter on other source parameters

Efficient x-ray source can be generated through efficient absorption of the laser energy and producing hot electrons with the appropriate energy to optimally create inner-shell vacancies in the target material. Few studies have been reported on the maximization of x-ray photon flux by varying the laser wavelength, pulse chirp, etc. There are some reports where the x-ray yield has been shown to increase by using a pre-pulse prior to the main laser pulse. All these studies were aimed at optimizing the plasma scale length for maximum K- α conversion by increasing the laser energy absorption. Optimal hot electron parameters were

achieved by controlling the laser intensity either through offsetting the target from the best focus position or using a longer duration chirped laser pulse. The influence of the techniques used to enhance the x-ray yield on the duration of the x-ray line radiation is widely studied by several groups. For example, a high intensity of irradiation is necessary to increase the photon flux, but the resultant high energy of the hot electrons leads to emission over a longer duration.

In the present research work, we have experimentally studied the x-ray emission from the plasma generated by the interaction of long (3 ns), short (30 ps), and ultra-short (45 fs) laser pulses. The influence of various laser and target conditions on the x-ray source has been investigated. The keV x-ray line emission yield from the magnesium plasma produced by laser pulses of duration extending from nanosecond to femtosecond, at a constant laser fluence, was studied to infer the role of ionization dynamics. There is a great interest in methods that could enhance the x-ray yield by variation of the laser or target conditions so as to make them competitive / attractive for various applications. We have studied the role of high-Z impurity on the keV x-ray emission from copper target. The key issue in the ultra-short high intensity laser plasma interaction is the understanding of the initial processes leading to the production of hot dense plasmas. Further, any realistic high intensity ultra-short irradiating laser pulse has a pedestal and pre-pulse associated with it. The optical emission of 2ω and $3/2\omega$ harmonics in the ultra-short high-intensity laser plasma interaction was used as a diagnostic for pre-formed plasma. We have performed simultaneous measurements of the inner-shell and the ionic line radiation from ultra-short laser-produced magnesium plasma to investigate the laser energy absorption mechanisms. Bright ultra-short K- α x-ray source between 1-8 keV photon energy, generated by high intensity femtosecond laser produced plasma, was optimized for maximizing the x-ray photon flux. The probe x-ray pulses were used for studying the shock wave propagation in a silicon crystal under laser excitation. A chapter-wise summary of these studies is given below.

Chapter 1 gives a brief introduction to the theoretical background of the plasma and the laser-plasma interaction physics in the long pulse (ns) and the ultrashort pulse (fs) regimes. This is followed by a brief description of the ionization equilibrium in the plasma. Various x-ray emission processes in laser produced plasma interaction are briefly described.

Chapter 2 starts with description of the nanosecond, picosecond and femtosecond laser systems used in present research work. The characterization of the parameters of the driving laser namely: pulse duration, spectral profile etc. is outlined. This is followed by a

brief description of the plasma chamber and the target setup. Two x-ray spectroscopic diagnostics were developed for characterization of the spectral properties of the x-ray emission from the plasma source. The first one was based on flat crystals, coupled with an x-ray CCD camera recording the first order reflection of x-ray line radiation satisfying the Bragg condition. This diagnostic was aimed at achieving high resolution spectra capable of resolving the individual contribution of the x-rays of various transitions ($K\text{-}\alpha_1$, $K\text{-}\alpha_2$ etc.) to the total emission. Next diagnostic is the dispersion-less spectrograph, a spectroscopic technique based on the direct use of a cooled CCD operating in the single photon detection mode. This detection technique enables simultaneous measurement of the spectral properties and the incident flux of the x-rays. A detailed description on the characterization of the spectrograph and the reconstruction algorithms used to identify the single pixel event, is presented.

The x-ray emission from highly charged ionic species was used to study the role of the ionization dynamics during the evolution of the plasma. **Chapter 3** describes the measurements of the x-ray yield of different ionic lines from the plasma produced by the laser pulses of nanoseconds to femtosecond duration. It was observed that the x-ray yield of the resonance lines from the higher ionization states such as H-like and He-like ions decreases on decreasing the laser pulse duration, even though the peak laser intensities for the 45 fs duration pulses are much higher than those for the 3 ns laser pulses. Analytical calculations of the ionization equilibrium time for the different ionization states in the heated plasma, carried out to explain the experimental observation, are described.

In the indirect scheme of inertial confinement fusion using hohlraum targets, it is desirable to enhance the thermal x-ray yield in the sub-keV region. It has been shown that if two or more different elements are mixed such that the high opacity regions of one overlap with the low opacity regions of the other, the mixture can have a higher Rosseland mean opacity than that of the individual elements. On the other hand, an increase in the keV x-ray conversion may have negative implication for inertial confinement fusion as the harder component of the driver spectrum, having a longer penetration depth, can preheat the fuel which may result in a poor fuel compression. In **Chapter 4**, we discuss important findings related to the sharp decrease in the intensity of the copper L -shell line radiation (7.8–10.9 Å) as well as the integrated keV x-ray yield with increasing atomic fraction of gold in the mix-Z target. The results can be explained from the physical consideration of the high value of free-

bound opacity of gold in the spectral region of the L -shell emission of copper ions and down conversion of the absorbed keV line radiation.

In order to understand the effect of the laser irradiation on the laser energy absorption mechanism, simultaneous measurements of the inner-shell and the ionic line radiation from ultra-short laser-produced magnesium plasma was carried out. In **Chapter 5**, we describe the effect of the variation of the laser intensity, the offset from the best focus position, and the pre-pulse contrast on the He- α and K- α line emissions. He- α and K- α x-ray yield are observed to scale with the laser intensity as $I_L^{1.5}$ and $I_L^{0.6}$ respectively. The K- α x-ray conversion shows a maximum at the best focus and reduces symmetrically on either side of the best focus position, whereas the He- α conversion peaks when the target is placed before the focussed laser beam. The angular distribution for the He- α as well as the K- α emission shows a maximum in the forward direction and the intensity reduces with the angle with respect to the target normal as $\cos^\alpha \theta$. The value of α is 0.7 and 3 for He- α and K- α respectively. The experimentally observed variation of the He- α line conversion for different laser parameters has been explained by considering the change in the pre-formed plasma conditions, and the variation in the K- α emission has been explained by considering the generation of hot electrons and their propagation in the bulk solid target. The plasma conditions prevalent during the emission of the x-ray spectrum were identified by comparing the experimental spectra with the synthetic spectra generated using the spectroscopic analysis code PrismSPECT.

K- α line emission in the 1–8 keV energy region from Ti, Fe and Cu solid targets was experimentally studied using ultra-high intensity femtosecond laser pulses. In **Chapter 6**, we describe the absolute yield of the K- α x-rays as a function of the laser pulse contrast ratio and irradiation intensity. The x-ray yield was maximized with the laser pulse duration (at a fixed fluence) which was varied in the range of 45 fs to 1.8 ps. It showed a maximum at a laser pulse duration of ~ 420 fs, 350 and 250 fs for Ti (4.5 keV), Fe (6.4 keV) and Cu (8.05 keV) respectively. The scaling of the K- α yield ($\propto I_L^\beta$) for 45 fs and the optimized pulse duration were measured for laser intensities in the region of $3 \times 10^{14} - 4 \times 10^{17}$ W/cm². The x-ray yield shows a high scaling exponent $\beta = 2.1, 2.4$ and 2.6 for Ti, Fe and Cu respectively at the optimized pulse duration, compared to the scaling exponents 1.3, 1.5, and 1.7 obtained for the 45 fs duration laser pulses. The results are explained in terms of efficient generation of optimal energy hot electrons at longer laser pulse duration, and the change in density scale length by changing the laser pulse duration and energy.

The influence of various laser and target conditions has been the subject of many recent studies. The pre-plasma formation has been investigated in detail as one of the prominent ways of improving the x-ray yield. The influence of techniques used for increasing photon flux on the crucial aspect of monochromaticity of the spectral line profile is generally overlooked. The K- α spectral lines have a very high degree of monochromaticity. However, the blending of K- α emission from the ionized medium with that from the cold material increases its bandwidth. The knowledge of appropriate laser irradiation parameters to achieve minimum spectral width of the K- α radiation is therefore desirable. In **Chapter 7**, we present our study on 2ω and $3/2\omega$ harmonics in ultra-short high-intensity laser plasma interaction as a diagnostic for pre-formed plasma. Experimental results and analysis of the dependence of the 2ω and $3/2\omega$ intensity on the laser intensity and on the chirp of laser pulse have been presented. The correlation of the K- α x-ray line shape with the 2ω and $3/2\omega$ emission is also highlighted. The high resolution Ti x-ray spectrum shows the K- α line radiation (4510 eV) broadened (upto ~ 9 eV) predominantly on the higher energy side. The broadening has been studied as a function of the laser intensity ($7 \times 10^{16} - 10^{18} \text{ W cm}^{-2}$), the laser pulse duration (45 fs – 800 fs), and the laser fluence ($3 \times 10^3 - 6 \times 10^4 \text{ J cm}^{-2}$). The spectral width of the K- α radiation increased with increase in the laser intensity. At constant fluence, there is no significant difference in their spectral profiles with increasing the laser pulse duration. The optical spectrum was also measured for the above laser intensity and pulse duration parameters. The spectrum has well defined peaks at wavelengths corresponding to 2ω and $3/2\omega$ radiation. The spectral features vary with the laser intensity and show an increasing blue shift with increasing laser intensity. At a constant laser fluence, there is no significant difference in the $3/2\omega$ radiation with increase in the laser pulse duration. This shows that the spectral broadening of the K- α x-ray line is strongly correlated with the optical spectrum of the light scattered from a solid surface irradiated by the laser pulses. The K- α radiation has smallest line width when the interaction conditions are such that only the 2ω emission can be seen. On the other hand, maximum broadening corresponds to the presence of only $3/2\omega$ emission. The generation of 2ω and $3/2\omega$ radiation was found to depend mainly on the density scale length of the plasma created by the pre-pulse. A comparison of line shape of the K- α x-ray radiation with the optical measurements indicates that the inner-shell transitions in the multiply charged titanium ions in the low temperature plasma produced by the pre-pulse, have a strong contribution in the observed spectral broadening.

In **Chapter 8**, an experimental study on the time resolved x-ray diffraction from a laser shocked silicon crystal, carried out using a 10 TW, 45 fs Ti:sapphire laser system, is presented. The characteristic K- α x-ray line radiation generated by the plasmas of two different target materials (iron and copper) was used as the probe. The stretched pulse of sub-nanosecond duration (pump), derived from the same laser, was used to shock compress the sample. The use of x-ray probe of different photon energies yields information about the strain over a greater crystal depth. The dynamics of the strain propagation was inferred by monitoring the evolution of the rocking curve width of the shocked sample at different time delays between the pump and the probe pulse. The shock velocity deduced from these measurements was $\sim 10^6$ cm/s, consistent with the sound velocity in bulk silicon. The maximum elastic compression observed was 0.4 %, indicating a pressure of 0.8 GPa.

Finally, the thesis concludes in **Chapter 9** with a summary of the results, and a brief discussion on the possible extension of the present thesis work in future.

LIST OF FIGURES

Figure No.	Figure Caption	Page No.
1.1	<i>The dispersion curve for electromagnetic, electron plasma wave and ion acoustic wave.</i>	9
1.2	<i>Plasma expansion geometry.</i>	12
1.3	<i>A schematic of electron density and temperature spatial profile depicting various zones in LPP.</i>	13
1.4	<i>Dispersion curves depicting the process of parametric decay.</i>	18
1.5	<i>Dispersion curves for Two Plasmon Decay.</i>	19
1.6	<i>Dispersion curve depicting Stimulated Brillouin Scattering.</i>	20
1.7	<i>Dispersion curves for the (a) Forward (b) Backward Raman Scattering.</i>	20
1.8	<i>The typical length scale involved for the parametric decay processes.</i>	22
1.9	<i>A schematic representation of electron density variation in ultra-short laser produced plasma.</i>	23
1.10	<i>A schematic representation of resonance absorption of obliquely incident p-polarised light.</i>	24
1.11	<i>Dielectronic recombination process.</i>	33
1.12	<i>Charge exchange recombination process.</i>	35
1.13	<i>Resonance and intercombination transitions.</i>	42
1.14	<i>Dielectronic satellite transition.</i>	43
1.15	<i>The radiative transitions of electrons from the outer shells lead to the generation of inner-shell characteristic lines.</i>	45
1.16	<i>Fraction of the transmitted laser energy is used to induce changes in the lattice properties of the crystal sample. The changes are probed by the $K\alpha$ line and detected by an x-ray CCD camera.</i>	47
1.17	<i>Several approaches for analysing Bragg diffraction data.</i>	48
2.1	<i>Schematic of nanosecond Nd: phosphate glass laser chain.</i>	50
2.2	<i>Multi-picosecond 100 GW Nd: glass laser chain.</i>	52
2.3	<i>Block diagram of the Ti: sapphire laser system.</i>	53
2.4	<i>A schematic diagram of the experimental setup for focal spot measurement.</i>	55
2.5	<i>a) Magnified image of laser focal spot on CCD, b) the intensity profile of the laser spot closely matching the Gaussian fit.</i>	56

2.6	<i>Generation of autocorrelator trace in SHG crystal.</i>	56
2.7	<i>(a) Autocorrelator signal, and (b) its trace using “Promise” software.</i>	57
2.8	<i>Variation of laser pulse duration with grating separation relative to the compressor zero.</i>	59
2.9	<i>Pre-pulse due to amplified spontaneous emission (ASE) measured with a fast photo-diode. The colours of traces correspond to different switching times of the pulse cleaning Pockel’s cell.</i>	61
2.10	<i>A photograph of the plasma chamber.</i>	62
2.11	<i>Bragg reflection geometry for x-ray crystal spectrograph.</i>	63
2.12	<i>Transmission characteristics of a B-10 foil.</i>	65
2.13	<i>Quantum efficiency of x-ray CCD as per manufacturer.</i>	66
2.14	<i>A schematic diagram of the experimental set up of the on-line x-ray spectrograph.</i>	66
2.15	<i>X-ray spectrum as seen on x-ray CCD camera (top) and its intensity plot (bottom).</i>	68
2.16	<i>X-ray emission spectrum obtained with standard histogram method. The inset shows an over-exposed raw image obtained with the dispersion-less spectrograph.</i>	74
2.17	<i>The x-ray emission spectrum from data in Fig.2.16, obtained with the special algorithm. The inset shows the genuine, all single photon events image obtained after applying the algorithm.</i>	76
2.18	<i>A schematic diagram of the experimental setup (left) schematic (right) x-ray CCD mounted on the chamber.</i>	77
2.19	<i>X-ray emission spectra of (a) titanium, copper, zinc (b) stainless steel, and gallium arsenide (c) zirconium, and molybdenum.</i>	79
2.20	<i>Energies of various inner-shell line transitions corresponding to different ADU. The solid line shows the fitting of the data to the energy.</i>	80
2.21	<i>Relative energy resolution (Γ/E) as a function of the photon energy.</i>	81
2.22	<i>X-ray emission spectrum from the rear side of the 24 μm thick titanium foil irradiated at a laser intensity of $\sim 1.2 \times 10^{18} \text{ W cm}^{-2}$.</i>	82
2.23	<i>Variation of quantum efficiency (electrons seen by external circuit/photon) of xuv pin diodes with photon energy.</i>	84
2.24	<i>Pin diode biasing circuit.</i>	84
3.1	<i>X-ray spectrum of magnesium plasma produced using nanosecond laser pulses at an intensity of $5 \times 10^{12} \text{ W cm}^{-2}$.</i>	91
3.2	<i>X-ray spectrum of magnesium plasma produced using a picosecond laser pulse at an intensity of $6 \times 10^{14} \text{ W cm}^{-2}$.</i>	91

3.3	<i>X-ray spectrum of magnesium plasma produced using fs laser pulses at an intensity of $3.5 \times 10^{17} \text{ Wcm}^{-2}$.</i>	92
3.4	<i>The relative conversion efficiency of the magnesium He-α, He-β, He-γ, H-α and H-β lines is plotted for the three different pulse durations used in the experiment. The curves are drawn to guide the eyes.</i>	93
3.5	<i>Ionization equilibrium time calculated for ionization of He-like magnesium ions to H-like ions for different values of T_e (up to 2.5 keV) at a fixed value of n_e of 10^{21} cm^{-3}. The dashed curve is for ionization of Li-like magnesium ions to He-like ions.</i>	99
3.6	<i>Ionization equilibrium time required for ionization of magnesium ions from He-like to H-like and from Li-like to He-like ions for different values of T_e (up to 100 keV) and a fixed value of n_e of $1.5 \times 10^{21} \text{ cm}^{-3}$.</i>	100
4.1	<i>X-ray spectrum of pure Cu in the wavelength range from $\lambda = 7.8\text{\AA}$ to 10.9\AA.</i>	109
4.2	<i>X-ray spectrum of mix-Z target having 0.88 atomic fraction of copper and 0.12 atomic fraction of gold.</i>	109
4.3	<i>Variation of the integrated x-ray yield in the spectral range of $\lambda = 7.8\text{\AA}$ to 10.9\AA as a function of atomic fraction of gold in the mix-Z target.</i>	110
4.4	<i>Variation of the intensity of Cu XX ($2p^6 - 2p^5 4d$) line at $\lambda = 9.1\text{\AA}$ with atomic fraction of gold in the mix-Z target.</i>	110
4.5	<i>Variation of the x-ray signal from x-ray p-i-n diode as a function of atomic fraction of gold in the mix-Z target.</i>	111
4.6	<i>Bound-free opacity spectrum computed for Cu and Au plasmas.</i>	113
4.7	<i>Bound-bound opacity spectrum computed for Cu and Au plasmas.</i>	113
4.8	<i>Integrated x-ray conversion per unit solid angle for Cu, Au, and Au 0.43 – Cu 0.57 mix-Z plasma.</i>	115
4.9	<i>Variation of x-ray intensity with atomic composition.</i>	115
5.1	<i>A schematic diagram of the experimental setup.</i>	120
5.2	<i>High resolution x-ray spectrum of magnesium plasma produced by 45 fs duration laser pulses focussed at an intensity of $4 \times 10^{17} \text{ Wcm}^{-2}$.</i>	122
5.3	<i>He-α and K-α emission as a function of the laser intensity. The variation in the laser intensity was accomplished by changing the laser energy, keeping the laser focal spot size unchanged.</i>	124
5.4	<i>He-α and K-α emission as function of the distance of the focus position from the target surface irradiated with laser pulses of fixed energy of 135 mJ. “Zero” corresponds to the best focus position. Negative distance corresponds to laser focussed after the target.</i>	126
5.5	<i>(a) Laser beam entering from vacuum ($\mu = 1$) always deviates away from the</i>	

	<i>normal which leads to further focusing of a converging beam. (b) Divergence of laser beam focussed in front of the target surface (diverging beam).</i>	127
5.6	<i>Angular distribution of He-α and K-α emission. Solid and dashed curves represent the fit of the form $\cos^3 \theta$ and $\cos^{0.7} \theta$ to the angular distribution for K-α and He-α emission, respectively.</i>	129
5.7	<i>X-ray yield as a function of incident laser pulse duration for a constant fluence of $3.8 \times 10^4 \text{ J cm}^{-2}$ (a) K-α (b) He-α.</i>	131
5.8	<i>Synthetic spectra of Mg computed using PrismSPECT software to fit the experimental spectrum at an intensity of $4 \times 10^{17} \text{ W cm}^{-2}$. a) Region around the He-α resonance, best fit for the parameters: $T_e = 130 \text{ eV}$, $T_{\text{hot}} = 50 \text{ keV}$, hot electron fraction = 0.01, and $n_e = 5.4 \times 10^{20} \text{ cm}^{-3}$; b) Region around the K-α emission, best fit for the plasma conditions: $T_e = 10 \text{ eV}$, $T_{\text{hot}} = 130 \text{ keV}$, hot electron fraction = 0.01, and $n_e = 4.4 \times 10^{22} \text{ cm}^{-3}$.</i>	133
6.1	<i>Schematic of the generation of Kα line radiation when solid target is irradiated with ultra-short high intensity laser pulse.</i>	137
6.2	<i>X-ray emission from Ti, Fe, and Cu target recorded with dispersion less spectrograph.</i>	143
6.3	<i>Plot of K-α x-ray yield of Ti, Fe, and Cu as a function of incident laser pulse duration for a constant fluence of $3.8 \times 10^4 \text{ J cm}^{-2}$.</i>	144
6.4	<i>K-α intensity (I_x) as a function of the laser intensity (I_L) on log – log scale at a fixed pulse duration of 45 fs. The scaling of I_x with I_L is expressed as power law $I_x \sim I_L^\beta$.</i>	146
6.5	<i>K-α intensity (I_x) as a function of the laser intensity (I_L) on log – log scale at an optimized pulse duration of 440 fs, 325 fs, and 250 fs for Ti, Fe, and Cu target.</i>	147
6.6	<i>Experimentally observed ratio of optimal hot electron temperature and K-shell energy as a function of atomic number.</i>	149
6.7	<i>The line profile across the knife edge. The FWHM of the line spread function gives the x- ray source size.</i>	151
7.1	<i>The spectrum of laser at the chamber at full power after the focusing lens.</i>	157
7.2	<i>A schematic diagram of the experimental setup.</i>	158
7.3	<i>Harmonic spectrum recorded at a laser intensity of $8.8 \times 10^{16} \text{ W cm}^{-2}$.</i>	159
7.4	<i>Harmonic spectrum recorded for different intensity of laser pulse.</i>	160
7.5	<i>Harmonic spectrum recorded for different chirp of laser pulse.</i>	161
7.6	<i>The second harmonic, and the 3/2-harmonic radiation intensity as a function of the pump laser pulse duration for a constant fluence of $1.8 \times 10^4 \text{ J cm}^{-2}$.</i>	162
7.7	<i>Intensity scaling of 2ω and $3/2 \omega$.</i>	163
7.8	<i>Inner-shell x-ray emission spectrum from laser irradiated titanium target. Inset shows the spectrally resolved K-α_1 and K-α_2 fine structure components.</i>	165

7.9	<i>The deconvoluted spectral width (FWHM) of the K-α_1 line as function of the laser intensity, for a fixed pulse duration of 45 fs. The curve is drawn to aid the eye. The dashed line represents the natural line width. The error in spectral width measurement is estimated to be less than 10 %.</i>	166
7.10	<i>Normalized K-α line radiation profile at two different laser intensities of $7.8 \times 10^{16} \text{ W cm}^{-2}$ and $8.5 \times 10^{17} \text{ W cm}^{-2}$, at a fixed laser pulse duration of 45 fs.</i>	167
7.11	<i>Normalized K-α line radiation profile at two different pulse durations of 45 fs and 600 fs, at a fixed fluence of $4.2 \times 10^4 \text{ J cm}^{-2}$.</i>	169
7.12	<i>The dependence of the deconvoluted spectral width of the K-α_1 line on the laser pulse duration, at a fixed fluence of $4.2 \times 10^4 \text{ J cm}^{-2}$. The curve is drawn to aid the eye. The solid line represents the natural line width of the K-α_1 line. The error in spectral width measurement is estimated to be less than 10 %.</i>	169
7.13	<i>Normalized K-α line radiation profile at two different laser fluences of $3.5 \times 10^3 \text{ J cm}^{-2}$ (45 fs) and $4.2 \times 10^4 \text{ J cm}^{-2}$ (600 fs), at a fixed laser intensity of $\sim (7.4 \pm 0.4) \times 10^{16} \text{ W cm}^{-2}$.</i>	170
8.1	<i>A schematic diagram of the basic concept of Bragg reflection from the crystal planes.</i>	176
8.2	<i>Diverging polychromatic beam incident on the crystal, subtending a certain range of angles, then the x-rays of different wavelengths satisfying Bragg condition are recorded on the detector.</i>	177
8.3	<i>Basic concept of diffraction from the lattices along the x-ray penetration depth in the sample, having contribution of both shocked and unshocked lattices.</i>	178
8.4	<i>A schematic diagram of the experimental setup.</i>	180
8.5	<i>(a) Space resolved CCD image of the diffracted iron K-α x-rays from laser irradiated Si (111) surface at a delay of +600 ps (b) fitted line profile of the pristine sample.</i>	182
8.6	<i>Broadening of the FWHM of Ti K-α line with the time delay between pump and probe pulse.</i>	183
8.7	<i>Evolution of Si (111) rocking curve for various time delays, at a fixed fluence of 2.3 J cm^{-2}.</i>	185
8.8	<i>Variation of the FWHM of the K-α_1 line of Fe as a function of the delay between the pump and the probe pulse for two different fluences of 2.3 J cm^{-2} (solid squares) and 1.2 J cm^{-2} (hollow circles). The curve is to drawn to guide the eye.</i>	186
8.9	<i>Variation of the FWHM of the Kα_1 line radiation as function of the delay between the pump and the probe pulse, for Ti, Fe and Cu. The curve is to drawn to guide the eye.</i>	188
8.10	<i>Strain variation as a function of the delay between the pump and the probe pulse, for Fe (hollow circles) and Cu (solid squares).</i>	188

8.11	<i>XRD pattern obtained from a pristine and irradiated part of the sample.</i>	192
8.12	<i>The extent of irreversible broadening of the rocking curve of Si (111) sample for different laser irradiances.</i>	193
8.13	<i>Raman spectroscopy measurements to investigate the effect of laser irradiation in near surface region.</i>	193

LIST OF TABLES

Table No.	Table Caption	Page No.
2.1	<i>Important parameters of the crystal used in the spectrograph to record x-ray spectrum.</i>	64
4.1	<i>Mix-Z targets composition in terms of weight fraction and atomic compositions.</i>	107
6.1	<i>Optimal laser pulse duration for obtaining maximum x-ray yield, scaling exponent with laser intensity obtained at 45 fs and optimal pulse duration, absolute K-α photon flux from different target material.</i>	145
6.2	<i>Optimal laser intensity for K-α photon flux determined experimentally, expected from theoretical consideration and conversion.</i>	149

Chapter 1

Introduction

Curiosity for insight into the temporal dynamics of solids with spatial resolution of atomic scale has led to the search of newer methods of generating easy-to-set-up ultra-short (femtosecond duration) bright x-ray sources with low construction and running cost. The experimental applications of an ultra-fast x-ray source, ranging from medical imaging to material science [1-10], need ultra-short x-ray probes to obtain time-resolved information. For example, x-ray pulses of few tens of femtoseconds allow one to investigate the structure of complex molecules, and study the phenomena relevant to non-linear physics [7, 10]. The growing scientific interest in the ultra-fast x-ray source has led to the advancement of radiation sources as a result of the acceleration of electrons with a conventional large-scale accelerator third generation low emittance storage ring, as well as development of fourth generation sources [11] which are large central facilities. The barrier of the minimum pulse length of the x-ray pulse which was limited to about a few tens of picoseconds was overcome by the x-ray free electron lasers (XFELs) and it became possible realize much shorter x-ray pulses of duration ~ 10 fs [9, 10]. The sources based on third generation low emittance storage rings are extensively used for studying relatively slow phenomena such as structures of short-lived species, their formation, and decay kinetics [7]. The time resolved x-ray diffraction experiments such as creation and diagnosis of solid density plasma, photoionization x-ray laser etc. are being planned at LCLS at SLAC and the XFEL at Hamburg is slated to become fully functional sometime in 2015 [9-11]. However, their construction and running costs are extremely high, and the beam time access will be very limited. Hence, it is prudent to look for the relatively easy-to-set-up ultra-fast (sub-ps) x-ray source in a laboratory.

Ultra-fast laser induced plasma x-ray source is suitable alternative which is easy to set up in the laboratory due to the availability of compact, ultra-short pulse, high power laser systems. When a high power pulsed laser beam is focussed on a solid target, a high density, high temperature plasma is formed on the surface of the target. This hot, dense plasma is an x-ray source. The plasma so created is unique since no other plasma source on laboratory scale can achieve a density close to the solid density, and temperature of the order of millions of Kelvin. Such a plasma is the most promising high brightness source of ultra-short x-ray radiation [12] for many scientific investigations in laser driven inertial confinement fusion [13, 14], x-ray laser [15], coherent high order harmonic generation [16, 17] and technological applications for microlithography [18], phase contrast imaging [19] , contact x-ray microscopy of biological cells [20], backlighting of imploding pellets etc. [21, 22], time resolved x-ray diffraction studies for probing impulsive strain and lattice dynamics [2-4] etc. Quantitative analysis of the keV x-ray spectrum in is often used to derive diagnostic information [23, 24] on electron temperature, density, ionization states, and expansion velocity of the plasma. With the developments in laser technology, ultra-high intensities up to 10^{21} W cm⁻² are readily achieved. This paves the way for many exciting research areas ranging from particle acceleration [25, 26] to nuclear reactions (for example (γ , n) reactions [27] and photo-fission of actinides [28]).

In this thesis, spectroscopic studies of the x-ray emission from laser-produced plasmas have been used for both scientific studies (laser matter interaction), and its technological applications. For carrying out the work, the required x-ray spectrographs were made in house. An on-line x-ray crystal spectrograph with an x-ray CCD camera as detector was made for the high resolution measurements of the x-ray emission from the plasma and used for recording the high resolution x-ray emission spectrum in the range of 1-8 keV described in the thesis. A dispersion-less spectrograph based on the x-ray CCD camera operation in the

single photon counting mode was designed, set up, and characterized. A detailed x-ray spectroscopic study of the plasmas generated from nanosecond and picosecond laser pulses has been carried out to investigate the dynamics of x-ray emission. A comparative study of the keV x-ray emission from gold-copper mix-Z targets of different atomic compositions has been carried out to outline the role of a high-Z impurity in the x-ray emission. The x-ray emission from plasmas produced by the interaction of 45 fs Ti: sapphire laser pulses has been investigated. In this study, both ionic line radiation and inner-shell line radiation were simultaneously measured and the conditions prevalent during the emission of the x-rays have been identified by comparing the experimental spectra with the synthetic spectra generated using a spectroscopic code. A study on the 2ω and $3/2\omega$ harmonic generation in the ultra-short, high-intensity laser-plasma interaction as a diagnostics for pre-formed plasma has been carried out. A correlation of the K- α x-ray line shape with the 2ω and $3/2\omega$ emission is also shown. The K- α line emissions between 1–8 keV, from Mg, Ti, Fe and Cu solid targets, has been studied using ultra-high intensity 45 fs laser pulses. The K- α x-ray probe of different photon energies was used to derive information about the strain over a greater crystal depth. The dynamics of the strain propagation has been inferred by monitoring the evolution of the rocking curve width of the shocked sample at different time delays between the pump and the probe pulse.

We start this chapter with a brief introduction to the general features of the plasma state followed by a discussion of the important properties of plasma produced by laser ablation. In particular, the physical processes related to the ionization equilibrium of plasma and to the emission of x-ray radiation are described.

1.1 Plasma

Plasma is one of the four fundamental states of matter. Plasmas are by far the most common phase of ordinary matter in the universe, both by mass and by volume, and it constitutes approximately 99% of all observable matter in the universe. It has no definite form or volume making it closely related to the gas phase. Although it differs in number of ways for instance, in ordinary gas, collisions control the particle motion but, in plasma the behavior of particles in some region of plasma depends not only on local conditions but on the state of the plasma in faraway regions as well because of the electromagnetic forces associated with the charged particles. Plasma therefore described as a quasi-neutral mixture of electrons, ions and neutral exhibiting collective behaviour [29, 30]. The term quasi-neutral implies that there can be charge imbalance over the length scale represented by Debye length, as we would see in the discussion below.

The collective behavior exists since plasma is conductive and the electrons and ions respond to the electric and magnetic fields and particle in the plasma moves according to the forces produced by the interaction between its charge and the electromagnetic fields within the plasma. The electrons are highly mobile under the influence of the electromagnetic fields in comparison to ions because of their smaller mass. This leads to each ion being surrounded by a number of electrons to ensure that the densities of positive and negative charges in any sizeable region are equal. However, on the scale of the Debye length (λ_D) there can be charge imbalance [29 - 31]. This parameter gives the distance over which the electrostatic potential due to a single charge is screened by the surrounding charges. It is the radius of a sphere called Debye sphere, in which there is an influence of the electrostatic field of the ion, and outside of which enough electrons are present so ion charges are screened and charge neutrality is nearly maintained under equilibrium condition in plasma. It is defined by [30]

$$\lambda_D = \frac{\epsilon_0 k T_e}{n e^2} \quad (1.1)$$

$$\lambda_D (\text{cm}) = 7.43 \times 10^2 \sqrt{\frac{T_e (\text{eV})}{n_e (\text{cm}^{-3})}} \quad (1.2)$$

where n , e and T_e are the density, the electron charge, and the temperature of the electrons respectively in the plasma. Hence for Debye shielding to be a statistically meaningful concept there should be enough electrons in a Debye sphere i.e. the number of particles (N_D) within Debye sphere should be large. Mathematically it is described as $N_D = n \frac{4\pi}{3} \lambda_D^3$, where n is the electron density.

It has been discussed above that plasma is quasi neutral macroscopically. When plasma is instantaneously disturbed from the equilibrium condition, the resulting internal space charge fields (due to Coulomb forces) rearrange themselves collectively such that it tries to maintain original charge neutrality. If the electrons in plasma are displaced from a uniform background of ions, the electric field will built up in such a way, so as to restore the neutrality of plasma by pulling the electrons back to their original positions. However, due to their inertia, the electrons will overshoot and oscillate around their equilibrium positions with a characteristic frequency known as the plasma frequency [29 – 31]. For this description to be valid and an ensemble to behave as plasma, it is required that the collision frequency of particles must be less than the plasma frequency.

The plasma frequency ω_p is given by [29]

$$\omega_p = \left[\frac{n_e e^2}{\epsilon_0 m} \right]^{1/2} \quad (1.3)$$

By substituting physical constants, we can get formula for plasma frequency as

$$\omega_p \left(\frac{\text{rad}}{\text{s}} \right) = 56.4 \sqrt{n_e (\text{cm}^{-3})} \quad (1.4)$$

The inverse of this frequency (ω_p^{-1}) is the time-scale in which electrons respond to external perturbations. The field with a frequency of less than the plasma frequency is shielded by the plasma by the more rapid electron response. It is thus a plasma parameter that plays an important role in the propagation of electromagnetic waves in the plasma.

The criteria for a system to be described as plasma are described in terms of the basic plasma parameters [29 - 31].

1. The dimensions of the entire plasma (L) should be much larger than the Debye length.

i.e. $L \gg \lambda_D$

This condition is to satisfy the quasi-neutrality condition in the plasma.

Taking an example of laser produced plasma with a typical electron density $n_e = 10^{21} \text{ cm}^{-3}$ and an electron temperature $T_e = 100 \text{ eV}$, value of λ_D comes out to be 23.5 \AA .

This is much smaller than the typical plasma size of 100 microns.

2. The number of particles (N_D) within the Debye sphere should be large.

i.e. $N_D \gg 1$

Mathematically, this number is given by $N_D = n \frac{4\pi}{3} \lambda_D^3$, where n is the electron

density. For $n_e = 10^{21} \text{ cm}^{-3}$ and $\lambda_D = 23.5 \text{ \AA}$, N_D comes to be 54, which is $\gg 1$

The condition $N_D \sim n \lambda_D^3 \gg 1$ means that the average distance between the ions, which is roughly given by $n^{-1/3}$, must be very small compared to λ_D .

3. Since ω_{pe} is the characteristic frequency of the collective oscillation of the electrons, it is required that it should be more than the frequency of collisions, so that the collective behavior can be sustained. This means

$$\omega_p \tau \gg 1$$

where τ is the mean time between the collisions.

In short, for a quasi-neutral ensemble of charge particles to be called a plasma, it has to satisfy the following three criteria :

$$1) L \gg \lambda_D; \quad 2) N_D = n_e \lambda_D^3 \gg 1; \quad \text{and } 3) \omega_p \tau \gg 1$$

1.2 Waves in plasma

An un-magnetized plasma can support the propagation of longitudinal electron and ion waves, associated with oscillations of the charge density [31]. Due to the difference in mass between electrons and ions, their respective oscillations have a quite different behaviour. An introduction to the wave propagation is presented in this section.

A) The *electron plasma waves* are the longitudinal oscillations of the electron density. It is also called *Langmuir waves* or *plasma waves* [32]. As these are high frequency oscillations, the ions, due to their inertia, can be regarded as a fixed background. The wave equation for the electron plasma wave can be set up by starting from fluid theory equations of motion and by applying the continuity equation and the Poisson's equation to the electron fluid. The dispersion relation is given by [31- 33]

$$\omega^2 = \omega_p^2 + k^2 v_{th}^2 \tag{1.5}$$

where ω_p is the electron plasma frequency ω and k are the frequency and wave vector of the electron plasma wave. The frequency of the electron plasma wave is more than or equal to the plasma frequency. Further, the electron plasma wave frequency depends dominantly on the electron density in the plasma and weakly on its wave vector and on the temperature.

B) The lower frequency longitudinal waves arising due to the periodic fluctuation of the ion density are called *ion acoustic waves* [31]. The electrons closely follow the ions in order to preserve the charge neutrality. The wave equation for ion acoustic wave is treated in the same way as for the electron plasma wave, but for the ions. The dispersion relation obtained from the wave equation is given as

$$\omega = k \left(\frac{KT_e}{m_i} + \frac{\gamma KT_i}{m_i} \right)^{\frac{1}{2}} = kC_s \quad (1.6)$$

where $C_s = \left(\frac{KT_e}{m_i} + \frac{\gamma KT_i}{m_i} \right)^{\frac{1}{2}}$ is called the ion sound or ion acoustic speed.

It can be noted from the Eq.1.6, this wave is similar to a sound wave. Therefore, these waves are also known as ion sound waves. The ion acoustic wave frequency is small compared to that of the electron plasma wave.

Both of these waves are electrostatic waves because the electric field is generated due to displacement of the charge. The electric field can be very high (> 1 GV/ cm) for electron plasma waves and they are used to accelerate electrons [25, 34] to a very high energy over a small distance.

C) The propagation of an *electromagnetic wave* in a plasma follows the dispersion relation [31]

$$\omega^2 = \omega_p^2 + k^2 c^2 \quad (1.7)$$

The phase velocity of electromagnetic wave in plasma is given by

$$v_{\phi} = \frac{\omega}{k} = \frac{c}{\sqrt{1 - (\omega_p^2/\omega^2)}} \quad (1.8)$$

The plasma behaves as a dielectric medium with refractive index given by

$$\eta = \frac{c}{v_{\phi}} = \sqrt{1 - (\omega_p^2/\omega^2)} \quad (1.9)$$

This relation implies that an electromagnetic wave at frequency ω can propagate inside the plasma only in regions where $\omega > \omega_p$. In the regions $0 < \omega < \omega_{pe}$, an electromagnetic wave will not be able to enter the plasma. At $\omega = \omega_p$, the electromagnetic wave will be reflected back completely.

The dispersion relations on the dispersion curve can be represented on the energy-momentum diagram as shown in Fig. 1.1. Any decay processes leading to the conversion of an electromagnetic wave to the electron plasma waves and / or ion acoustic waves, can be represented through these curves [30].

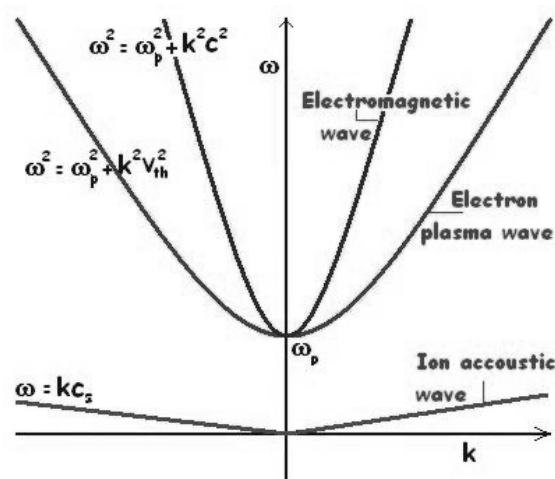


Fig. 1.1: The dispersion curves for electromagnetic wave, electron plasma wave, and ion acoustic wave.

1.3 Laser produced plasma

When a high power pulsed laser beam is focussed on a solid target, a high density, high temperature plasma is formed on the surface of the target. Most of the initial ionization occurs through multi-photon ionization, tunneling, and over-the-barrier mechanisms, depending on the intensity and the laser pulse duration [30]. The electrons generated by various ionization mechanisms oscillate under the laser electric field and collide with the surrounding ions, thereby randomizing their motion (velocity) and also ionizing the ions further. This is repeated at a rapid rate leading to catastrophic breakdown (ionization) of the medium. The free electron population increases exponentially during this process. The catastrophic breakdown of the medium leads to the formation of plasma in front of the target and the laser energy is absorbed with even higher efficiency because of the different absorption mechanisms of plasma [29]. The interaction of the radiation depends on the duration of the laser pulse. For long laser pulses (\sim ns) with sufficient energy density, the plasma formation initiates in the rising part of the laser pulse and the rest of the laser pulse interacts with plasma.

The plasma expands rapidly away from the target surface and therefore large spatial gradients in plasma parameters are formed along the direction of plasma expansion. The density decreases with distance from the target surface. A great variety of laser - matter interaction processes such as ionization, propagation of incident laser, generation of plasma wave, and the subsequent hydrodynamic evolution of the plasma can take place at different positions along the longitudinal direction having widely different density and temperature [12, 35]. The laser generated plasmas last typically for the time of the order of laser pulse duration [35]. The hydrodynamic codes have shown that density evolves rapidly from near solid density (10^{23} cm⁻³) to a vacuum level (10^{17} cm⁻³) over a distance of a few hundred

microns, on a time scale of about a nanosecond. Therefore controlled experiments for interpretation of transient plasma is a challenging task [12, 35].

There is another important parameter called density scale length, which is defined as a distance over which the density of the plasma decreases by a factor of $1/e$. In general, for any density profile, density scale length L , is defined as $L = \frac{n}{dn/dx}$ where x is the direction of propagation of the laser light [35]. The density scale length depends on the laser pulse duration. For a longer laser pulse (≥ 1 ns), the plasma gets sufficient time to expand as compared to that formed by ultra-short laser pulses (\sim fs) where the density gradient will be steeper. The effective plasma length encountered by the laser pulse is important in many mechanisms of absorption of laser energy. The laser - matter interaction may be divided into two regimes viz. long pulse laser – matter interaction and short pulse laser – matter interaction as described in the following subsections.

1.3.1 Long pulse laser - matter interaction

The threshold intensities for generation of plasma depend upon the pulse duration and it is usually 10^{8-9} W cm⁻² for ns / sub-ns laser pulses [35-36]. The process of production of plasma is as follows: at first the target material absorbs some laser light. The surface electrons and the electrons produced by multi-photon ionization would gain energy. The material gets ionized and it evaporates forming a plasma. Subsequent part of the pulse heats up this plasma and produces more plasma from the target due to cascade process, in which the collisions between the free electrons and neighbouring atoms facilitate further ionization. This heated plasma, due to its large $n_e K T_e$ pressure, rapidly expands outwards to form an outwardly monotonically decreasing density profile [37].

In laser-irradiated planar targets with a finite-size focal spot, the plasma expansion may be considered to be nearly planar to an expansion distance d of the order of focal spot radius r_0 as schematically represented in Fig. 1.2. The plasma expansion time to reach this

position is $t_{\text{exp}} = r_0 / c_s$, where $c_s = \frac{2}{\gamma-1} \left[\frac{ZkT_e}{m_i} \right]^{\frac{1}{2}}$ is the sound speed in plasma. For $t_L \ll t_{\text{exp}}$,

the plasma expansion would remain nearly planar and its expansion distance will be much smaller than r_0 . The typical sound speed for the temperature of few hundred eV is of the order of 10^7 cm/sec. Considering a focal spot diameter of a few tens of microns, the plasma expansion time comes out to be of sub-ns duration. Therefore, in the case of ns duration pulses, the density scale length is taken equal to the focal spot radius [38].

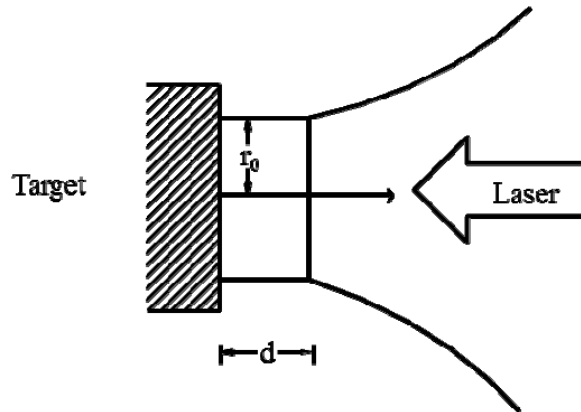


Fig. 1.2: *Plasma expansion geometry.*

In general, the physical structure of the plasma produced by nanosecond/sub nanosecond laser pulses from solid targets may be described by Fig. 1.3, which shows typical spatial profiles of electron density (n_e) and electron temperature (T_e). The laser beam can propagate upto a maximum density n_c , called the critical density, given by $n_c = 1.1 \times 10^{21} \lambda_L^{-2}$ (μm) cm^{-3} , where λ_L (μm) is the wavelength of the laser in vacuum [12, 35]. The region of plasma up to critical density is thus directly heated by absorption of the laser energy and it is

referred to as coronal region. The absorbed laser energy is then transported as heat via thermal conduction and radiation transport in to the over dense region. The x-ray emission occurs from either side of the critical density surface, as governed by the density and temperature in the coronal and overdense regions [12, 35].

There are three major processes of laser light absorption in laser produced plasmas viz. 1) Inverse bremsstrahlung, 2) Resonance absorption, and 3) Parametric decay instability.

1.3.1.1 Inverse bremsstrahlung

The radiation emitted by a charged particle during collision with another particle is customarily called bremsstrahlung as it was first detected during stopping of high-energy electrons in thick metallic targets. In inverse bremsstrahlung absorption, the electrons take energy from the oscillating electric field of the laser and get randomly scattered by the ions [12, 35, 39]. Thus the laser energy is converted into thermal energy of particles, resulting in laser light absorption in the plasma.

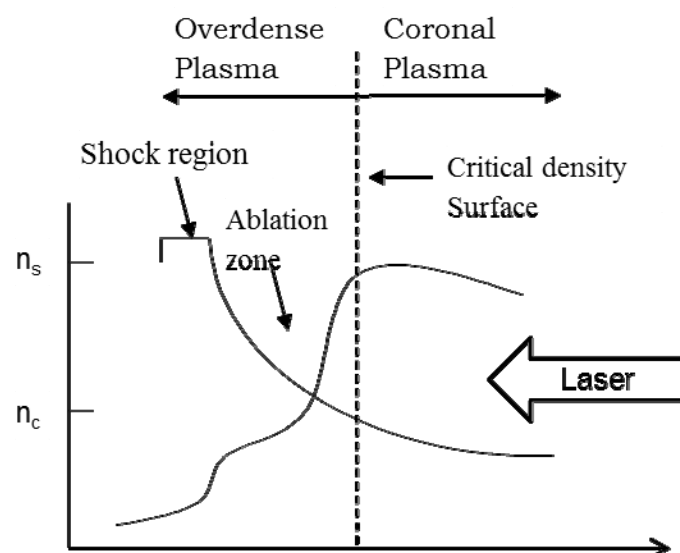


Fig. 1.3: A schematic of electron density and temperature spatial profile depicting various zones in LPP.

To visualize the role of these collisions in coupling the laser energy to the plasma, we consider a simple model [29]. In this model we consider i) the plasma to be infinite and homogeneous, ii) the ions are immobile, iii) no external static electric and magnetic field is present, iv) thermal motion of the electrons is neglected, and v) the quantities do not evolve with time.

Under these assumptions, the equation of motion for the electrons can be written as

$$\frac{dv}{dt} = -\frac{eE}{m_e} - \frac{v}{\tau_c}.$$

Here $\tau_c (= \nu_{ei}^{-1})$ is the effective time between the electron-ion collisions and ν_{ei} is the electron-ion collision frequency. τ_c can be expressed as

$$\tau_c = \nu_{ei}^{-1} = \frac{3}{4} \frac{(k_B T_e)^{3/2} m_e^{1/2}}{(2\pi)^{1/2} Z_i^2 e^4 n_i \ln \Lambda} = 3.44 \times 10^5 \frac{T_e (\text{eV})^{3/2}}{Z_i^2 n_i \ln \Lambda} [\text{s}]; \Lambda \equiv \frac{\lambda_D}{l_{\min}} \quad (1.10)$$

where, n_i is the ion density, Z_i is the degree of plasma ionization, T_e is the electron temperature, $\ln \Lambda$ is the Coulomb logarithm, λ_D is the Debye length and l_{\min} is the minimum impact parameter defined by the classical distance of closest approach between an electron and ion.

The dispersion relation for an electromagnetic wave in plasma, including the effect of collisions can be obtained by solving Maxwell's equations in free space containing the electric charge and the electric current, similar to the derivation followed earlier. After simplification, one gets the dispersion relation:

$$k^2 = \frac{\omega_L^2}{c^2} - \frac{\omega_p^2}{c^2 (\omega_L + i\nu_{ei})} \quad (1.11)$$

Therefore, the spatial damping rate of the laser energy by collisional absorption, κ_{ib} , can be expressed as:

$$\kappa_{ib} = 2\text{Im}\kappa = \left(\frac{v_{ei}}{c}\right) \left(\frac{\omega_p^2}{\omega_L^2}\right) \left(1 - \frac{\omega_p^2}{\omega_L^2}\right)^{\frac{1}{2}} \quad (1.12)$$

Using the definition of critical density, $n_{cr} = \frac{m_e \omega_L^2}{4\pi e^2}$, the laser energy damping rate can be written as:

$$\kappa_{ib} = \frac{v_{ei}(n_{cr})}{c} \left(\frac{n_e}{n_{cr}}\right)^2 \left(1 - \frac{n_e}{n_{cr}}\right)^{\frac{1}{2}} \quad (1.13)$$

It can be seen from the dependence of κ_{ib} on n_e/n_{cr} that a significant fraction of absorption takes place in the vicinity of critical density, $n_e/n_{cr} \approx 1$. Now consider the change in laser intensity I , as it passes through a slab of plasma in Z (laser propagation) direction. The change in laser intensity can be expressed as $\frac{dI}{dz} = -\kappa_{ib}I$. For a slab of plasma of length L , the absorption coefficient α_{abs} can be written as

$$\alpha_{abs} = \frac{I_{in} - I_{out}}{I_{in}} = 1 - \left(-\int_0^L \kappa_{ib} dz\right) \quad (1.14)$$

where I_{in} and I_{out} are the incoming and outgoing laser intensities respectively. For weak absorption case ($\kappa_{ib}L \ll 1$), $\alpha_{abs} \approx \kappa_{ib}L$, and for strong absorption case, $\alpha_{abs} \rightarrow 1$.

It should be noted that for an inhomogeneous plasma, the expression for rate of energy deposition is far more complicated as it not only depends on the electron density and plasma temperature, which in turn depend on the time evolution of the expanding laser

produced plasmas. Now for a linear density profile, $n_e = n_c \left(1 - \frac{z}{L}\right)$; $0 \leq z \leq L$; the absorption coefficient can be expressed as

$$\alpha_{\text{abs}} = 1 - \exp \left\{ -\frac{32}{15} \frac{v_{ei}(n_{\text{cr}})L}{c} \right\} \quad (1.15)$$

Similarly for an exponential density profile: $n_e = n_{\text{cr}} \exp\left(-\frac{z}{L}\right)$; the absorption coefficient can be expressed as

$$\alpha_{\text{abs}} = 1 - \exp \left\{ -\frac{8}{3} \frac{v_{ei}(n_{\text{cr}})L}{c} \right\} \quad (1.16)$$

At high laser intensities, the large electric field of the laser can distort the thermal distribution of the electrons, therefore changing the v_{ei} . In this case, it can be shown that κ_{ib} depends on the laser intensity. In presence of strong electric field the electron mean square velocity can be written as $v_{\text{eff}} = \sqrt{(v_{\text{th}}^2 + v_E^2)}$. Since, κ_{ib} scales as $T_e^{-3/2} \mu_e \left[v_{\text{eff}}^{1/2} \right]^{-3}$, at higher laser intensities κ_{ib} can be written as

$$\kappa_{ib} \rightarrow \frac{\kappa_{ib}}{\left[1 + \left(\frac{v_E^2}{v_{\text{th}}^2} \right) \right]^{3/2}} \propto \frac{1}{E_L^3} \propto \frac{1}{I_L^2} \quad (1.17)$$

for $v_E/v_{\text{th}} > 1$. For $v_E/v_{\text{th}} < 1$, the expression can be written as

$$\kappa_{ib} \rightarrow \frac{\kappa_{ib}}{1 + \frac{3}{2} \left(v_E^2 / v_{\text{th}}^2 \right)} \quad (1.18)$$

It follows from this equation that the shorter wavelength lasers and high-Z targets result in a better absorption of laser light by the process of inverse bremsstrahlung. In fact, the inverse bremsstrahlung is the dominant process of laser energy absorption for laser intensity $I_L \leq 10^{13}$ W/cm². The collisional absorption process is polarization independent, although the maximum absorption occurs at normal incidence and reduces with increase in the angle of incidence. The collisional absorption increases with increasing density scale length [40]. For the same laser energy, the efficiency of collisional absorption decreases with reduction in the laser pulse duration. This is due to the fact that with the increase in laser intensity the electron temperature increases and the electron ion collision rate decreases.

1.3.1.2 Parametric Decay Processes

At higher intensities, the laser energy couples to the plasma by resonance absorption and excitation of various plasma modes [29]. When the excited plasma modes are such that they propagate out of the plasma, it constitutes a loss of energy, and if these modes are subsequently damped inside the plasma, it leads to absorption. In the parametric decay instability, the electromagnetic wave couples energy to resultant plasma modes viz. electron-plasma wave and an ion acoustic wave. The growth rate of these collective modes largely depends on the interaction length governed by the plasma density scale length. In general, longer duration laser pulses producing a large density scale length plasma result in a higher growth of various scattering modes [41]. The dispersion relations for waves supported by plasma were discussed in the section 1.2.

Depending on the mode of decay of incident electromagnetic the processes can be classified as [29, 30]

a) Parametric decay process: In this process, the incident electromagnetic wave decays into an electron plasma wave and an ion acoustic wave i.e. $\omega_{em} = \omega_{ep} + \omega_{ia}$. This implies, $\omega_L = \omega_p [1 + 3k_{ep}^2 v_{th}^2 / \omega_p^2]^{1/2} + K_{ia} c_s \geq \omega_p$. Therefore, $\omega_p \leq \omega_L$ implying $n_e \leq n_c$ i. e. the parametric decay instability takes place up to the critical density layer. The dispersion curve for this process is shown in Fig. 1.4.

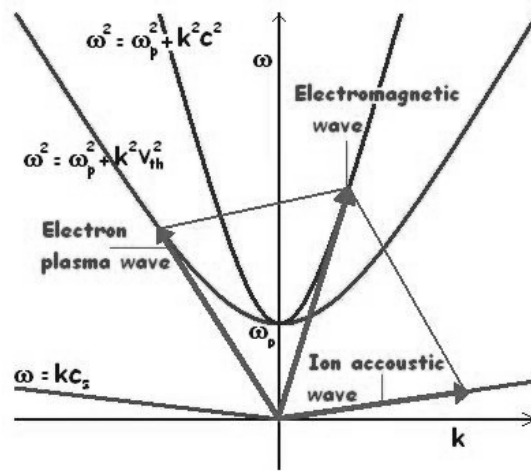


Fig. 1.4: Dispersion curves depicting the process of parametric decay.

b) Two plasmon decay: In this process the electromagnetic waves decay into two plasma waves i. e. $\omega_{em} = \omega_{ep1} + \omega_{ep2}$. This implies $\omega_L = \omega_p [1 + 3k_{ep1}^2 v_{th}^2 / \omega_p^2]^{1/2} + \omega_p [1 + 3k_{ep2}^2 v_{th}^2 / \omega_p^2]^{1/2} \geq 2 \omega_p$. Therefore considering the extremes, $\omega_p \leq \omega_L / 2$ i. e. $n_e \leq n_c / 4$. Therefore the two plasmon decay can take place only up to the critical density. The dispersion curve for this process is shown in Fig. 1.5.

There are two more decay processes which can lead to partial absorption and reflection of the laser light. These processes are known as stimulated Brillouin scattering (SBS) and stimulated Raman scattering (SRS).

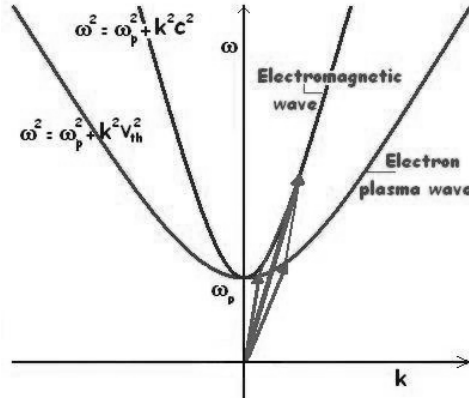


Fig. 1.5: Dispersion curves for Two Plasmon Decay.

c) Stimulated Brillouin scattering: In this process, the incident electromagnetic wave excites an ion acoustic wave and the rest of the energy is scattered as an electromagnetic wave i.e. $\omega_{em}(\text{incident}) = \omega_{em}(\text{scattered}) + \omega_{ia}$. Therefore, one has $\omega_L = \omega_p [1 + k_s^2 c^2 / \omega_p^2]^{1/2} + k_{ia} c_s \geq \omega_p$. This implies $\omega_L \geq \omega_p$ i.e. $n_e \leq n_c$. In other words, this process can occur up to the critical density surface. The dispersion relation is shown in Fig. 1.6.

d) Stimulated Raman scattering: In this process, the incident electromagnetic wave excites an electron plasma wave and the rest of the energy is scattered as an electromagnetic wave i. e. $\omega_{em}(\text{incident}) = \omega_{em}(\text{scattered}) + \omega_{ep}$. This implies $\omega_L = \omega_p [1 + k_s^2 c^2 / \omega_p^2]^{1/2} + \omega_p [1 + 3k_{ep}^2 v_{th}^2 / \omega_p^2]^{1/2} \geq 2 \omega_p$. Therefore, $\omega_L \geq 2 \omega_p$ i. e. $n_e \leq n_c / 4$. Therefore this process can take place only up to the critical density. Unlike in the case of stimulated Brillouin scattering where one has only backward scattering, in this case, one can have Backward Raman Scattering as well as Forward Raman Scattering. The dispersion curves for both these cases are shown in Fig. 1.7 (a) and (b) respectively.

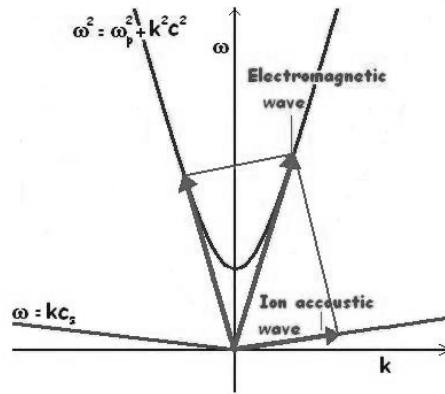


Fig. 1.6: Dispersion curve depicting Stimulated Brillouin Scattering.

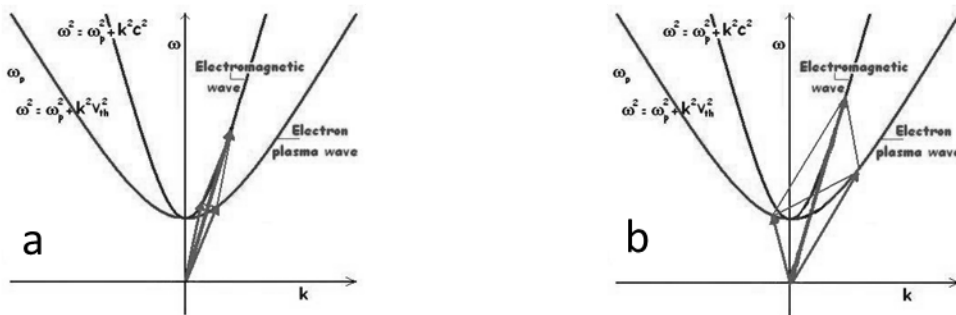


Fig. 1.7: Dispersion curves for the (a) Forward (b) Backward Raman Scattering.

In Solid State Physics, the stimulated Brillouin scattering implies scattering of electromagnetic waves by acoustic phonons (ion acoustic wave in plasma) while the stimulated Raman scattering is the result of scattering of electromagnetic waves by optical phonons (electron plasma wave). The typical length scale involved for the parametric decay processes is shown in Fig. 1.8.

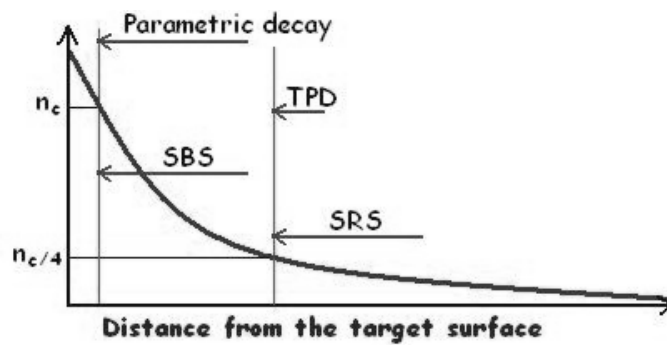


Fig. 1.8: The typical length scale involved for the parametric decay processes.

The waves in plasma scatter the incident laser light at appropriate frequency satisfying the conservation laws. The incident and scattered waves can produce beat frequency of $\omega_L - \omega_S$ which is exactly equal to the plasma wave. The ponderomotive force in the longitudinal direction of the beat wave will have a wavelength exactly equal to the plasma wave. As the frequency and direction of perturbation matches with the wave, the wave amplitude grows. This wave will scatter more of incident light, thereby increasing the intensity of the scattered light. As a result the ponderomotive force of the beat wave will also increase. Due to this cyclic positive feedback loop, the plasma wave and the scattered wave grow in amplitude at the cost of incident light. As the incident laser light stimulates the growth of the plasma wave as well as the scattered wave, these processes are called stimulated processes [42].

SRS and SBS are threshold processes. Since they depend on excitation of plasma waves, they take place only when $\langle \text{Oscillatory energy of plasma wave} \rangle / \langle \text{Random (Thermal) energy} \rangle \geq 1$. Let the electric field of the electromagnetic field be $E = E_0 \cos \omega t$. The quiver velocity of the electrons under the electromagnetic wave can be expressed as $v = [eE_0/m\omega] \sin \omega t$. Therefore the oscillatory energy of the electromagnetic radiation is $\frac{1}{2} m v^2 \propto E^2/\omega^2 \propto I\lambda^2$. Therefore to satisfy the threshold condition $\alpha I\lambda^2 \geq 1$ i. e. $I\lambda^2 \geq 1/\alpha$. α is proportionality constant which depends on the wave involved. Depending on the value of α (i. e. the wave involved) the process has a threshold on intensity. For SBS, the threshold is given by $I\lambda^2 \geq 10^{13} \text{ W cm}^{-2} \mu\text{m}^2$ and for SRS, the threshold is given by $I\lambda^2 \geq 10^{14} \text{ W cm}^{-2} \mu\text{m}^2$ [42].

The resonance absorption mechanism will be discussed in the next section.

1.3.2 Short pulse laser - matter interaction

When an ultra-short laser pulse is incident on a solid target, solid density plasma is generated by the initial fraction of the pulse. This plasma cannot expand significantly during the laser

pulse (due to the very short time involved) and rest of the interaction occurs with the near solid density plasma, as depicted in the Fig. 1.9. Hydrodynamic simulations have shown that the gradient scale length L can be much smaller than the laser wavelength with lasers of ~ 100 fs duration and typical expansion velocities in the 10^7 cm/s range [43]. The absorption occurs within a layer thickness of a skin depth (~ 10 nm) [36]. Typically, in interactions where the laser intensity exceeds 10^{15} Wcm $^{-2}$, the collisionless processes become the dominant mechanisms of energy absorption. The most prominent processes are the resonance absorption, the vacuum/Bruneel heating [29] and the $j \times B$ heating.

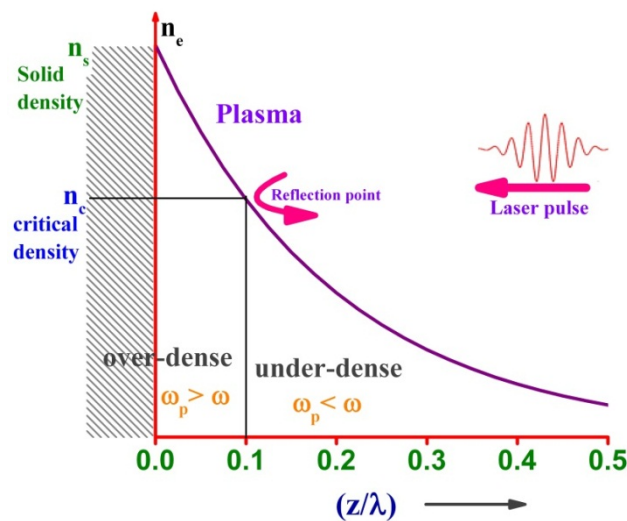


Fig. 1.9: A schematic representation of electron density variation in ultra-short laser produced plasma.

a) Resonance absorption: This is a process which occurs when a p-polarized light wave is incident obliquely on the plasma with a density gradient. As depicted in Fig. 1.10, the laser, that is incident on the plasma at an angle θ is reflected at lower density given by $n_e = n_c \cos^2(\theta)$. The evanescent wave excited by the reflected wave in the overdense region has longitudinal as well as tangential components, with a frequency equal to the laser light frequency. The component of this evanescent wave in the direction of the density gradient

resonantly excites plasma wave at the critical density surface [12, 44]. The plasma wave can grow resonantly over several laser oscillations and then transfers its energy to the plasma through wave breaking, collisional damping, or Landau (collisionless) damping [45]. The efficiency of the resonance absorption process depends on the plasma scale length and the angle of incidence.

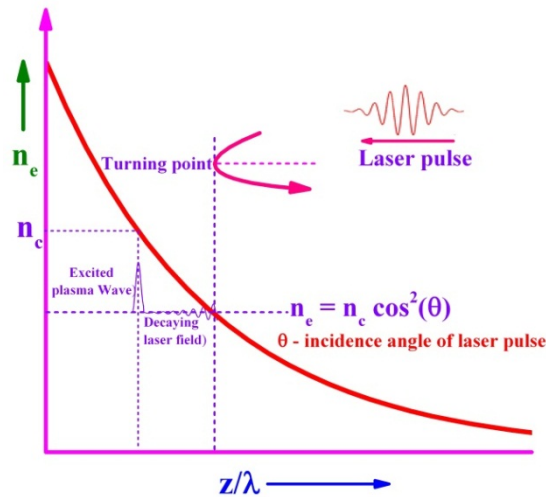


Fig. 1.10 A schematic representation of resonance absorption of obliquely incident p-polarized light.

In the resonance absorption, as mentioned above, the strong electron plasma wave transfers its energy to [45] plasma by collisions, collisionless mechanisms [45] such as Landau damping, wave breaking etc. Of these, Landau damping is a collisionless mechanism which couples the energy from the electron plasma wave to the plasma. Consider a plasma wave with a phase velocity $v_{ph} = \omega/k$ propagating in the plasma. The plasma with a finite temperature will have free electrons with velocity distribution according to the plasma temperature. If the electron velocities are far from the plasma wave velocity, then they will not interact with this propagating plasma wave. However, those electrons whose velocity lies closely to the plasma wave velocity, will interact with the wave. The electrons having a little higher velocity than the wave velocity will lose their energy to the wave, whereas the

electrons having a little lower velocity will gain energy from the wave. The electrons in the plasma have Maxwell's velocity distribution $n(v) = n_0 \exp\left(-\frac{1}{2}mv^2/k_B T_e\right)$ where, $n(v)$ represents the number of electrons having a velocity distribution lying between v to $v+dv$, m is the mass, k_B is the Boltzmann constant and T_e is the temperature. Hence, the number of electrons having velocity smaller than the plasma wave phase velocity will always be larger than those having larger velocity than the plasma wave. Therefore, the electrons will gain net energy from the wave. Therefore wave gets damped as it loses energy to electrons by Landau damping.

b) Brunel or vacuum heating: Resonantly driven plasma waves are not able to survive when the amplitude of the electron oscillations exceed the plasma scale length. It happens when the density gradient is less than λ , which is the case for plasma produced by ultra-short pulse lasers. In such a case, it was proposed by Brunel [46] in 1987 that an electron at this sharp plasma-vacuum interface is first accelerated by the laser electric field into the vacuum. When the field of the laser reverses, the electron is pushed back into the plasma. The electron penetrates deeper into the plasma eventually thermalizes by subsequent collisions. This mechanism is most efficient for ultra-short laser pulses as longer pulses tend to produce plasmas with longer scale length density gradients. For steep density gradients, the scale length of the pre-plasma becomes comparable to the skin depth for the laser. Under those conditions, electrons in the plasma can be easily pulled out in the vacuum by the electric field of the laser and then sent back into the target to undergo a large amount of kinetic energy loss.

c) $\mathbf{j} \times \mathbf{B}$ heating: For ultra-high intensities, the electron motion becomes relativistic and is dominated by the $\mathbf{v} \times \mathbf{B}$ term of the Lorentz force [47, 48]. The ponderomotive force of the laser can be written as [48]

$$f_{pond} = -\frac{\partial}{\partial x} \left(\frac{mv_{osc}^2}{2} \frac{4\omega_0^2}{\omega_{pe}^2} \exp^{\frac{2\omega_{pe}}{c} x} \left[\frac{1 + \cos 2\omega_0 t}{2} \right] \right) \quad (1.19)$$

Here, the heating is due to the component of the $\mathbf{j} \times \mathbf{B}$ force that causes oscillations of the electrons at the vacuum-plasma interface with a frequency of twice the laser frequency. It may be noted that the magnitude of the force is dependent on $\frac{\omega_0^2}{\omega_{pe}^2}$ or equivalently n_{cr}/n .

Thus, as the electron density increases, the magnitude of the force goes down, and so less energy is transferred to hot electrons. The net result is that the amount of laser light absorbed decreases with increasing density in one dimension. The second term in the equation leads to the heating of electrons and the first term is usual ponderomotive force. This $\mathbf{j} \times \mathbf{B}$ term which works for any polarization other than circular, is most efficient for normal incidence and becomes significant at relativistic quiver velocities.

A second interesting effect arises from the fact that the electron exposed to such a high intensity or electric field oscillates in the direction of the electric field with very high velocity. The energy associated with this velocity can easily reach MeV levels. Therefore, the relativistic effects become important for these interactions. Thus it is clear that the interaction of a short-pulse (fs) with the target (solid or gas) differs substantially from the conventional interactions of the pulses of long duration (ns/ps). Thus, much of the traditional laser-matter interaction physics would not apply to sub-picoseconds interaction.

1.4 Equilibrium in plasma

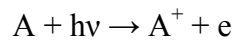
Interpretation of spectral characteristics of emission from the plasma necessitates the knowledge of both, the charge state distribution as well as the excited level population of different ions [12, 23-24, 35]. In general, this requires a solution of a complex system of rate equations, describing the population and depopulation of levels by various processes like

ionization, recombination (radiative or three-body), collisional excitation and de-excitation, radiative decay, absorption etc. The ionization and recombination processes and equilibrium models will be discussed briefly in the following sub-sections.

1.4.1 Ionization and recombination processes

Ionization processes: The ionization is a process in which the electron gets ejected out from the field of an atom when sufficient energy is supplied to it by some external means. This energy can be supplied to the electron either by photons, or by electrons, or by mutual sharing of the energy. The main ionization processes are as follows [24]:

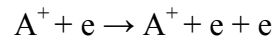
a) Photo-ionization: This is a process of ionization wherein the energy is supplied by a photon. The absorption of the photon by an atom will result in ejection of an electron if the photon energy exceeds the ionization energy of the atom. The electron gets ejected out leaving the atom ionized. It can be represented in the following form



where, A is the atom, A^+ is the ionized atom, $h\nu$ is the photon energy, and e is the ejected electron. Since ionization potentials are generally in the range of 5 to 15 eV, the critical wavelength needed for photoionization lies in the broad range of ~ 800 to 2500\AA , i.e. the vacuum ultra-violet or soft x-ray region. Hence, the electromagnetic radiation in the ultra-violet range or the x-rays or γ rays produce photo-ionization. The probability of occurrence of photo-ionization is rather low and hence the interaction cross-section for this process is very small. The photo-ionization cross-section maximizes sharply at a photon energy just slightly greater than the minimum energy required and falls off rather quickly as the photon energy rises [12]. Photo-ionization is an important process in hot plasmas only if the local radiation field density, that is, the photon density is high enough to induce a sufficiently large rate of

photo-ionization relative to the *collisional ionization*. This occurs only in optically thick plasmas i.e. when it does not allow the radiation to escape from it [12].

b) Collisional ionization: is a process wherein an energetic electron supplies the energy. An electron is ejected out along with the ion and colliding electron. This is represented as



If the mean electron velocity v_e is sufficiently large, some collisions with atoms/molecules will be elastic, some will result in excitation, and others will result in ionization, all depending on the cross-sections. The elastic collisions of electrons and atoms and molecules result in very small electron energy loss because of the small mass ratio (m_e/m_a), the electron losing at most $4 m_e/m_a$ of its energy. Inelastic collisions always result in an electron energy loss, at least equal to the excitation or ionization energy. For electron impact ionization, the incident electron must have initial kinetic energy in excess of the threshold energy for ionization (i.e. the ionization potential). The cross-section for electron-impact ionization (σ) rises steeply from zero just below ionization potential to a maximum of the order of 10^{-16} cm^2 at energy between ~ 3 - 6 times the ionization potential, from which it decreases in an approximately hyperbolic [49].

In a plasma there is distribution of energies and the mean electron energy is $3/2 kT_e$. Therefore, electron impact ionization within a plasma is maximum when the electron temperature is several times the ionization potential of the gas being ionized. At very high electron temperature also, the ionization efficiency will again decrease. In the case of multiple ionization, when one or more electrons are removed from the atom, the ion is said to be multiply ionized, and the ion charge state is then greater than unity, ($Z = 2^+, 3^+, \dots$). Similar to the case where minimum electron energy is needed for removal of the first

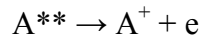
electron to form the singly charged ion, a similar condition applies for formation of the more highly stripped ionization states [50]. The electron must have energy at least equal to the n^{th} ionization potential for formation of ions of charge state $Z = n^+$. The energy needed to create a very highly-stripped ion can be very high, over 100 keV for fully stripped uranium for example. Multiply-stripped ions can be formed, in principle, in two different ways: by a single electron-atom encounter in which many electrons are removed in a single event, or by multiple electron-atom/ion "encounters" in which a single electron is removed at each step and the high charge state is built up by a sequence of many ionizing events. It turns out that both of these processes are possible and do occur, but for most conditions encountered it is the stepwise ionization process that dominates. This simple picture can be further complicated by the formation of metastable states.

Ionization can be caused by the impact of energetic ions with neutral atoms, but the ion energies required are high compared to the electron impact ionization. This is because of the ion-electron mass ratio and the high energy required for the ion to have the same speed as a lower energy electron; the ionization cross-section maximizes when the fast particle has a speed equal to that of the orbital electron to be removed.

As the interaction cross-section between an ion and an electron is much higher than that between a photon and an ion, the rate of occurrence of the collisional ionization is much more than the rate of photo-ionization. For high density and low temperature cases, the interaction cross-section further increases with the increase in collisional ionization [50].

c) Auto-ionization: The process of auto ionization takes place in a doubly excited atom. When the electron (in excited level) from the outer shell of a doubly excited atom comes to the lower level, instead of a photon being emitted, the difference in energy is transferred to

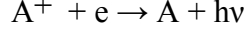
another electron (also in an excited level) and this electron get ejected out from the system. This process is called auto-ionization [51]. This can be written as



where, A^{**} is a doubly excited atom. The probability of existence of doubly excited atoms is low and also it is a highly energy selective phenomena. Due to this reason, the auto ionization is not a dominant process.

Recombination processes: Through recombination processes, an atomic system goes from an initial charged state (positive ion and electron or positive ion and negative ion) to a neutralized state of lower energy. Our discussion here is concerned mainly with electron-ion recombination. In electron-ion recombination, the capture process requires that the electron goes from a free (positive energy) to a bound (negative energy) state, and thus in some manner the electronic energy of the system must be reduced [51]. Hence one must provide a means of removing electronic energy from the system at a ‘recombination’ encounter. This energy may appear in the form of electromagnetic radiation, internal modes of vibration or rotation (if molecules are involved), or translational kinetic energy of the particles participating in the processes. Recombination process can proceed by a direct, two-body interaction or may require the assistance of a third body, such as a neutral molecule or an electron, to take away the excess energy. We first consider processes in which the electron capture by the ion is affected directly at two-body encounter and then discuss processes requiring the assistance of third body for the capture. These processes are discussed in detail in following subsections.

a) Radiative recombination: In this process in which a positive ion combines with an electron and the excess energy is given out as a photon. The process can be represented as follows:



The energy of this emitted photon is given by $h\nu = \varepsilon + \chi_j$, where χ_j is the ionization energy of the shell in which the electron is captured and ε is the kinetic energy of the electron before recombining. Since the kinetic energy of the recombining electron is continuously variable, the energy of the emitted photon is also continuous: i.e. it will be a continuum spectrum. The radiative recombination process is also called two-body recombination as only two bodies are involved in this process. Rate of radiative recombination is given by [24],

$$\partial n_e / \partial t = \alpha_Z n_e n_i \quad (1.20)$$

where α_Z is the radiative recombination rate constant and n_e and n_i are the electron and ion densities respectively.

The radiative recombination coefficient α_Z is related to the recombination (capture) cross-section σ by $\alpha_Z = \langle \sigma v_{\text{rel}} \rangle$. The brackets indicate averaging over the distribution of relative velocities v_{rel} of the charged particles.

The probability of radiative capture depends on the likelihood of a free-bound radiative transition occurring during the electron-ion encounter (collision) [52]. A thermal electron will negotiate the region around the ion (i.e. within $10A$) where strong radiative transitions ($\tau_{\text{rad}} \sim 10^{-8} - 10^{-9}$ s) may be expected in a time $t_{\text{coll}} \sim R/v = 10^{-14}$ s. The probability of capture while moving through this region is therefore $P \sim t_{\text{coll}} / \tau_{\text{rad}} \sim 10^{-6}$ to 10^{-5} . The region itself represents a cross-sectional area somewhat greater than 10^{-14} cm², so that the thermal electron capture cross-section is expected to be of the order of 10^{-19} cm², which is rather small compared even to ordinary gas kinetic cross-section (10^{-16} to 10^{-15} cm²). Quantitative calculations of the electron capture rate for simpler atomic ions confirm that the capture cross-sections and consequently the recombination coefficients are rather small even

at low energies. The quantum calculations yield recombination cross-section $\sigma \sim 10^{-19} \text{ cm}^2$ and two-body recombination coefficient $\alpha_z \sim 10^{-12} \text{ cm}^3 / \text{s}$ at thermal (300 K) energies.

It is found that for electron capture into the lower levels of the excited atom, the partial recombination coefficient varies as $T_e^{0.5}$, whereas for capture into the highly excited states lying within about kT_e of the continuum varies approximately as $T_e^{-1.5}$, leading to a variation of the total coefficient approximately as $T_e^{-0.7}$, where T_e is the electron temperature [52, 53]. As a result of the small capture rate, radiative recombination has been extremely difficult to study in the laboratory. Vainshtein formula for α_z [54, 55] is given by

$$\alpha_z = 8.5 \times 10^{-14} Z \beta^{3/2} / (\beta + 0.6) \quad (1.21)$$

where $\beta = Z^2 \chi_H / T_e$, χ_H -- Hydrogen ionization potential

For low temperature: $\beta \gg 1 \Rightarrow \alpha_z \propto \beta^{1/2} \propto (T_e)^{-1/2}$

For high temperature: $\beta \ll 1 \Rightarrow \alpha_z \propto \beta^{3/2} \propto (T_e)^{-3/2}$

b) Three-body recombination: This is the inverse process of collisional ionization. In three body recombination process, the excess energy, instead of being given out as radiation, is given to a third body (M) as shown below.



In principle a neutral atom can also serve as the third body. However, in electron-ion recombination, stabilization by neutral is relatively inefficient because of the small elastic recoil loss by an electron striking a massive atom. Therefore, the neutral stabilized process is important only at rather high gas densities. However, a plasma electron serves as an efficient third body since : 1) It provides an equal-mass particle for efficient recoil, and 2) it interacts

with the electron to be captured by the long-range Coulomb force. Therefore only electrons that have small positive energies and that have been accelerated close to a positive ion can lose enough energy at a collision with a neutral to be captured into even a high-lying state of the resulting excited atom or molecule. In this case, the three-body recombination coefficient is of the order of $\sim 10^{-26} \text{ cm}^6/\text{s}$ at 300 K, with an approximate $T_e^{-5/2}$ dependence on electron temperature. The process can be represented as



Rate of three-body recombination is given by,

$$\partial n_e / \partial t = \alpha_{3B} n_e^2 n_i \quad (1.22)$$

where, α_{3B} is the three-body recombination rate coefficient and is given by the Bates formula [54, 55] as

$$\alpha_{3B} = 10^{-19} \times (T_e(\text{K})/300)^{-9/2} \text{ (cm}^6/\text{sec)} \quad (1.23)$$

With an increases in temperature (T_e), the rate of three body recombination decreases faster in comparison to the radiative recombination rate, as from equation (1.21) and the rate increases with the increase in the density (n_e) equation (1.23).

The excess energy (few kT_e), is given to the free electron. If the recombining atom is in an excited state, it can undergo inelastic collision, super-elastic collision with another electron, or undergo transition to lower energy by emission of radiation.

c) Dielectric recombination: In this process, an electron is captured by an ion and a bound electron is simultaneously excited to a higher energy level [53]. This forms a doubly excited state which has energy above the ionization limit (an autotomizing state). The ion rapidly

rearranges to a more stable configuration emitting either a photon (dielectronic recombination) or an electron (Auger effect). The dielectronic recombination is a three-step process as shown in Fig. 1.11.

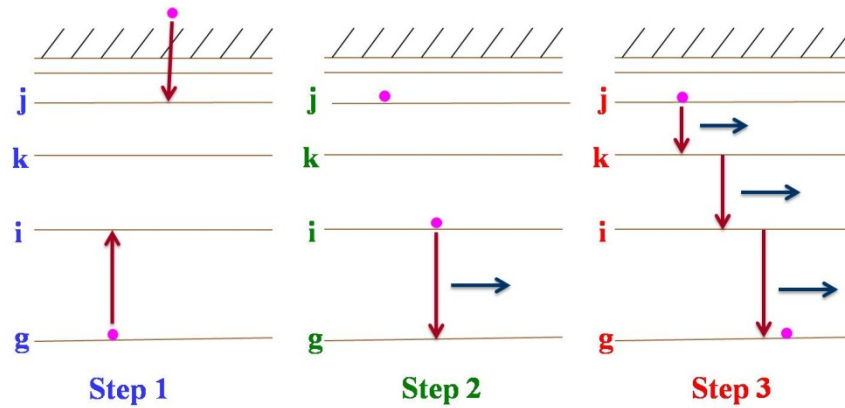


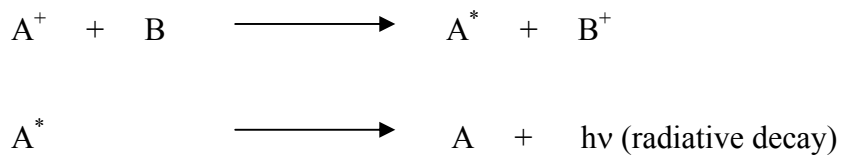
Fig. 1.11 Dielectronic recombination process.

In the first step, a free electron is resonantly captured into a high level j , with simultaneous excitation of one of the bound electrons of the recombining ion to level i . The result of this process is a double excited ion. This doubly excited ion has two channels of decay: auto-ionization and radiative decay of one of the excited electrons into a lower state. If auto-ionization follows the recombination, there is no change in the state of excitation or ionization of the ion. The process is called di-electronic recombination only in the second case, when radiative stabilization of the ion follows the recombination. Radiative stabilization occurs when the lower excited electron decays to the ground state, with a spectator electron remaining in an upper state. The radiative decay goes, in most cases, from the lower state, because this state has the larger oscillator strength. In the third step, the higher electron comes to ground state by a radiation cascade.

The process of dielectronic recombination is highly energy selective and hence only a limited number of electrons can recombine by this process as compared to the radiative recombination, by which any electron having any energy can recombine. Hence, though both

the processes have n_e, n_i or n_e^2 dependence, the dielectronic recombination rate cannot exceed the rates of three-body recombination or rate of radiative recombination. Hence, it is rarely taken into consideration.

d) Charge exchange recombination: Ion-atom collisions that involves the transfer of an electron between the interacting particles are called charge transfer or charge exchange collisions [51]. In the simplest case, an energetic ion collides with a low energy neutral atom to produce a cold ion and a fast neutral. When the two particles involved are of the same atomic species, then the ionization states of the incident fast ion and the resultant slow ion are the same and the process is called *resonant charge exchange*. Charge exchange can be an important loss mechanism in hot plasma, e.g. in experimental fusion plasmas. Here one ion A^+ picks up an electron from atom B, and recombines to A^* leaving atom B ionized. The excited atom radiatively decays to lower state. The process is shown in Fig. 1.12



In charge exchange, the energy differences between the energy levels of the participating species have to match exactly. During charge exchange, one species recombines and the other one gets ionized. So, both ionization and recombination processes are present in one process. Charge exchange process depends upon the density of neutrals and therefore its effects are important when neutral beams are deliberately injected into a plasma either for purpose of heating the plasma or specifically for diagnostics. In general, in a hot plasma the effects of charge exchange upon excited states can be ignored as the number of neutrals (with which charge exchange would occur) is much less than the number of electrons (which are responsible for the competing collisional processes). An exception is the radiative

recombination for which the cross-section is so much smaller than other cross-sections (including charge exchange) that it may not dominate over charge exchange.

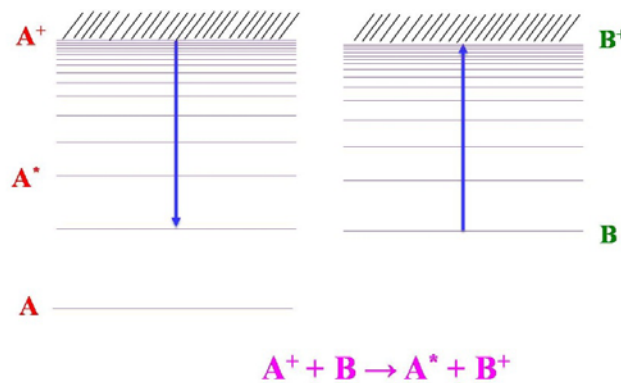


Fig. 1.12 Charge exchange recombination process.

1.4.2 Ionization models

Interpretation of the spectral characteristics necessitates the knowledge of both, the charge state distribution as well as the excited level population of different ions. In general, this requires a solution of a complex system of rate equations, describing the population and depopulation of levels by various processes like ionization, recombination (radiative or three-body), collisional excitation and de-excitation, radiative decay, absorption etc. Any given degree of ionization is connected to the two neighbouring ionization degrees through the above mentioned processes. The following three models [24] are most commonly used: 1) Local thermodynamic equilibrium model, 2) the Coronal equilibrium model and 3) the Collisional-radiative model. The suitability of the models depends upon plasma parameters viz. electron density, electron temperature etc. These models will be discussed briefly in the following sub-sections.

1.4.2.1 Complete thermal equilibrium (CTE)

Although this kind of equilibrium does not apply to the laboratory plasmas and is only approached in the stellar interiors, it can be considered as a reference condition in the

limit of high plasma density. A plasma is said to be in CTE when electrons, ions and radiations are strongly coupled to each other and share the same temperature [56, 57]. The populations N_u and N_l of the two ionic bound levels, u and l , with statistical weights g_u and g_l , are given by the Boltzmann equation:

$$N_u / N_l = (g_u / g_l) \exp[- \Delta E_{u,l} / k_B T] \quad (1.24)$$

where, $\Delta E_{u,l}$ is the energy difference between the two levels and T is the thermodynamic temperature of the plasma. The population of ionization states is given by the Saha equation [12]

$$N(Z+1) n_e / N(Z) = [g_0(Z+1) / g_1(Z)] [2\pi m k_B T / h^2]^{3/2} \exp [- \chi_0(Z) / k_B T] \quad (1.25)$$

which gives the ratio between the population densities of two contiguous ionization states with charges Z and $Z+1$, and statistical weights $g_0(Z)$ and $g_0(Z+1)$, respectively. The subscript '0' refers to the ground state of the ion, which in CTE, is by far the most populated one. $\chi_0(Z)$ is the ionization potential of the ion with charge Z , n_e is the electron density, m is the electron mass and h is the Planck constant.

Free electrons are distributed among the available energy levels and their velocity distribution follows the Maxwell distribution [12];

$$f_e = n_e [m / 2\pi k_B T_e]^{3/2} \exp [- mv^2 / 2 k_B T_e] \quad (1.26)$$

The number of electrons with velocities between v and $v + dv$ is therefore given by the relation $dN_{v, v+dv} = 4 \pi f_e v^2$.

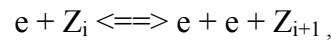
Finally, the spectral energy density of the radiation emitted by a plasma in TE is that of a black body and is given by Planck's formula [12].

$$u_\lambda = [8\pi hc / \lambda^5] [\exp (hc/\lambda k_B T) - 1]^{-1} \text{ erg cm}^{-4} \quad (1.27)$$

Planck's formula along with the above equations completely define the spectral properties of a plasma in TE.

1.4.2.2 Local thermodynamic equilibrium model:

In this model, it is assumed that the distribution of the ion species is determined only by particle collision processes occurring with sufficient rapidity for the distribution to respond instantaneously to any change in the plasma condition. The forward process of collisional ionization is balanced by the reverse process of three-body recombination [57]. Both the processes occur at equal rates as governed by the principle of detailed balance. Consequently, the system behaves as if it is in a complete thermodynamic equilibrium. Though there may be spatial and temporal variations in temperature and density, the distribution depends entirely on the local instantaneous values of temperature and density. Thus for, local thermodynamic equilibrium, we have



where Z_i and Z_{i+1} denotes the i^{th} and $i+1^{\text{th}}$ charge species. For a Maxwellian distribution of free electrons, the charge states are determined by the Saha equation [12] as

$$\beta_e n_e n_i = \alpha_{3B} n_e^2 n_{i+1} \quad (1.28)$$

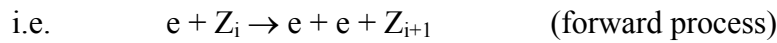
$$n_{i+1} n_e / n_i = \beta_e / \alpha_{3B} = (U_{i+1} U_e / U_i) (2\pi m k T_e / h^2)^{3/2} \exp (-\chi_i / k T_e) \quad (1.29)$$

where n_e is the electron density, n_i and n_{i+1} are the ion densities, and U_i and χ_i are the partition function (for the ground state) and ionization energy of the i^{th} ionization state respectively. As the forward process is proportional to n_e and reverse process is proportional to n_e^2 , detailed

balance is not possible at very low electron densities. Hence, the local thermodynamic equilibrium model is more applicable at higher electron densities.

1.4.2.3 Coronal equilibrium model

In this model, the equilibrium is assumed to be through a balance between collisional ionization and radiative recombination.



where $h\nu$ is the energy of the emitted photon. The equation of balance between collisional ionization and radiative recombination is given by [12]

$$n_e n_i S_z(T_e, Z) = n_e n_{i+1} \alpha(T_e, Z+1)$$

where $S_z(T_e, Z)$ and $\alpha_{z+1}(T_e, Z+1)$ are collisional ionization and radiative recombination coefficients for electron temperature T_e , electron density n_e and ion charge Z . This gives

$$n_{i+1} / n_i = S_z(T_e, Z) / \alpha(T_e, Z+1)$$

Since this ratio is independent of the electron density, Saha ionization formula is not applicable here.

As it is assumed in this model that the reverse process of radiative recombination balances the forward process of collisional ionization, it is mandatory for the validity of this model that the plasma should be optically thin for the emitted radiation to leave the plasma. Hence, this model is well suited for those plasmas, which have high electron temperature and lower electron density. The density – temperature range where both models predict the same ratio of ionization (n_{i+1} / n_i) is given by equating the ratios for the two models as $n_e / \sqrt{T_e} = 3x$

$10^{13} \chi_i^3$ (χ_i , T_e in eV). When $n_e/\sqrt{T_e}$ is much greater than $3 \times 10^{13} \chi_i^3$, one gets LTE or CE otherwise. An important condition to apply in any of these models is that the plasma has to be in equilibrium i.e. the velocity distribution has to be Maxwellian.

1.4.2.4 Collisional-radiative model

For laser-produced plasmas, neither of the previously discussed models describes the plasma ionization distribution accurately. The essential difference between the corona model and the collisional radiative model [12, 58] is that in the latter, electron collision process causing transition between upper levels, including three-body recombination, step wise ionization, and ionization from highly populated excited states are taken into consideration. At higher densities, collisional radiative model reduces to local thermodynamic equilibrium model. In the limit of low density, this model reduces to corona model.

1.5 X-ray emission processes

The overall emission spectrum from laser produced plasma is a superposition of line radiation (bound-bound radiation) on a broad continuum due to free-free and free-bound radiation [12, 59]. The relative yield due to these processes depends on the plasma parameters (n_e , T_e). The x-ray emission processes from unmagnetized plasma are discussed in the following subsection.

1.5.1 Bemsstrahlung emission

This radiation is emitted when a charged particle is accelerated or retarded in the Coulomb field of another charged particle. Here the particle emitting radiation is free before and after emission [24, 60]. Hence it is called *free-free radiation*. It is also called *bremstrahlung* (braking radiation). Thus in a plasma, when an energetic electron comes in the Coulomb field of an ion, it gets deflected, undergoes acceleration and emits radiation. The

ions, along with the electrons, also get deflected but being massive accelerate a little and thus do not make a significant contribution in the emission. The interactions between ion-ion and electron- electron do not result in the emission of radiation (except at relativistic velocities). This is because when two identical particles of equal charge and mass interact, they produce equal and opposite acceleration and the radiation emitted by the two cancel out.

The power emitted/volume of bremsstrahlung radiation [23, 61] W_B is proportional to $\sqrt{T_e}$, and the power emitted per unit volume per wavelength is given by the expression,

$$W_B^\lambda = 2.2 \times 10^{-27} Z n_e^2 [T_e]^{-1/2} [(1/\lambda^2) \exp(-hc/\lambda kT_e)] \text{ erg sec}^{-1} \text{ cm}^{-4} \quad (1.30)$$

It may be noted from equation 1.30 that for $\lambda \gg (hc/kT_e)$, the exponent becomes close to zero so that the bremsstrahlung spectrum depends weakly on the temperature i.e. $W_B^\lambda \propto T_e^{1/2}$. On the other hand for $\lambda \ll (hc/kT_e)$, the spectral shape depends strongly on temperature. The temperature can be estimated by plotting $\lambda^2 (\ln W_B^\lambda)$ v/s $1/\lambda$. The slope of this line will give the temperature of the plasma [51].

1.5.2 Free-bound radiation

This radiation is emitted when a free electron is captured in the bound state of an ion. Since the electron is free before the emission and bound after the emission, this radiation is called *free-bound radiation*. The radiation is emitted in the form of a photon of energy $h\nu = KE + \chi_j$, where KE is the kinetic energy of the free electron and χ_j is the ionization potential of the shell in which the electron is captured. The recombination spectrum is continuous as the free electrons have a continuous energy distribution (Maxwellian distribution). However, since the recombination can occur in various shells with different values of E, the overall spectrum is quasi-continuous showing discontinuities at various shell energies.

The recombination radiation power/ volume (W_R) is given by [23, 59],

$$W_R = 2.4 \times W_B \times [Z^2 E / kT_e] \quad (1.31)$$

The shape of the recombination radiation spectrum is similar to that of the bremsstrahlung radiation spectrum except near the edges. The continuum x-ray emission spectrum from a plasma consists of both free-free radiation and free-bound radiation. Power emitted as recombination radiation may exceed that as bremsstrahlung radiation at low temperatures and high ionization potentials. At very high temperatures, the free-free radiation dominates as ions become completely stripped.

1.5.3 Bound-bound radiation

Bound-bound radiation or line radiation is emitted as a result of transition between two bound states of an ion or an atom. The spectrum of emitted radiation therefore consists of lines at discrete wavelengths rather than being continuous. Power emitted per unit volume as line radiation from plasma is given by [23-24, 59]

$$P_{bb} = 3.5 \times 10^{-25} (kT_e)^{-1/2} N_e \sum N_{i+1} \exp(-E_i / kT_e) \text{ W/cm}^3 \quad (1.32)$$

where $E(i)$ is the energy of radiation emitted by an ion of charge i . The line radiation can be put into three different categories [24, 62] as described below:

a) Resonance lines: These are the transitions from excited state and the ground state of partially ionized species [51, 62]. The selection rules followed by these transitions are same as those of the optical transitions. The resonance lines play an important role in the diagnostics of plasma. The intensity ratio of the two resonance lines can be used for temperature estimation and these lines with the combination of other lines can be used for density and temperature estimation in plasmas. Since the oscillator strengths of resonance

transitions are very high, such lines are quite likely to be reabsorbed in dense plasma and thus the opacity of such radiation should be taken into account for quantitative analysis.

b) Intercombination lines: The intensity of the optically allowed transitions occurring between states of same multiplicity is very high (as in the case of resonance transitions). Relatively weaker lines which arise due to transitions between states of different multiplicities, are called *intercombination transitions*. The energy of an intercombination line is slightly less than that of the corresponding resonance line [51, 62]. These weaker lines thus appear as satellite of the resonance lines on the higher wavelength side. The ratio of the intensity an intercombination line to that of the resonance line can be used for the density estimation of plasmas. The intercombination and the resonance transitions in He-like ions are shown in Fig. 1.13 where $1s2p\ ^3P_1 \rightarrow 1s^2\ ^1S_0$ is the intercombination transition, and $1s2p\ ^1P_1 \rightarrow 1s^2\ ^1S_0$ is the corresponding resonance transition.

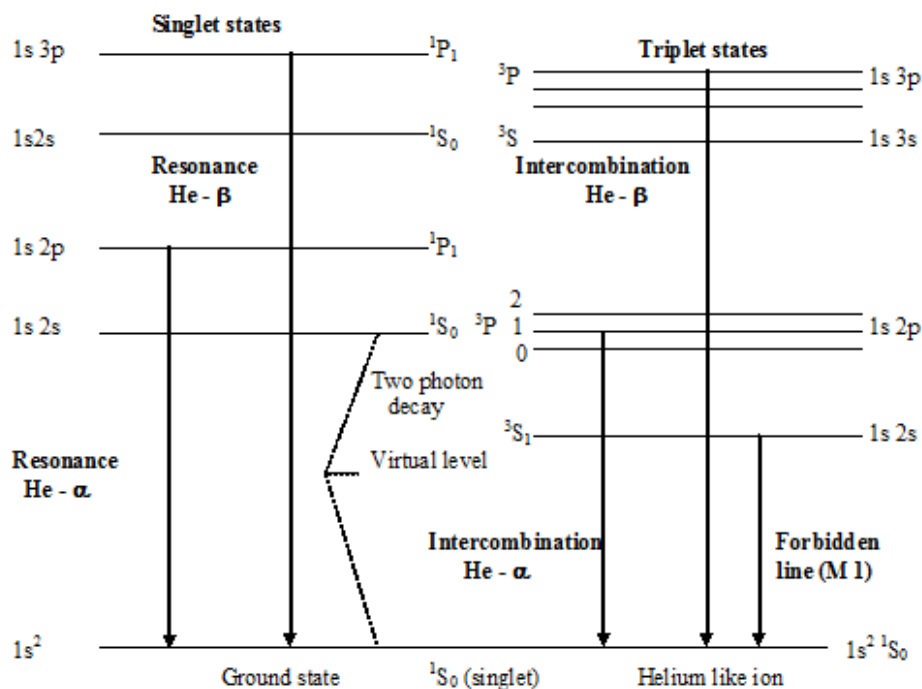


Fig. 1.13 Resonance and intercombination transitions.

c) Dielectronic satellite lines: In an x-ray spectrum, the dielectronic satellite lines arise as a result of transitions originating from doubly excited states of multiply charged ions. An example of such a transition is shown in Fig. 1.14. Due to the presence of an additional electron, called the *spectator electron*, the Coulomb shielding decreases, this results in transitions occurring at slightly lower energy than that of the resonance line. Depending on the excited state of the additional electron, there can be a number of satellites but the most distant from the resonance line and at the same time the strongest are those corresponding to the transition in the presence of an additional electron in the state of lowest possible quantum number. The ratio of the intensities of dielectronic satellites can be used for density estimation.

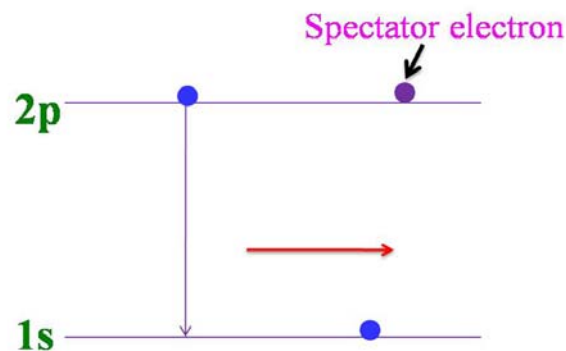


Fig. 1.14 : Dielectronic satellite transition.

d) Inner-shell transitions : The study of this radiation is important, as it is related to the presence of hot electrons in ultra-short laser produced plasma [63-65]. The energetic electrons with average kinetic energies of several tens of keV penetrate into the underlying colder material. Here they knock out electrons preferentially from the K-shell (or M- or N-shell) of the atoms through inelastic collision. The vacancy in the shell is filled by recombination of electrons from higher shells, emitting the characteristic line radiation as

depicted in Fig. 1.15. The inner-shell recombination takes place on a time scale of femtoseconds or even attoseconds. The inner-shell vacancies are created until the energy of the electrons is more than the K-shell ionization threshold. Under optimized condition, the x-ray pulse duration is of the order of laser pulse duration because the driving electron pulse is generated only during the ultra-short laser pulse [66]. Further, under optimized conditions when electrons do not penetrate deep inside the bulk solid target and undergo lateral scattering, the source dimension is comparable to the laser focal spot size [67-68].

In a simplified description, the K- α line (or L,M shell line) radiation generation is two-stage process. The first stage is the generation of hot electrons in the plasma and the second stage is the scattering of these electrons in the solid. The electrons are assumed to move in a straight line from the acceleration point to the solid, and in the simplest modeling each electron enters the solid perpendicular to the surface. The K- α yield essentially depends on the energy distribution $f(U_0, T)$ of the hot electrons and the K-shell ionization cross-section σ_K for electron impact. $U_0 = E_0/E_K$ where E_0 the incident electron energy, E_K the ionization energy of the K-shell. Next, the energy dependent path length of the electrons in the target of finite thickness and quantum yield η of the K-transition is to be taken into account. The number of K- α photons $N_{K-\alpha}$ produced in a metal foil with a density of atoms n is given by [69-71]

$$d^2N_{K-\alpha} = \eta n N_e f(U_0, T) \sigma_K(U_0) dx dU_0 \quad (1.33)$$

where n is density of the atoms in the target.

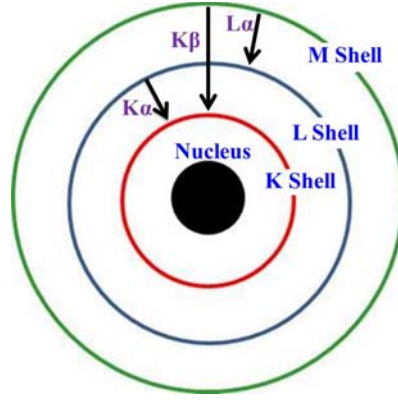


Fig. 1.15 : The radiative transitions of electrons from the outer shells lead to the generation of characteristic inner-shell lines.

It is assumed that: i) the hot electron energy distribution is Maxwellian, and ii) the K- α photons generated by the hot electrons with certain energy are emitted at a mean depth. Reich *et al* [70] predicted existence of an optimum laser intensity for the K- α yield as equilibrium between K- α production and reabsorption in bulk targets. It occurs when the mean depth z is comparable to the absorption length for K- α . They have calculated the yield of K- α radiation generated during short pulse laser-solid interaction by means of Monte Carlo and particle-in-cell simulations. It is found that there is both an optimal target thickness and hot-electron temperature for forward emission. This temperature is shown to be 6 times the K-shell ionization energy and it was independent of Z of the target. It is due to the approximation that electrons with energies beyond a fixed multiple of E_K are produced too deep into the target to be detected. Salzmann *et al* [71] modified this model to account the electrons with the energy much above U_0 . They have predicted that optimal temperature varies between 4 and 12 times the K-shell ionization energy, depending on the atomic number. The hot electron temperature is related to the laser absorption mechanism. The number of K- α photons generated by an incident electron with initial energy E_0 is given as

$$N_{K-\alpha} = 4 \times 10^{-3} Z^{-1.67} E_0^{3/2} \quad (1.34)$$

It is important to optimize the energy distribution of the hot electrons in experimental conditions to achieve high conversion efficiency.

The x-ray yield (efficiency) depends on the thickness of the target for thin foil targets. There exists an optimal target thickness for efficient generation K- α radiation. The target should be thick enough to stop the incident hot electrons to generate K- α , and thin enough not to reabsorb the generated K- α photons. The optimal thickness occurs when the mean depth of the hot electrons in the foil is comparable to the absorption length of the K- α radiation

In the context of inner-shell x-rays (also called *fluorescence x-rays*), it is necessary to consider the competitive *Auger processes*. The various Auger processes are discussed below:

1) Auger ionization: In this case, the inner-shell vacancy is filled by an electron in the next outer shell and the excess energy, instead of being emitted as a photon, is given out to eject a second electron called Auger electron. This process is basically a radiation-less transition which gives rise to doubly ionized ion.

2) Radiative / semi-Auger process: Radiative Auger transition is a double electron process in which an outer electron makes a radiative transition to an inner-shell and another outer shell electron is simultaneously excited into the bound or continuum state ϵ by absorbing the ejected photon. If ϵ is a bound state, the transition is called Semi Auger process or Radiative process. The radiation appears as a discrete or diffused satellite.

3) Auto-ionization: By absorbing photons or electrons of suitable energies, an electron gets excited to the outer level. If the energy of the excitation exceeds the ionization energy of any of the electrons present, the excited atom will eject one electron and reorganize to an ion. This process of ionization is called auto-ionization and the ejected electron is called an auto-ionization electron.

The Auger processes in x-ray spectroscopy influence the width of the x-ray line, since it competes with the radiative process in the de-excitation of ions. It also influences the

intensity of x-ray line, since it transfers the vacancy from one shell to another. It gives rise to satellites to the inner-shell lines, as it leads to double ionization. It should be noted that for $Z < 15$, Auger processes dominates over fluorescence but at higher Z , fluorescence dominates.

1.6 Application of LPP x-ray source in time resolved x-ray diffraction

Availability of high brilliance ultra-short duration ($< \text{ps}$) x-ray pulses from variety of sources has triggered considerable interest in the time resolved x-ray diffraction (TXRD) measurements for studying the ultra-fast dynamics in solids [72-76]. Measuring ultra-fast melting, acoustic phonons, and strain in bulk materials has been an on-going area of interest in the time-resolved research community. The time resolved studies are performed in pump-probe scheme where an optical pump laser deposits its energy in the sample to modify the lattice. It causes changes in the electron distribution function leading to changes in the atomic interaction potential so that the matter loses crystalline order and becomes molten on a sub-ps time scale. The melting can be seen by observing a large decrease of the integrated intensity of the Bragg-reflections.

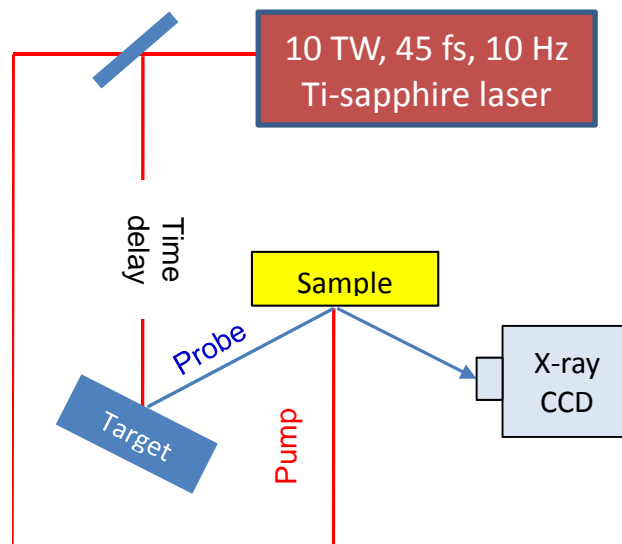


Fig. 1.16: Fraction of the transmitted laser energy is used to induce changes in the lattice properties of the crystal sample. The changes are probed by the $K\text{-}\alpha$ line and detected by an x-ray CCD.

A typical pump-probe setup with laser produced plasma x-ray source as shown in Fig. 1.16. It consists of an optical femtosecond laser pulse, which is a small fraction of plasma forming pulse, used to modify the lattice structure of the crystal sample. With a variable delay line, the x-ray probe is made to diffract from the perturbed structure at different times after the crystalline lattice is distorted. The x-ray diffraction profile changes as the distance between atomic planes changes, leading to the change in angle for Bragg reflection. The line shape and position of the reflected line radiation indicate the state of the lattice as transient effects pass through the penetration depth of x-rays. In these experiments, inhomogeneous spacing and lattice expansion are observed [77]. The transient dynamics in the material is resolved by analysing the shift or broadening of the diffraction signal as shown in Fig. 1.16.

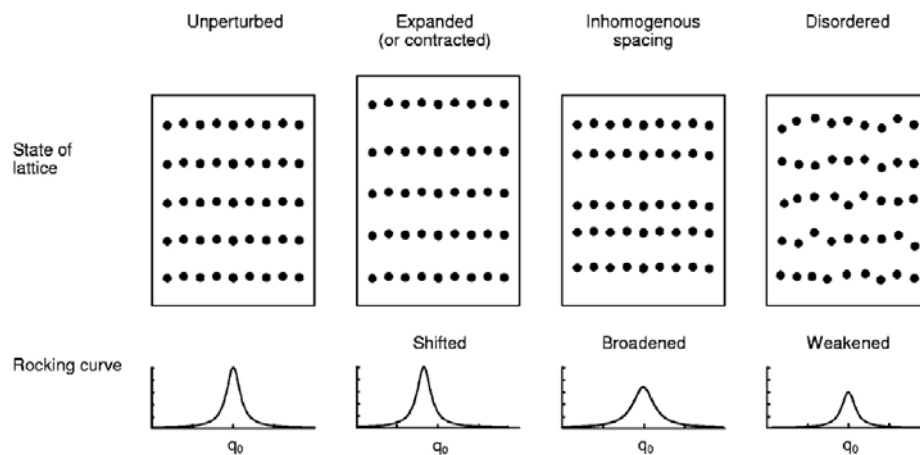


Fig. 1.17: Several approaches for analysing Bragg diffraction data.

To summarize, in this chapter, a brief outline of the basic physics of the LPP has been given. We have explained the interaction of long duration and short duration laser pulses with the solid density matter. The physical processes related to the ionization equilibrium of plasma and to the emission of x-ray radiation are described. A brief introduction to the time resolved x-ray diffraction technique with ultra-fast x-ray probe that allows for picosecond resolution of transient dynamics has been presented.

Chapter 2

Laser system and x-ray diagnostics

The present research work has been carried out using three different laser facilities at Laser Plasma Division, RRCAT. The first two were indigenously developed high power Nd:glass laser systems providing intense laser pulses of nanosecond and picosecond durations. The ultra-short duration laser used in the present experimental study is a commercial 10 TW, 45 fs, 10 Hz Ti: sapphire laser system. In this chapter we briefly describe the important features of these laser systems, the experimental plasma chamber, and various x-ray diagnostics setups used for the research work described in this thesis.

2.1 Nanosecond Nd: phosphate glass laser chain

Studies on the dependence of the x-ray line emission on the laser pulse duration and the keV x-ray emission from gold-copper mix-Z plasmas of different elemental compositions have been performed using multi-nanosecond laser pulses from an Nd:phosphate glass laser chain. This laser chain has been designed and set up on MOPA (Master Oscillator-Power Amplifiers) configuration [78]. A schematic diagram of this laser chain is shown in Fig. 2.1. It comprises of a Q-switched master oscillator (Nd:phosphate glass laser rod of 5 mm diameter and 100 mm length) followed by four amplifier stages of Nd:phosphate glass laser rods of successively increasing aperture size viz. 10, 15, 25, and 50 mm respectively. The laser beam spatial profile is cleaned using three vacuum spatial filters-cum-image relay systems. Two Faraday optical isolators are also installed in the laser chain to protect the amplifiers and the oscillator from optical damage caused by any back-reflected laser light from the plasma. The final energy output of the last amplifier stage is ~ 12 J in 4 ns (FWHM) pulse. Second harmonic conversion of the second harmonic crystal (KD*P of size: 45 x 45 x 22 mm³). This system provided output laser energy of 4 J energy in 3 ns (FWHM) pulse duration at $\lambda_L = 0.53$ μm . The maximum intensity on the target was determined to be $\sim 10^{13}$ W cm⁻² corresponding to the measured focal spot diameter of ~ 130 μm .

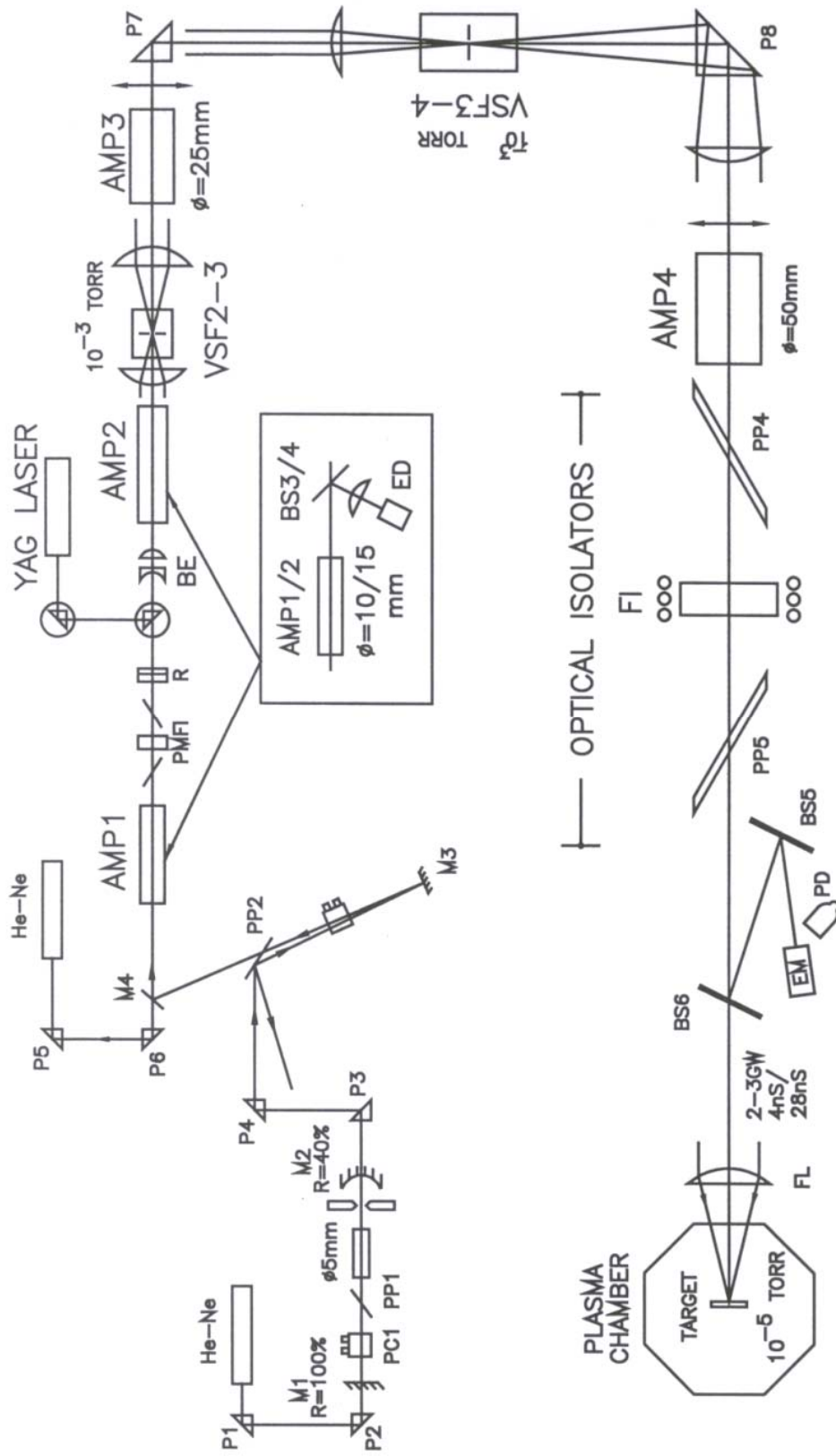


Fig. 2.1: Schematic of nanosecond Nd:phosphate glass laser chain.

2.2 Multi-picosecond 100 GW Nd: glass laser chain

Studies on the dependence of the x-ray line emission on the laser pulse duration were carried out using a 100 GW, 27 ps Nd:glass laser chain set up in our laboratory [79]. This laser chain, also based on MOPA configuration, consists of an active-passive mode-locked Nd:YLF oscillator, an electro-optic pulse selector, four Nd:glass amplifiers, three spatial filter-cum image relay systems, and two Faraday isolators. Fig. 2.2 shows a schematic diagram of this laser chain. The Nd:YLF oscillator along with its pre-amplifier (Quantel, France: Model TLF 501-10) and its pulse selector, provided single laser pulses of $\sim 300 \mu\text{J}$ energy and 27 ps (FWHM) duration. The beam energy and the peak power were increased in four amplifier stages, each of Nd:phosphate glass. Nd:YLF was chosen for oscillator as its peak wavelength matches with the peak wavelength (1.054 nm) of Nd:glass. The above laser system provided single laser pulses of up to 2.5 J energy in a pulse duration of ~ 27 ps (FWHM) measured using an optical S-1 streak camera set up in our laboratory [80]. The focal spot diameter on the target using an F/10, 70 cm focal length lens was determined from the measurements of intensity distribution in the focal plane. It was estimated to be $\sim 70 \mu\text{m}$ at $1/e^2$ intensity points. Thus, a peak laser intensity up to $1.5 \times 10^{15} \text{ W cm}^{-2}$ was achieved on the target. A pulse contrast in excess of 10^5 was achieved between the main laser pulse and the background leakage intensity. This is important to avoid creation of any low temperature plasma prior to the arrival of the main laser pulse.

2.3 Ti:sapphire laser system

A chirped pulse amplification technique based commercial Ti:sapphire laser system was used in the experimental study of inner-shell and the ionic line radiation from magnesium plasma and for generation of a bright, ultra-short keV K- α x-ray source and its application in time resolved x-ray diffraction studies. Fig. 2.3 shows a schematic diagram of this laser system. The oscillator generates nanojoule pulses of ~ 20 fs duration at a repetition rate of 75 MHz. Such small duration pulses are generated by a Kerr-lens mode-locking technique. These pulses are then stretched using a pulse stretcher. The pulse stretcher uses a grating pair and a cylindrical mirror (known as Öffner type stretcher [81]), introduces positive linear chirp in the laser pulse and increases its duration from ~ 20 fs to ~ 200 ps. In a positive linearly chirped pulse, the wavelength of the pulse decreases linearly in time *i.e.* the initial portion of the pulse has longer wavelengths and the later portion of the pulse have shorter wavelengths. A single pulse is then selected out of this train at every 100 ms (10 Hz) and its energy is amplified to few micro joules in a regenerative amplifier [82]. This pulse is then further amplified in a three-stage multi-pass amplifier to achieve its final energy of ~ 700 mJ. The pulse is then ejected using a pulse ejector switch.

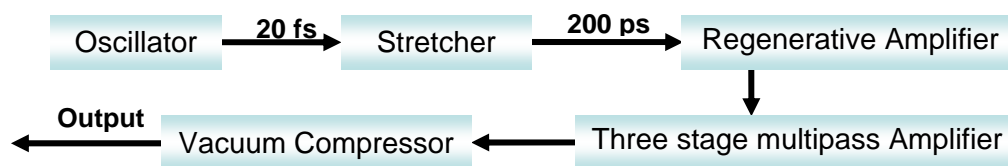


Fig. 2.3 Block diagram of the Ti: sapphire laser system.

In addition to the main 700 mJ pulse, there are laser pre-pulses present before the main pulse. The pre-pulses present in this laser pulse are mainly of two types, 1) ASE Pre-pulse : It is the amplified spontaneous emission (ASE) generated by the amplification of

spontaneous emission in the regenerative amplifier and the multi-pass amplifiers, and 2) Replica pre-pulse : It is the pre-pulse generated by the leakage of the mode-locked train of pulses. A pulse cleaner is used to reduce the amount of the pre-pulses in the laser. The pulse cleaner contains a fast Pockels-cell which rotates the polarization only to let the main laser pulse pass but not the leakage pulses preceding it. The rejection ratio of the pre-pulse depends on the quality of the polarizer (i.e. its discrimination between s- and p-polarizations) and the speed of the Pockels cell switching.

The pulse is then allowed to pass through a pulse compressor resulting in a laser pulse of 45 fs duration, and energy ~ 450 mJ. The pulse compressor employs a parallel grating pair along with a retro mirror to compensate for the positive chirp of the laser pulse [83]. The negative chirp introduced by the pulse compressor depends on the separation between the two gratings. As one increases the separation, the negative chirp increases and at the optimum value of the grating separation, the negative chirp introduced by the compressor compensates the positive chirp of the stretched laser pulse. Increasing/decreasing the grating separation from this optimum value results in negatively/positively chirped pulses. It may be mentioned here that the laser pulse is not compressed to its original duration it had at the oscillator. This effect arises due to the reduction of pulse spectrum through gain narrowing during the amplification of the laser pulse [84].

2.3.1 Characterization of laser parameters

In laser-plasma interaction experiments, peak intensity of the focussed laser beam on the target is an important parameter that governs the interaction processes. It is therefore necessary to measure the focal spot size. The peak laser intensity is given by

$$I_0 = E/\tau(\pi\omega^2) \quad (2.1)$$

The laser focal spot on the target was magnified and imaged on a CCD camera using a microscope lens as shown in Fig. 2.4. To avoid any damage to the CCD sensor, the pulse energy prior to focusing the laser beam was reduced by reflecting the beam from multiple glass surfaces. The FWHM diameter ($2\omega_0$) of the focal spot was measured to be $\approx 18 \mu\text{m}$. Fig. 2.5 shows the measured focal spot of the laser. One can see that the spot is nearly circular and the intensity profile of the laser spot is close to Gaussian.

The femtosecond pulses were temporally characterized by intensity auto-correlation method using an in house developed second order auto-correlator. In the intensity auto-correlator (IA), a beam splitter splits the incoming laser beam into two, which are then passed through a nonlinear crystal for second harmonic generation. If the two beams overlap both in space and time, a second harmonic beam is generated in the direction mid-way between the two beams. The temporal overlap of the two beams is achieved by the adjustment of the delay line of one arm of the auto-correlator. The angle between two beams determines the spatial width of the second harmonic correlated beam, and the same is related to the laser pulse duration.

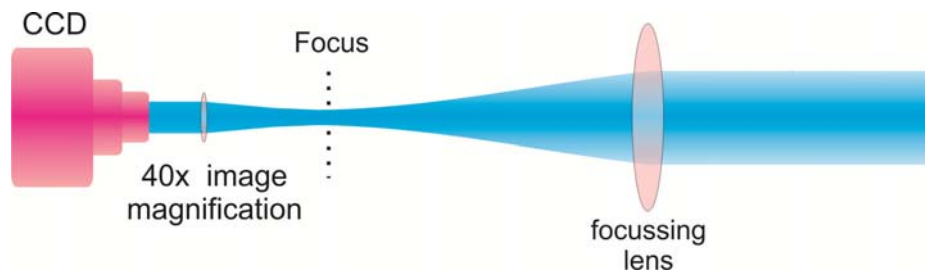


Fig.2.4: A schematic diagram of the experimental setup for focal spot measurement.

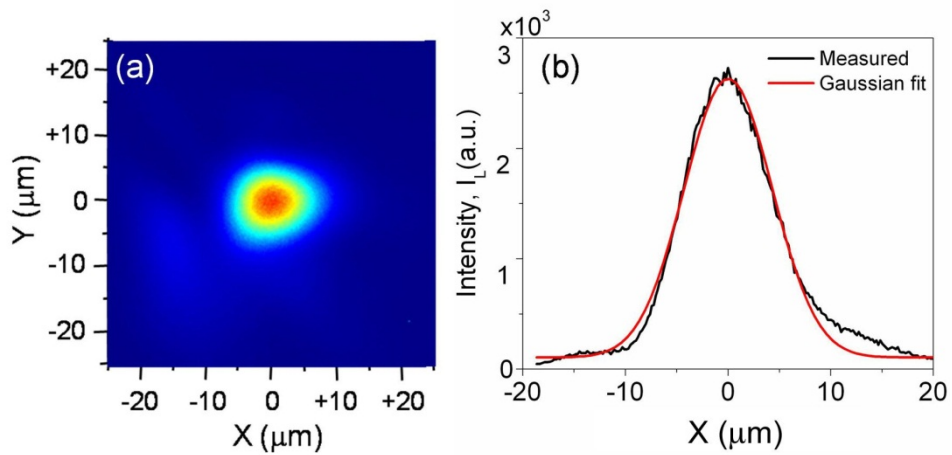


Fig. 2.5 a) Magnified image of laser focal spot on CCD, b) the intensity profile of the laser spot closely matching the Gaussian fit.

A ray diagram for the generation of auto-correlation trace from the overlap of the two ultra-short pulses is shown in Fig. 2.6. Only in the case of spatial and temporal overlap of two beams the central second harmonic pulse is generated, known as auto-correlator trace. It should be noted here that the width of the central trace depends on the duration of the laser pulse and the temporal profile of the laser pulse. In a way the measurement of the auto-correlation trace width does not give us full information about the ultra-short pulse, i.e. one has to know (or assume) the shape of the laser pulse in order to know the exact duration of the pulse.

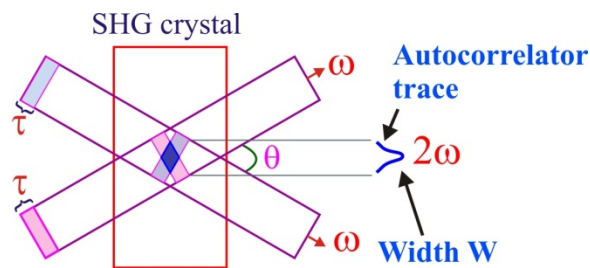


Fig. 2.6 Generation of autocorrelator trace in SHG crystal.

The width of the auto-correlator trace can be related to the pulse width τ (FWHM) of the laser pulse. If W is the width of the second harmonic correlated beam (FWHM) then, for a cross-over angle θ between the two beams, the overlapping beams as shown in Fig. 6.1, the laser pulse width is given by the relation [85]

$$\tau = \frac{2}{K} \frac{W \sin(\theta / 2)}{c} \quad (2.2)$$

where K is a constant which depends on the exact temporal shape of the laser pulse, θ is the angle between the overlapping beams, and c is the velocity of light. For a hyperbolic secant squared (sech^2) pulse, $K = 1.35$. Figure 2.7 shows a typical autocorrelator signal and its trace obtained using *Promise* software.

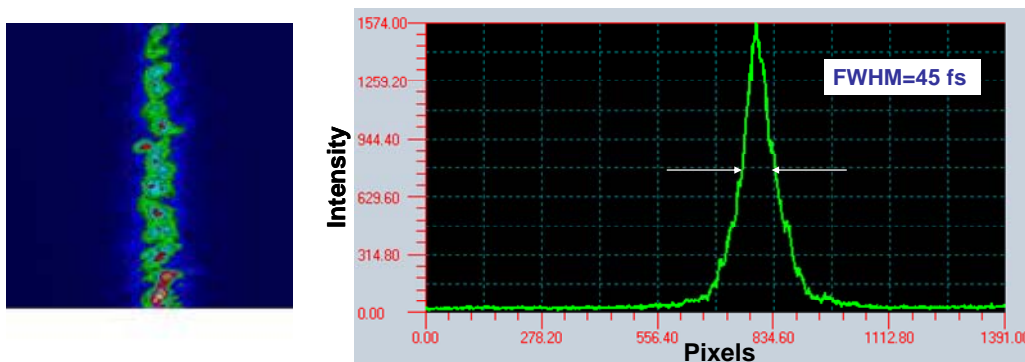


Fig. 2.7 (a) Auto-correlator signal, and (b) its trace using “*Promise*” software.

Precise measurement of the cross-over angle θ is a difficult task and an element of error is always involved with such measurement. We have used another simple approach for the calibration of time axis to CCD pixels. In this method, a small delay is introduced in one of the laser pulse. The peak of auto-correlation trace gets shifted laterally by an amount proportional to the delay. The difference between the two auto-correlation peaks directly gives the time delay in terms of the CCD pixel. For example, if the delay between two pulses

is changed by 10 μm , the peak of overlapping pulse is shifted by ~ 33.3 fs. Thus the pixel shift of autocorrelator trace is equal to 33.3 fs. This method gives an accurate means of the measurement of the pulse duration. In this geometry the formula for pulse duration measurement gets modified as

$$\tau = \left(\frac{W(\text{pixel})}{K} \right) \times \text{calibration factor} \left(\frac{\text{fs}}{\text{pixel}} \right) \quad (2.3)$$

The temporal profile of the laser pulse is hyperbolic secant squared (sech^2) type. Intensity auto-correlation method [85] is used for the measurement of temporal duration laser pulses. The auto-correlation trace gives a laser pulse duration of FWHM (45 ± 5) fs.

The variation of laser pulse duration was also measured by increasing and decreasing the grating separation from the “compressor zero”. Figure 2.8 shows dependence of the pulse duration on the grating separation. This data is important for compensation of the additional positive chirp introduced into the laser pulse due to any transmission optics (lenses/mirrors etc.) in the beam path. After the compressor stage, the laser beam was transported in vacuum to avoid beam distortion in air. Therefore, in order to obtain the shortest pulse at laser - target interaction point in vacuum, the positive chirp introduced in the laser pulse by the group velocity dispersion in the glass window (the contribution of air being negligibly small) during pulse duration measurement was compensated by reducing the grating separation to add same amount of positive chirp. This position of the gratings was taken as the “compressor zero” for the experiments. In order to intentionally increase the laser pulse duration by adding either positive or negative chirp during the experiments, the grating separation was varied by known amount.

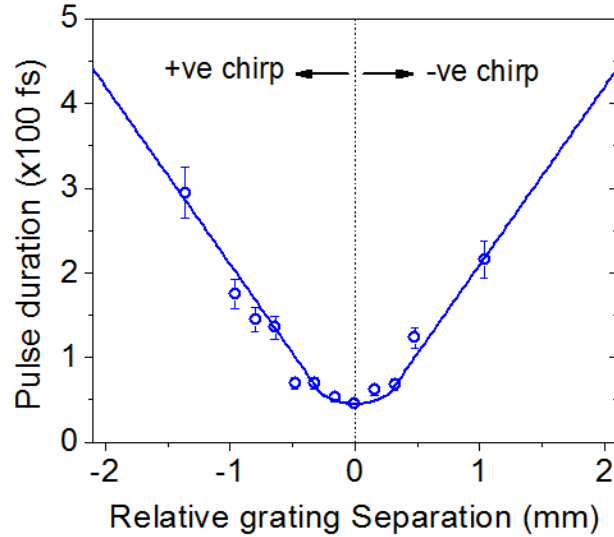


Fig. 2.8: Variation of laser pulse duration with grating separation relative to the compressor zero.

It is well known that any high intensity ultra-short laser pulse of typically tens of femtoseconds duration generated by the chirped pulse amplification (CPA) technique is accompanied by pre-pulse. As mentioned in section 2.3, one has a nanosecond duration pre-pulse pedestal due to the amplified spontaneous emission (ASE pre-pulse), and a femtosecond duration pre-pulse (replica pre-pulse) due to leakage of the mode-locked pulse one round trip time before the actual pulse. In addition, there is also a several picosecond duration pedestal (ps pre-pulse) due to unavoidable limit in the compression of the chirped pulse. The intensity of the pre-pulse is defined in terms of contrast ratio, and it is defined as the ratio of the intensity of main pulse to that of the pre-pulse. The temporal profile of the femtosecond pulse of laser system used consists of pre-pulse(s) accompanying the ultra-short high intensity pulse. The contrast ratio of the replica pre-pulse (8 ns before the main pulse) was better than 10^6 , and the contrast ratio of the ASE pre-pulse were about 10^6 . The ps pre-pulse contrast ratio was 10^3 and 10^4 at 1 ps and 5 ps, respectively, before the main pulse. The ASE pre-pulse and replica pulse contrast ratios were measured using a fast photo-diode with

0.8 ns rise time on a 500 MHz digital oscilloscope, whereas the ps contrast ratio was measured using a third order autocorrelator (Sequoia). The contrast ratio of replica pre-pulse was measured to be more than 10^6 which corresponds to replica pre-pulse intensity $\sim 10^{12}$ W cm^{-2} and energy ~ 100 nJ.

Although ps pre-pulse will be able to form plasma, it is not expected to modify the interaction conditions significantly as the hydrodynamic evolution of the plasma is negligible on few ps time scale. However, the ASE pre-pulse, which forms a few nanoseconds long, low intensity pedestal to the ultra-high high intense main 45 fs laser pulse, depending on its duration, may have a significant fraction of the laser pulse energy (unlike the replica pre-pulse), and create pre-plasma. The duration of the ASE pre-pulse pedestal can be controlled by changing the switching-on time of the 5 ns wide high voltage pulse on the Pockels cell of the pulse cleaner (located after the regenerative amplifier). The measured signals due to the ASE with different pedestal durations and the main pulse are shown in Fig. 2.9. The switching-on time of the high voltage pulse on the Pockels cell was varied to change the pedestal duration. The green trace in the Fig. 2.9 is due to the 45 fs duration main laser pulse, while the different coloured traces are due to ASE pre-pulses of varying duration. The ASE pre-pulse duration could not be reduced below ~ 1 ns before the main pulse due to the limit set by the rise time (~ 1 ns) of the electrical pulse on the Pockels cell. Attempt to further reduce the ASE pre-pulse duration was found to lower the main laser pulse energy. It also leads to large shot-to-shot fluctuation in the laser energy due to the jitter in switching time of Pockels cell. The intensity of the ASE pre-pulse was estimated from the signals shown in Fig. 2.9 to be around 3×10^{12} W/ cm^2 . The nanosecond duration ASE pre-pulse with relatively low intensity but having energy of few μJ , as in this case, can form plasma by cascade ionization

and collisional heating mechanism. This is because the threshold intensity for plasma production for a nanosecond duration pulse is much lower than that for a femtosecond duration pulse. Therefore, it is expected to form plasma before the arrival of the main femtosecond laser pulse.

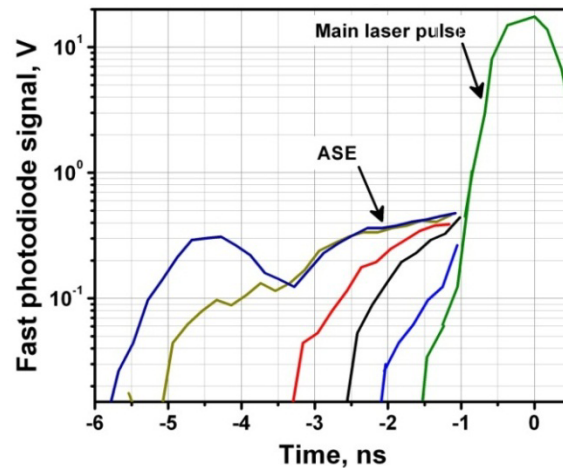


Fig. 2.9: Pre-pulse due to amplified spontaneous emission (ASE) measured with a fast photo-diode. The colours of traces correspond to different switching times of the pulse cleaning Pockels cell.

2.4 Plasma chamber and target setup

An octagonal plasma chamber evacuated by turbo-molecular pump backed by a rotary pump system was used for laser plasma interaction experiments. Figure 2.10 shows a photograph of the chamber. It is made up of stainless steel, has an overall height of 48 cm and octagonal face to face distance of 70 cm. It has demountable flanges on all the eight sides as well as on the top. This enables easy installation of various diagnostic devices. Diagnostic port-holes are located in different directions making angles of 22.5°, 45°, 67.5°, and 90° w.r.to the target normal. The plasma chamber is routinely evacuated to a level of 10^{-5} torr.

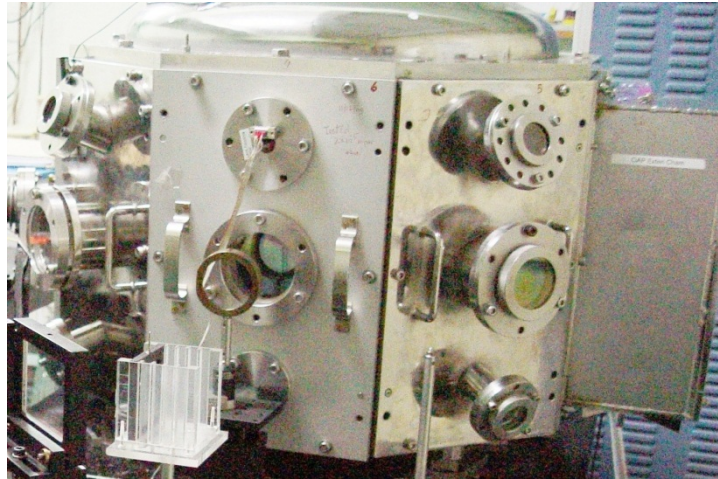


Fig. 2.10 *A photograph of the plasma chamber.*

Plasma was produced by focussing high power laser beam on planar slab targets using an AR coated plano-convex lens kept outside the interaction chamber. The target was mounted on a holder coupled to a precision 3-axis stepper motor based translation stage. The target positioning in the centre of the chamber was accomplished using a computer controlled stepper motor driver. For the operation of laser at 10 Hz, the target was moved at a constant speed of 1mm/s (i.e. 100 μm between every shot) with the help of an x-y stage, so that each laser pulse irradiated a fresh spot for a laser operation at 10 Hz. The run out from the focal plane while moving the target was checked by imaging the target plane with an objective onto a CCD camera. The run out from the focal plane was less than 25 μm , which is much smaller than the Rayleigh range. The target motion was controlled with an accuracy of ~ 10 μm . Further, an optical telescope was used to view the target to ensure that it is positioned precisely in the centre of the plasma chamber.

2.5 X-ray CCD camera based crystal spectrograph

X-ray emission spectrum of LPP is a valuable source of diagnostic information of the plasma, and it is also helpful in determining the suitability of the LPP for various

applications. X-ray spectrographs based on Bragg reflection from crystals are most commonly used for recording x-ray emission spectrum in the wavelength range of 1 Å to 10 Å [23, 51, 86-89].

Figure 2.11 illustrates the basic geometry of an x-ray crystal spectrograph. The x-rays are reflected from the crystal according to the Bragg condition

$$2d \sin\theta = n \lambda \quad (2.4)$$

where d is the inter planar spacing of the reflecting planes, and θ the angle of incident x-rays w.r.to the crystal plane.

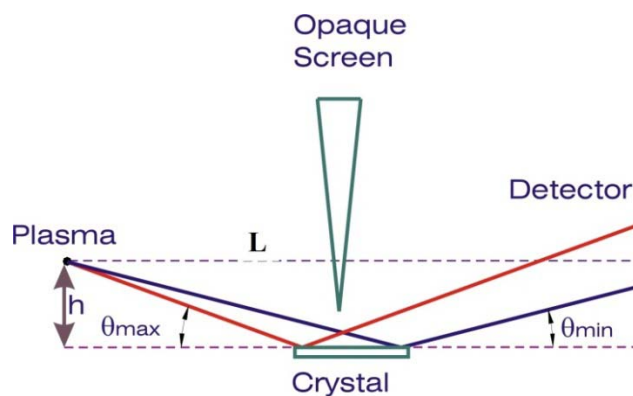


Fig. 2.11: Bragg reflection geometry for x-ray crystal spectrograph.

In the case of laser produced plasmas, the x-rays from the point-like plasma source incident on the planar crystal subtend a range of angles θ_{B1} to θ_{B2} . The x-rays of different wavelengths incident at different points along the length of the crystal, satisfying the above condition, are Bragg reflected and thereby get spectrally dispersed. The spectrum is recorded on a planar detector such as an x-ray film or an x-ray CCD.

We have set up an x-ray spectrograph using planar slabs of a variety of crystals to access different spectral ranges. For instance, to record the K-shell x-ray emission from Mg

and L-shell x-ray emission from Cu, a TAP (Thallium Acid Phthalate) crystal ($2d = 25.75 \text{ \AA}$, 001 plane) of size 50 x 25 x 1mm (thickness) was used as a Bragg reflector for covering a spectrum range from $7.5 \text{ \AA} - 11 \text{ \AA}$. A planar slab of PET (penta erythritol) crystal crystal of a double inter-planar spacing ($2d$) of 8.742 \AA [(002) plane] was used to measure in the spectral range of $2.5 \text{ \AA} - 2.8 \text{ \AA}$ where the emission around Ti K- α radiation lies. For recording a high resolution spectrum around the wavelength of Ti, Fe, and Cu K- α radiation, a 500 μm thick flat Si (111) crystal with (111) orientation ($2d = 6.271 \text{ \AA}$) was used with Bragg angle between 13.8° and 26° . Table 2.1 shows the data [23] for the crystals used in our experiment.

Crystal	Reflection Planes	$2d$ (\AA)	Bragg angle	Rocking curve half width $\delta\theta$ (mrad)
TAP (Thallium Acid Phthalate)	(001)	25.75	20.5°	0.45
PET (Penta erythritol)	(002)	8.742	18.3°	0.5
Silicon	(111)	6.271	18°	0.09
Silicon	(111)	6.271	13.8°	0.1

Table 2.1 *Important parameters of the crystals used in the spectrograph to record x-ray spectrum*

In the initial experiments, Kodak DEF-5 x-ray film was used as a detector. The x-ray film was placed in a suitable holder, and made light tight using aluminized polycarbonate (code-named: B-10) foils having an atomic composition aluminum: 0.05 mg/cm^2 , oxygen : 0.0375 mg/cm^2 and carbon : 0.15 mg/cm^2 . The transmission characteristics of this filter foil is shown in Fig. 2.12. The cut-off energy (corresponding to $1/e$ transmission) of two B-10 foils is $\sim 0.9 \text{ keV}$. Direct radiation from the plasma on to the film holder was blocked by

placing a thick black plastic sheet. The exposed x-ray film was developed for a period of 5 minutes in D-19 developer with a standard procedure.

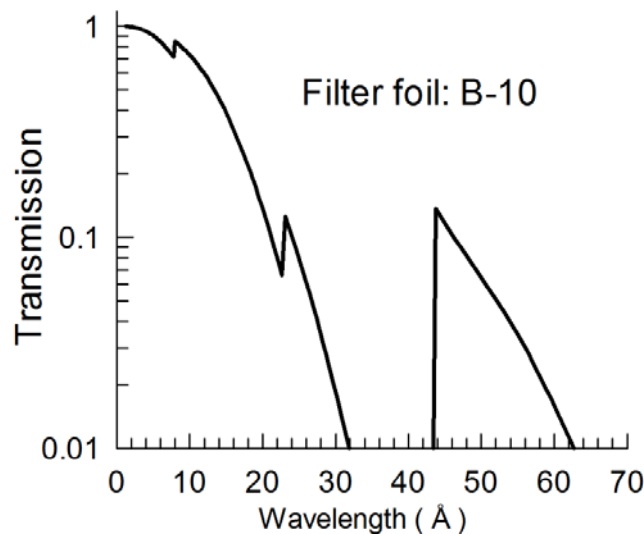


Fig. 2.12: *Transmission characteristics of a B-10 foil.*

In the major part of the thesis, an x-ray CCD camera was used for on-line measurements and analysis of the x-ray emission from the laser produced plasmas. It is a commercial system from Reflex SRO (Czech Republic) [90]. The CCD used in our experiments is a back illuminated one, which is reverse in structure in the way that the x-ray photons interact with the thin silicon layer ($\sim 20 \mu\text{m}$) and electrode assembly is on the back of the silicon to store and move these photo-electrons. It is equipped with a Marconi[™] back-illuminated chip consisting of 2048×2048 pixels, each of $13.5 \times 13.5 \mu\text{m}^2$: Its active image area is $27.6 \times 27.6 \text{ mm}^2$. The peak signal is 100,000 e^- per pixel, and the digitization level is $\sim 1.5 e^-$ per analog to digital unit (ADU). The chip has a regulated two stage thermoelectric cooler to attain a temperature up to -30°C . The temperature stability of the CCD was 0.1°C across entire temperature range. The CCD, operating in full-frame mode, was read using the 16 bit ADC at a read-out speed of more than 25 k pixels per second. The quantum efficiency curve for the CCD chip given in Fig. 2.13 as per manufacturer specification.

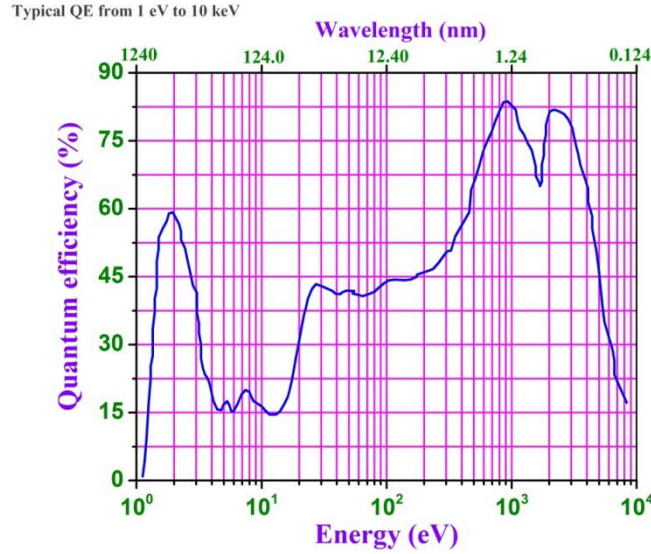


Fig. 2.13: *Quantum efficiency of x-ray CCD as per manufacturer.*

A schematic diagram of the experimental setup of the on-line x-ray spectrograph is shown in Fig. 2.14. A planar TAP crystal of 50 mm length, 25 mm width, and 2 mm thickness was placed in the horizontal plane in the interaction chamber such that its centre is midway between the plasma source and the detector. The crystal was mounted on an Oriol™ motor mike drive for precise adjustment of the wavelength by changing the angle. This drive has a backlash compensation feature and is equipped with a controller which provides a translational travel upto 50 mm with a travel accuracy of 1 micron.

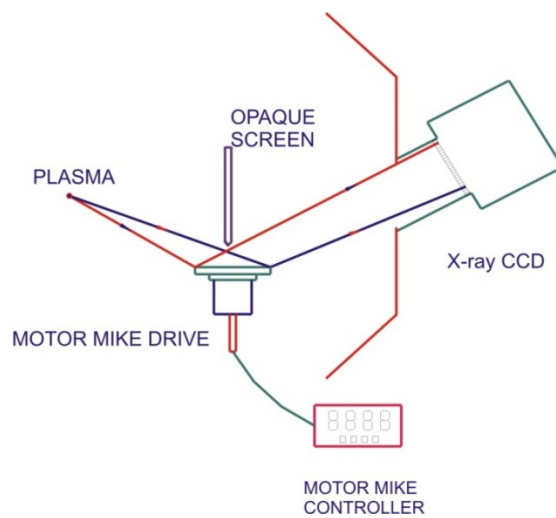


Fig. 2.14 *A schematic diagram of the experimental set up of the on-line x-ray spectrograph.*

The crystal was positioned so as to subtend a mean Bragg angle of 19° at the source, and the total distance from the source to the crystal and the crystal to the detector was kept to be 567 mm. Two aluminized polycarbonate foils were used to prevent any scattered light in the plasma chamber from coupling to the detector. A 6 mm thick lead screen was placed to block x-ray emission from falling directly on the detector. For this geometry, the spectrograph had a plate factor of $0.045 \text{ \AA} / \text{mm}$. The spectral resolution of the crystal spectrograph is given by the expression [87]

$$\delta\lambda = D_\theta \delta\theta + D_x \delta x \quad (2.5)$$

where D_θ is the angular dispersion, $\delta\theta$ is the angular half width of the crystal rocking curve, δx is the overall spatial resolution determined from the source size Δx_s , and spatial resolution of the detector Δx_D . For an angular half width of the crystal rocking curve $\delta\theta = 0.45 \text{ mrad}$, $D_\theta = 23.9 \text{ \AA}/\text{radian}$ (for $\lambda = 9 \text{ \AA}$), and source size of $\sim 50 \text{ \mu m}$, the spectral resolution comes to $\sim 13 \text{ m\AA}$.

The spectrograph was tested by measuring x-ray line spectrum of copper plasma produced by a portion of the uncompressed radiation (pulse energy $E = 30 \text{ mJ}$, pulse duration $\tau = 300 \text{ ps}$, central wavelength $\lambda = 793 \text{ nm}$) which was split from the main beam of the Ti:sapphire laser system by a beam splitter. A typical x-ray spectrum recorded in 50 shots at a laser intensity of $3.9 \times 10^{13} \text{ Wcm}^{-2}$ and its intensity plot are shown in Fig. 2.15. The characteristic lines and ionization states have been identified [91]. The dominant spectral lines are the ones originating from the Ne-like Cu^{+19} ions ($2p^6 - 2p^5ns, 2p^6 - 2p^5nd$). Somewhat weaker F-like Cu XXI lines from the Cu^{+20} ions are also seen. The spectral resolution was determined by measuring the FWHM of various lines. The smallest width was observed to be $\sim 15 \text{ m\AA}$. This

provided an upper limiting value of spectral resolution and it is in good agreement with the theoretically expected value of $13 \text{ m}\text{\AA}$ calculated by considering a source size of $50 \text{ }\mu\text{m}$, crystal rocking curve half width of 0.45 mrad , and pixel size of CCD camera. The spectral range can be changed by suitable positioning of the appropriate crystal placed on a translation stage.

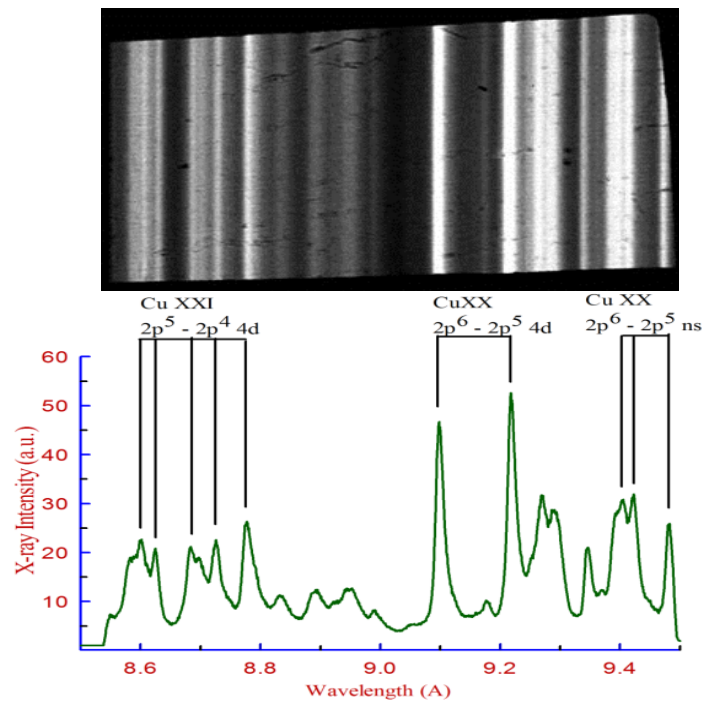


Fig. 2.15 X-ray spectrum as seen on x-ray CCD camera (top) and its intensity plot (bottom).

2.6 Dispersion-less spectrograph

Different types of spectrographs have been reported in literature for the measurements of x-ray emission in the multi keV region from laser produced plasmas. Wavelength dispersive spectrographs such as crystal spectrographs [23,87] are most widely used for x-ray spectroscopic studies in the 1-8 keV energy range, which cover the characteristic K- α emission from mid- Z target such as copper, nickel etc. Although a crystal spectrograph provides very high resolution, the spectral range covered is very small and necessitates a

change of the crystal / spectrograph setting with the target material. The efficiency of such a spectrograph is rather low due to the smaller solid angle subtended by the crystal having narrow rocking curve width and reduced reflectivity of a crystal at higher photon energies [23]. Such spectrographs are particularly not suited for relativistic laser plasma interaction environment where the fluorescence emitted by the crystal will degrade the signal to noise ratio [92, 93].

On the other hand, the solid state detectors working in single photon counting regime are often used as energy dispersive spectrographs to record spectrum in a much larger spectral range extending from a few keV to a few tens of keV [92-95]. The spectral information is retrieved under the condition that only one photon enters the detector during a time window determined by the time taken by the multi-channel analyser (MCA) coupled to the detector to sort out the height of the signal corresponding to the incident photon energy. If an x-ray photon of energy E is absorbed completely, it will produce a photo-electron having energy almost equal to that of the incident photon. This electron will lose its energy in the detector medium by producing several electron-hole (e-h) pairs. If ϵ is the average energy required for e-h pair creation (e.g. ~ 3.7 eV in silicon) and E is the energy of incident photon, then the average number of the e-h pair produced is approximately E/ϵ . The charge generated by the x-ray photon is collected and transported to the output amplifier. The amplified signal is fed to an MCA through an analog to digital converter (ADC) to display pulsed height distribution spectra. The MCA is calibrated using standard x-ray sources to get unknown spectra. Cooled Si (Li) detectors, CZT or CdTe detectors in single-photon counting mode have been most widely used in x-ray spectroscopic systems in the multi keV region. As mentioned earlier, recording of a single spectrum requires a very large number of the laser shots. The availability of x-ray sensitive CCDs having large number of pixels (typically one to four million) allows one to record the entire x-ray spectrum in a single shot, by

simultaneous detection of a large number of single photon counting events [92-93, 96]. This is equivalent of capturing events equal to the number of pixels, in a single shot, and subsequent construction the spectrum from these events. Such a spectrograph where no external dispersive element is used, is referred to as a dispersion-less spectrograph.

A back illuminated x-ray CCD detector working in single photon counting mode has been used for absolute measurement of x-ray emission spectrum without any additional dispersive device. An algorithm for identifying the single photon counting events from the over-exposed CCD raw data has been developed to reconstruct the x-ray spectra even from a CCD frame which was exposed above the single photon counting threshold. Characterization of the spectrograph was carried out by measurement of characteristic line and continuum x-ray emission from high intensity femtosecond laser produced plasma in the 2- 20 keV energy range. Image analysis software is developed for deriving spectral information from photons detected by CCD. The details are provided in the following subsection.

2.6.1 Description of the spectrograph

A CCD detector has a large number of pixels, with each pixel acting as an individual detector, for simultaneous detection of a large number of single-photon events. This permits recording of the spectrum in a single laser shot, simply from the histogram of the pixel intensity. The 4M, Reflex SRO x-ray CCD camera is used in the present experiment has a thinned back-illuminated image sensor. The dark frame recorded at temperature of -30°C had a systematic noise pattern with a root mean square value (rms) of 256 ADU, and rms deviation (σ) of ~ 5.3 ADU. Taking minimum of 2.5σ for discriminating signal with noise, lower energy detection limit comes to 269 ADU. This corresponds to ~ 1.5 keV by taking 3.7 eV as the average energy [97] required for producing one electron pair. The number of

photons of energy $h\nu$ detected by the spectrograph per unit solid angle may be expressed in terms of the number of photons emitted by the source as

$$dN_\nu / d\Omega = N_x(\nu) T_\nu \eta_\nu \quad (2.6)$$

where $N_x(\nu)$ is the photon flux emitted from the source, T_ν is the transmission of material filter, and η_ν is the quantum efficiency of the CCD chip at photon energy $h\nu$. The quantum efficiency data was provided by the manufacturer for the photon energies up to 10 keV to account for the energy dependence of the spectrograph. An active region thickness of 25 – 40 μm is estimated from the quantum efficiency data. For energies in the range of 10 – 20 keV, the quantum efficiency is assumed to vary inversely with the photon absorption length, with an assumption that photon is completely absorbed in the substrate [98]. The higher energy detection limit of the spectrograph is mainly set by the quantum efficiency of the CCD. It is to be noted that despite rapidly decreasing quantum efficiency at higher photon energies, we were able to record the spectrum up to 20 keV, from the high flux laser plasma x-ray source.

The spectral resolution is governed by the thermal noise, readout noise, and the interaction statistics [97, 99]. Moreover, if a K- α photon from an excited atom of the Si substrate escapes from the detector sensitive area, a separate line (escape peak) would be seen at an energy location corresponding to the incident photon energy minus the silicon K- α photon energy (1.74 keV). The spectrum of the detected photons from a monochromatic x-ray source can get broadened due to the loss of absorbed photon energy in processes other than the creation of electron pair [97]. This is mostly due to heating or diffusion of electron cloud to the other channel [96-97]. This brings the Fano limit [97] for the resolution. The contribution to the detector FWHM energy resolution Γ are defined by Eq. 2.7

$$\Gamma \equiv \sqrt{\left[\left(2.35\sqrt{\mathcal{E}FE} \right)^2 + \Gamma_{other}^2 + \Gamma_{noise}^2 \right]} \quad (2.7)$$

The first term is the broadening due to ionization statistics. F is the Fano factor given by $\frac{\sigma_n^2}{n}$, where n is the average number of electron pairs produced in the detector by a photon of energy E and σ_n^2 is the expected variance in this number. ε is the average energy required to produce one electron pair. Γ_{noise} is the contribution of the thermal and readout noise. Γ_{other} is the line broadening contribution such as natural line width. The energy resolution at 4.5 keV, taking $F = 0.115$ for Si detector, $\varepsilon = 3.7$ eV, $\Gamma_{\text{noise}} = 74$ eV (2.5σ), $\Gamma_{\text{other}} = 1.6$ eV, the natural line width of Ti K- α line radiation, the overall energy resolution expected is 127 eV which is ~ 2.8 %. The typical resolution reported in literature in the spectral range of 2- 20 keV is less than 5 %.

2.6.2 Reconstruction algorithms to identify the single pixel event

Single photon counting condition is often difficult to ensure while recording the x-ray emission spectrum from a high photon flux x-ray source. In such a case, low energy photons can be eliminated by appropriate material filters. The high energy photons can be reduced by restricting the solid angle by increasing the distance between the x-ray source and the detector. This is often difficult due to a widely unknown x-ray flux for different experimental conditions. Further, the charge generated at each pixel after absorption of x-ray photon also undergoes drift, diffusion and absorption across multiple pixels in the CCD [100-101]. The multi-pixel events lead to improper energy identification of the photons when the spectral data is reconstructed using standard histogram which assumes that the exposure at every pixel is due to a single photon only. It is necessary to develop algorithms to identify the single pixel event to get the energy spectrum from the raw data of the CCD. Various reconstruction algorithms are used to identify the real single pixel events. For instance, Zamponi *et al* [102] identify the split event with an algorithm developed to recognize simple patterns. If a pattern

matches with the distribution of the signal on different pixels then the values from these pixels were summed up to reconstruct the original signal. It may be noted that a split event (or multi-pixel event) is defined when more than a certain fraction of the generated charge is shared with the neighbouring pixels. Maddox *et al* [100] developed an algorithm to identify the single pixel events by comparing the charge in each pixel to the sum of the charge in it and the 8 neighbouring pixels. If the charge in the pixel is more than the 49% of the sum of the charges (in 9 pixels), then it is considered as an isolated, single pixel event, and is used to build the histogram with better resolution. Else, it is discarded as a split event. This algorithm faces problem when one has over-exposed (i.e. where the fraction of multi pixel events is more than the single pixel events) raw CCD data.

As mentioned earlier, a CCD can have events wherein a single photon may be registered by two or more pixels (split event or multi-pixel event). Further, when the flux is very large, one gets multiple photons incident on a single pixel. The corresponding counts are erroneously registered as harmonics of the incident spectrum. Once the CCD is exposed to radiation and the "data image" is taken, the data is processed first by correcting it for the dark charge pattern of the CCD. This is done by subtracting an unexposed image, acquired under identical detector setting conditions, from the data image, pixel by pixel. Further, to reduce the random noise in the background image, a master background image generation facility has been incorporated, by adding multiple background images, and then normalizing the composite image by the number of images (N) added. This reduces the effect of random noise by a factor equal to the reciprocal of the square root of the number of images added ($1/\sqrt{N}$). The spectrum is generated by standard histogram of the pixel intensity from the processed image. The inset of Fig.2.16 shows a typical raw data image of titanium plasma produced by 45 fs Ti: sapphire laser pulses at an intensity of $1.2 \times 10^{18} \text{ Wcm}^{-2}$. The image consists of spots corresponding to the interaction of x-ray photon with single / multiple pixels. The spectrum

was recorded from the front side, at a viewing angle of 45° with respect to the target normal. X-ray filters are used in front of the CCD to adjust the signal level of the K-shell emission and to improve the signal to background ratio. It is often difficult to obtain the K-shell emission at low energy (< 5 keV) with good signal to noise ratio. Here, the noise events primarily arise from the fluorescence radiation from the plasma chamber wall or fractional deposition of energy by high energy x-ray photons. Fig. 2.16 shows the x-ray spectrum obtained by the standard histogram method, where it is assumed that at each pixel single photon counting condition is satisfied i.e. the charge is proportional to the incident x-ray photon energy, and there are no multi-pixel events. The x-ray emission spectrum shows a broad continuum (bremsstrahlung) generated by the propagation of fast electrons in the bulk target behind the hot plasma. The inner-shell line transitions namely K- α and K- β , which are a typical signature of hot electron propagation in the cold target, are not clearly resolved (seen as a hump at ~ 4.5 keV) due to the heavy background emission.

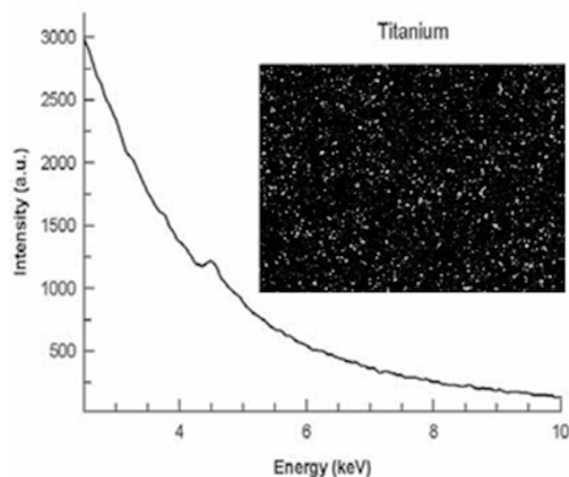


Fig. 2.16: X-ray emission spectrum obtained with standard histogram method. The inset shows an over-exposed raw image obtained with the dispersion-less spectrograph.

The reason for the poor resolution using the standard method of computing histogram of the CCD signal is that it does not differentiate between the single pixel events and multi-

pixel events. If charge spreads in adjacent pixels, that pixel is read as pixel of lower energy, thus lowering the resolution due to this spread. As mentioned earlier, in order to use a CCD as a dispersion-less x-ray spectrograph, it has to be ensured that number of photons hitting a pixel should not be more than one. A careful analysis of the data is required for spectral identification and quantitative estimation of the flux. Various reconstruction algorithms are used to identify the real events. The simpler algorithms use rejection threshold to distinguish between the pixels with x-ray photon and the noise. However, advanced algorithms are required to identify the contribution from the single events and split events for obtaining better resolution. A special algorithm has been developed to correct for the contribution of split events. This algorithm identifies the single pixel events by taking the ratio (δ) of the charge in the pixel under examination, to the sum of the charges in the selected neighbourhood of pixels (4 nearest neighbours or 4 diagonal neighbours or 4 nearest + 4 diagonal neighbours, as desired). If this ratio is greater than a specified value, then that pixel is considered as an isolated, single pixel event, and the charge in the adjacent pixels is added to it. If the ratio is less than the specified value, that pixel is rejected as a doubtful one. After doing this for all pixels, the histogram is built. A value of $\delta \sim 1$ means charge in the pixel under examination is equal to the sum of the charge of the adjacent pixels. It gives higher flux but lower resolution. A value of $\delta \sim 10$ gives better resolution, but more pixels are discarded. A higher value of δ is useful in the over-exposed case to get better resolution, whereas lower δ can give good resolution as well as flux in a data file where the fraction of multi-pixels is very low. In general, the resolution will be higher for a larger value of δ but the detection efficiency will be reduced and vice versa. A graphical user interface (GUI) has been provided to configure the lower and upper energy cut-off levels, to select the pixel neighbourhood (4 adjacent or 4 diagonal, or all 8 adjacent + diagonal), and to specify the value of the ratio (δ) can be set from 1 to 10) to obtain the energy spectrum with best resolution. The pseudo-code

of the routine by which the energy spectrum is generated from the raw data on the x-ray CCD is written in the vb.net language. Fig.2.17 shows the spectrum obtained with this algorithm for $\delta = 10$. The inset of Fig.2.17 shows a data image processed with the developed algorithm. The inner-shell line transitions namely K- α and K- β are now clearly visible over the continuum background (c/f Fig.2.16). This illustrates the merit of this algorithm to identify the single pixel event from the over-exposed data to generate spectrum with high resolution. This also tells why the resolutions in the earlier algorithms were not very high. For example, in the algorithm used in ref. 100, the effective value of δ was 0.49 ($\sigma = 0.98$), and in ref.102 it was ~ 5.7 (85% charge in the central pixel).

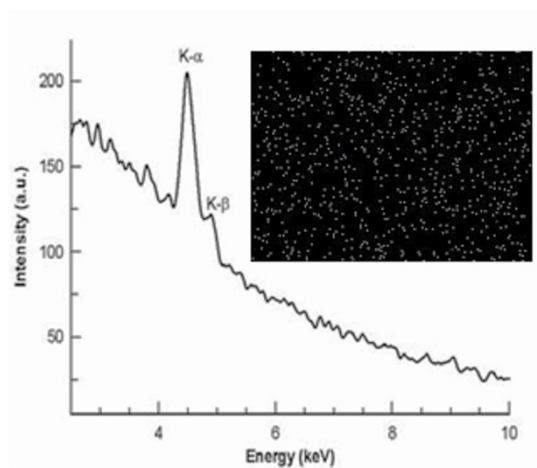


Fig. 2.17: *The x-ray emission spectrum from data in Fig.2.16, obtained with the special algorithm. The inset shows the genuine, all single photon events image obtained after applying the algorithm.*

2.6.3 Characterization and performance of the spectrograph

Figure 2.18 shows the schematic diagram of the spectrograph setup. The spectrograph faced the target from the front side, in the horizontal plane, at a distance of 580 mm from the target. A 13 μm thick aluminium foil, mounted on a 6 mm thick lead disc, was placed before the CCD camera to prevent the scattered laser light going directly to the CCD, and to limit

the background noise. Suitable filters mounted on a filter wheel were used, depending on the x-ray spectral range of interest. The noise coming from the bremsstrahlung emission from the interaction of charged particle with the filter itself was stopped by the strong magnets diverting the electrons from the plasma. The magnets deflect the fast electrons so that they do not strike the foil placed before the CCD camera and produce bremsstrahlung radiation, which would give rise to a large background on the CCD camera. The distance at which the electrons would strike the filter foil increases with increasing distance between magnet and foil. However, it cannot be increased too much due to the setup limitation. The distance in our setup was chosen so that the magnets used in the experiment (magnetic field of ~ 500 G inside the pole gap of 35 mm) would deviate electrons with energy < 1 MeV. The measured hot electron spectrum (by Rao *et al* [123]) shows that there are not many hot electrons with energy higher than 1 MeV.

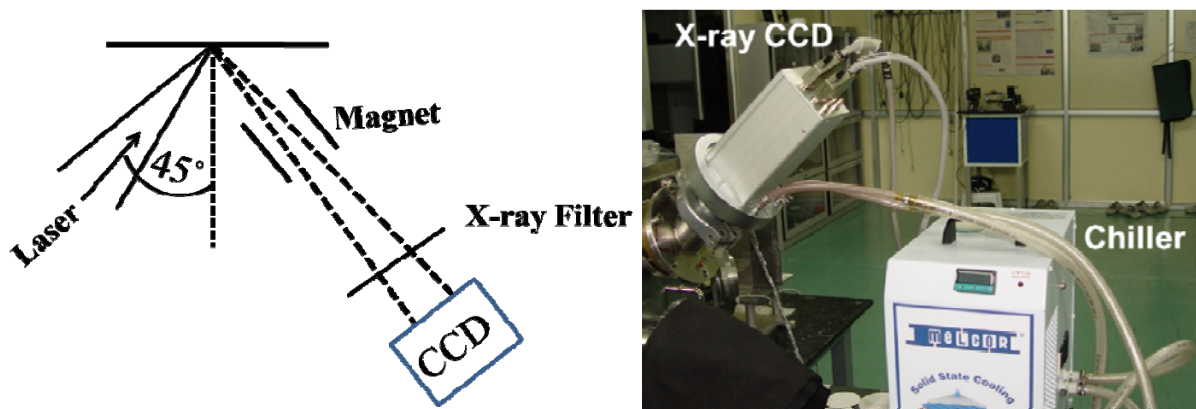


Fig. 2.18 : (left) A schematic diagram of the experimental setup; (right) x-ray CCD mounted on the chamber.

The performance of the spectrograph was tested by recording the x-ray emission spectrum from plasmas of various targets irradiated by the ultra-short, high intensity Ti:sapphire laser pulses of 150 mJ energy in 45 fs (FWHM) at $\lambda=800$ nm. The plasma was produced by focusing the laser pulses using an f/8 lens, onto a target, placed at an angle of

45° with the laser beam. The maximum focussed intensity of the laser on the target was $\sim 1.2 \times 10^{18} \text{ W cm}^{-2}$, for a measured focal spot diameter of 18 μm . The interaction chamber was evacuated to a pressure of 10^{-6} mbar. The laser plasma x-ray spectral characteristics were varied by changing the laser energy and the pulse duration. The laser pulse duration was varied from 45 fs to ~ 2 ps by introducing either positive or negative chirp in the laser pulse, by changing the grating separation in the pulse compressor stage of the laser system. The calibration of the CCD signal with the photon energy was done in the spectral range of 2 – 20 keV. For this purpose, planar targets of titanium, copper, stainless steel, zinc, gallium arsenide, zirconium, and molybdenum were used.

Figures 2.19 (a)–(c) show the spectra of x-ray emission from titanium, copper, zinc, stainless steel, gallium arsenide, zirconium and molybdenum. Each x-ray spectrum shows the characteristic line radiation and the continuum radiation generated by the fast electrons produced during the interaction of the ultra-short, ultra-high intensity laser pulse with the target. For instance, in spectrum of titanium (Fig. 2.19(a)), both K- α at 4.5 keV and K- β at 4.9 keV can be seen. In the same figure, copper spectrum shows Cu K- α at 8 keV and the silicon escape peak at ~ 6.3 keV (as the silicon K- α photon energy is 1.74 keV). The Cu K- β (8.9 keV) was not seen due to its strong attenuation by the Ni filter used in front of CCD. Similarly, the characteristics line at 8.6 keV was seen in the spectrum of zinc (Fig. 2.19(a)). The stainless steel spectrum (Fig. 2.19(b)) shows the characteristic lines of its constituent namely Cr K- α at 5.4 keV, Mn K- α at 5.9 keV, Fe K- α at 6.4 keV and K- β at 7.1 keV, Ni K- α at 7.5 keV. Similarly, the characteristics lines of gallium arsenide constituents viz. Ga at 9.3 keV and As at 10.5 keV were shown in Fig. 2.19(b). Figure 2.19 (c) shows the spectra of zirconium, and molybdenum with characteristic line at 15.8 keV and 17.5 keV respectively.

The above-stated energies of various inner-shell line transitions are shown as data points corresponding to different ADU in Fig. 2.20. It is noted that spectrograph shows a

good accuracy in determining the value of the photon energy. The solid line shows the fitting of the data to

$$\text{Energy} = 6.7 * (\text{ADU} - 270) \text{ eV} \quad (2.8)$$

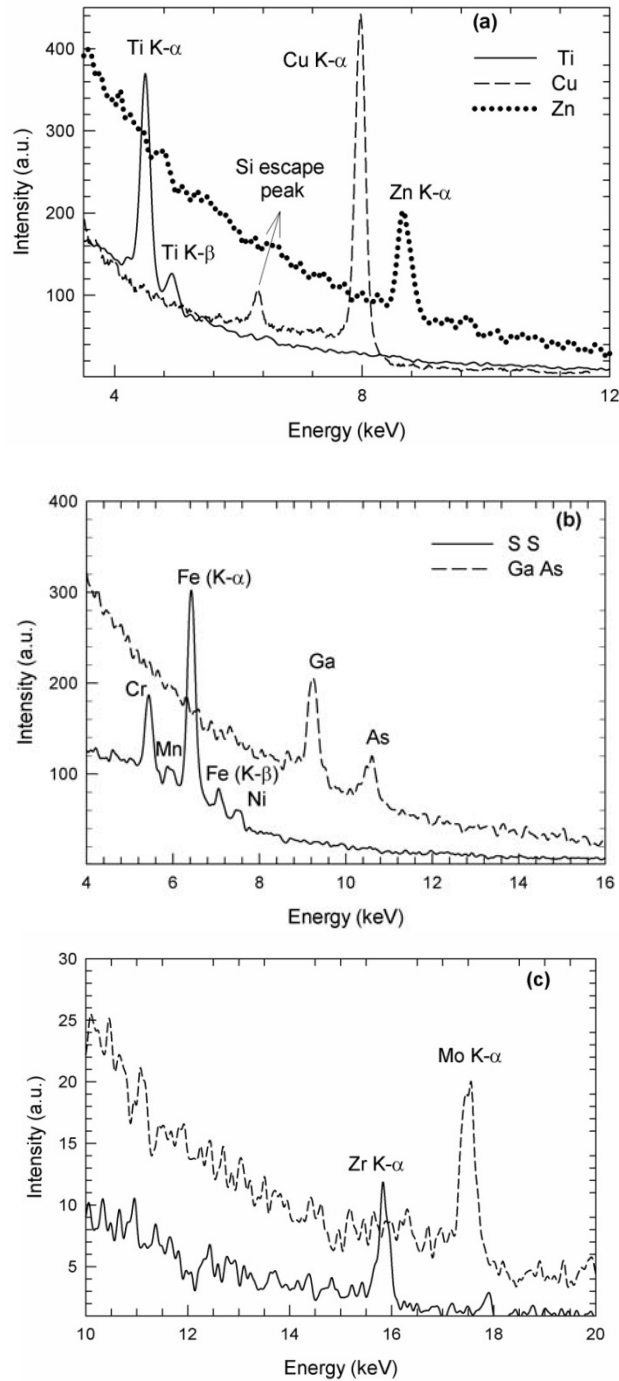


Fig. 2.19: X-ray emission spectra of (a) titanium, copper, zinc (b) stainless steel, and gallium arsenide (c) zirconium, and molybdenum.

The X-intercept is due to the noise which gives a background count of ~ 270 . The slope gives a calibration factor of ~ 6.7 eV per ADU. The calibration factor is about 20 % higher than the manufacturer supplied data of 5.55 eV per ADU. The higher calibration factor is perhaps due to the difference in stated value of the peak signal obtained from the sensor. This also highlights the fact that independent characterization of the spectrograph is necessary in the actual experimental conditions of utilization.

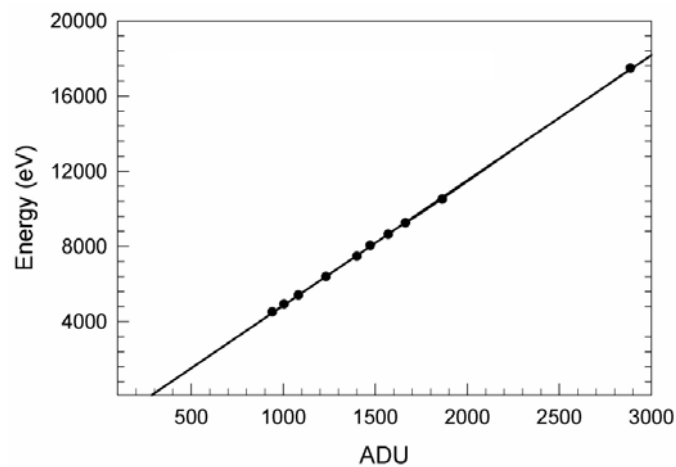


Fig. 2.20 Energies of various inner-shell line transitions corresponding to different ADU. The solid line shows the fitting of the data to the energy.

An estimate on the spectral resolution can be obtained from the FWHM of a sharp line observed in the spectrum. For instance, in Fig.2.19 (a), the FWHM of the Ti K- α at 4.5 keV is only 144 eV. This can be taken as an upper bound on the spectral resolution, and it is very close to the spectral resolution of 127 eV expected from the parameters of the spectrograph. The observed spectral width (FWHM) increases with increasing x-ray photon energy in confirmation with the Eq. (2.7) describing spectral resolution in solid state detector. The relative energy resolution (defined as Γ/E) is shown as a function of photon energy in Fig.2.21. The resolution improves from ~ 3.2 % at 4.5 keV to ~ 1.6 % at 17.5 keV. Next, the line intensity ratio of the Ti K- β to K- α was calculated by taking into account the foil

transmission and the detector quantum efficiency. The ratio was observed to be 0.12 compared to the cold value of 0.3 [103]. The observation of lower K- β / K- α ratio is perhaps due to the population in the M-shell being slightly depleted because of target heating by the hot electrons. The variation of K- β / K- α ratio can serve as diagnostics for the bulk plasma environment [104]. The absolute number of the K- α photons was determined by summing the number of hits contained in the K- α line shape and by taking into account the solid angle, the filter transmission, and the quantum efficiency of the CCD in single-pixel analysis mode. An isotropic emission into a 4π sr solid angle can be assumed, for simplicity. The yield of the copper K- α photons (8 keV) emitted into the full solid angle was estimated to be $\sim 5.5 \times 10^{10}$ / s / unit energy interval consistent with the reported values [73].

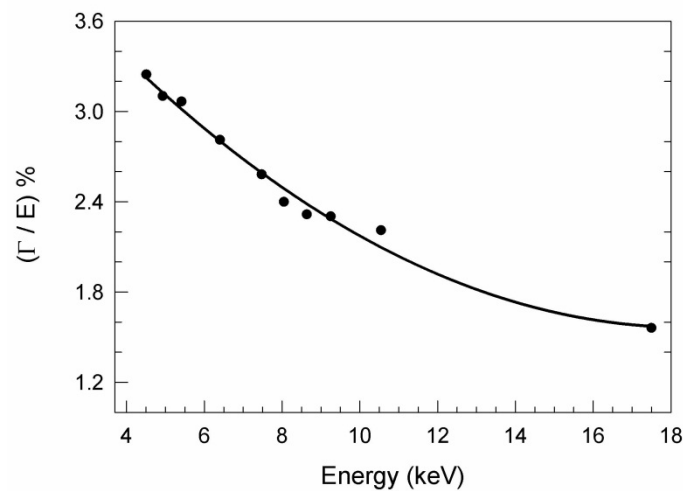


Fig. 2.21: Relative energy resolution (Γ/E) as a function of the photon energy.

The inherent higher detection efficiency [97] of the energy dispersive spectrograph compared to a wavelength dispersive spectrograph makes it suitable for the measurement of low x-ray flux from the rear side of a foil irradiated at sub-relativistic laser intensities. In this case, the electrons enter the target and undergo scattering to lose their energy, and the emitted radiation also undergoes absorption while coming out from the rear side of the foil target. The

performance of the spectrograph was tested by recording the x-ray emission from the rear side of a 24 μm thick titanium foil used as a target. The x-ray CCD was kept in the horizontal plane, along the rear target normal, at a distance of 580 mm from the target. A 13 μm aluminium foil was placed before the CCD. Similar to the earlier experiment where the emission was measured in the front direction, the laser pulse was incident making 45° angle with the target normal. Fig.2.22 shows the x-ray emission spectrum from the rear side of the titanium foil irradiated at a laser intensity of $\sim 1.2 \times 10^{18} \text{ W cm}^{-2}$. For a quick comparison, this figure also shows the spectrum from the front side under the identical laser irradiation conditions. It can be seen that the back-side spectrum has much better signal to noise ratio compared to the measurement from the front direction. The advantageous features of using the present setup in such measurements lie in its simple, quantitative, and single shot operation.

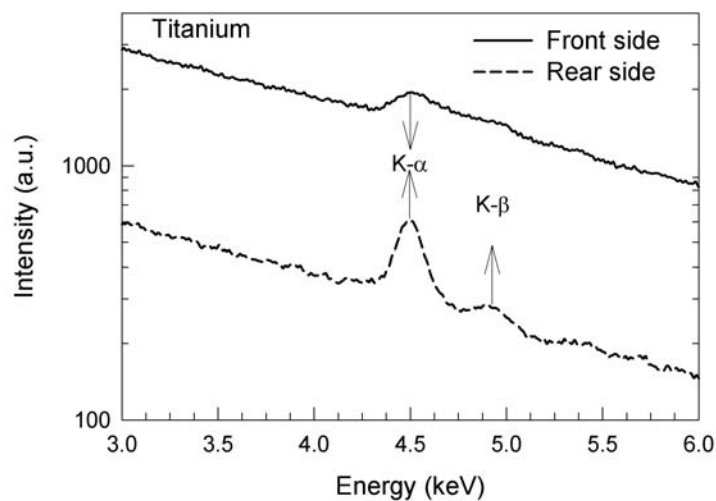


Fig. 2.22: X-ray emission spectrum from the rear side of the 24 μm thick titanium foil irradiated at a laser intensity of $\sim 1.2 \times 10^{18} \text{ W cm}^{-2}$.

2.7 X-ray p-i-n diode

Measurements of soft x-ray intensity from the plasma have been performed using silicon p-i-n x-ray diodes (PIN-XRD) [105]. These diodes consist of an active intrinsic region

sandwiched between p- and n- type semiconductor layers. The incident x-ray photons are completely absorbed in the active region, resulting in a current proportional to the incident photon flux or energy. As almost all the energy of the x-ray photon is used to generate electron-hole pairs (about 3.63eV energy is required to generate one electron-hole pair), these diodes have a very high sensitivity. Moreover, their sensitivity does not degrade with time as is the case with vacuum x-ray diodes. The photon energy range of detection is restricted to a lower cut-off of ~ 0.8 keV due to the dead layer, and reduction in response at high photon energy > 10 keV due to poor absorption. However, ultra-thin window diodes have also now become available which extends the soft x-ray spectral response down to a few eV. Figure 2.23 shows the variation of the quantum efficiency of xuv p-i-n diodes (IRD Inc., USA: AXUV series) with the photon energy. It is evident from this graph that for the photon energy exceeding 10 eV, the response of the pin diode is almost linear and therefore, they are quite suitable for absolute xuv flux measurement.

In the present study, we have used various p-i-n diodes, which are procured from different manufacturers. These are: 100-PIN-250 from Quantrad Inc., USA, XUV-05 from UDT Sensors Inc., USA, and AXUV-HS5 International Radiation Detectors (IRD) Inc., USA. They differ in their dead layer thickness (and hence in the spectral range) and temporal response. The Quantrad p-i-n diodes have sensitivity above 0.8 keV and have large detection area of 1cm^2 . The rise time of the diode is ~ 2 ns at reverse bias of about 330 volt. The quantum efficiency as per manufacturer data sheet is 0.2 C/J for 1 keV photons. On the other hand, both UDT and IRD pin diodes have spectral response from 10 eV to ~ 10 keV. The detector sensitive area of these diodes is 5 mm^2 and 1 mm^2 respectively. The rise time of these diodes is ~ 700 ps at a reverse bias voltage of 100 volt.

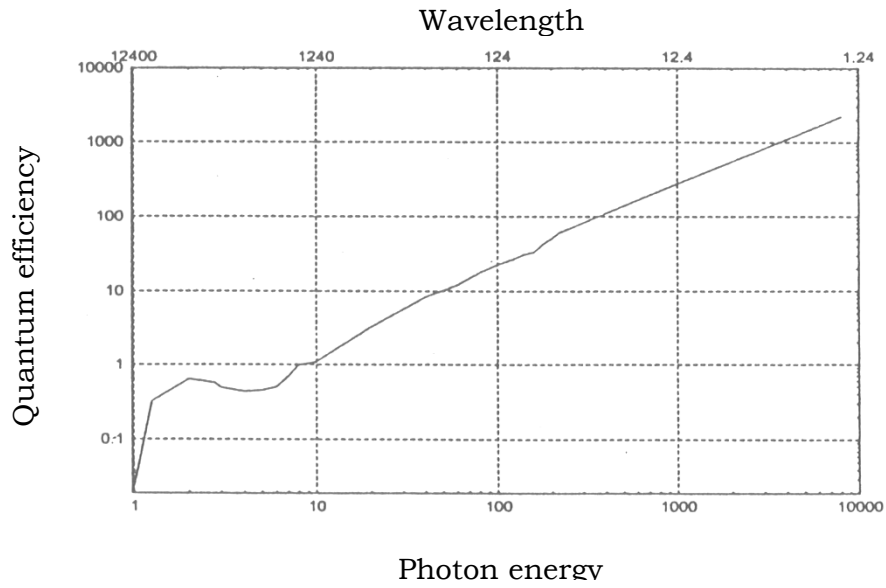


Fig. 2.23: Variation of quantum efficiency (electrons seen by external circuit/photon) of xuv p-i-n diodes with photon energy.

The x-ray pulse energy was measured from the x-ray p-i-n diode signal obtained using a biasing circuit shown in Fig. 2.24. The signal from the p-i-n diodes was taken across a 50Ω load connected at the oscilloscope. The signal was measured in terms of area under the pulse in units of V-s (volt-seconds) by using the integration feature in the digital oscilloscope used (Lecroy: Model 9350A). Therefore, the signal in terms of V-s, divided by the resistance value of 50Ω provides a direct measure of charge collected at the external circuit due to incident x-ray photon flux. The energy of the x-ray pulse incident on the p-i-n diode was derived by using known value of p-i-n diode sensitivity (Fig. 2.23).

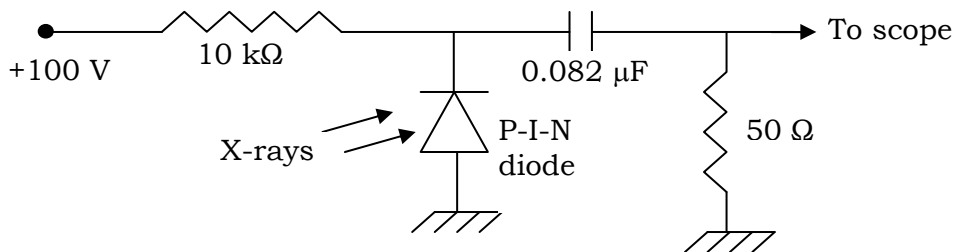


Fig. 2.24: P-i-n diode biasing circuit.

Next, the saturation flux of these diodes is $\sim 1 \mu\text{J}/\text{cm}^2$. Care was taken to avoid saturation of these diodes by mounting them at sufficiently large distance from the plasma and attenuating the x-rays by using appropriate x-ray filters.

To summarize this chapter, a description of the laser systems and the plasma chamber used for studying the x-ray emission from the laser produced plasma has been described. Three different laser system providing laser pulses of duration ranging from 3 ns to 45 fs have been used to study the ionization dynamics in plasma. The main features of the high resolution x-ray crystal spectrograph have been described. The characteristics of the x-ray film and the x-ray CCD camera which were used as detectors with the spectrograph are described. A detailed description of the dispersion-less spectrograph based on the x-ray CCD camera, working in single photon counting mode, has been presented. The spectrograph was characterized in detail and optimized for better performance. The various reconstruction algorithms used to identify the single pixel event have been described. A special algorithm has been developed to correct for the contribution of the split events. The inherent higher detection efficiency of the energy dispersive spectrograph compared to a wavelength dispersive spectrograph makes it suitable for the measurement of low x-ray flux from the rear side of a foil irradiated at sub-relativistic laser intensities.

Chapter 3

Dependence of the ionic x-ray line emission on laser pulse duration

The optimization of the conversion of laser energy into x-rays is one of the objectives of research of high-intensity laser-produced plasmas. It is motivated by its potential application in the field of inertial confinement fusion [12], pumping of the inner-shell x-ray lasers [15], backlighting of the fuel pellets in laser driven inertial confinement fusion [21-22], lithography [18] etc. In the past few years, the plasma generated with a sub-picosecond laser has been shown to be useful as a bright short duration x-ray source for its application in time resolved x-ray diffraction [1-10] measurements. In particular, the ionic x-ray line radiation due to the electronic transitions in the highly charged ionic species (H-like, He-like) present in the plasma heated to a high temperature can serve as a bright, quasi-monochromatic x-ray probe [106-108]. A number of theoretical and experimental studies have shown that the spectral and temporal characteristics of the ionic x-ray lines depend on the laser irradiation parameters. The efficient production of this radiation depends on the plasma parameters, viz. the electron density, the temperature, the average degree of ionization and the opacity of the hot plasma medium [109 - 110]. The pulse duration of the ionic line radiation can be less than a picosecond [109] and is governed by the heating laser pulse duration, hydrodynamical parameters and ionization dynamics [109–112].

The evolution of the multi-charged ion population in transient plasma is determined by the hydrodynamic evolution of the plasma. If the density and the temperature of the plasma changes on a time scale that is much greater than the time scale for the atomic processes, in such a case, the steady state coronal model can describe the ionization equilibrium [35]. On such a long time scale, there is an abundance of H-like and He-like ions

in the plasma of a low- Z target heated to a temperature of more than hundred eV. Such highly charged ionic species are produced by collisional ionization in the high temperature plasma. Nevertheless, the ionization dynamics plays a major role in the early stages of the plasma formation by the nanosecond or sub nanosecond duration laser pulses [113- 114]. On the other hand, in the short duration laser - matter interaction, due to negligible expansion and heat conduction during the laser pulse, a high density and high temperature plasma is formed. For such plasma, the characteristic times of different atomic processes are comparable with time scales on which the temperature and density changes occur. In such a case, transient collisional radiative model is used to describe the ionic population density and the modelling of x-ray emission necessitates the use of time-dependent atomic-physics code coupled to the multi-dimensional hydrodynamics with radiative-transfer calculations. An accurate modelling of the radiative properties and behaviour of high-density, high-temperature plasmas is a challenging task and more and more experimental studies are desirable to validate the atomic physics codes.

X-ray emission spectroscopy is a very powerful tool for the study of ionization dynamics of rapidly evolving hot and dense plasmas. A systematic study of the H-like and He-like transition lines and their dielectronic satellites emitted during and slightly after the laser pulse can give direct knowledge of these ionic species in the ground level. Several studies have been reported on the effect of the laser pulse duration [109, 115-119] on the x-ray line emission from rapidly evolving plasmas. For instance, the time integrated sub-keV ($10 \text{ \AA} - 70 \text{ \AA}$) x-ray emission from the laser produced carbon plasma as a function of the pulse duration (130 fs – 1.3 ps) was studied by Altenbernd *et al* [117]. They observed that at a constant laser intensity, the continuum x-ray emission is much larger for the shorter laser pulse duration, and the H-like lines are much weaker than those from He-like ions. On the other hand, at a constant laser fluence ($2.2 \times 10^4 \text{ J cm}^{-2}$), they noted that the spectral shapes

and relative fractions of individual lines and continuum are nearly independent of the pulse duration. For instance, in the pulse duration range of their study, the intensity of the x-ray line from H-like ions from the plasma produced with the longest laser pulse duration (1.3 ps) was only three times more in comparison to that of the shortest pulse duration (130 fs). In the keV x-ray energy range, the line emission from aluminium plasma has been studied by Limpouch *et al* [119] as a function of laser pulse duration in the range of 1.5 ps to 1 ns, for a fixed laser fluence $[(5-6) \times 10^6 \text{ J cm}^{-2}]$. They observed that the conversion efficiency of both the H-like and He-like resonance lines increased with the pulse duration, and this was supported by theoretical modelling of the x-ray emission using a standard particle-in-cell code with appropriate modification for the shorter laser pulse interaction with matter. They noted that when going from 1.5 ps to 1 ns, the peak intensity of the He- α resonance line increases slightly but the intensity of the H- α line increases by two orders of magnitude. However, in this study, the smallest value of the laser pulse duration was limited to 1.5 ps. It is desirable to have more theoretical and experimental data on effect of pulse duration on x-ray emission. There is no study on the keV x-ray line emission reported which compares the relative x-ray yield from the plasmas produced by laser pulses of duration extending from nanosecond to femtosecond, at a constant laser fluence. In this chapter, we present a systematic study of the keV x-ray line emission from the plasmas produced by femtosecond, picosecond, and nanosecond duration laser pulses. The role of the hydrodynamics becomes critical in the transient regimes of plasma formation, when the x-ray emission takes place from the plasma regions characterized by rapid changes and strong spatial gradients of hydrodynamic quantities. The description of experiment and results showing transient ionization effect are given in section 3.2 and 3.3 respectively. Section 3.4 gives details of a simple analytical calculation of the ionization equilibrium time for the heated plasma, as well as that during its expansion, using a simple hydrodynamic model to explain the experimental results.

3.1 Description of the experiment

The experiment was carried out using three different laser systems delivering laser pulses of duration varying from femtoseconds to nanoseconds. Pulses of 45 fs (FWHM) duration were obtained from the 10 Hz Ti: sapphire laser operated at 800 nm (already described in section 2.3 of Chapter 2). The incident angle of laser beam was set to be 45° (w.r. to the laser direction). In the current experiments, laser was focussed to a maximum intensity of $\sim 3.5 \times 10^{17} \text{ W cm}^{-2}$ for a measured focal spot diameter of 30 μm . For picosecond laser irradiance, the 100 GW Nd:glass laser system ($\lambda = 1054 \text{ nm}$) was used (described in section 2.2 of Chapter 2). It provided single laser pulses of 25 ps (FWHM) duration. In the present experiment, the focussed laser intensity was estimated to be $\sim 6.2 \times 10^{14} \text{ W cm}^{-2}$ for a focal spot of 70 μm . The nanosecond laser pulses were obtained from the 3 GW, 3 ns Nd:glass laser system operated at second harmonic ($\lambda = 527 \text{ nm}$) wavelength (described in section 2.3 of Chapter 2). For this experiment, the laser pulses were focussed on planar targets to an intensity of $\sim 5 \times 10^{12} \text{ W/cm}^2$, for a focal spot size (diameter) of $\sim 130 \mu\text{m}$.

The x-ray line emission from the plasma produced by femtosecond, picosecond, and nanosecond duration laser pulses was measured at a fixed laser fluence of $\sim 1.5 \times 10^4 \text{ J cm}^{-2}$. The high resolution x-ray spectrum was recorded with the x-ray crystal spectrograph [87] described in Chapter 2. It was set to cover a wavelength range of 6.9 \AA to 9.6 \AA , with a linear dispersion of 0.26 $\text{\AA}/\text{mm}$. This spectrograph had a planar slab of thallium acid phthalate (TAP) crystal having a double inter-planar spacing ($2d$) of 25.75 \AA [(001) plane]. The spectrum was recorded on a Kodak DEF-5 x-ray film placed normal to the x-rays reflected from the crystal. Two aluminized polycarbonate foils (trade name B-10, energy cut-off of 0.9 keV) were used to prevent any scattered light in the plasma chamber from coupling to the film. An opaque screen was placed to prevent any x-ray emission from the plasma falling

directly on the film. While using this spectrograph with femtosecond laser, it was set to record the x-ray emission with a spectral resolution of 0.013 Å in the spectral range of 7.6 Å to 9.7 Å

3.2 Results and discussion

Figure 3.1 shows the x-ray emission spectrum of magnesium plasma produced by the 2 J, 3 ns laser pulses at an intensity of $\sim 5 \times 10^{12} \text{ W cm}^{-2}$. The spectrum was recorded in two laser shots of similar energy. Various prominent lines in the spectral range of 6.9 Å to 9.6 Å are identified as transitions in He-like (Mg^{+10}) and H-like (Mg^{+11}) magnesium ions, viz. (in increasing order of wavelength) Mg XII $1s - 3p$ at $\lambda = 7.11 \text{ Å}$ (H- β), Mg XI $1s^2 - 1s 6p$ at $\lambda = 7.23 \text{ Å}$ (He- ϵ), Mg XI $1s^2 - 1s 5p$ at $\lambda = 7.31 \text{ Å}$ (He- δ), Mg XI $1s^2 - 1s 4p$ at $\lambda = 7.47 \text{ Å}$ (He- γ), Mg XI $1s^2 - 1s 3p$ at $\lambda = 7.86 \text{ Å}$ (He- β), Mg XII $1s - 2p$ at $\lambda = 8.42 \text{ Å}$ (H- α), Mg XI $1s^2 - 1s 2p$ (He- α resonance) at $\lambda = 9.17 \text{ Å}$, and Mg XI $1s^2 - 1s 2p$ (He- α intercombination) at $\lambda = 9.23 \text{ Å}$. Figure 3. 2 shows the x-ray emission spectrum of magnesium plasma produced by using 0.6 J, 25 ps laser pulses at an intensity of $\sim 6.2 \times 10^{14} \text{ W cm}^{-2}$. The spectrum was recorded in six laser shots. This spectrum is similar to the spectrum recorded with nanosecond laser pulses (shown in Fig. 3.1) except that the intensity of the line radiation from the H-like ions is significantly reduced. For instance, the intensity ratios within full profile of the magnesium He- α (resonance) to H- α line for picosecond and nanosecond plasma are ~ 6.3 and ~ 3.8 respectively. Figure 3.3 shows the x-ray spectrum of magnesium plasma produced by 110 mJ, 45 fs laser pulses at an intensity of $\sim 3.5 \times 10^{17} \text{ W cm}^{-2}$. The spectrum was recorded in 18,000 shots. Unlike in the previous two cases, the line spectrum comprising of feeble He- α at $\lambda = 9.17 \text{ Å}$, He- β at $\lambda = 7.86 \text{ Å}$ and j, k satellites of He- α at $\lambda = 9.32 \text{ Å}$ is superposed over a prominent continuum. H-like emission was below the detection limit of the detector.

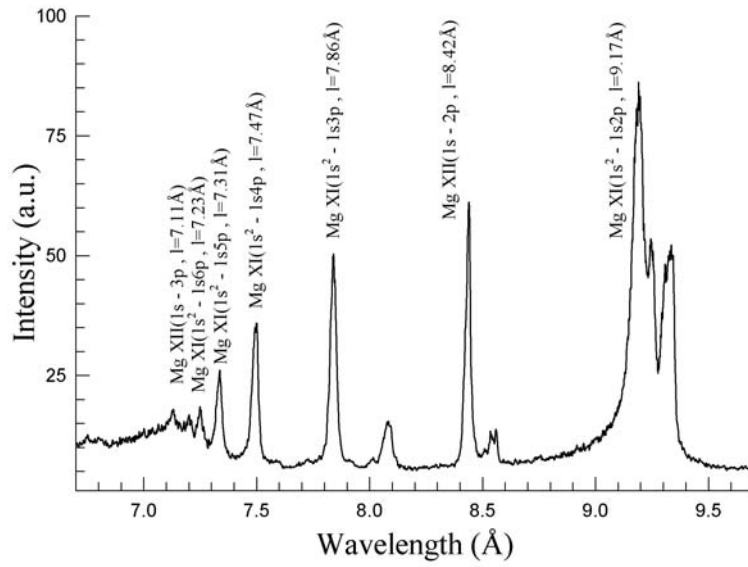


Fig. 3.1 : X-ray spectrum of magnesium plasma produced using nanosecond laser pulses at an intensity of $5 \times 10^{12} \text{ Wcm}^{-2}$.

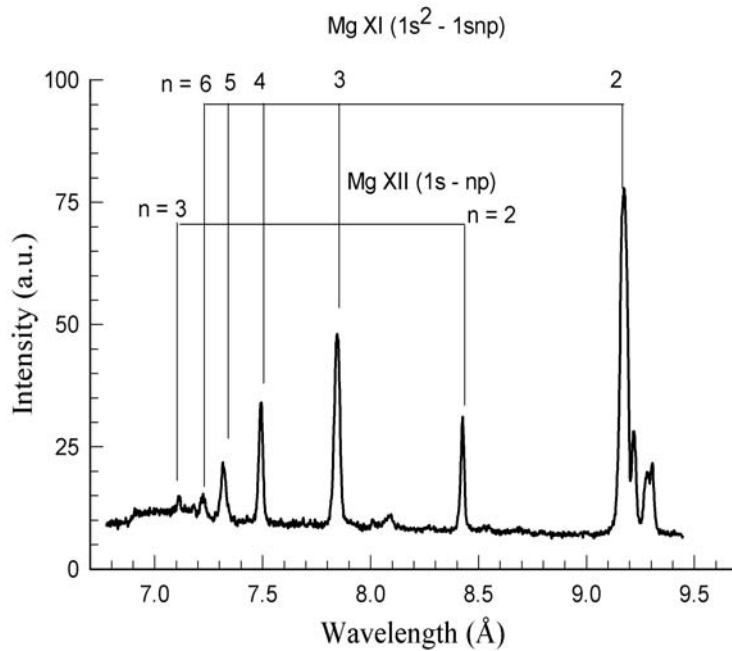


Fig. 3.2: X-ray spectrum of magnesium plasma produced using a picosecond laser pulse at an intensity of $6 \times 10^{14} \text{ Wcm}^{-2}$.

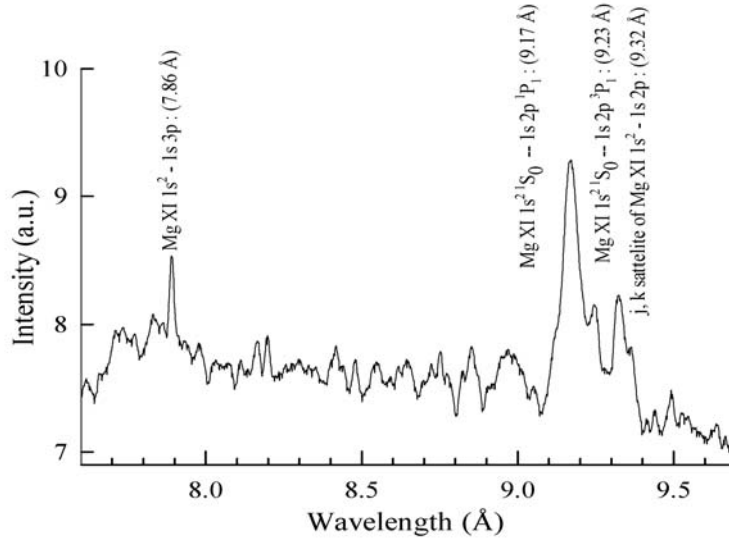


Fig. 3.3: X-ray spectrum of magnesium plasma produced using fs laser pulses at an intensity of $3.5 \times 10^{17} \text{ Wcm}^{-2}$.

In order to compare the x-ray line intensities in the three cases of different pulse durations, we have derived the relative x-ray yield for different resonance lines by normalizing with respect to the incident laser energy, the number of laser shots, and to a unit distance. In Fig. 3.4, the relative x-ray yields for different line radiations namely Mg XI $1s^2-1s 2p$ (He- α), Mg XI $1s^2-1s 3p$ (He- β), Mg XI $1s^2-1s 4p$ (He- γ), Mg XII $1s-2p$ (H- α) and Mg XII $1s-3p$ (H- β) lines are plotted for different pulse durations used in the experiment. The error bars indicate the experimental uncertainty in measuring the intensity of the x-ray line radiation. The x-ray yield for the He- α and He- β resonance lines first increases rapidly from 45 fs to 25 ps. It is more than four orders of magnitude larger for picosecond pulse duration. An increase in the x-ray yield from 25 ps up to 3 ns is only about 1.2 times for the He- β line and ~ 1.5 times for the He- α line. For the 45 fs laser produced plasma, the x-ray line intensity of the H- α line was below the detection limit of the detector. This gives an upper limit that x-ray yield of the H- α line radiation is smaller by a factor of 5.3×10^4 or more for the 45 fs case than for the 25 ps laser produced plasma. The x-ray yield of H- α , H- β ,

and He- γ lines increased from 25 ps to 3 ns pulse duration. It was ~ 2.4 , ~ 1.5 , and ~ 1.7 times for the H- α , H- β and He- γ lines respectively. Similar behaviour was also observed by Limpouch *et al* [119] in the picosecond to nanosecond pulse duration range. They also noted an increase in the conversion efficiency of the H- α and He- β resonance line radiation with the laser pulse duration. Their experimental data shows that conversion efficiency of H- α and He- α increases by ~ 50 and ~ 7.5 times respectively while going from 1.5 ps to 1 ns pulse duration, whereas their theoretical modelling predicted an increase of three orders and two orders of magnitude for the H- α and He- α lines respectively. They assigned the difference between observed and simulated results to the energy transport by the hot electrons.

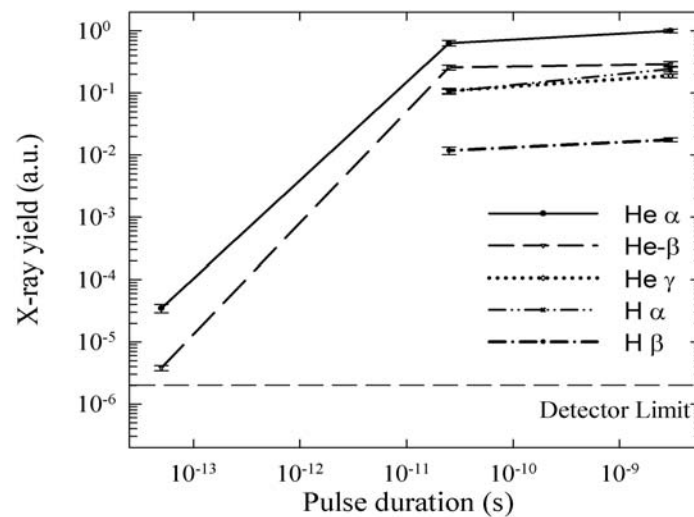


Fig. 3.4: The relative conversion efficiency of the magnesium He- α , He- β , He- γ , H- α and H- β lines is plotted for the three different pulse durations used in the experiment. The curves are drawn to guide the eyes.

The laser intensity can be varied either by varying the laser fluence keeping pulse duration fixed or changing the laser pulse duration at constant fluence. The laser intensity and the pulse duration play an important role in governing the laser plasma interaction, especially the energy absorption and its conversion to x-ray line radiation. The intensity dependence of

the x-ray line emission is due to the increase in the electron temperature [116, 120]. On the other hand, the laser pulse duration governs the density scale length of the plasma produced on the target, which, in combination with the laser intensity, governs the absorption of the laser energy up to the critical density surface, and the electron temperature achieved [120 - 121]. Moreover, the x-ray emission properties of dense plasmas in non-local thermodynamic equilibrium (NLTE), when ionization dynamics is expected to depart more from the steady-state regime, will be different. The use of widely different laser pulses for plasma formation can be a way to investigate ionization dynamics. However, the difference in x-ray yield is expected to be due to the different mechanisms of interaction for the high intensity (femtosecond), and low intensity (nanosecond) regime. Nevertheless, a comparison of relative fraction of ionization state for widely different laser pulse duration can give estimation of timescale of ionization.

For the nanosecond laser pulses with a peak intensity of $5 \times 10^{12} \text{ W cm}^{-2}$, the incident laser energy is absorbed in the under-dense region of the plasma, with the absorption being dominated by the inverse bremsstrahlung mechanism [29]. The plasma heating in such a situation can be well described using a self-regulating model [37]. The peak electron temperature of the corresponding region calculated on the basis of this model turns out to be 490 eV. This temperature supports the generation of both He-like and H-like ion species of magnesium, as the values of the ionization potential are 1761 and 1962 eV respectively for the two species. The electron temperature of the hot plasma produced by the picosecond laser pulses may be theoretically calculated using the analytical model by P. Mora [37] for the laser plasma interaction relevant to the experimental conditions of short pulse – high intensity regime, with weak inverse bremsstrahlung absorption of the laser light. This gives an electron

temperature of 2.4 keV. The average ionization state is expected to increase with increasing temperature. For instance, for the above estimated value of the temperature, one would expect the plasma to have a large fraction of Mg^{11+} ions and thus an intense line emission from H-like Mg^{11+} ions. However as seen from Fig.3.1 and Fig. 3.2, the relative intensity of the line emission from H- like Mg^{11+} ions for picosecond plasma is ~ 2.3 times smaller than for nanosecond plasma.

Next, for a high intensity femtosecond laser pulse, the energy is absorbed via hot electrons generated through a number of processes namely resonance absorption, Brunel heating, vxB heating etc. [122]. The less energetic electrons deposit their energy to heat the plasma, whereas the hot electrons penetrate into the target behind the hot plasma to generate inner-shell line radiation. At high intensity and steep density gradient, the bulk of the energy is taken by the hot electron. The hot electron temperature for the similar experimental conditions is in the range of few tens of keV to hundreds of keV [123]. Typical fast electron relaxation time at these temperatures in short pulse laser solid interaction at solid density is of the order of few tens of ps [124], which is significantly more than the duration of fs laser pulse used in our experiment. In such a case, the x-ray emission spectra may be due to the fs laser pulse interaction with the pre-plasma produced by the pre-pulse associated with CPA based ultra-short high intensity laser system. The presence of density sensitive intercombination line, whose upper level is a metastable state that is collisionally depopulated at density higher than 10^{21} cm^{-3} [23, 124], indicates that the lower density pre-plasma is indeed present before the arrival of the main laser pulse. The experimental observation of the lack of H-like ion emission and weak He-like ion emission, and presence of the Li-like satellite line, indicates that the bulk plasma is not sufficiently heated during the laser pulse.

Any role of optical field ionization in generation of these highly charged ionic species is rather unlikely as intensity requirement for that process is $> 10^{19} \text{ W cm}^{-2}$ [125].

3.3 Analytical calculation of the ionization equilibrium time

The x-ray spectroscopic measurement of the emission generated by a laser-produced plasma provides information about the inner plasma condition. Simulation of the x-ray spectrum would require a knowledge of the temperature and density profiles. Simultaneously, self-absorption of the x-ray line, the transient and nonlocal effects in the x-ray spectrum simulation should be taken into account. In other words, modelling of the x-ray emission of a plasma, the ionization equilibrium, that is the equilibrium between the different subsystems (i.e., different kinds of ions, electrons and radiation field) at any time and position inside the plasma must be identified. A laser produced plasma undergoes rapid changes in the density and temperature, both in space and time. Therefore, a system of rate equations, coupled with the hydrodynamic motion, would have to be solved simultaneously.

The observation of the absence of x-ray emission from the H-like ions from the femtosecond laser plasma and a relatively weak emission from the H-like ions in the picosecond laser produced plasma indicates that the We conclude from our time integrated x-ray measurement that the ionization to highly ionized species from the low ionized species, which requires much longer time, does not take place during the laser pulse if the former is longer than the latter. If we compare the x-ray emission from the plasma produced by ns laser pulse at a much lower intensity, where steady state is reached, the intensity of the H- α line emission is much stronger. The fact that the H- α line is much weaker from the ps laser produced plasma shows that during the ps laser pulse, steady state is not reached and hence

there is a substantial departure of ionization dynamics from the equilibrium regime. This can happen if the pulse duration is much shorter than the time required to reach ionization equilibrium between He-like and H-like ions. In fact, the time resolved radiation emission dynamics measurements [50, 113-114] have clearly shown evidence of transient ionization regime in the aluminium plasma produced during the rising part of the nanosecond pulse. Proper assessment of the ionization states would require calculations using time dependent atomic physics. Nevertheless, the ionization equilibrium time [54] can be calculated by solving the rate equations for collisional ionization, three-body recombination, and radiative recombination processes, as follows.

The rate of collisional ionization is given by

$$\left| \frac{\partial n_e}{\partial t} \right|_S = n_e n_i S_Z \quad (3.1)$$

where S_Z is the collisional ionization rate coefficient, n_e is the electron density, and n_i is the ion density. The collisional ionization rate coefficient as per Bate's formula [55] for ionization from charge state Z to $Z + 1$ is

$$S_Z(T_e) = 2.2 \times 10^{-6} [T_e^{1/2} \zeta_i \exp(-\chi_z^i / T_e)] / (\chi_z^i)^2 \text{ (cm}^3 \text{ sec}^{-1}) \quad (3.2)$$

where ζ_i is the numbers of electrons in the i^{th} subshell (n, l) having ionization energy χ_z^i .

(χ_z^i and T_e are in eV).

Next, the rate of radiative recombination is given by

$$\left| \frac{\partial n_e}{\partial t} \right|_\alpha = n_e n_i \alpha_Z \quad (3.3)$$

where α_Z is the radiative recombination rate coefficient for ions of charge Z . α_Z as given by [54] is

$$\alpha_Z = 8.5 \times 10^{-14} Z \beta^{3/2} / (\beta + 0.6) \text{ (cm}^3 \text{ sec}^{-1}\text{)} \quad (3.4)$$

where $\beta = Z^2 \chi_H / T_e$; χ_H is the hydrogen ionization potential.

Finally, the rate of three-body recombination is given by

$$\left| \partial n_e / \partial t \right|_{3b} = \alpha_{3b} n_e^2 n_i, \quad (3.5)$$

where α_{3b} is the three-body recombination rate coefficient, which as per Bate's formula [54] is

$$\alpha_{3b} = 8.75 \times 10^{-27} Z^3 / T_e^{9/2} \text{ (cm}^6 \text{ sec}^{-1}\text{)} \quad (3.6)$$

The ionization equilibrium time required between two adjacent ionization states may be expressed as

$$\tau_{\text{ionization}} = [1/\tau_S + 1/\tau_\alpha + 1/\tau_{3b}]^{-1} \quad (3.7)$$

where $\tau_S = n_e / \left| \partial n_e / \partial t \right|_S,$ (3.8)

$$\tau_\alpha = n_e / \left| \partial n_e / \partial t \right|_\alpha, \quad (3.9)$$

and $\tau_{3b} = n_e / \left| \partial n_e / \partial t \right|_{3b}$ (3.10)

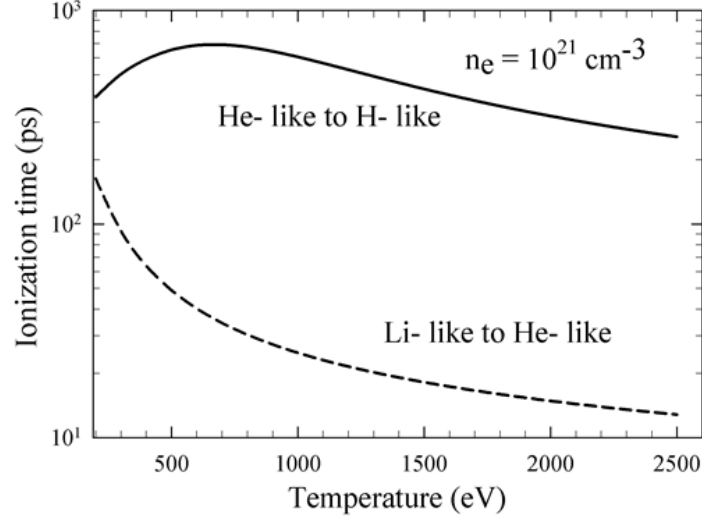


Fig. 3.5: Ionization equilibrium time calculated for ionization of He-like magnesium ions to H-like ions for different values of T_e (up to 2.5 keV) at a fixed value of n_e of 10^{21} cm^{-3} . The dashed curve is for ionization of Li-like magnesium ions to He-like ions.

The ionization equilibrium time was calculated using the above equations (3.1 to 3.10). Figure 3.5 shows the ionization time required for the ionization of the He-like magnesium ions to H-like ions, and for the Li-like magnesium ion to He-like ions, for different values of the electron temperature up to 2.5 keV, for a fixed value of electron density of 10^{21} cm^{-3} (the critical density for 1054 nm). For instance, the ionization equilibrium time between the Li-like ions and the He-like ions, and between the He-like ions and the H-like ions at the electron temperature of 2.4 keV is calculated to be 15 ps and 250 ps respectively. Similarly, Fig. 3.6 shows the ionization equilibrium time required for He-like magnesium ions to H-like ions and for Li-like magnesium ions to He-like ions for the electron density of $1.5 \times 10^{21} \text{ cm}^{-3}$ (\sim the critical density for the 800 nm Ti:sapphire laser). At a typical temperature of 50 keV, a time of ~ 600 fs is required for the ionization of the Li-like magnesium ions to He-like ions and a time of ~ 21.7 ps is required for the ionization of the He-like magnesium ions to H-like ions. This explains the complete lack of line emission from H-like ions and negligible emission from He-like ions in the spectrum recorded with 50 fs laser pulses. However, as the plasma expands after the laser pulse is over, it undergoes evolution of density and

temperature in the expanding plasma. During certain period of expansion the temperature may remain high enough to produce high ionization states of Mg^{11+} and Mg^{10+} provided the ionization equilibrium time is smaller than plasma expansion time scale.

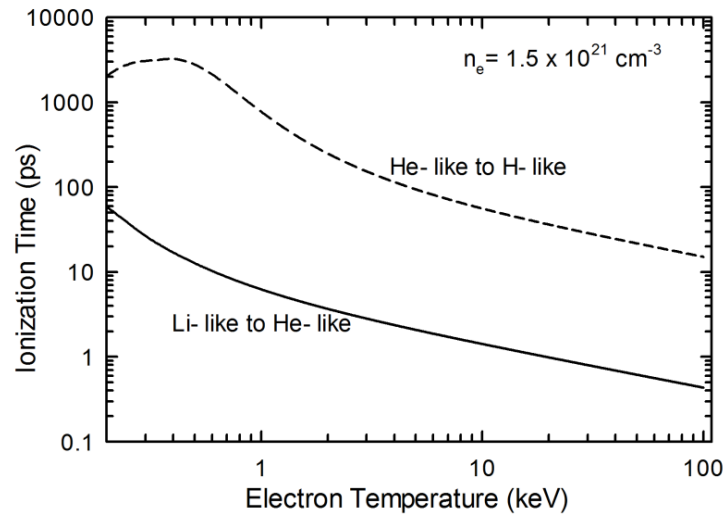


Fig. 3.6 : Ionization equilibrium time required for ionization of magnesium ions from He-like to H-like and from Li-like to He-like ions for different values of T_e (up to 100 keV) and a fixed value of n_e of $1.5 \times 10^{21} \text{ cm}^{-3}$

The above numbers for ionization equilibrium time may vary somewhat depending on the expressions used for the various processes. Nevertheless, when compared with the laser pulse duration of 25 ps, it is clear that while there is sufficient time for the production of the He-like ions, this is not true for their further ionization to H-like ions. During the initial period of expansion, the temperature may remain high enough to produce high ionization states of Mg^{11+} and Mg^{10+} , provided the ionization equilibrium time is smaller than the plasma expansion time scale. Further, as the plasma expands after the laser pulse is over, it undergoes evolution of density and temperature in the expanding plasma. The suppression of the high ion stage is broadly in agreement with the results of Milchberg *et al* [110] carried out for 100 fs laser pulse. Our results show that the high ion stages are suppressed even in the plasma produced by 25 ps and the ionization dynamics is expected to depart more from the

steady-state regime as the pulse duration is decreased to 45 fs. The work of Milchberg *et al* [110] is extended to calculate the ionization equilibrium time for reaching Li- like to He-like stage and He- like to H-like stage at the critical density layer at various temperatures.

A lower temperature of a few hundred eV may also be sufficient for dominant production of H-like ions over the He-like ions under the condition of ionization equilibrium. It may be looked into through the study of the temporal evolution of the emission since it is affected by both, the hydrodynamics and the atomic physics effect. The same has been studied by Gizzi *et al* [50] and they observed that in the case of the LiF target, the emission has a characteristic time of 39 ± 4 ps, as compared to the 12 ps laser pulse (FWHM) used to create the plasma. Therefore, it is important to examine the temporal evolution of the ionization time for the electron temperature and density of the plasma undergoing hydrodynamic expansion. In principle, such a calculation would require knowledge of the temperature and density profiles, which may necessitate detailed computer or numerical simulations [111,126]. For instance, Djaoui and Rose [111] modelled the atomic physics and hydrodynamics in a picoseconds or nanoseconds laser pulse produced plasma, with a hydrodynamic code MEDUSA. In their model, the hydrodynamic and atomic rate equations are solved in a self-consistent manner for predicting the variation in ionization as a function of space coordinates and time. However, one can use a simple hydrodynamic model to estimate the ionization time during plasma expansion [38]. For one dimensional expansion of the plasma, which is valid for time $t < R / c_s$, where R is focal spot radius and c_s is plasma expansion speed, the electron density would scale as t^{-1} . During the adiabatic expansion, after the laser pulse is over, the electron temperature T_e and the density n_e are related as $T_e \propto n_e^{\gamma-1}$. Taking $\gamma = 3$ (for one-dimensional expansion), T_e would scale with distance from the target as d^{-2} and hence $\propto t^{-2}$. The ionization equilibrium time was calculated for the plasma undergoing expansion using the density and temperature values as per the above scaling laws.

It is observed that the ionization time required at any stage during expansion of the plasma far exceeds the temporal duration for which the plasma remains sufficiently hot to be able to produce the H-like ions. This further corroborates the observed poor generation of the H-like ions and relatively small intensity of the MgXII 1s-2p line in the spectrum recorded with picosecond laser pulses, and lack of lines from H-like ions as well as negligible intensity of the lines from He-like ions in the spectrum recorded with femtosecond laser pulses.

To summarize this chapter, a comparative spectroscopic study of the x-ray emission from magnesium plasma produced by femtosecond, picosecond, and nanosecond lasers has been carried out, at a fixed laser fluence ($1.5 \times 10^4 \text{ J cm}^{-2}$). The spectrum recorded with shorter duration laser pulses at much higher intensity does not contain the line emission from higher ionization states. The analytical calculations using a simple hydrodynamic model show that the ionization time required to produce higher ionization states is much larger than the temporal duration of the hot plasma. The present results give the time scales of the ionization processes which explain the experimentally observed features of the x-ray line spectrum. The results can be useful in making the optimum choice of the laser pulse duration to produce short pulse, intense x-ray line emission, and for getting knowledge of the degree of ionization in the plasma.

Chapter 4

keV x-ray emission from gold-copper mix-Z plasma

In recent past, there has been a considerable interest in using mix-Z targets for enhancing the thermal x-ray yield in the sub-keV region [127–132]. It has been shown that if two or more elements are mixed such that the high opacity regions of one overlap with the low opacity regions of the other, the mixture may have a higher Rosseland mean opacity than that of the individual elements [128–132]. In the indirect scheme of inertial confinement fusion using *hohlraum* configuration, the increase in the mean opacity reduces the radiation conduction loss into the cavity wall, and thereby increases the coupling efficiency of the radiation to the fuel pellet. Since gold has been the most widely used material for *hohlraum* fabrication, its mixtures with some other elements, e.g., Au–Gd, Au–Sm, Au–Nd, Au–Cu, etc., have been theoretically investigated to determine the optimum composition to achieve higher opacity. Copper has advantage over Gd, Sm, Nd, etc., in that it is stoichiometrically compatible with gold and hence it can form an alloy with gold so that it can be easily used as a wall material in a *hohlraum* cavity. The dependence of the soft x-ray conversion on the atomic composition of the target has been studied experimentally [132] in the laser-produced plasma of gold-copper mix-Z targets which gives the optimum mixture for maximum XUV conversion efficiency. In this work, the x-ray yield in 15–150 Å spectral region was studied for different compositions of the mix-Z target and it was observed to be higher than those for the individual elements. The results were consistent with the variation of the Rosseland mean opacity with the atomic composition calculated using a screened hydrogenic average atom model [133]. However, no work has been reported on the keV conversion efficiency from such mix-Z targets. The keV x-ray emission from laser produced plasmas has great potential applications in proximity x-ray lithography [134] in semiconductor industry and x-ray contact

microscopy [135]. A high conversion efficiency is a prerequisite for the above applications. On the other hand, higher keV x-ray conversion may have negative implication for inertial confinement fusion as the harder component of the driver spectrum, having a longer penetration depth, can preheat [136,137] the fuel which may result in a poor compression. It is therefore desirable to study the keV x-ray emission intensity for different compositions of the mix-Z targets.

In this chapter, we present a comparative experimental study of the keV x-ray emission from gold-copper mix-Z targets of different atomic compositions. Section 4.1 details the opacity effect on x-ray emission. Description of the experiment is given in section 4.2. Experimental results and analysis of keV x-ray emission spectrum is given in section 4.3.

4.1 Effect of opacity on x-ray emission

The radiative properties of laser produced plasma are determined by the hydrodynamic parameters and energy transport. The opacity, as well as the emissivity, of the laser-produced high energy density plasma, heated to a temperature of a few hundreds of eV, is so high for keV emission such that the light emitted from deep inside the plasma is absorbed strongly during propagation through the surrounding plasma. Opacity refers to the ability of the radiation to escape from the plasma. Essentially it quantifies transparency or (opaqueness) of the plasma to the radiation.

The transmission of photons with intensity I_0 normally incident on uniform plasma is given by

$$T(\nu) = I(\nu)/I_0(\nu) = \exp [- \tau(\nu)], \quad (4.1)$$

where $h\nu$ is the photon energy and $I(\nu)$ is the attenuated photon intensity emerging from the plasma. The optical depth, $\tau(\nu)$, is related to the opacity by $\tau(\nu) = \kappa(\nu)\rho x$, where $\kappa(\nu)$ is the

opacity per unit mass (typically measured in units of cm^2/g), ρ is the density, and x is the optical path length. Experimentally, the transmission of photons $T(\nu)$ through a plasma of known characteristics is measured to validate the opacity models.

The opacity is generally a rapidly varying function of frequency. Therefore, the knowledge of the frequency dependent opacity is necessary to obtain high conversion of incident laser energy efficiency into x-ray emission. The other reason to study the opacity is that the x-ray line intensity ratios are often used for diagnosis of plasma parameter. It is therefore essential to account for self-absorption of line radiation particularly for high-density plasmas. Opacity depends on the plasma temperature, density, and elemental composition. It is difficult to experimentally measure the opacity as plasma undergoes rapid evolution over a wide parameter range from solid density to vacuum. Next, the presence of other element may alter the opacity of the plasma. It is important in applications for example *hohlraum* cavity where mixture of elements like gold and copper are used as ablator wall material to increase the sub-keV x-ray yield.

Rosseland mean opacity κ_R [30] is usually used to describe the radiation transport in laser produced plasmas because plasma size is much larger than the photon mean free path. It is defined as

$$\frac{1}{\kappa_R} = \frac{\int d\nu \frac{1}{\kappa(\nu)} \frac{dB}{dT}}{\int d\nu \frac{dB}{dT}} \quad (4.2)$$

where B is the Planck function, T is the plasma temperature, and the weighting function dB/dT peaks at roughly $3.8 kT$. Note that the Rosseland opacity is a harmonic mean depending on the reciprocal of $\kappa(\nu)$ and photons are most efficiently transported through the

“windows” where $\kappa(\nu)$ is the lowest. The absorption spectrum of any element at any given temperature is not constant over frequency: it has peaks and valleys, and the opacity is significantly lower in some frequency regions. The three main absorption processes of radiation by the other elements present in plasma include free-free, bound-free, and bound-bound electron transitions. These processes differ from one element to another and depend on the ionization. For the low $-Z$ elements, the only contribution to the opacity is from the free-free transitions in the ions, whereas elements that are ionized into the K-shell contribute absorption through bound – free and bound-bound transitions. For high $-Z$ elements, ionized into the L-shell or M-shell, the greater number of bound electrons renders the opacity contributions immensely complicated. Many transitions originate from the $n=2$ lower level, but there is also significant excited state population and transitions originate from $n = 3$ principal quantum number.

4.2 Mix-Z target preparation

Composite targets of Au-Cu mixture were produced by forming alloy of pure gold and copper (purity of both the elements is 99.999 %) metals in a crucible. Various atomic compositions of Au-Cu mix-Z target were achieved by mixing gold and copper in different weight fractions, starting with pure gold and successively adding copper by known weight fractions. Table 1 lists the various mix-Z targets composition in terms of weight fraction and atomic compositions used in the present study. The mix-Z target compositions thus formed were later examined through x-ray fluorescence technique to check on any impurity addition during alloy formation and secondly for any inhomogeneity in composition in the mix-Z target. No impurity was detected up to 10 ppm level. In the remainder of this chapter mix-Z target composition will be referred to in terms of atomic fraction only to avoid any confusion and to facilitate comparison with results of earlier theoretical studies.

S.No.	Weight Fraction (%)	Atomic Fraction (%)
	Au – Cu	Au - Cu
1.	100 – 0	1 - 0
2.	90 – 10	0.74 - 0.26
3.	70 – 30	0.43 - 0.57
4.	50 – 50	0.24 - 0.76
5.	40 - 60	0.18 - 0.82
6.	30 - 70	0.12 - 0.88
7.	20 - 80	0.08 - 0.92
8.	10 – 90	0.04 - 0.96
9.	5 - 95	0.02 - 0.98
10.	0 - 100	0 - 1

Table 4.1: Mix-Z targets composition in terms of weight fraction and atomic compositions

4.3 Description of the experiment

The experiment was carried out by irradiating thick planar foils of gold, copper, and mix-Z alloys of different atomic compositions, with a frequency-doubled 4 J, 3 ns Nd: glass laser beam focussed to an intensity of $\sim 10^{13}$ W cm⁻² in a plasma chamber evacuated to 10⁻⁵ torr. High resolution x-ray spectrum from the plasma was recorded by placing an x-ray crystal spectrograph inside the plasma chamber. The spectrograph had a planar thallium acid phthalate (TAP) crystal as a Bragg reflector. The spectrum was recorded in four to five laser shots on a Kodak DEF-5 film placed normal to the x-ray Bragg reflected from the crystal. Two aluminized polycarbonate foils (B-10) having 1/e cutoff of ~ 1 keV were used to prevent any scattered light in the plasma chamber from coupling to the film. The spectrograph was set to cover a wavelength range of 7.5–11 Å with a spectral resolution of 34 mÅ (limited by the source size). The film was developed by the standard procedure with D-19 developer and was analyzed using a Carl Zeiss densitometer with a slit width of 25 μm. The latter was connected to a personal computer for digitalization of the optical density data. The data processing was done using an in-house developed data acquisition and image

processing software. The intensities of the various lines were calculated by using a contrast ratio of $\gamma = 0.8$ measured *in situ* using step filters. The wavelength calibration of the spectrograph was done with known emission lines from H-like and He-like ions of magnesium recorded in one-half of the film, with copper spectrum recorded in the other half. The intensity of the x-ray emission in the keV energy region was also measured using filtered *p-i-n* diodes (Quantrad: 100 PIN 250) of known sensitivity of 0.2 C/ J. The transmission grating spectrograph [138] was used to record the sub-keV x-ray emission spectrum. It had a spectral resolution of $\sim 3 \text{ \AA}$ over the wavelength range of ~ 5 to 150 \AA . Spectra were recorded on UFSH-4 XUV sensitive film, which was calibrated for absolute sensitivity and contrast ratio using S-60 synchrotron radiation source [139]. The spectrograph viewed the plasma emission in a direction perpendicular to the target normal. The x-ray emission size of the plasma along the direction of target normal was estimated to be $\sim 120 \text{ \mu m}$.

4.4 Results and discussion

Figure 4.1 shows the x-ray spectrum of copper plasma in the wavelength range of $7.8 \text{ \AA} - 10.9 \text{ \AA}$ recorded at a laser intensity of $8 \times 10^{12} \text{ W/cm}^2$. The characteristic lines and ionization states [140] have been identified. The dominant spectral lines are the ones originating from the Ne-like Cu^{+19} ions ($2p^6 - 2p^5ns$, $2p^6 - 2p^5nd$). Somewhat weaker F-like Cu XXI lines from the Cu^{+20} ions are also seen. Figure 4.2 shows a typical x-ray spectrum of plasma produced from a mix-Z target having 0.88 atomic fraction of copper and 0.12 atomic fraction of gold, recorded under same laser irradiation conditions as in Fig. 4.1. Although the observed spectral characteristics are similar to those of pure copper, the overall intensity of the spectral lines is substantially lower. The similarity in the spectral characteristics observed for Au 0.12 – Cu 0.88 mix-Z and pure copper plasmas is due to the fact that in the wavelength range of $7.8 - 11 \text{ \AA}$, the gold plasma does not make much contribution because the M-shell line radiation as well as the recombination radiation from gold ions [141] occur at wavelengths below 6 \AA .

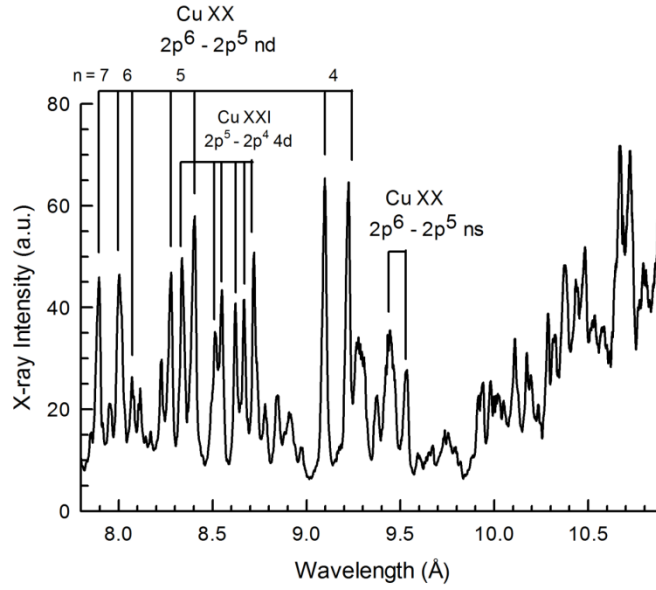


Fig. 4.1: X-ray spectrum of pure Cu in the wavelength range from $\lambda = 7.8\text{\AA}$ to $\lambda = 10.9\text{\AA}$.

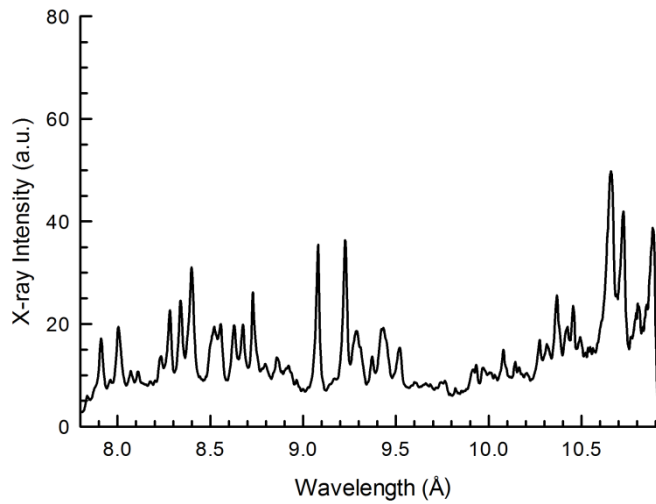


Fig. 4.2: X-ray spectrum of mix-Z target having 0.88 atomic fraction of copper and 0.12 atomic fraction of gold.

The x-ray intensity was integrated over the spectral range of 7.8 – 10.9 Å for different atomic compositions of Au–Cu mix–Z target. The dependence of this keV integrated x-ray yield on atomic fraction of gold is shown in Fig. 4.3. It is seen from this figure that the integrated keV x-ray yield decreases sharply with increase in the fraction of gold in the mix – Z plasma. A reduction factor of ~ 2.1 in the integrated keV x-ray yield is observed for 0.12 Au – 0.88 Cu mix–Z target with respect to pure copper. For the optimum composition for maximum sub-keV conversion (Au 0.43 – Cu 0.57) observed for the same laser irradiation

conditions [132], the keV x-ray yield is observed to reduce by a factor of ~ 6.7 compared to that for pure copper. Figure 4.4 shows the variation of the intensity of the strong neon-like Cu XX line transition ($2p^6 - 2p^54d$) at $\lambda = 9.1\text{\AA}$ with target composition. In this case also, one observes a strong decrease of the x-ray line intensity by a factor of ~ 1.7 and ~ 8.7 for 0.12 and 0.43 atomic fractions of gold in the mix-Z target respectively.

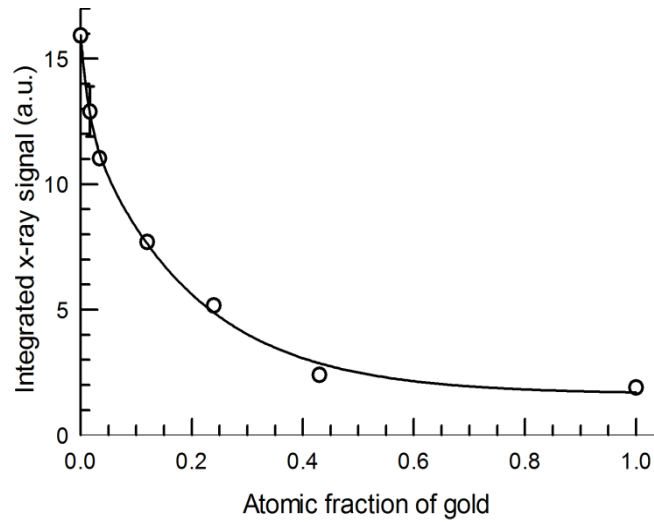


Fig. 4.3: Variation of the integrated x-ray yield in the spectral range of $\lambda = 7.8\text{\AA}$ to 10.9\AA as a function of atomic fraction of gold in the mix-Z target.

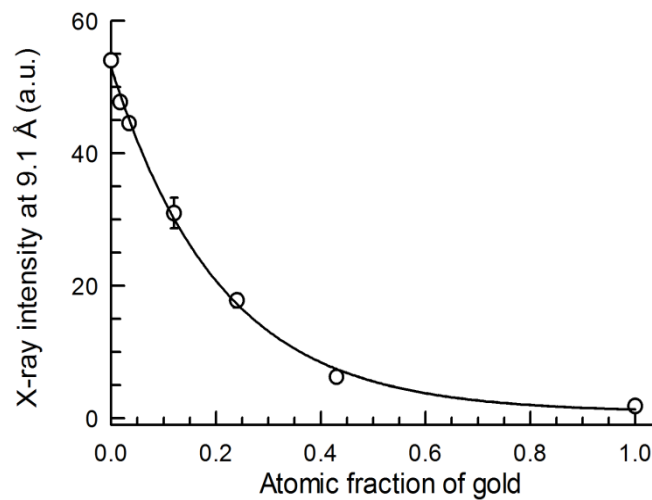


Fig. 4.4: Variation of the intensity of Cu XX ($2p^6 - 2p^54d$) line at $\lambda = 9.1\text{\AA}$ with atomic fraction of gold in the mix-Z target.

The absolute x-ray yield was also determined from the p-i-n x-ray diodes filtered with two B-10 foils (1/e cut-off energy ~ 1 keV). The conversion efficiency for photon energy ≥ 1 keV for copper target is $\sim 1.3\%$. A small addition of 0.1 atomic fraction of gold atoms results in reduction of the conversion efficiency to $\sim 0.5\%$. The variation of x-ray yield as a function of target atomic composition is shown in Fig. 4.5. It is seen from this figure that compared to pure copper, there is a decrease in conversion efficiency by a factor of ~ 2.5 for mix-Z target having 0.88 atomic fraction of copper and 0.12 atomic fraction of gold; and for the optimum mixture (0.43 Cu – 0.57 Au), it reduces by a factor of ~ 7.8 . These observations are in agreement with variation observed using the crystal spectrograph.

The above results on the substantial decrease in the keV x-ray yield in gold–copper mix–Z plasmas can be explained by considering the absorption of the L–shell line emission of copper ions offered by the gold ions present in the mix–Z plasma.

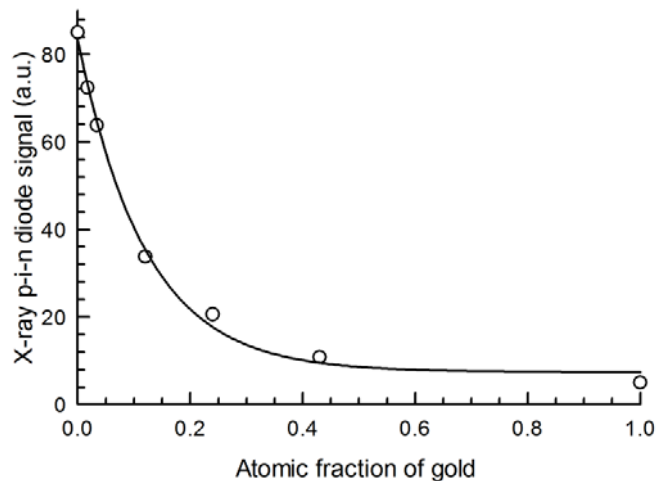


Fig. 4.5: Variation of the x-ray signal from x-ray p-i-n diode as a function of atomic fraction of gold in the mix-Z target.

In general, the spectral line opacity is given in terms of the optical depth τ_λ as

$$\tau_\lambda = \varphi(\lambda) \int_0^L k_\lambda(x) dx \quad (4.3)$$

where $\varphi(\lambda)$ is absorption line shape function, k_λ is the absorption coefficient of the plasma at wavelength λ , and L is the path length traversed in the plasma. The transmission of the radiation through the plasma is given by $\exp(-\tau_\lambda)$ which depends on the path length traversed and the absorption coefficient. The latter includes both the bound-bound absorption and the free-bound absorption (opacities).

Re-emitted radiation intensity from the target is governed by temperature of the optically thick region, which in turn depends on the source flux and the Rosseland mean opacity [142]. The latter comes into play as it determines the ability of the heated material to restrict thermal diffusion loss of radiation into the target. Theoretical calculations of Rosseland mean opacity were made for free-free and free-bound opacity of gold and copper. These calculations require models for computing atomic structure, level populations, radiative transition cross-sections, spectral line shapes, and plasma effects. The Rosseland mean opacity has been computed by our collaborators Gupta and Godwal [131]. They have used a screened hydrogenic, average atom model [133] in local thermodynamic equilibrium for their calculations. Computed energy spectrum of bound-free and bound-bound opacities for copper and gold plasmas at $T = 100$ eV and $\rho = 0.3$ g/cc is shown as an example in Fig. 4.6 and 4.7 respectively. One may visualize from the overlap of peaks of opacity of one element with valleys of the other that integrated opacity of an optimum mixture can be higher than the values for individual elements.

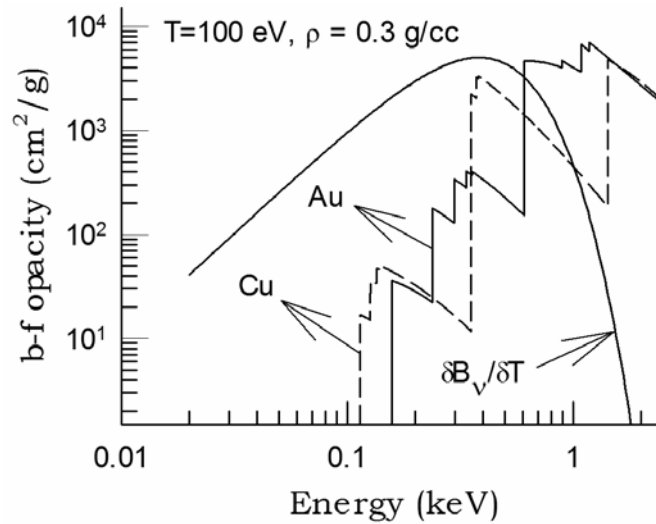


Fig. 4.6: Bound-free opacity spectrum computed for Cu and Au plasmas.

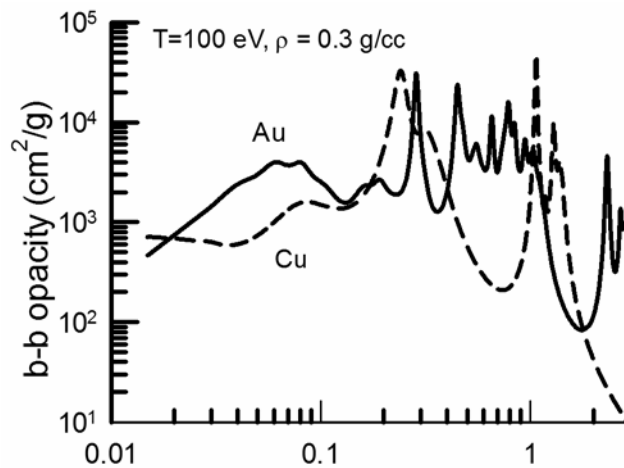


Fig. 4.7: Bound-bound opacity spectrum computed for Cu and Au plasmas.

For the temperature and density conditions of the present study, the opacity estimates indicate that gold has a higher free-bound opacity in the spectral region of the L-shell emission of the copper ions. The absorption of the copper L-shell line radiation in gold ions decreases the emission intensity of these lines from the mix-Z plasma containing gold ions. The electron vacancy in the gold ions created due to bound-free transition on absorption of copper L-shell line radiation is subsequently filled through a cascade of radiative transitions of electrons from the higher energy levels. This leads to the emission of radiation at a longer

wavelengths compared to the copper L-shell line wavelength. Since many such transitions are possible due to multiple N- and O-shells in gold ions, the emitted radiation occurs at different wavelengths in the sub-keV region. Thus, a fraction of the copper L-shell keV line radiation of the gold–copper mix–Z plasma reappears as enhanced sub-keV x-ray emission.

Chakera *et al* [132] in their investigations on dependence of soft x-ray conversion on atomic composition in laser produced plasma of Au-Cu mix-Z targets irradiated at a laser intensity of $\sim 10^{13}$ W cm⁻² of second harmonic of Nd:glass laser at $\lambda_L = 0.53$ μm . Radiation intensity in the spectral region $\sim 15 - 150$ \AA and integrated x-ray yield were found to be maximum for an atomic composition of Au 0.43 - Cu 0.57. Integrated conversion efficiency ($6 \text{ \AA} < \lambda < 150 \text{ \AA}$) per unit solid angle in the direction perpendicular to the target normal for Au, Cu, and Au 0.43-Cu 0.57 mix-Z targets is shown in Fig. 4.8. The conversion efficiency for the mix-Z target is observed to be higher than that of pure Au and Cu targets by a factor of 1.17 and 2.0, respectively. It may be mentioned here that the x-ray conversion efficiency shown in Fig. 4.8 represents only a lower bound because one expects the minimum of angular distribution of x-ray emission intensity to occur in the direction perpendicular to the target normal. A variation of x-ray intensity at two representative wavelengths $\lambda = 40$ \AA (in water-window region) and 80 \AA with atomic composition is depicted in Fig. 4.9. It is seen that the mix-Z target of atomic composition Au 0.43 – Cu 0.57 gives the maximum sub-keV x-ray emission. Radiation intensity in the spectral region $\sim 15 - 150$ \AA and integrated x-ray yield are found to be maximum for an atomic composition of Au 0.43 - Cu 0.57. This is consistent with the progressive down- conversion [127] in frequency of incident soft x-rays as observed from the dense backside of foil plasma. Since the back side plasma is of much higher density and is highly collisional, much of this absorbed radiation is collisionally quenched, resulting

in an increased temperature and ionization of the cold matter. The latter in turn re-radiates at lower photon energies corresponding to the dominant ionization stages of the colder matter. Next, as the fraction of gold increases in the mix-Z target, the corresponding decrease in the fraction of copper atoms leads to a further decrease in the L-shell line emission intensity and an increase in the bound-free absorption and emission of radiation at longer wavelengths.

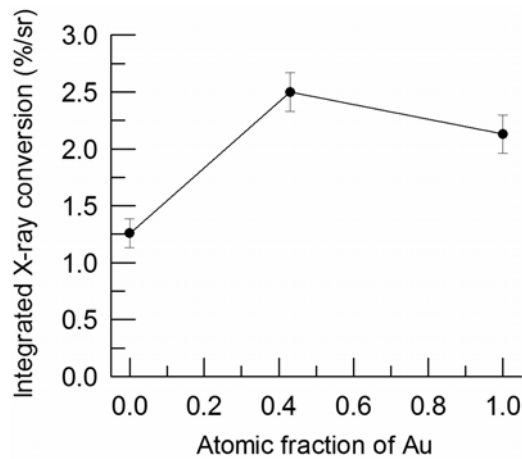


Fig. 4.8: *Integrated x-ray conversion per unit solid angle for Cu, Au, and Au 0.43 – Cu 0.57 mix-Z plasma.*

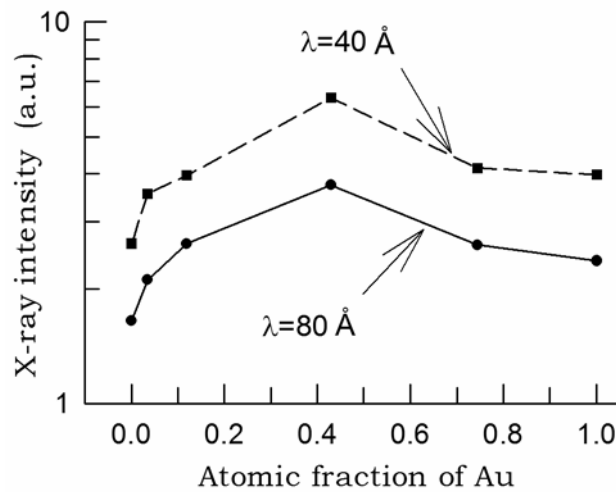


Fig. 4.9: *Variation of the x-ray intensity with atomic composition.*

A gross estimate of the absorption of the radiation energy can be made from the calculated bound–bound opacity energy spectrum of copper plasma in traversing the plasma. The optical depth for the keV emission from the copper ions can be varied by changing the composition and the path length traversed by the radiation in escaping from the plasma. For the long laser pulse of 3ns full width at half maximum (FWHM) duration used in the present study, the plasma may be considered to be consisting of two regions [143,144]: first an optically thick planar expansion region of high density and relatively low temperature, and the second one being an optically thin spherically expanding region with a fast decreasing density. The planar expansion region, due to its high density, makes a strong contribution in modification of the intensity of the emitted radiation. In laser irradiated planar targets with finite size focal spot, the plasma expansion may be considered to be nearly planar up to an expansion distance of the order of focal spot radius. The x-rays are absorbed in travelling the physical length of the plasma and the transmitted x-ray intensity for the radiation of wavelength λ will be given by $I_\lambda(0) \exp [- k_\lambda \rho L]$, where $I_\lambda(0)$ is the initial intensity, k_λ is the bound–free opacity, ρ is the density, and L is the path length. The bound–bound opacity spectrum of copper and gold is taken as the initial spectrum $I_\lambda(0)$, which is absorbed in traversing the plasma due to bound–free absorption by gold as well as copper ions. The respective values of the bound–free and the bound–bound opacity are varied as per the target atomic composition. The source size of the plasma is taken as the physical path length. For the case of mixtures, the bound–bound and the bound–free contributions to opacities are obtained as weighted averages as per the respective atomic fractions. Free–free contribution to opacities of mixture is obtained using weighted average ionization of the mixture [145]. The values of the bound–bound opacity of copper and gold at 9.1 Å at a temperature of 100 eV and a density of 0.12 gm/cc are 2604 cm²/gm and 180.5 cm²/gm respectively. The corresponding free–bound opacity values are 143.6 cm²/gm and 5223 cm²/gm respectively.

For an estimated plasma size of 120 μm , the transmitted x-ray intensity decreases by a factor of ~ 2 for 0.1 atomic fraction of gold in the mix – Z target. This is in close agreement with the experimentally observed decrement factor of ~ 1.7 . Similarly, the integrated keV x-ray yield can be calculated. A more accurate quantitative knowledge of the decrease of the x-ray yield would be possible using detailed computer simulations based on plasma hydrodynamic codes including radiation transport along with opacity model codes [146,147] coupled to spectroscopically accurate atomic data. Nevertheless, the observed results are reasonably well explained from physical consideration of the opacity of the mix–Z targets as discussed above.

To summarize this chapter, we have presented an experimental study on the keV x-ray emission from laser irradiated copper–gold mix-Z targets of different atomic compositions. The keV x-ray yield is observed to decrease even for a small fraction of gold in the mix–Z target compared to that for pure copper. The results have been explained from physical considerations of the absorption of L–shell line emission from copper ions by gold plasma due to the high value of the free–bound opacity of the latter, followed by down-conversion of the absorbed radiation. The study can be of interest in view of the potential of reduction in preheat in mix–Z targets for inertial confinement fusion and it also brings out the role of high–Z elements whose presence may be detrimental in efficient keV x-ray conversion in laser plasma x-ray source for various applications.

Chapter 5

Inner-shell and the ionic line radiation from magnesium plasma

The x-ray sources based on the ionic line radiation [22, 148-149] (He- α , H- α) as well as inner-shell x-ray lines [21, 68, 150-151] (K- α , K- β , L- α etc.) from various target forms have been developed for a variety of research investigations and applications. It should be noted here that the ionic line emission is due to the electronic transitions in the highly charged ionic species (H-like, He-like etc.) present in the plasma heated to a high temperature. The spectral and temporal characteristics of such radiation depend on the plasma parameters viz. electron density, temperature, average degree of ionization, and opacity of the hot plasma medium [12]. On the other hand, the characteristic inner-shell emission originates from cooler near-neutral ions interacting with hot electrons. Therefore, the simultaneous measurement of both spectral lines provides information for a more complete description of intense ultra-short laser interaction with the solid target.

High temperature plasma of moderate- Z material produced at intensities $> 10^{15} \text{ W cm}^{-2}$ using sub-ns duration laser pulses is an efficient source of high energy K-shell ionic line radiation [152]. Further, plasma of high- Z material produced at high intensity ($> 10^{17} \text{ W cm}^{-2}$) using ultra-short duration laser pulses (sub-ps) is an efficient source of high energy K- α like inner-shell x-ray line radiation [153]. Plasma of low- Z target produced by an ultra-short duration laser can be a source [154-155] of both 1-2 keV inner-shell and ionic line radiation. The photon yield of these line radiations is determined by the laser irradiation parameters such as intensity, pulse duration, and pre-pulse contrast of the laser system. Further, the self-generated magnetic field may pinch the hot electrons leading to much smaller x-ray source size. A simultaneous observation of both these line radiations can give better insight into the

conversion process of the absorbed laser energy into thermal and non-thermal electron energy. Next, a knowledge of the angular distribution of the x-ray intensity is necessary not only for a correct estimation of x-ray conversion efficiency, but also in deriving plasma diagnostics information as well. Moreover, since the x-ray emission intensity is governed by the plasma hydrodynamics and the radiation transport involved, study of the angular distribution of the x-ray emission can be helpful in understanding these processes in the plasma.

In this chapter, we describe the measurement of the K- shell x-ray line spectra, containing both ionic and inner-shell radiation, with a Bragg crystal spectrograph. The x-ray line radiation intensity has been studied as a function of laser intensity, focus position and pulse duration. X-ray spectra were recorded in three angular directions 0° , 45° , and 87° with respect to the target normal direction. The plasma conditions prevalent during the emission of x-ray spectrum were identified by comparing the experimental spectra with the synthetic spectra generated using the spectroscopic analysis code PrismSPECT.

5.1 Description of the experiment

The experiments were performed using the Ti:sapphire laser delivering 45 fs pulses at 10 Hz repetition rate, at 800 nm wavelength. Figure 6.1 shows a schematic diagram of experimental setup. The plasma was produced by focusing the 50 mm diameter laser beam onto a 2 mm thick magnesium target, placed at 45° (with respect to the laser direction), using a 500 mm focal length lens. The focal spot was measured by the procedure described in Chapter 2. The measured focal spot has diameter of $18\ \mu\text{m}$ in the vertical direction and $25\ \mu\text{m}$ in the horizontal direction for 45° incidence of laser beam at the target surface. The laser focal spot was changed by moving the lens away from the best focus position on either side. The Rayleigh range calculated for the focussed laser beam was $613\ \mu\text{m}$. The target was

moved at a constant speed of 1mm/s (i.e. 100 μm between every shot) with the help of a computer controlled precision x-y stage, so that each laser pulse irradiated a fresh spot for a laser operation at 10 Hz. The run out from the focal plane while moving the target was checked by imaging the target plane with an objective onto a CCD camera. The run out from the focal plane was less than 25 μm , which is much smaller than the Rayleigh range.

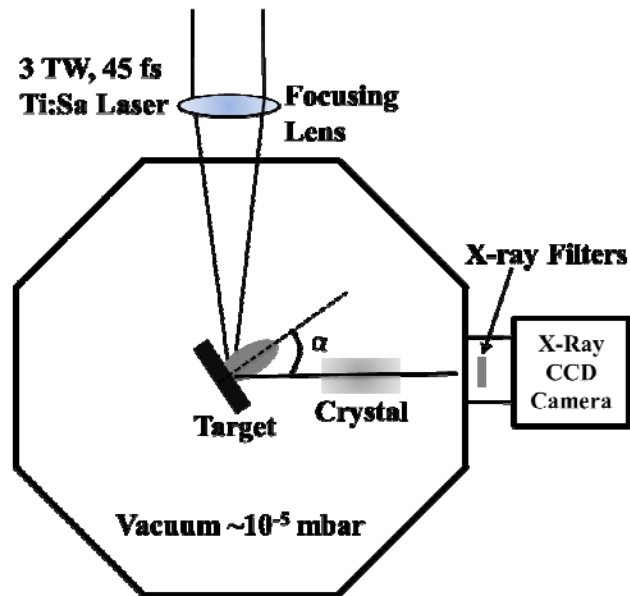


Fig. 5.1: A schematic diagram of the experimental setup.

The x-ray spectrum from the target was recorded in the wavelength range of 9 \AA - 10 \AA using a high resolution x-ray crystal spectrograph and the x-ray spectrum was recorded on a 16 bit, back-illuminated, cooled, x-ray CCD camera (Reflex SRO). This spectrograph had a planar thallium acid phthalate (TAP) crystal of a double inter-planar spacing ($2d$) of 25.75 \AA [(100) plane]. The spectrograph was set up with a linear dispersion (on the x-ray CCD) of 6.2×10^{-4} $\text{\AA}/\text{pixel}$. The spectral resolution of the spectrograph was estimated to be 12 m \AA . An opaque screen was placed to prevent any x-ray emission from the plasma falling directly on the CCD. Three layers of aluminized polycarbonate (B-10) filter were placed in front of CCD camera to block entry of any scattered light in the plasma chamber. To prevent the fast electrons from the plasma bombarding the filter and thereby producing fluorescence

x-rays, leading to a background on the CCD camera, a permanent dipole magnet was placed between the source and the filter. The dipole magnet, having an effective magnetic field of ~ 500 G inside the pole gap of 35 mm, was placed between the x-ray source and the detector, at a distance of 10 cm from the detector (CCD camera of chip size 27 mm x 27 mm). It was estimated that the magnet would deviate electrons with energy < 1 MeV and hence shield the CCD camera. The use of this magnet improved the intensity contrast of the peak to background to ~ 10 , which is much higher than the intensity contrast of ~ 3 which was obtained in measurements without the magnet. The angular distribution was recorded in three different settings by placing the spectrograph at an angle of 0° , 45° , and 87° with respect to the target normal. The effect of the laser intensity on the x-ray emission was carried out by a) changing laser energy through calibrated neutral density filters (before the laser pulse compressor stage), keeping the laser focal spot and the pulse duration fixed, and b) by varying the laser focal spot size, keeping the laser pulse duration and the energy constant

5.2. Main features of x-ray emission spectrum from Mg plasma

The keV x-ray emission spectrum from magnesium plasma has well defined ionic x-ray line features corresponding to high temperature plasma, as well as characteristic K- α emission from cold atom and lower charge ions caused by the hot electrons, produced from the interaction of the laser radiation with the solid target. Figure 5.2 shows a high resolution x-ray spectrum of magnesium plasma produced by the 45 fs duration laser pulses, focussed at an intensity of 4×10^{17} W cm $^{-2}$. The intensity of the ASE pre-pulse was estimated to be around 3×10^{12} W cm $^{-2}$ for this setting. In this case, the detector was kept at 45° with respect to the target normal, and the spectrum was accumulated in 300 laser shots.

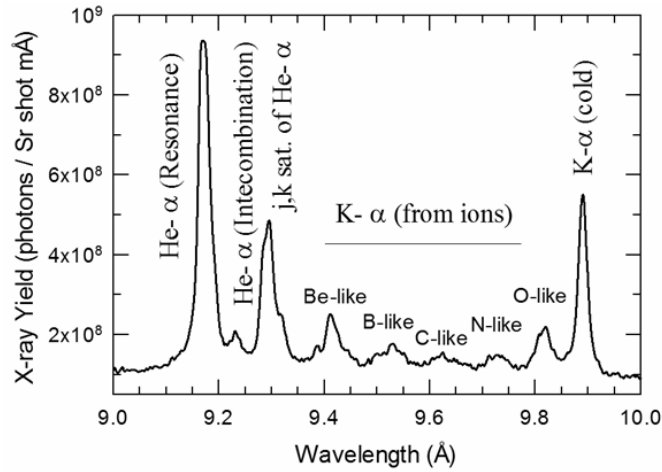


Fig. 5.2: High resolution x-ray spectrum of magnesium plasma produced by 45 fs duration laser pulses focussed at an intensity of $4 \times 10^{17} \text{ W cm}^{-2}$.

The identified lines are He- α resonance transition Mg XI $1s^2 \ ^1S_0 - 1s \ 2p \ ^1P_1$ at $\lambda = 9.17 \text{ \AA}$, weak He- α intercombination transition (IC) Mg XI $1s^2 \ ^1S_0 - 1s \ 2p \ ^3P_{1,2}$ at $\lambda = 9.23 \text{ \AA}$ blended with the s, t, m, n satellite lines, the group of q, r and j, k dielectronic satellite lines of the Li-like transitions at $\lambda = 9.32 \text{ \AA}$, and the K- α emission from un-ionized Mg atoms at 9.87 \AA . The q, r and j, k satellites lines are not well resolved due to the degraded spectral resolution on account of the source size broadening, but are well resolved from the IC line. The satellites lines s (9.235 \AA), t (9.236 \AA), m (9.218 \AA), n (9.221 \AA) are unresolved from IC line in the spectrum due to their small difference in wavelength and limited spectral resolution of the x-ray crystal spectrograph. A relatively lower intensity shifted K- α emission, from Be-like, B-like, C-like, N-like, and O-like Mg ions, is also observed on the lower wavelength side of the K- α emission from the Mg atoms. The spectral dispersion was calibrated from the tabulated [23] values of the He- α resonance line, inter-combination line, and the associated satellite lines. In the subsequent analysis, we compare the ionic lines from He-like ions i.e. He- α resonance line (and its satellites) and the K- α emission from un-ionized Mg atoms for various laser irradiation parameters. These lines are well resolved and are above the background.

A typical K-shell x-ray spectrum [154] of the Mg plasma produced by high contrast ultra-short duration high intensity laser pulse shows that the thermal x-ray spectrum has a strong He- α line, with the satellites of the different ions from O-like to Li-like, limited by the K- α line from un-ionized Mg atoms. One of the observations in x-ray emission spectrum from such high density plasma is the absence of IC line as it is expected to be quenched by electron collisions [156] (at densities higher than 10^{22} cm^{-3}). Duston *et al* [157] have shown that in the dense plasma, several helium like satellite lines are usually blended with the IC line. For example, the m, n and s, t satellites overlap with the aluminium IC line. At higher density, their intensities become significant and cause difficulty in spectrum identification. Further, doubly excited levels of some of the satellite lines are populated by recombination. For instance, in the pioneering experimental work on x-ray emission from ultra-short ultra-high laser-produced plasma, Cobble *et al* [156] have shown that the intensities of the j, k, l lines have a significant contribution from recombination at later times. However, when moderate contrast ultra-short laser pulses are used to create the plasma, it is observed that the emission of the ionic lines originates from the under-dense region up to critical density [158]. In such a case, the intercombination line may have significant intensity indicative of the emission region having low density. However, the K- α line excitation is by the hot electrons which are generated through collective mechanisms [29] such as resonance absorption, vacuum heating, etc. These electrons, on penetration into the cold target material, generate continuum hard x-ray bremsstrahlung and the characteristic K- α line radiation. Simultaneous presence of the K- α lines from un-ionized atoms as well as the satellite K- α lines from Be- to O-like ions, is due to the presence of pre-plasma. The satellite lines are inner-shell K- α transitions induced by the hot electrons in lower charged ionic species present in the initial low temperature pre-pulse plasma [159]. These satellite lines have been used as a diagnostics tool to infer the fraction of hot electrons in the plasma [154].

5.3 X-ray line intensity scaling with laser intensity

The aim of this work was to achieve an efficient conversion of the ultra-short duration laser pulse energy into x-ray by optimizing the laser irradiation parameters. The intensity of the x-ray line was obtained by integrating it over the spectral width. The x-ray emission was studied as a function of the laser intensity since the laser intensity is the main laser parameter which controls the interaction of a high intensity laser beam with a solid surface. Figure 5.3 shows the He- α (resonance) and the K- α emission as a function of laser intensity on the target, for 45 fs duration laser pulses. The intensity of laser was varied by varying the laser energy, keeping its spot size and the pulse duration unchanged. For intensities $< 2 \times 10^{17}$ W cm $^{-2}$, the K- α emission was more than the He- α emission. It is seen from the figure that the intensities of both He- α and K- α lines increase with the laser intensity approximately as a power law given as I_L^β , where β is the scaling exponent. The scaling exponent was found to be 1.5 for He- α and 0.6 for K- α lines. The higher scaling for the ionic line He- α indicates that an increasing amount of the absorbed laser energy is converted into thermal plasma energy [158] at higher intensities.

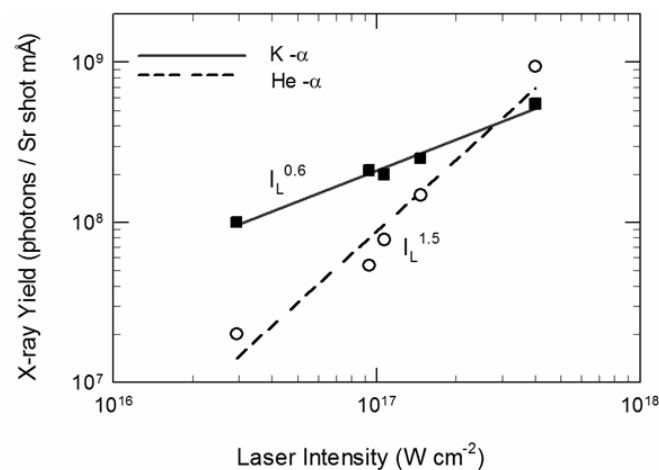


Fig. 5.3: He- α and K- α emission as a function of the laser intensity. The variation in the laser intensity was accomplished by changing the laser energy, keeping the laser focal spot size unchanged.

The resonance absorption is the dominant mechanism of absorption for femtosecond duration laser pulses of moderate contrast when focussed to intensities $> 10^{17} \text{ Wcm}^{-2}$. With the increasing laser intensity, the absorption mechanisms are such that both fraction and temperature of hot electrons increase. The energy distribution of the fast electrons produced in the resonance absorption can be approximated by a Maxwellian distribution with a temperature T_{hot} . In the intensity regime of 10^{17} – $10^{19} \text{ W cm}^{-2}$, Beg *et al* [160] have inferred a scaling of electron temperature as $kT_{\text{hot}}(\text{keV}) = 100 (I_{17} \lambda^2)^{1/3}$, which is compatible with the production mechanism of fast electrons based on resonant absorption. Using the above scaling law, we expect production of fast electrons with temperature around 100 keV in the plasma under our experimental conditions. Further, the temperature corresponding to the fast electrons was obtained by Rao *et al* [123] from the energy spectrum of the fast electrons in a similar experimental conditions. The hot electron temperature for the similar experimental conditions is in the range of few tens of keV to hundreds of keV. For intensity $> 10^{17} \text{ W cm}^{-2}$, a slower scaling of the thermal emission with the laser intensity is expected for the shorter duration laser pulses [158]. Scaling of $\beta = 1.2 - 1.5$ has been reported [161-162] with sub-ps laser pulses, compared to the scaling of $\beta = 2 - 2.5$ reported for the ns duration [163] laser pulse. A relatively faster scaling of 1.5 for 45 fs laser pulses was observed in our experiment. It may be due to the increased hot electrons fraction with increasing laser intensity will shift the ionization balance towards higher ionization states due to the hot electrons enhanced ionization rate in ultra-short laser-produced plasma [63], leading to the higher scaling with fs laser pulses. When the higher energy hot electrons generated with increasing laser intensity would penetrate deep inside the target, K- α photons generated from the deep region of the target will be reabsorbed as they propagate out of the target surface. This effect causes a reduction of the detected K- α photons [164] giving rise to the observed lower intensity scaling ($\beta = 0.6$).

5.4 X-ray line emission intensity variation with focusing

Figure 5.4 shows He- α (resonance) and K- α emission as a function of the distance of focal position from the target, d , irradiated with 45 fs duration laser pulses of fixed laser energy of 135 mJ. It may be noted from the figure that whereas the He- α yield shows a maximum at $d = 2.5 \pm 0.5$ mm, when the laser focus position lies after the target, the K- α emission maximizes at the best focus position. It is similar to the observation by Khattak *et al* [165] of the central peak of K- α emission being symmetrical about the best focus position. In all the subsequent measurements, the target was kept at the best focus position.

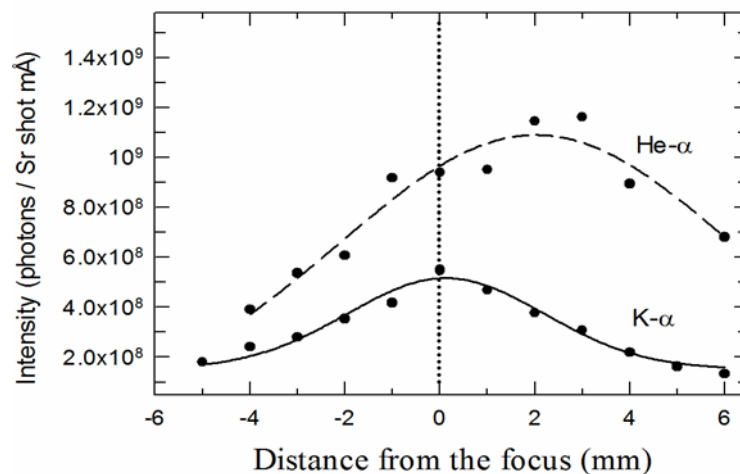


Fig. 5.4: He- α and K- α emission as function of the distance of the focus position from the target surface irradiated with laser pulses of fixed energy of 135 mJ. “Zero” corresponds to the best focus position. Negative distance corresponds to laser focussed after the target.

The shift of the peak of the He- α emission towards laser focussed inside the target can be simply explained by the geometric focusing effect [166] due to the pre-plasma [25] formed at the target surface. The refractive index (μ) of plasma is given by $\mu = (1 - n_e/n_c)^{1/2}$ where n_e is the electron density and n_c is the critical density. The refractive index of the plasma is less than one in the under dense region. Therefore a converging beam entering from vacuum ($\mu=1$) undergoes further focusing and diverging beam further diverges, as depicted in Fig. 5.5 (a)

and Fig. 5.5 (b). Thus the laser beam which enters the pre-plasma before reaching the best focus will have higher intensity of the laser beam on the target. This leads to a higher emission of He- α line. On the contrary, when the laser beam is focussed before the target, it is diverging when it enters the pre-plasma region and diverges further. As a result, the intensity further decreases and the He- α line emission intensity decreases faster.

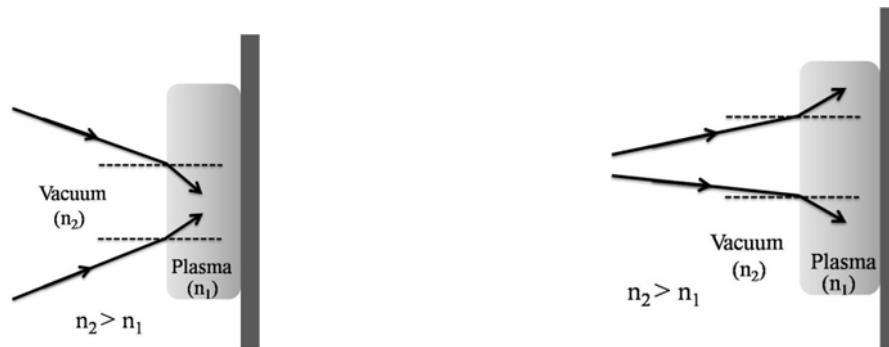


Fig.5.5: (a) Laser beam entering from vacuum ($\mu= 1$) always deviates away from the normal which leads to further focusing of a converging beam. (b) Divergence of laser beam focussed in front of the target surface (diverging beam).

However, we observe a central peak in K- α x-ray yield and no difference due to refraction of the beam in the pre-formed plasma. Moreover, generation mechanism of K- α radiation from a given solid target is such that there lies an optimal laser intensity for creating efficient K- α radiation. It is because the K-shell ionization cross-section of electrons is maximum when the electron energy is about three to four times the binding energy of the K-shell electron. The optimal laser intensity [70, 71] for the efficient generation of K- α radiation from the bulk Mg target has been reported as $\sim 10^{16}$ W cm $^{-2}$. However, it can be seen that in our experiment it is 4×10^{17} W cm $^{-2}$ at the best focus position (Fig. 5.6). It should be further mentioned that K- α conversion at the focal position corresponding to $d = \pm 4$ mm, with the laser intensity of 10^{16} W cm $^{-2}$, is smaller by a factor of ~ 2.5 compared to the conversion at the best focal position.

At the best focus, the scale length of the pre-formed plasma is large and decreases monotonically on either side due to reduction in the laser intensity. This change in scale length affects the absorption processes [167] and the x-ray emission of ionic line and inner-shell radiation differently. It is expected that intensity of ionic line radiation from highly charge species (He-like) will get enhanced with increase in laser intensity as increased hot electrons fraction will shift the ionization balance towards higher ionization states. Asymmetry in He- α emission with respect to best focus position is attributed to the geometrical focusing effect where a converging beam converges further and diverging beam diverges more in the pre-formed plasma. However, this behaviour is not seen in the K- α emission which is symmetrical about the best focus position. The decrease of K- α emission on both sides of the best focus is due to reduction of laser intensity which leads to the decrease in the number of hot electron generated through resonance absorption. Though the laser intensity increases due to the geometric focusing effect but this does not result in the increase of K- α emission. This is due to the fact that length of pre-formed plasma in front of bulk solid is significantly smaller. The generated hot electrons face less attenuation in the plasma travelling deep into the target and hence contribute little in the K- α emission.

5.5 Angular dependence of x-ray emission

The angular dependence of x-ray line radiation from plasma source was also measured by recording the x-ray emission spectrum by placing the spectrograph at an angle of 0° , 45° , and 87° with respect to the target normal. The measurements were performed with the 45 fs laser pulse irradiating the target at an intensity of $4.2 \times 10^{17} \text{ W cm}^{-2}$. The angular distribution obtained for both He- α and K- α x-ray emission is shown in Fig 5.6. It is observed that maximum emission is in the forward direction and the intensity reduces with an increase in the angle (θ). The dashed and solid curves corresponding to $\cos^{0.7} \theta$ and $\cos^3 \theta$ are shown

as approximate fits to the experimental data, for He- α and K- α x-ray line radiations respectively.

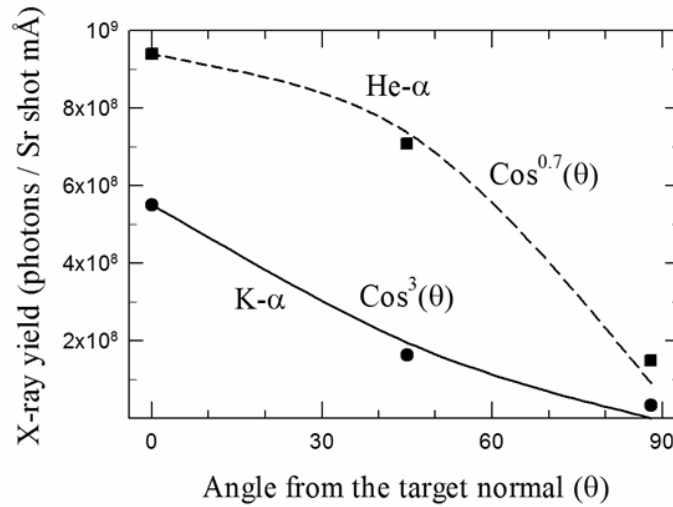


Fig. 5.6: Angular distribution of He- α and K- α emission. Solid and dashed curves represent the fit of the form $\cos^3 \theta$ and $\cos^{0.7} \theta$ to the angular distribution for K- α and He- α emission, respectively.

The anisotropy of x-ray emission can be understood to be due to the effect of plasma opacity. The angular distribution of the radiation intensity at a particular wavelength, from a plasma of certain volume and shape, containing a given number of emitters, would be governed by the escape factor $\exp(-\tau)$, where τ is optical depth faced by the radiation in traversing the plasma in different directions [38]. For an optically thin plasma (i.e., $\tau \ll 1$), the escape factor is nearly equal to unity in all directions. In this case, the angular distribution is expected to be isotropic [115, 168]. On the other hand, if the plasma is not optically thin, the escape factor may be different for different directions. For example, for a coin-shaped plasma, the escape factor in the direction of target normal is highest because of the smallest plasma thickness encountered in that direction. The escape factor decreases with increasing angle from target normal as the plasma thickness increases. As a result, the x-ray intensity will show a monotonically decreasing angular distribution of the form $\cos^\alpha \theta$, where the value of exponent α increases with the increasing thickness and increasing density of the emitting plasma leading to opacity effects [115, 152].

As shown in Fig.5.6, the measured angular dependence of the He- α and K- α x-ray emission fits well to an assumed power law $\cos^\alpha \theta$ with a value of α being 0.7 and 3 for He- α and K- α emission respectively. The observation can be explained by considering that the source of He- α is an extended plasma formed at the surface and the radiation experiences attenuation depending on the physical length of the plasma encountered by radiation to escape from the source in the direction of detection [38, 115, 152]. Hence this angular dependence ($\cos^{0.7} \theta$) is more closer to an isotropic one. In contrast, the K- α distribution is much more forward peaked. For example, the signal of K- α is ~ 16 times smaller at an angle of 87° than that along the target normal. This is due to the fact that K- α source lies inside the bulk target material (compared to He- α source being outside the target) and the emission gets more and more strongly attenuated in the target as the angle increases.

5.6 Effect of laser pulse duration on x-ray emission

The dependence of K- α and He- α intensity on the laser pulse duration for a constant fluence of $3.8 \times 10^4 \text{ J cm}^{-2}$ is shown in Fig.5.7a and b respectively. The pulse duration was varied in the range of 145 fs – 1400 fs by changing the distance between the compressor gratings as described in Chapter 2. The measured spectra were identical for both positive and negative chirp pulse of same duration. It can be seen that the Mg K- α intensity increases with pulse duration has a maximum at (740 ± 140) fs and thereafter decreases. The x-ray intensity at optimal pulse duration is ~ 2 times of the intensity measured at 45 fs. The optimization of x-ray intensity at lower laser intensity (corresponding to 740 fs duration) is due to trade-off between the increase in the hot electron temperature with laser intensity and reabsorption of the K- α radiation in coming out of the target [164].

The intensity of the He- α x-ray radiation depends on the dynamics of atomic processes in the plasma and the electron temperature. Simple analytical calculations [149] of ionization equilibrium time for the heated plasma shows that the ionization time required to produce He-

like ionization state from Li-like ionization state is ~ 15 ps. It is therefore expected that an increase in the laser pulse duration would increase the relative abundance of He-like ions compensating the decrease in electron temperature. The intensity of He- α therefore increases with the laser pulse duration, despite decrease in laser intensity.

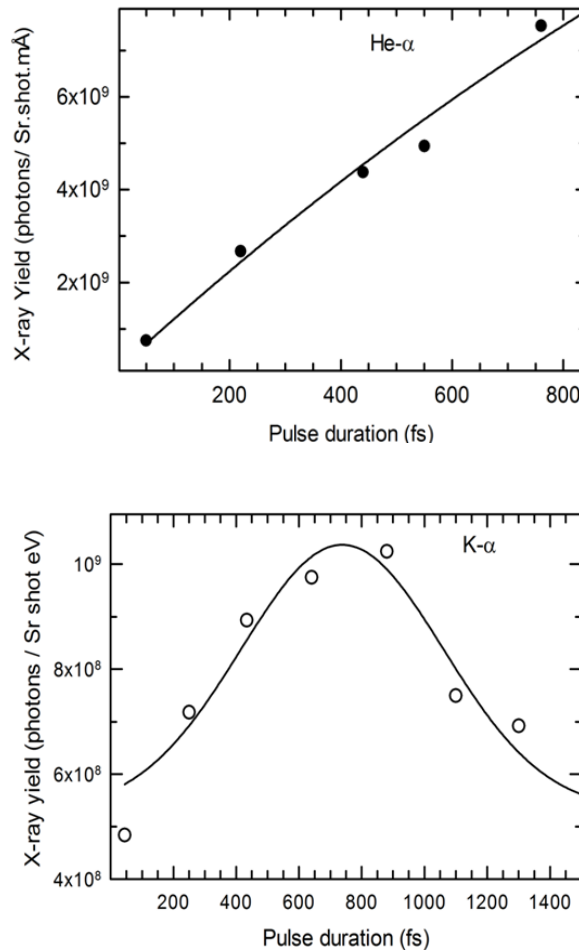


Fig. 5.7: X-ray yield as a function of incident laser pulse duration for a constant fluence of 3.8×10^4 $J cm^{-2}$ (a) K- α (b) He- α .

5.7 Discussion of the observed x-ray spectrum

In our study, the x-ray spectrum was recorded with a time integrated x-ray spectrograph. The observed x-ray spectrum corresponds to the time and space averaged values of density and temperature of the plasma undergoing rapid hydrodynamic evolution [169-171]. Modelling the x-ray spectrum at each distinct condition of temperature and

density, in space and time, would require sophisticated computer simulations coupled to plasma hydrodynamic codes including radiation transport. Nevertheless, some important features can be realized by approximating the plasma to be of some geometrical shape, and making certain simplifying assumptions on the spatial variations of plasma density and temperature. For example, hot electrons are emitted during the laser pulse and the inner-shell line emission originates mainly from the dense bulk of the target, which is also heated to a temperature of few tens of eV by the hot electrons generated during the interaction process. Spectroscopic analysis and modelling of K-shell spectrum of Mg plasma produced by the interaction of femtosecond laser pulses has been carried out using the single cell spectral analysis code PrismSPECT [172]. It generates K-shell emission spectra based on either steady-state or time-dependent plasma conditions. User inputs are : range of density, temperature, and size of the plasma typical of those found in experimental condition. PrismSPECT allows the user to specify the equilibrium (LTE or non-LTE), and the expansion geometry (planar or spherical) to be used in the spectra calculations. Time dependent calculations allow the user to specify the time duration over which the ionic populations are to be calculated for the user specified temperature and density.

The spectrum was computed by time-dependent solution of rate equations considering non-local thermodynamic equilibrium (NLTE). Least-squares comparison of normalized PrismSPECT spectrum with the experimentally observed spectrum shown in Fig.5.2 was carried out. Figure 5.8a shows a fit for ionic line emission with temperature $T_e = 130$ eV, and electron density $n_e \sim 5.4 \times 10^{20} \text{ cm}^{-3}$, $T_{\text{hot}} = 50$ keV and the hot electron fraction = 0.01. A spatially and temporally averaged value of the electron temperature of ~ 100 -200 eV and a hot electron fraction of ~ 0.01 is expected in our experimental conditions [153]. The electron density value which fits the spectra is close to the turning point density ($\sim 7.8 \times 10^{20} \text{ cm}^{-3}$) for a 45° obliquely incident 800 nm Ti:sapphire laser beam. The hot electron temperature is the

order of, but slightly lower than 100 keV as expected from the scaling law of Beg *et al* [160]. It shows that lower energy electrons share their energy within the under-dense pre-formed plasma. Figure 5.8b shows the experimental and computed spectra in the wavelength region around K- α emission. The fit corresponds to the plasma condition having temperature $T_e = 10$ eV, $T_{hot} = 130$ keV (hot electron fraction = 0.01) and electron density $n_e = 4.4 \times 10^{22} \text{ cm}^{-3}$. K- α line from un-ionized magnesium atoms and the shifted K- α lines from O-like magnesium ions seen in the spectrum are the signature of a low temperature bulk solid plasma heated by the energetic electrons penetrating the solid target. The synthetic spectra in Figs. 5.8a and b clearly demonstrate that the plasma under consideration has density and temperature gradients. The spectral region around the He- α line mainly comes from the hot under dense plasma and that around K- α arises from the bulk dense region. In order to accurately generate the synthetic spectra for this situation, one would need a multi-cell code. However, the single-cell code used here has successfully brought out the essential physics of the experimentally observed spectra.

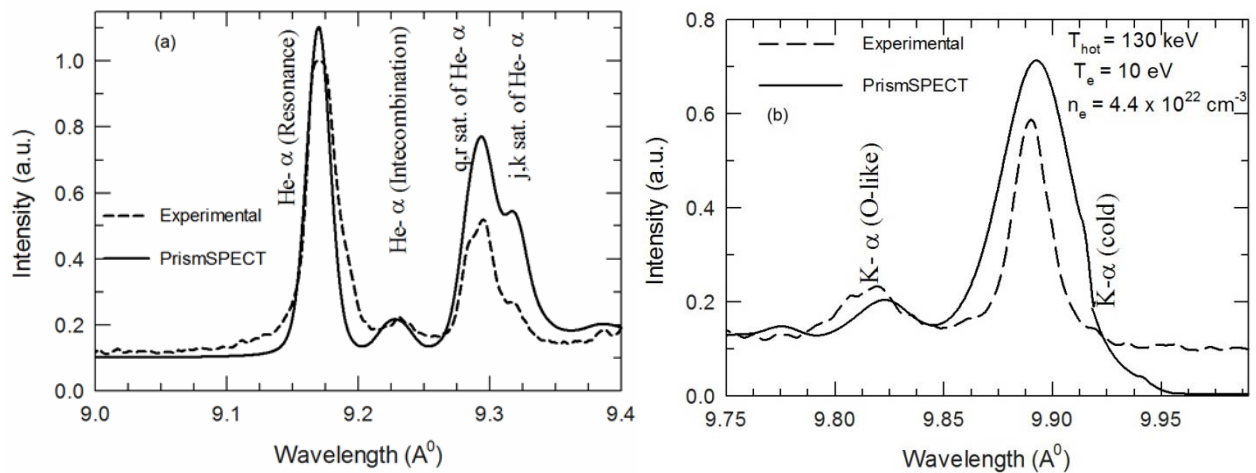


Fig. 5.8: Synthetic spectra of Mg computed using PrismSPECT software to fit the experimental spectrum at an intensity of $4 \times 10^{17} \text{ W cm}^{-2}$. a) Region around the He- α resonance, best fit for the parameters: $T_e = 130$ eV, $T_{hot} = 50$ keV, hot electron fraction = 0.01, and $n_e = 5.4 \times 10^{20} \text{ cm}^{-3}$; b) Region around the K- α emission, best fit for the plasma conditions: $T_e = 10$ eV, $T_{hot} = 130$ keV, hot electron fraction = 0.01, and $n_e = 4.4 \times 10^{22} \text{ cm}^{-3}$.

It has been shown that the ionic line emission arising due to a short-pulse laser drive is very efficient with controlled pre-pulse intensity as the laser energy is absorbed efficiently in the pre-formed plasma through the excitation and subsequent damping of the electron plasma wave. The electron plasma wave can be excited in the plasma either through resonance absorption or parametric instabilities. Parametric instabilities, namely two plasmon decay (TPD) and stimulated Raman scattering (SRS), are expected to grow in long scale length (tens of microns) plasma and contribute to the absorption of laser energy. In this case, SRS is responsible for backscattering of laser radiation and thus limits the absorption of laser energy. For the similar laser irradiation parameters, we have observed [173] $3\omega/2$ radiation emission arising either due to TPD or SRS instability which provides additional confirmation that the keV x-ray emissive region has lower density. Nevertheless, control over the pre-pulse and/or amplified spontaneous is important to optimize the conversion efficiency of x-ray line radiation.

A particularly strong motivation to study the x-ray line radiation from laser-produced plasmas, is to make it suitable for its use as an x-ray back-lighter for diagnosing a large variety of high-energy-density phenomena. Many theoretical and experimental studies have been carried out for getting the conditions leading to higher x-ray conversion efficiency. Long-pulse (>500 ps) laser back-lighters have been found to be more efficient than short-pulse back-lighters for photon energies <10 keV. For low photon energy, ionic line radiation is quite efficient, converting up to 1% of the laser energy into He- α photons. With the shorter duration sub-picosecond laser pulses focussed at a intensity of 10^{17} W cm $^{-2}$, a conversion efficiency of $\sim 0.5\%$ was reported by Cobble *et al* [174] for Al He- α line radiation. The maximum conversion efficiency of the laser energy into Mg He- α in the present experiment was $\sim 0.2\%$. The smaller conversion efficiency in our experiment is perhaps due to the smaller pulse duration laser used and the ionization dynamics is expected to depart

significantly at smaller pulse duration. Using the scaling law obtained in our experiment, it is estimated that a conversion efficiency of $\sim 1\%$ can be achieved with a laser system operating at 8 – 10 TW laser power.

To summarize this chapter, high-resolution keV x-ray spectral measurement of magnesium ionic and inner-shell radiation from ultra-short laser-produced plasmas was carried out for different laser irradiation parameters. The x-ray line radiation intensity was studied as a function of the laser intensity, focus position, and angular distribution. The variation of He- α line conversion with the laser intensity and focus position has been explained by considering the change in conditions of the pre-formed plasma. The variation in K- α emission for different laser parameters has been explained by considering the resonance absorption process for the hot electrons generation and their propagation in the bulk solid target. The observed angular distribution can be understood to be due to the source of He- α x-rays being located at the surface, whereas the K- α x-ray source being inside the surface of the target. The plasma conditions prevalent during the emission of x-ray spectrum have been identified by comparing the experimental spectra with the synthetic spectra generated by the spectroscopic analysis code PrismSPECT. The results will be of considerable value in designing laser-produced plasma x-ray line radiation source of photon energy in the range of 1–2 keV, for its use as a probe pulse in x-ray backlighting or time resolved x-ray diffraction studies.

Chapter 6

Bright ultra-short 4 -8 keV K- α x-ray source

The K- α radiation from ultra-short, ultra-intense laser produced plasmas has been proposed and demonstrated as a probe pulse for studying the time evolution of samples relevant to material science [76], biological science [175], or as a back-lighter source for probing high density matter [176]. For practical application of K- α radiation from femtosecond-laser plasmas in the fast x-ray diffraction experiments to study the temporal response of crystalline sample, it is essential to develop an efficient, bright x-ray source. The x-ray photon energy in the range 1 – 10 keV is used for structural modification or depth analysis of sample perturbed by the visible ultra-short pump pulse. High energy x-ray photons are more suitable for the x-ray radiography of objects with higher areal density encountered in experiments related to high energy density physics and inertial confinement fusion. Further, low photon energy (1–8 keV) probes having a low penetration depth are more to probe the changes induced by the optical pulse in the skin or penetration depth of the sample. Moreover, it can be used for x-ray-induced photo-electron spectroscopy of surfaces.

The important characteristics of K- α source for application in time resolved x-ray diffraction experiments are high brightness, ultra-short duration and monochromaticity [159, 177]. A source with all the above characteristics improves the sensitivity of detection, gives high temporal resolution and best imaging performance. The photon energy of K- α radiation is determined by the atomic number of the target irradiated by laser. For optimization of the K- α source, it is essential to understand the mechanism of its generation and factors controlling the source characteristics. In section 6.1 important parameters of K- α source are described. Details of experiment and results are given in section 6.2 and 6.3 respectively.

6.1 K- α source characteristics

The process of K- α radiation generation when a solid is excited with a high intensity femtosecond laser pulse is illustrated in Fig. 6.1. When ultra-short, high intensity laser pulses are focussed onto a solid target, the absorption mechanism of the laser energy are such that the hot electrons are generated [30]. The duration of this electron pulse is in the order of the laser pulse duration because electrons are generated during the presence of the driving femtosecond laser pulse [69-71]. When these energetic electrons penetrate into the underlying colder material, they knock out electrons preferentially from the K- shell of the atoms through inelastic collisions and generate bremsstrahlung radiation. The holes in the K-shell are filled by recombination of electrons from higher shells, emitting the characteristic line radiation. Inner-shell recombination takes place on a time scale of femtoseconds or even attoseconds. The x-ray radiation is generated until the electrons energy is more than the K-shell ionization threshold. Under optimized condition, it is of the order of laser pulse duration. Ideally, the source dimension comparable to the laser focal spot can be realized if electrons do not penetrate deep inside the bulk solid target and undergo lateral scattering. The source characteristics are discussed in the following subsections.

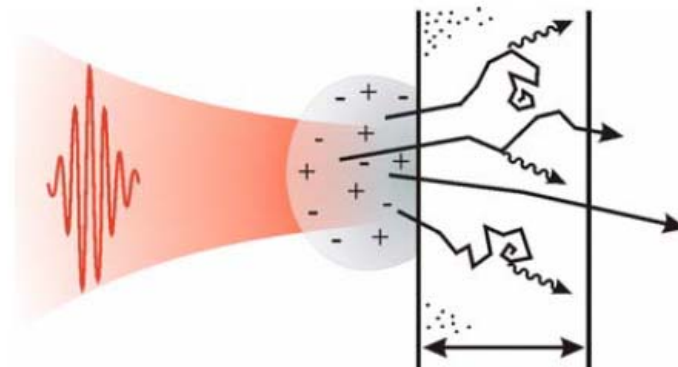


Fig. 6.1: Schematic of the generation of K- α line radiation when solid target is irradiated with ultra-short high intensity laser pulse.

6.1.1 X-ray photon yield

Improvement of the conversion of the laser energy to the energy of K- α radiation can be achieved by varying the parameters of an irradiating laser pulse and target. It has been shown that absorption depends on the geometrical shape and dimensions, and it is possible to increase the absorption and obtaining higher temperatures [178-179]. It leads to the generation of larger number of the fast electrons which in turn will raise the x-ray photon yield.

However, the increase in the number of the fast electrons and in their energy does not necessarily result in increase in x-ray conversion. In particular, the logarithmic growth of the cross-section for the K- α photon emission for relativistic electron energies [69] in a thick target does not entail an increase in the conversion. Further, the x-ray radiation is up to the K- α photon absorption length can be collected from the target. The high electrons penetrate substantially deeper into the target and are unable to escape. Thus the laser irradiation conditions have to be optimized for controlling the electron energies.

Reich *et al* [70] predicted existence of an optimum laser intensity for the K- α yield as equilibrium between K- α production and reabsorption in bulk targets. It occurs when the mean depth z is comparable to the absorption length for the K- α radiation. The number of K- α photons generated by an incident electron with initial energy E_0 is given as

$$N_{K-\alpha} = 4 \times 10^{-3} Z^{-1.67} E_0^{3/2} \quad (6.1)$$

It is important to optimize the energy distribution of the hot electrons in experimental conditions to achieve high conversion efficiency.

6.1.2 Pulse duration of the K- α radiation

The pulse duration of the K- α radiation depends on the hot electron energy distribution. With the increasing electron energy, K- α radiation is generated deeper into the

target. The K- α emission in bulk solid target occurs till the energy of electron is higher than the K-shell ionization threshold. The photons detected in the front direction (plasma expansion direction) can be approximated to be limited to the time, τ_{tr} , of electron transit through the layer of thickness λ_{ph} . The total duration, $\tau_{K-\alpha}$, of the K- α emission is the sum of the laser-pulse duration, τ_L , and the electron-transit time, τ_{tr} [69, 70]

$$\tau_{K-\alpha} = \tau_L + \tau_{tr}, \quad (6.2)$$

This is because the hot electrons are generated during the laser pulse and the x-ray emission continues till the energy of electron decreases to a value smaller than the K-shell ionization energy deep inside the target [70].

6.1.3 Monochromatic line radiation

Ultra-short laser interaction with solids produces plasma with bi-Maxwellian electron energy distribution function with bulk temperature and hot electron temperature. It has been mentioned in Chapter 1 that the maximum K- α yield occurs for an optimal T_{hot} of 3-6 times the K- α energy, using optimal laser irradiance. On the other hand, increasing the bulk temperature leads to the generation of K- α radiation from ions which is blue shifted and broadens the K- α lines [159, 177, 180]. It is to be noted that the narrow bandwidth probe radiations are desirable in time resolved x-ray diffraction setup to obtain better angular resolution which increases the sensitivity of the detection [159]. The contribution of this factor in the overall temporal resolution becomes important when the extent of modification of the diffracted signal is rather small, particularly for smaller delays or at smaller pump fluence. The angular resolution is determined by the line profile of the probe beam and is given by $\Delta\theta = \frac{\Delta E}{E} \tan\theta$ where $\Delta\theta$ is the full width half maximum (FWHM) of diffracted signal, θ is Bragg angle, and E is the photon energy of probe x-ray radiation. Thus, it is essential to obtain minimum bandwidth of K- α probe in order to increase the angular

resolution of the pump – probe experimental setup and which in turn improves the temporal resolution.

A detailed investigation on the dependence of laser parameters for generating monochromatic K- α x-ray radiation has been carried out. It is observed that there is a correlation between the optical emissions at 2ω and $3/2\omega$ from the interaction of ultra-short, intense laser pulses and the monochromaticity of the K- α x-ray radiation. It is described in the section 7.4.

6.1.4 Source size

The K- α x-ray source is generated by the hot electrons produced during the laser pulse. The spatial profile of the x-ray source is governed by the trajectories of the hot electrons, along which the K- α photons are generated [67]. The hot electrons density is highest at the focus of the laser beam. It is therefore expected to obtain x-ray source size comparable to the laser focus size. However, K- α source is expected to be larger than that of the laser focus due to the entrance angles of the hot electrons and their lateral scattering in the solid. For higher laser intensities, self-induced electric and magnetic fields modify the trajectories of hot electrons. It was found in simulations that the lower energy fraction of the hot electrons was reflected by the magnetic field and prevented from entering the solid at the centre of the laser focus [68]. The hot electrons which pass the magnetic field are deflected and enter the solid at shallow angles. Further, the magnetic field of pre-pulses can reflect a large portion of the hot electrons [67, 68]. The reduced pre-pulse intensity helps to achieve the smaller source size.

The source size of x-ray emission can be obtained from x-ray shadowgraphy, using a knife edge technique. In this technique, a blade is placed between the x-ray source and a detector (such as x-ray film or CCD camera) covered with a material foil. The CCD gets

uniformly exposed except for the regions where the x-ray source was partially or completely covered with the blade (Fig.3.7).

The edge spread function obtained with this technique is fitted with a Fermi function given by,

$$I(x) = \frac{I_1 - I_2}{1 + \exp\left(\frac{x - x_0}{dx}\right)} + I_2 \quad (6.3)$$

$$I_1 = (\lim_{x \rightarrow -\infty}) I(x)$$

$$I_2 = (\lim_{x \rightarrow \infty}) I(x)$$

(6.4)

where x_0 and dx are the edge position and the width respectively.

The derivative of the Fermi function $dI(x)/dx$ gives the line spread function, which can be well fitted by a Gaussian distribution function. The full width at half maximum of this function is defined as x-ray emission size. This technique has advantage of simplicity, good signal to noise ratio, and can give high spatial resolution due to very high magnification imaging. The limitation on resolution mainly comes from the criticality of alignment at high magnification and smoothing of the raw data which was performed in the numerical analysis of x-ray shadowgraph.

6.2 Experimental details

The experiments were carried out with the 10 TW Ti: sapphire laser system as described in Chapter 2. In the present experiment, the laser was operated at 3 TW power to reduce the ASE from the laser amplifier. Plasma was produced by focusing the 45 fs duration laser pulses, at 10 Hz repetition rate, onto the target (thick titanium, iron and copper) placed at 45° using an f/8 lens. The maximum laser pulse energy used in the current experiment was 135 mJ corresponding to a focussed intensity of $\sim 8.4 \times 10^{17} \text{ W cm}^{-2}$, for a measured focal

spot diameter of 18 μm in the vertical direction and 25 μm in the horizontal direction for 45° incidence of laser beam at the target surface. The target was mounted on a motorized X-Y translation stage in order to expose fresh surface of the target in each laser shot.

The x-ray spectrum of Ti, Fe, and Cu, in the energy range of 2 – 20 keV was recorded with dispersion less spectrograph [181] described in detail in Chapter 2. In short, the spectrograph consists of a 16 bit, back-illuminated x-ray CCD camera working in a single photon counting mode so that the CCD count is proportional to the deposited photon energy. The CCD array consists of 2048 x 2048 pixels. The CCD count can be converted to individual x-ray photon with the help of independent energy calibration and the histogram of the energy deposited in all pixels represents the incident spectrum. A custom made algorithm for identifying the single photon events was used to for constructing the x-ray spectrum and for analysis of the data from CCD camera [181]. The absolute number of K- α yield was determined by summing the number of hits contained in the K- α line shape and by taking into account the solid angle, the filter transmission, and the quantum efficiency of the CCD in single-pixel analysis mode.

In this experiment, the x-ray yield was optimized with the laser pulse duration (at fixed fluence) which was varied in the range of 45 fs to 1.8 ps, as described in detail in Chapter 2. The variation of laser pulse duration was also measured for increasing or reducing grating separation from the “compressor zero”. The femtosecond pulses were temporally characterized using an intensity autocorrelation method [182].

6.3 Experimental results and discussion

Figure 6.2 shows the x-ray spectrum of Ti, Fe and Cu recorded in the spectral range of 4 – 10 keV with the dispersion less spectrograph. The x-ray emission spectrum of titanium plasma, generated at a laser intensity of $\sim 7.1 \times 10^{16} \text{ W cm}^{-2}$ at $\tau = 440 \text{ fs}$, shows the well-resolved K- α and K- β lines at 4510 eV and 4930 eV, respectively superimposed over the

bremsstrahlung continuum. The x-ray emission spectrum from the thick Fe target irradiated with the laser pulses of 325 fs duration at a laser intensity of $\sim 1.1 \times 10^{17} \text{ Wcm}^{-2}$ clearly shows the Fe K- α at 6.4 keV. The Fe K- β line and 7.06 keV is not seen clearly due to the high bremsstrahlung background. The spectrum of Cu plasma produced by focusing 250 fs duration laser pulses at an intensity of $1.5 \times 10^{17} \text{ W cm}^{-2}$ shows K- α line at 8 keV. The K- β line is not visible due to nickel filter used to protect the CCD from low-energy bremsstrahlung and visible light. The peak around 6.4 keV is due to K- α escape event. It may be noted that the slope of continuum bremsstrahlung emission is more for copper plasma produced at higher intensity. This indicates that higher hot electron temperature is required for efficiently generating high photon energy K- α radiation [183]. Further, the peak to background ratio for Ti, Fe, Cu is 2.5, 1.8, 1.4 respectively. This is expected as the overall bremsstrahlung emission is proportional to Z^2 thereby reducing the peak to background ratio.

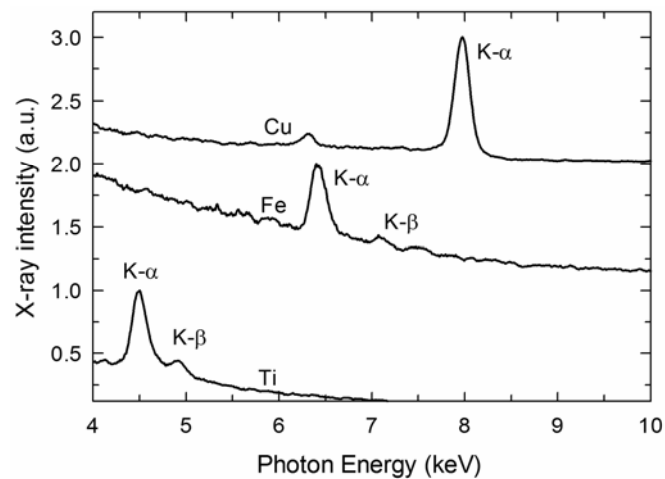


Fig. 6.2: X-ray emission from Ti, Fe, and Cu target recorded with dispersion less spectrograph.

The x-ray yield of the K- α radiation in the units of number of photons emitted per unit solid angle per shot per unit photon energy measured as a function of incident laser pulse duration (τ) for a constant fluence of $3.8 \times 10^4 \text{ J cm}^{-2}$ is shown in Fig. 6.3. The pulse duration

was varied in the range of 45 fs – 1400 fs by changing the distance between the compressor gratings. Ti K- α intensity increases with pulse duration, has a maximum at (420 ± 90) fs, and thereafter decreases. The x-ray intensity at optimal pulse duration is ~ 1.5 times the intensity measured at 45 fs. Fe K- α yield shows a small increase with laser pulse duration and has a maximum at (325 ± 75) fs and thereafter decreases. The x-ray intensity at optimal pulse duration of 325 fs is ~ 1.4 times the intensity measured at 45 fs. Cu K- α yield shows a slight increase with laser pulse duration and has a maximum at (250 ± 50) fs and thereafter decreases rapidly for pulse duration longer than 400 fs. The x-ray intensity with 250 fs duration pulses is ~ 1.3 times compared to that obtained with 45 fs duration pulses. The measured spectra were identical for both positive and negative chirp pulse of same duration. It indicates that in the present experimental conditions, the generation process of the K- α does not depend on the pulse shape of the incoming laser pulse as observed in the experiments with high contrast laser system [184, 185]. The optimal laser pulse duration and x-ray yield for studied K- α radiation is summarized in Table 6.1. At the optimal pulse duration, it is expected that the hot electron temperature is optimum and x-ray source is located close to the surface and does not get reabsorbed.

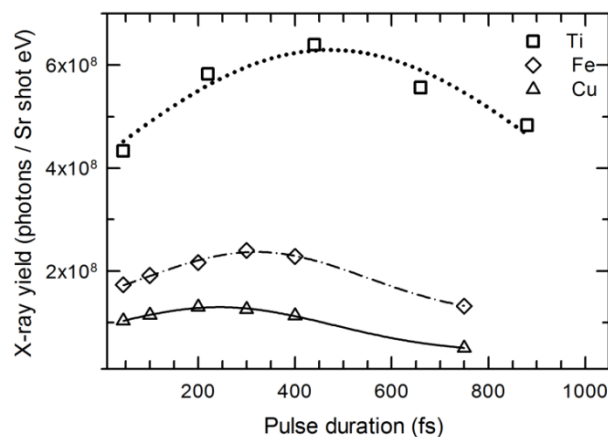


Fig. 6.3: Plot of K- α x-ray yield of Ti, Fe, and Cu as a function of incident laser pulse duration for a constant fluence of $3.8 \times 10^4 \text{ J cm}^{-2}$.

Target	Photon Energy (eV)	Optimal pulse duration (fs)	Scaling exponent with laser intensity		Yield of photons / (Sr eV shot)
			45 fs	Optimal pulse duration	
Ti	4510	420 ± 90	1.3	2.1	4 x 10 ⁸
Fe	6400	325 ± 75	1.5	2.3	2.4 x 10 ⁸
Cu	8048	250 ± 50	1.7	2.6	1.3 x 10 ⁸

Table 6.1: *Optimal laser pulse duration for obtaining maximum x-ray yield, scaling exponent with laser intensity obtained at 45 fs and optimal pulse duration, absolute K- α photon flux from different target material.*

We have measured the x-ray spectra for each target at different laser intensities in the range of $3 \times 10^{17} - 8.4 \times 10^{17} \text{ W cm}^{-2}$ keeping the laser pulse duration fixed at 45 fs. The laser intensity was changed by changing the laser energy in the range of 8 – 135 mJ without changing the focusing conditions. The plot of the absolute K- α x-ray yield ($I_{K-\alpha}$) as a function of the laser intensity (I_L) on a log – log scale for 45 fs duration laser pulse is shown in Fig. 6.4. The scaling of I_x with I_L is expressed as power law $I_{K-\alpha} \sim I_L^\beta$. The fitted results are shown by the line. The value of scaling exponent β is 1.3, 1.5, and 1.7 for Ti, Fe, and Cu respectively. The value of β less than 1 is an evidence of saturation of the x-ray intensity due to reabsorption of the x-rays in the bulk target. With increasing laser intensity, the generated hot electrons will produce the x-ray photons deeper inside the target because of their higher energy and smaller collision cross-section [164, 186]. The x-rays will be reabsorbed while coming out from deep in the target. Further, the K- shell ionization cross-section for electron decreases with increasing hot electron temperature or laser intensity [186]. The x-ray yield

increases faster for high $-Z$ target as the high energy x-rays have less reabsorption and require a higher hot electron temperature for optimal K- shell ionization.

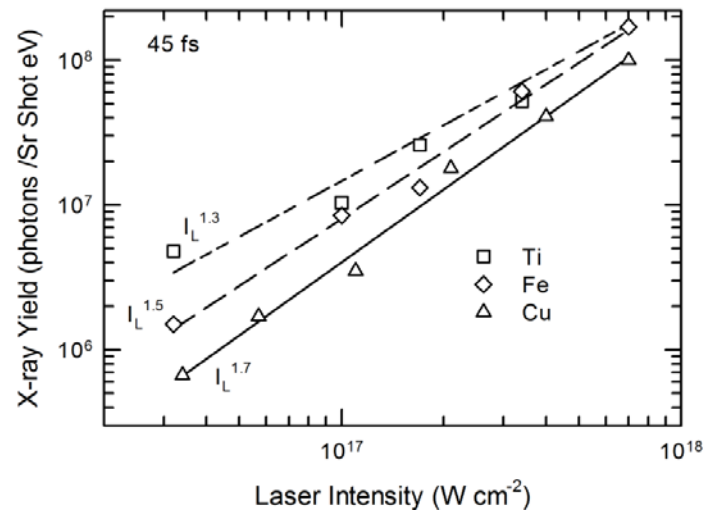


Fig. 6.4: $K\text{-}\alpha$ intensity (I_x) as a function of the laser intensity (I_L) on log – log scale at a fixed pulse duration of 45 fs. The scaling of I_x with I_L is expressed as power law $I_x \sim I_L^\beta$.

The scaling of x-ray with the laser intensity was also obtained by recording the x-ray spectra with the laser pulses of optimal duration for maximum conversion. In the Fig. 6.5, the Ti, Fe, and Cu $K\text{-}\alpha$ yield is shown as a function of laser intensities in the range of 2.5×10^{15} – $1.3 \times 10^{17} \text{ W cm}^{-2}$. The value of scaling exponent β is 2.1, 2.3, and 2.6 for Ti, Fe, and Cu respectively. The x-ray intensity increases much faster with the increasing laser intensity when the source is generated with the laser pulses of longer duration. The faster x-ray intensity scaling observed can be understood in terms of the dependence of $K\text{-}\alpha$ x-ray emission on the laser intensity ($\propto 1/\tau$) and applicable absorption mechanism [29, 30]. It suggests that the x-ray flux is not in saturation regime and can be increased with increasing laser fluence. The probable reason for this behaviour is that source is located at nearly the surface of the target. This is also advantageous since in such a case the source size broadening due to spatial spread of electron beam propagation in the bulk solid target would be minimal. It is expected that the source size will be close to the laser focal spot size. The

maximum value for the yield of K- α per shot in the unit of photons / eV/ Sr is estimated be 4×10^8 , 2.4×10^8 , 1.3×10^8 for Ti, Fe, Cu respectively.

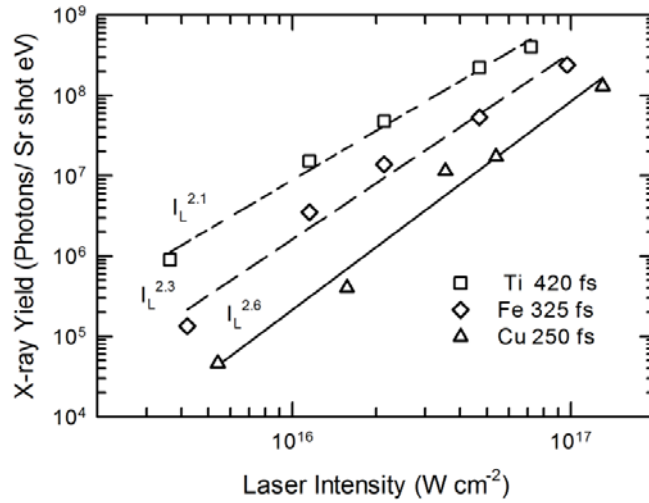


Fig. 6.5: K- α intensity (I_x) as a function of the laser intensity (I_L) on log – log scale at an optimized pulse duration of 880 fs, 440 fs, 325 fs, and 250 fs for Mg, Ti, Fe, and Cu target.

The conversion efficiency from laser energy to x-ray energy is listed in Table 6.2. It is calculated by assuming the nearly isotropic x-ray distribution in full sphere. The highest conversion efficiency of 3.2×10^{-5} and 2.7×10^{-5} is estimated for Ti and Fe K- α . The conversion efficiencies are in broad agreement with that reported earlier [107, 160]. The K- α x-ray conversion for a given fraction of laser energy taken by hot electrons, depends on the hot electron temperature [70, 71]. The hot electron temperature, considering the resonance absorption as the dominant mechanism of absorption of laser pulses from the moderately contrast laser system, can be approximated by a Maxwellian distribution with a temperature T_{hot} . In the intensity regime of 10^{16} – 10^{19} $W\ cm^{-2}$, Beg *et al* [160] have inferred a scaling of electron temperature as $kT_{hot}(keV) = 100 (I_{17}(Wcm^{-2})\lambda^2(\mu m))^{1/3}$. The K- α intensity increases rapidly with increasing laser intensity as the hot electron temperature approaches the value of few times of K-shell energy. The ratio of T_{hot} to the K-shell energy depends [70] weakly on Z and the ratio vary from around 12 for magnesium to 6 for high $-Z$ target like copper. The

optimal hot electron temperature estimated to be 31.5 keV, 41.6 keV and 48 keV for Ti, Fe and Cu respectively. On further increasing the laser intensity, the generated high energy hot electrons penetrate deeper into the solid target. There exists optimal laser intensity for the maximization of K- α x-ray intensity due to trade-off between the increase in the hot electron temperature with laser intensity and reabsorption of the emitted radiation in coming out of the target. For given fluence of $3.8 \times 10^4 \text{ J cm}^{-2}$ and the optimal laser pulse duration for the optimal laser intensities for maximum conversion is determined. The optimal hot electron temperature (laser intensity) calculated are 99 keV ($1.5 \times 10^{17} \text{ Wcm}^{-2}$), 92 keV ($1.2 \times 10^{17} \text{ Wcm}^{-2}$), and 83 keV ($9 \times 10^{16} \text{ Wcm}^{-2}$) for Cu, Fe, and Ti respectively.

The experimentally observed ratio of optimal hot electron temperature and K-shell energy as a function of atomic number is shown in Fig. 6.6. It varies from 12 for Cu to 53 for Mg respectively. The theoretically predicted optimal temperature varies between 4 and 12 times the K-shell ionization energy, depending on the atomic number. The experimentally observed values of optimal hot electron temperature are 2 – 4 times larger than that predicted using models. It indicates that the hot electrons are losing its energy before entering the cold target to generate K- α photon. The deviation is much larger for low photon energy K- α . Such a situation arises where the short duration laser pulse is interacting with the large pre-formed plasma and the density profile is primarily determined by the ASE pre-pulse. The scale length of pre-formed plasma estimated by 1-D hydrodynamical code for similar experimental conditions [123] is a few times the laser wavelength. In such a scenario, the hot electrons undergo orbiting [187] in front of the target and may give energy to the expanding pre-formed plasma. The optimal hot electron temperature is expected to be higher for efficient generation of K- α . Table 6.2 summarizes the K- α photon flux from different target material, optimal pulse duration and laser intensity for obtaining maximum x-ray yield.

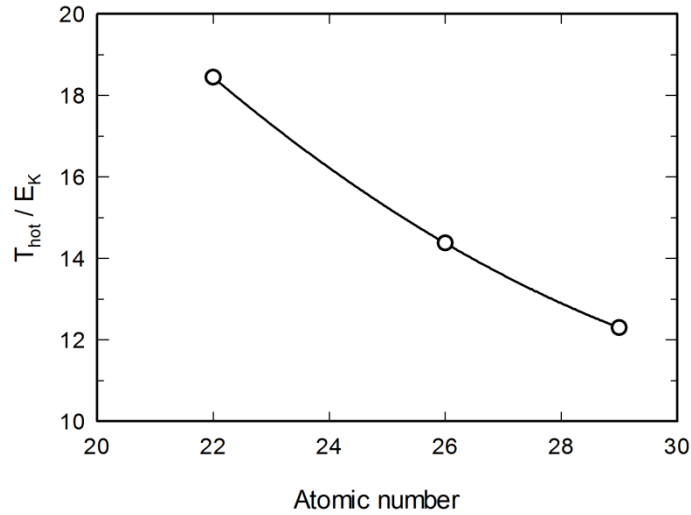


Fig. 6.6: Experimentally observed ratio of optimal hot electron temperature and K-shell energy as a function of atomic number

Target	Photon Energy (eV)	Experimental Optimal laser intensity ($W\ cm^{-2}$)	Theoretical optimal laser intensity ($W\ cm^{-2}$)	Conversion
Ti	4510	9×10^{16}	4.9×10^{15}	3.2×10^{-5}
Fe	6400	1.2×10^{17}	1.2×10^{16}	2.7×10^{-5}
Cu	8048	1.5×10^{17}	1.8×10^{16}	1.9×10^{-5}

Table 6.2: Optimal laser intensity for K- α photon flux determined experimentally, expected from theoretical consideration and conversion.

It has been shown that varying the laser pulse duration is the effective way to optimize laser intensity for maximizing x-ray yield and maintaining smaller x-ray source size. However, it will increase the total duration [69-71] of the K- α emission as it is the sum of the laser-pulse duration and the electron-transit time. Nevertheless, electron-transit time is usually much larger than the laser pulse duration particularly at higher laser intensities realized with shorter duration pulses [69]. Therefore longer afterglow emission elongates the

x-ray pulse duration. The optimization of x-ray yield and pulse duration can be made by optimizing the duration of laser pulse.

6.4 X-ray source size

The knife-edge method is used to determine the size of the copper plasma x-ray source. A knife edge of stainless steel of ~ 3 mm thickness was placed between the x-ray source and an x-ray CCD camera. A $3 \mu\text{m}$ thick nickel x-ray filter was placed between the x-ray CCD and knife edge. A magnet was placed before the x-ray CCD to reduce the background generated by hot electrons. The overall magnification was ~ 5.1 X. The CCD was uniformly exposed except for the region where the x-ray source was partially or completely covered with the blade. A knife edge of 3 mm thick lead was placed at a distance of 67 mm from the target to produce the magnification of 7.7. The camera was protected from charged particles by a magnet and from visible light by a nickel filter of $25 \mu\text{m}$ thickness. Figure 6.7 shows the line profile across the edge. The differentiation of the fitted Fermi function yields the line spread function. The FWHM of this function gives the x-ray source size. The estimated source size was $\sim 93 \mu\text{m}$. An x-ray source size of $\sim 120 \mu\text{m}$ was estimated at an intensity of $\sim 10^{18} \text{ W cm}^{-2}$. The x-ray source size was larger than the laser focal spot size which is due to the entrance angles of the hot electrons and their lateral scattering in the solid [154]. At a lower intensity, the x-ray source size is expected to be smaller [154]. At a constant intensity of $\sim 10^{17} \text{ Wcm}^{-2}$, the source size was $\sim 90 \mu\text{m}$ and it was independent of pulse duration in range of 45–800 fs. It may be noted that the source size in our experimental conditions is ~ 4 -5 times larger than the laser focal spot size. This finding shows that there is significant pre-plasma which results in x-ray source size considerably larger than the laser spot diameter [67, 164].

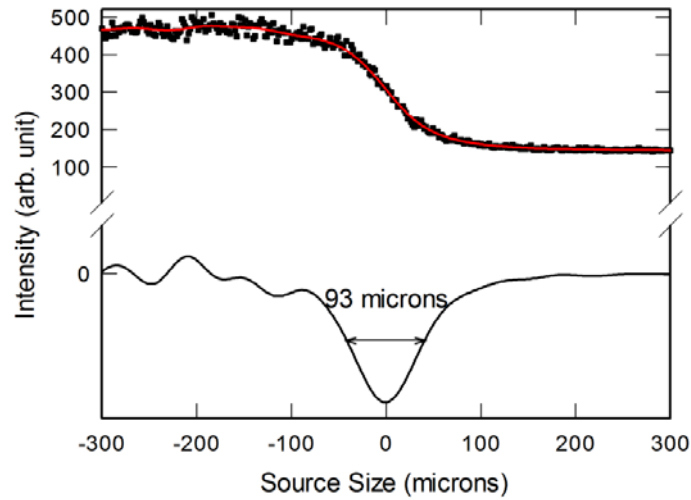


Fig. 6.7: *The line profile across the knife edge. The FWHM of the line spread function gives the x-ray source size.*

To summarize this chapter, a systematic study for the optimization of K- α line emission in photon energies between 1.3 - 8 keV has been performed. The conversion efficiency is optimized with the laser pulse duration. The optimized pulse duration of 420 fs, 350 fs and 250 fs are obtained for Ti (4.5 keV), Fe (6.4 keV) and Cu (8.05 keV) respectively. The energy conversion efficiency obtained is 3.1×10^{-5} , 2.7×10^{-5} , 1.9×10^{-5} respectively. The optimal laser intensity for maximum conversion is much higher compared with theoretical predictions due to presence of pre-formed plasma before the arrival of the ultra-short laser pulse. The x-ray source generated with longer duration pulses gives higher photon flux and will saturate at higher fluence.

Chapter 7

2ω and $\frac{3}{2}\omega$ harmonics as a diagnostic for pre-formed plasma

Existence of a pre-pulse ahead of any fs laser pulse has been a matter of concern for the study of ultra-short high intensity laser plasma interaction, especially in developing laser plasma as a source of high energy x-rays [188] and particles [25-26] (electrons, protons, ions) for potential applications in radiography [21], nuclear physics [28] etc. The driving laser used for such applications is invariably a chirp pulse amplification (CPA) based system. A typical laser pulse is usually preceded by a pedestal that is often caused by amplified spontaneous emission (ASE) in the amplifiers. Further, there are one or more pre-pulses originating from imperfect compression of the stretched pulse in the pulse compressor, leakage from pulse selector used in the laser chain. It may be noted that of these pre-pulses, the ASE pedestal is of relatively longer time duration and thus has lower plasma formation threshold, and hence contributes most to the degradation of the contrast. Therefore, this pre-pulses can lead to an uncontrolled formation of plasma that changes the initial properties of the target (such as the electron density and the electron temperature) prior to the main pulse arriving the target and hence dramatically change the main laser-plasma interaction.

In all ultra-short high intensity laser-plasma experiments, the knowledge of the target parameters is of great importance. It is necessary to know the conditions of pre-formed plasma at the time the main laser pulse hits the target. Depending on the intensity and temporal profile of pre-pulse, the pre-formed plasmas usually expand on a very short time scale, with strong gradients of density and temperature. Understanding of the pre-formed plasma characteristic is crucial for modelling the laser-plasma interaction [189]. The

conventional technique is to measure the pre-pulse level on every shot through some leaking mirror [190]. Time resolved interferometry has been used to measure the density profile of the pre-formed plasma [191]. One way to characterize the target before and during the laser-plasma interaction is the measurement of optical spectrum of the laser light scattered from solid surface. The spectrum has well defined features at frequency corresponding to twice and 3/2 times the fundamental frequency of laser (2ω and $\frac{3}{2}\omega$). The radiation arises due to different processes which occur at plasma regions of quarter critical density and near the critical density. During the interaction of 800 nm Ti: Sa laser light with the solid target, the emission of blue light (2ω) and strong green light $\frac{3}{2}\omega$ can serve as a very versatile and simple diagnostic technique to monitor the pre-formed plasma condition. Second-harmonic (2ω) and three-halved harmonic ($\frac{3}{2}\omega$) emission from a laser-produced plasma has been experimentally studied by many authors since the first observation by Bobin *et al* [192].

In chapter 6, we have described that the source size and spectral profile of K- α line generated during the intense laser matter interaction may get broadened through the inner-shell transitions in multiply charged ions present in the pre-plasma. Practical application of the K- α x-ray source necessitates *in situ* monitoring of the ultra-short high intensity laser plasma interaction conditions for controlling the K- α spectral profile. In this chapter, we present an experimental study on the generation mechanisms of the emissions at 2ω and $\frac{3}{2}\omega$ from the interaction of ultra-short, intense laser pulses and use it as a technique to monitor the conditions of pre-formed plasma for generating monochromatic K- α x-ray radiation. In particular the laser intensity, pulse duration dependence on the optical emission is studied to understand the femtosecond laser induced parametric instabilities.

7.1 General properties of optical emission spectrum

The optical emission spectrum of the plasma produced by ultra-short intense laser beam has well defined peak at wavelength corresponding to 2ω and $\frac{3}{2}\omega$ radiation [192-195]. General description of the processes responsible for 2ω and $\frac{3}{2}\omega$ emission are given in the following subsection.

7.1.1 2ω generation

The laser - matter interaction in the ultra-short pulse duration regime is characterized by a step-like density profile where the density drops from solid density to vacuum over a very small distance $L < \lambda$ (the wavelength of laser radiation). Generation of odd as well as even harmonics in such case has been explained to be due to strongly anharmonic motion of electrons across the sharp density step e.g. as in moving mirror model [196]. According to this model, the intense laser field drives a oscillation of plasma surface, which causes a periodic phase modulation of the reflected light and, hence, the emission of harmonics of the laser frequency. The sharp density gradient near the critical density surface and the laser intensity $> 10^{15} \text{ W cm}^{-2}$ are the key requirement of the efficient harmonic generation.

There is another process called the coherent wake emission (CWE), in which the integral harmonic emission can be driven by the electron plasma waves generated around the critical density by the ponderomotive force of a laser pulse [197]. CWE is a mechanism that qualitatively consists of three main steps:

i) Electrons at the plasma surface are pulled out in vacuum by the laser field, and then pushed back into the dense plasma after having gained energy from the field.

ii) These fast electrons propagating in the dense part of the plasma form ultra-short bunches, which impulsively excite plasma oscillations in their wake.

iii) In the inhomogeneous part of the plasma formed by the density gradient at the plasma vacuum interface, these collective electron oscillations radiate light at the different local plasma frequencies found in this gradient.

Since this process occurs periodically once every laser optical cycle, the spectrum of the associated light emission consists in harmonics of the laser frequency. This harmonic spectrum can extend up to the maximum up to the plasma frequency.

7.1.2 $\frac{3}{2}\omega$ generation

The production of plasmons with a frequency of about $\frac{\omega}{2}$ is the first step in the $\frac{3}{2}\omega$ generation. Two plasmon decay (TPD) and stimulated Raman scattering (SRS) instability are the main process responsible for it [29]. A combination of three plasmons or a combination of an incident or reflected laser photon with a plasmon can lead to the generation of $\frac{3}{2}\omega$ radiation. The former is a higher order process having negligible probability. The basic conservation laws of the latter coupling process are

$$\omega_{3/2} = \omega + \frac{\omega}{2}, \quad k_{3/2} = k + k_0$$

where $\omega_{3/2}$ and $k_{3/2}$ are the frequency and wave vector of the three-halves harmonic radiation.

Two plasmon decay: As described in the Chapter 1, in this instability the laser light decays resonantly into two electron plasma waves, or in quantum picture a decay of an incident laser photon into two plasmons whose frequencies are roughly half the laser frequency. The process should satisfy the frequency and phase matching conditions

$$\omega_0 = \omega_{e1} + \omega_{e2}, \quad k_0 = k_{e1} + k_{e2}$$

where ω_0 , k_0 are the frequency and wave vector of the laser light and ω_{e1} , ω_{e2} , k_{e1} and k_{e2} are the frequency and wave vector of the electron plasma wave 1 and 2.

From the dispersion of the plasma waves, this process occurs at electron densities equals to $\frac{1}{4}$ times the critical density (also called quarter critical density). The plasma waves of this instability lie with their wave vectors in the plane of the electric field of the incident light field with a non-zero component perpendicular to the wave vector of the incident light field. In inhomogeneous plasmas, the TPD threshold is determined primarily by the density gradient length near $n_c/4$ and is given by Kruer [29] as

$$I_{th} \sim 5 \times 10^{15} T_e(\text{keV}) / (L_n(\mu\text{m}) \lambda_L(\mu\text{m})),$$

where L_n is the gradient length of the electron density, T_e is the electron temperature (both evaluated near $n_c/4$), and λ_L is the laser wavelength. The electron plasma waves grow exponentially due to the instability, but this growth is limited by nonlinear processes [193, 195]. In the short pulse regime, the expected dominant saturation mechanism is the trapping and wave breaking [198]. The primary TPD plasmons are expected to undergo significant secondary scattering processes once the instability is driven above threshold and saturation sets in. This process broadens the plasma-wave spectrum in wave number and frequency space [42].

Stimulated Raman scattering (SRS): This instability is a resonant decay of the laser light into a scattered light and an electron plasma wave. It is responsible for backscattering of laser radiation [29]. The harmonic generation takes place in a plasma layer where the phase matching condition

$$\omega_0 = \omega_1 + \omega_e, \quad k_0 = k_1 + k_e$$

where ω_0 , k_0 and ω_1 , k_1 are the frequency and wave vector of the laser light and scattered electromagnetic radiation. ω_e and k_e are the frequency and wave vector of the electron plasma wave. From the above phase matching conditions it follows that SRS can take place at all densities up to quarter critical density but generates plasmons with $\frac{\omega_0}{2}$ energy that fulfills the energy conservation for $\frac{3\omega_0}{2}$ production only around $n_c/4$. The instability threshold is mostly determined by the plasma gradient scale length L and is usually much higher for SRS compared to TPD.

7.2 Description of the experiment

Experiments were carried out with femtosecond pulses of 45 fs (FWHM) duration, obtained from the Ti:sapphire laser system operating at a 10 Hz pulse repetition rate. The laser has central wavelength of 790 nm with a bandwidth of 16 ± 2 nm after the compressor as shown in Fig. 7.1. The spectrum was recorded at full laser power after the focusing lens. The dotted line shows the spectrum obtained in the single shot and solid line represents the averaged smoothed spectrum over 10 laser shot.

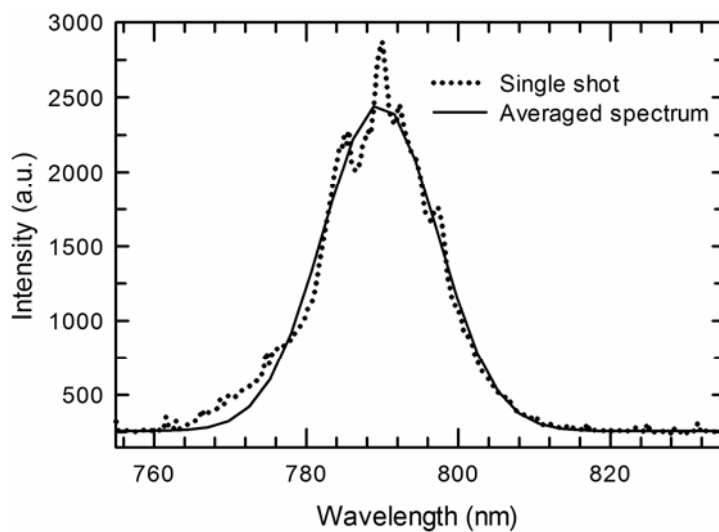


Fig. 7.1: The spectrum of laser at the chamber at full power after the focusing lens.

A schematic diagram of the experimental setup is shown in Fig. 7.2. The plasma was produced by focusing the 50 mm diameter laser beam onto a aluminium target placed at 45° (w.r. to the laser direction) using an f/8 500 mm focal length lens. The light scattered in the specular reflection direction was focussed with an f/4, 200 mm focal length lens on to a spectrograph (USB 2000, Ocean Optics). This spectrograph operates in the spectral range of 200 – 900 nm with a resolution of 0.8 nm. Coloured glass filters (Schott BG 39) were used to attenuate the strongly scattered laser light at the fundamental wavelength. The image processing and capturing was done with the indigenously developed software “Tarang”.

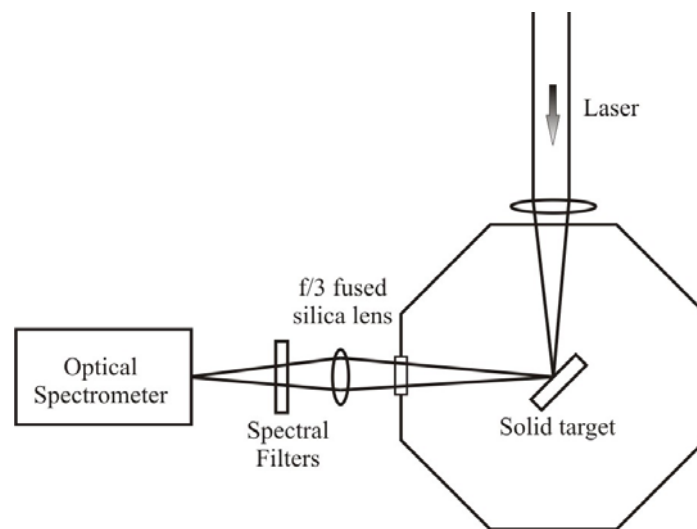


Fig. 7.2: A schematic diagram of the experimental setup.

7.3 Experimental results and analysis

Figure 7.3 shows the typical optical spectrum averaged over three laser shots. The spectrum has well defined peak at wavelength 393 nm and 522 nm corresponding to 2ω and $\frac{3}{2}\omega$ radiations respectively. The emission spectrum of the 2ω harmonic is observed to be shifted by ~ 2 nm toward the short wavelength with respect to the expected value of 395 nm. The $3/2\omega$ with central wavelength of 522 nm is strongly blue shifted by about 5 nm with respect to the expected wavelength of 527 nm. The spectral width of the $3\omega/2$ harmonic was

5 nm, whereas the expected spectral width of the radiation was ~ 10.6 nm. Observation of sharper harmonics indicates that the harmonics are not generated during full laser pulse duration because the bandwidth of harmonic is generated from laser bandwidth ($\Delta\lambda_{3/2} / \lambda_{3/2} = \Delta\lambda_L / \lambda_L$). The observed narrowing of the $\frac{3}{2}\omega$ harmonic bandwidth can be attributed to fulfilment of occasional phase-matched conditions only for the central part of the spectral distribution of the incident radiation possessing a higher intensity [198]. The small blue shift for 2ω can be attributed to the self-phase modulation of the incident beam. Ganeev *et al* [198] have also reported a small blue shift of second harmonic and they attribute it to the temporally unstable Doppler shift of the spectrum caused by an unstable motion of the critical surface of the plasma.

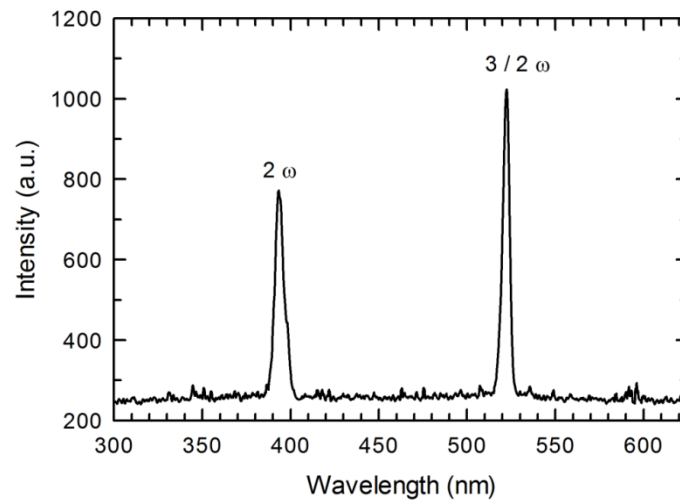


Fig.7.3: Harmonic spectrum recorded at a laser intensity of $8.8 \times 10^{16} \text{ W cm}^{-2}$.

Figure 7.4 shows the optical spectrum for three different laser intensities. Here, the laser intensity was varied by changing the laser energy, while keeping the pulse duration and the focal spot fixed. At a low intensity of $8.2 \times 10^{16} \text{ W cm}^{-2}$, the spectrum shows 2ω emission at a wavelength of 398 nm. As the intensity is increased to $3.6 \times 10^{17} \text{ W cm}^{-2}$, $\frac{3}{2}\omega$ emission appears at wavelength of 521 nm, along with the 2ω emission at 392 nm. On further

increasing the intensity to $1.2 \times 10^{18} \text{ W cm}^{-2}$, only a more blue shifted $\frac{3}{2}\omega$ emission (centred at 515 nm) is seen.

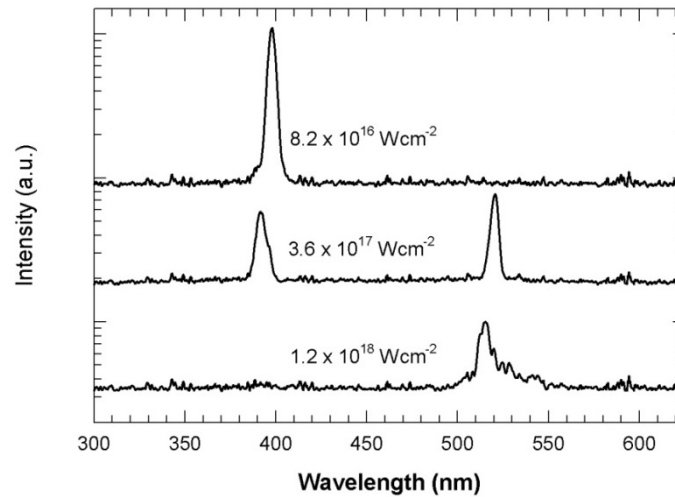


Fig. 7.4: Harmonic spectrum recorded for different intensity of laser pulse.

Harmonic emission spectrum was measured in the direction of specular reflection for different values of laser intensity ranging from $3 \times 10^{15} - 10^{18} \text{ W cm}^{-2}$. As the intensity was increased, a broader $3/2$ harmonic emission was seen. This may be due to high electron temperature at higher intensity which leads to an electron density range of generation of TPD instability or threshold intensity for instability is reached in temporal wings of the laser pulse [194].

The $\frac{3}{2}\omega$ emission depends on the plasma density scale length. The growth rate of the two plasmon decay instability in an inhomogeneous plasma increases with the plasma scale length at the quarter critical density. It appears that the foot of the laser pulse, tens of ps before the peak of the pulse, has sufficient intensity to create plasma (pre-plasma), with which the main pulse interacts, instead of interacting with the solid target. As the laser intensity is increased, the plasma formation takes place at an earlier time, leading to a longer

scale length pre-plasma. Since the scale length of the pre-plasma increases with increasing laser intensity, there is an increase in the $\frac{3}{2}\omega$ emission intensity. On the other hand, an increase in the scale length means the laser beam gets reflected at a larger distance from the critical density, leading to reduced excitation of the plasma wave at the critical density (by the evanescent wave), resulting in lower second harmonic generation at the critical density. Hence one gets reduction in second harmonic generation with increase in the laser intensity.

Figure 7.5 shows the scattered light spectrum with the laser pulse duration, in a range of 45 – 800 fs, for a fixed fluence of $1.6 \times 10^4 \text{ J cm}^{-2}$ (corresponding to $3.6 \times 10^{17} \text{ Wcm}^{-2}$ for the 45 fs pulse). The laser pulse duration is varied by changing the separation between the two gratings in the pulse compressor, with no change in the laser pulse energy. It can be observed that the 2ω signal increases on decreasing laser pulse duration whereas the $\frac{3}{2}\omega$ shows a blue shift.

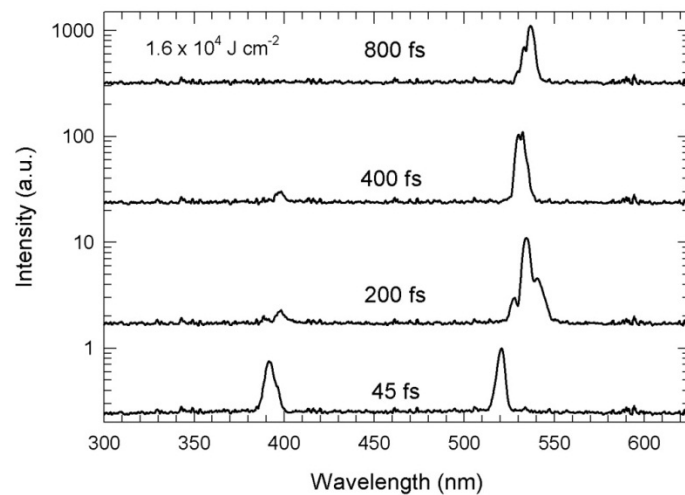


Fig. 7.5: Harmonic spectrum recorded for different chirp of laser pulse.

Figure 7.6 shows the second harmonic, and the 3/2-harmonic radiation intensity as a function of the pump laser pulse duration for a constant fluence of $1.8 \times 10^4 \text{ J cm}^{-2}$. The

second harmonic signal intensity decreases with increasing laser pulse duration. It should be noted that increasing the pulse duration means increasing the density scale length ($c_s\tau$). Hence, with increasing pulse duration, the second harmonic intensity reduces due to increasing distance between the reflecting surface and the critical density surface. On the other hand, for the $3/2\omega$ emission, the increase in scale length means a longer region for the two plasmon decay instability to grow. The TPD instability grows exponentially for time less than the time when saturation is reached from the initial thermal noise [42]. With increasing pulse duration collisional damping increases and reduces the growth rate of the instability and $3/2$ signal. Therefore, the intensity of $\frac{3}{2}\omega$ signal has a maximum at ~ 400 fs and thereafter decreases.

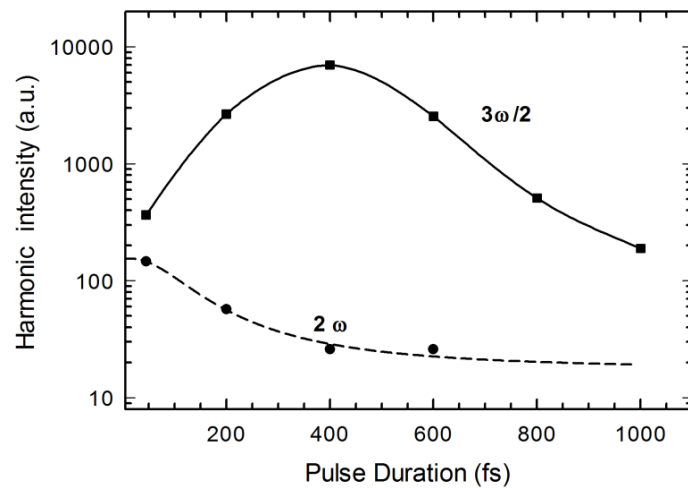


Fig. 7.6: The second harmonic, and the $3/2$ -harmonic radiation intensity as a function of the pump laser pulse duration for a constant fluence of $1.8 \times 10^4 \text{ J cm}^{-2}$.

The $\frac{3}{2}\omega$ and 2ω intensity from as a function of pump laser energy for a pulse duration of 400 fs is shown in Fig. 7.7. The data can be represented by a power law of the form $E_H \propto E_L^\alpha$ where the intensity scaling exponent α is for 2ω and $\frac{3}{2}\omega$ radiation is 1.2 and 2.4,

respectively. The mechanisms of 2ω and $\frac{3}{2}\omega$ generation in plasmas produced from ultra-short laser irradiated solid surfaces are needed to consider in order to explain the observed scaling laws of harmonic with laser energy. The second harmonic emission due to wave coupling at critical density or anharmonic motion of electrons across a steep density gradient of the surface plasma is expected to give energy scaling exponent of 2 and 1, respectively [199]. The energy scaling exponent of 1.2 lies between the scaling exponents predicted by two mechanisms. The faster energy scaling exponent for $\frac{3}{2}\omega$ is due to dependence of two plasmon decay instability on density scale length at quarter critical density [194]. With increasing laser energy, the production of a long scale length underdense plasma region is either due to increased pre-pulse or sufficient intensity in the temporal wings of the pulse increases the growth rate of $\frac{3}{2}\omega$ signal.

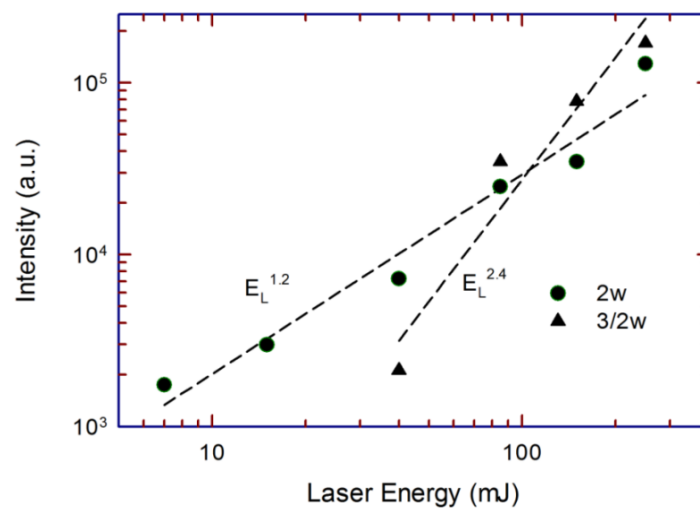


Fig. 7.7: Intensity scaling of 2ω and $\frac{3}{2}\omega$.

A study of the specularly reflected $\frac{3}{2}\omega$ and 2ω harmonic from aluminium solid targets irradiated with high intensity femtosecond laser pulses. Measurements of the scaling

laws of harmonic intensity with laser energy is explained by considering mechanisms of 2ω and $\frac{3}{2}\omega$ generation in plasmas produced from ultra-short laser irradiated solid surfaces. The measurement of $\frac{3}{2}\omega$ for different laser pulse duration showed a maximum yield at laser pulse duration of 400 fs whereas the intensity of 2ω radiation decreases monotonically with increasing laser pulse duration. The observations were correlated with the x-ray emission measurement from the plasma to understand the role of pre-formed plasma in controlling the spectral profile of K- α line radiation.

7.4 Conversion efficiency and spectral broadening of the K- α line emitted from planar titanium targets

A study of the conversion efficiency and line shape of the K- α x-ray line radiation from a planar titanium target irradiated by an ultra-short laser pulse is performed. The conversion efficiency and spectral broadening is studied as a function of laser intensity ($5 \times 10^{16} - 10^{18} \text{ W cm}^{-2}$), laser pulse duration (45 fs – 800 fs), and laser fluence ($2 \times 10^3 - 4.2 \times 10^4 \text{ J cm}^{-2}$). The study was aimed at observing the correlation between K- α x-ray line emission characteristics and optical spectrum of the laser light scattered from solid surface.

Figure 7.8 shows the inner-shell x-ray emission spectrum of titanium plasma at a laser intensity of $\sim 7.1 \times 10^{16} \text{ W cm}^{-2}$ at $\tau_L = 45 \text{ fs}$. The identified lines are K- α transition at 4510.8 eV and K- β transition at 4931.8 eV. The spectrum in the inset of the Fig.7.8 shows clearly resolved two fine-structure components of K- α viz. K- α_1 (4510.8 eV) and K- α_2 (4504.9 eV). The intensity ratio of the K- α_2 to K- α_1 components is measured to be ≈ 0.54 , which is in good agreement with the theoretically expected ratio of 0.5. The spectral width (FWHM) of

the $K\text{-}\alpha_1$ line radiation is noted to be ~ 4.1 eV. A gross estimate of the actual line width of ~ 1.8 eV is obtained, from the deconvolution of the effect of the instrumental broadening which is close to the natural line width of the Ti- $K\text{-}\alpha_1$ radiation.

The x-ray spectra were recorded as a function of laser intensity in a range of 5×10^{16} - 10^{18} W cm^{-2} . The laser intensity was varied by changing laser energy, keeping pulse duration and laser focus diameter constant. No shift in the mean x-ray energy of the $K\text{-}\alpha$ transition with the laser intensity was observed within the estimated errors of the data (~ 0.4 eV). The intensity of the $K\text{-}\beta$ radiation on detector is small, particularly at low energy, for commenting on its spectral shift. In a similar range of laser intensity, Senegebusch *et al* [200] observed a small red shift of average line position of the chlorine $K\text{-}\alpha$ and $K\text{-}\beta$ lines. The shift was less than 0.5 eV for $K\text{-}\alpha$ and less than 5 eV for the $K\text{-}\beta$ transition, and it has been assigned to the free electron screening and ionization effect.

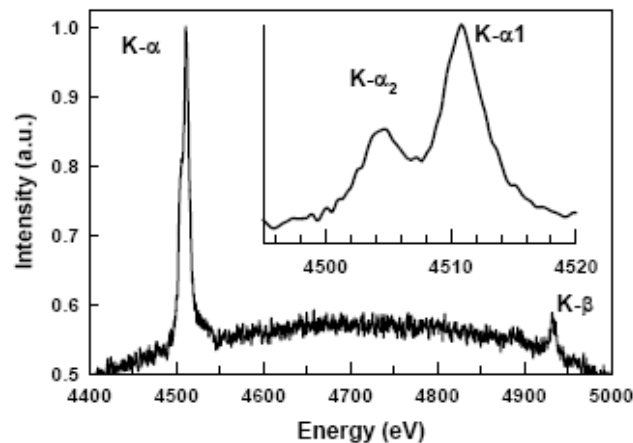


Fig. 7.8 : Inner-shell x-ray emission spectrum from laser irradiated titanium target. Inset shows the spectrally resolved $K\text{-}\alpha_1$ and $K\text{-}\alpha_2$ fine structure components.

On the other hand, the spectral width of the $K\text{-}\alpha$ radiation increased with increasing the laser intensity. The relative broadening of the source size with the laser intensity may contribute to the observed behaviour. The corresponding deconvoluted spectral width for 45

fs pulse duration as function of laser intensity is shown in Fig. 7.9. The dashed line represents the natural line width of the K- α_1 transition. It can be seen that the spectral width increases from 1.8 eV to 7.6 eV as the laser intensity increases from 7.1×10^{16} W cm $^{-2}$ to 8.5×10^{17} W cm $^{-2}$.

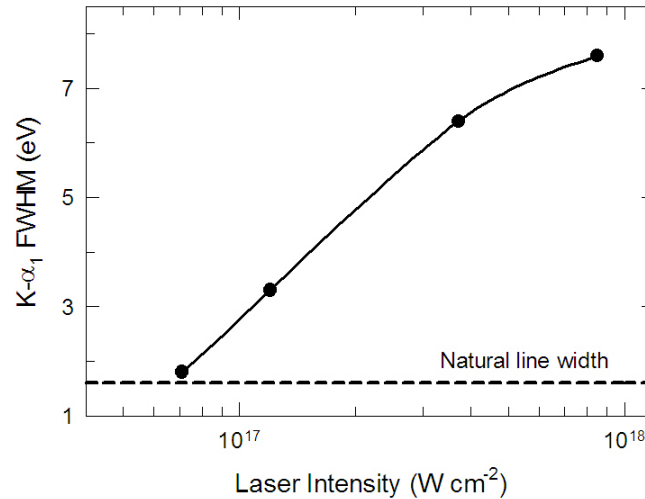


Fig. 7.9 : *The deconvoluted spectral width (FWHM) of the K- α_1 line as function of the laser intensity, for a fixed pulse duration of 45 fs. The curve is drawn to aid the eye. The dashed line represents the natural line width. The error in spectral width measurement is estimated to be less than 10 %.*

Figure 7.10 shows the K- α line spectrum at two different laser intensities of 7.8×10^{16} W cm $^{-2}$ and 8.5×10^{17} W cm $^{-2}$, for the same laser pulse duration of 45 fs. The two spectra are normalized to the same peak value, to facilitate visual comparison. The FWHM of the K- α_1 component increases from ~ 4.2 eV at 7.8×10^{16} W cm $^{-2}$ to ~ 8.8 eV at 8.5×10^{17} W cm $^{-2}$. Further, it is observed from Fig.7.10 that the spectral broadening for the K- α_1 and K- α_2 components is predominantly on the higher energy side. The observed spectral broadening of the K- α line emission can be due to the blending of K- α radiation from Ti $^{4+}$ to Ti $^{7+}$ ions [201-204] with the radiation from cold atom. This indicates that the solid bulk target is heated [201] to a temperature of 20 – 50 eV.

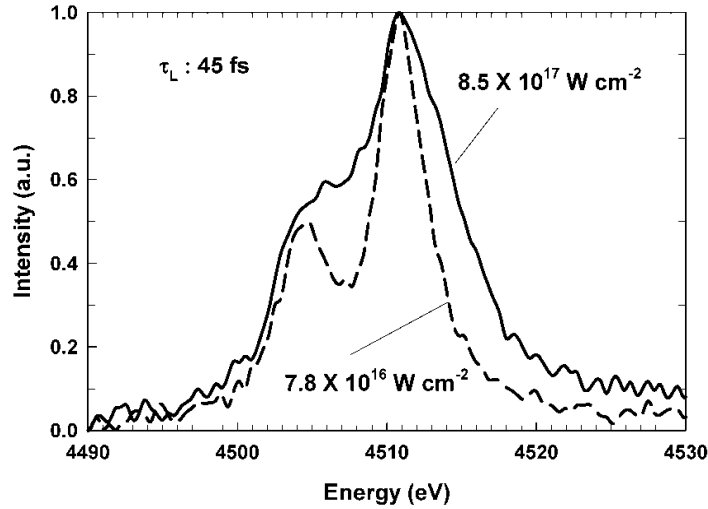


Fig. 7.10 : Normalized $K\text{-}\alpha$ line radiation profile at two different laser intensities of $7.8 \times 10^{16} \text{ W cm}^{-2}$ and $8.5 \times 10^{17} \text{ W cm}^{-2}$, at a fixed laser pulse duration of 45 fs.

The hot electrons generated in laser matter interaction can heat the bulk target to such a temperature to produce solid density plasma behind the hot surface plasma [201, 205-206]. The hot electrons generated by the resonance absorption process are accelerated down the density gradient. The resultant electric field generated along the density gradient pulls back the electrons into the target. In the presence of self generated magnetic fields, these electrons undergo a rapid lateral acceleration by the $\mathbf{v} \times \mathbf{B}$ force. The hot electron would deposit their energy through collisions to heat the bulk target to such temperature to produce solid density plasma behind the hot surface plasma [201, 205-206]. In this way, the hot electrons temperature reduces by collisional cooling and equilibrates with the bulk solid temperature. It may be noted that the collisional cooling rates [207] are lower at higher temperature, since the collision frequency scales as $T^{-3/2}$. In addition, the hot electrons also cool adiabatically due to expansion, particularly in the initial phase, when their temperature is high and limits the rise in temperature [207]. However, the adiabatic cooling of the hot electrons is expected to be more important in the case [207] of reduced mass targets irradiated at intensities $\sim 10^{19} \text{ W cm}^{-2}$ than in the case of a thick solid target irradiated at sub-relativistic intensities.

In the present experimental condition, one may expect that the increase in laser intensity would lead to more broadening. Since at higher laser intensity, the hot electron temperature is expected to high and this will induce heating of solid density plasma to higher temperature having relatively large fraction of highly charged titanium ions [200, 203- 204] (with a charge more than + 7). The inner-shell transition in these ions will be shifted more towards high energy side and eventually their blending with the transition in cold atom would increase the line bandwidth. It may be noted that the appearance of strong inner-shell transitions from ionized atoms will lead to an increase in the integrated inner-shell x-ray conversion efficiency [208] as well as broaden the line profile on the higher energy side. This is advantageous for the experiments that require an x-ray probe bandwidth of the order of ten eV. However, this may be detrimental for the applications which require an x-ray probe bandwidth much less than ten eV.

To bring out the role of alternative mechanism for observed broadening of K- α line, the spectra was recorded for different laser irradiation parameters. Figure 7.11 shows the K- α line spectrum at two different laser pulse durations of 45 fs and 600 fs, for a fixed fluence of $4.2 \times 10^4 \text{ J cm}^{-2}$. There is no significant difference in the spectral profiles. Figure 7.12 shows the dependence of the spectral width on the laser pulse duration, at a fixed fluence of $4.2 \times 10^4 \text{ J cm}^{-2}$. The spectral width did not change much with the pulse duration. For instance, at the two laser pulse durations of 45 fs and 600 fs, the spectral width were $\sim 7.8 \text{ eV}$ and $\sim 8.2 \text{ eV}$ respectively, even though the laser intensity for $\tau_L = 45 \text{ fs}$ was about 13 times higher than that for the longer pulse irradiation. As stated earlier, the heating of bulk solid by the hot electrons is expected to be more efficient for high intensity femtosecond laser matter interaction [206]. The similar spectral profile observed at constant fluence for laser pulse duration from 45 fs to 800 fs indicates that in the present experimental conditions laser intensity alone do not control the heating of bulk solid density plasma. In other possible scenario, similar bulk temperature at longer pulse duration (lower intensity) may be attributed

to the efficient direct laser heating of bulk solid due to increased absorption of laser light. Further, for sub-picoseconds laser pulse, the plasma scale length may be optimal for transferring large fraction of laser energy to hot electrons through resonance absorption mechanism. This can also heat the cold titanium to higher bulk temperatures at solid density. Although, at constant fluence the photon flux and spectral profile are similar but the x-ray pulse duration is expected to be larger for longer duration laser pulse irradiation

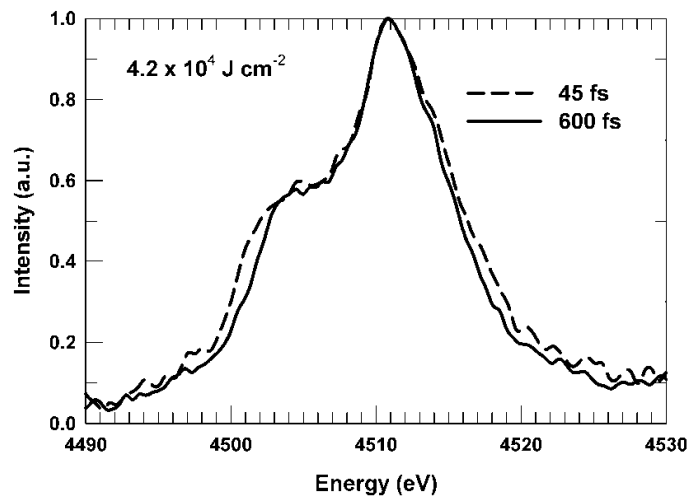


Fig. 7.11 : Normalized $K\text{-}\alpha$ line radiation profile at two different pulse durations of 45 fs and 600 fs, at a fixed fluence of $4.2 \times 10^4 \text{ J cm}^{-2}$.

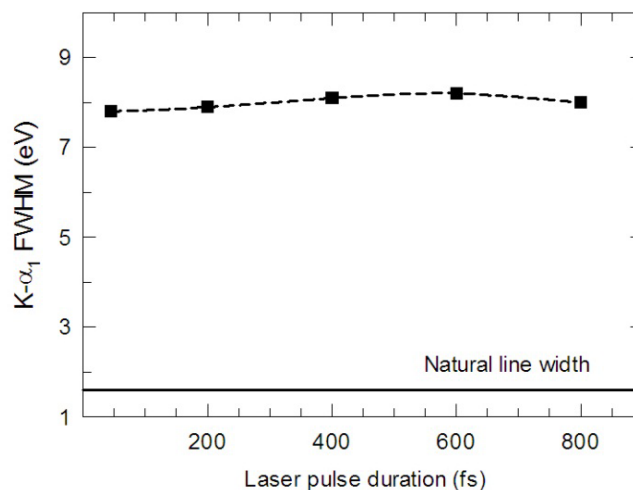


Fig. 7.12 : The dependence of the deconvoluted spectral width of the $K\text{-}\alpha_1$ line on the laser pulse duration, at a fixed fluence of $4.2 \times 10^4 \text{ J cm}^{-2}$. The curve is drawn to aid the eye. The solid line represents the natural line width of the $K\text{-}\alpha_1$ line. The error in spectral width measurement is estimated to be less than 10 %.

Alternatively, broadening may also be due to the ions present in the long-scale length plasma produced in front of the target by pre-pulse [200]. It is well known that ultra-short pulse laser systems based on chirped pulse amplification (CPA) are invariably associated with an ASE pre-pulse prior to the main pulse. In the subsequent text, we shall refer to the ASE pre-pulse as the "pre-pulse". The pre-plasma formed by the pre-pulse expands before the arrival of the main laser pulse. In our experiment, the pre-pulse intensity was $\sim 10^{11}$ W cm $^{-2}$, which can produce plasma of few tens of eV temperature, with multiply charged titanium ions.

To clearly bring out the role of laser fluence on spectral broadening spectrum was recorded for fixed laser intensity. Figure 7.13 shows the inner-shell x-ray emission spectra for two different laser fluences of 3.5×10^3 J cm $^{-2}$ (45 fs) and 4.2×10^4 J cm $^{-2}$ (600 fs), at a fixed laser intensity of $\sim (7.4 \pm 0.4) \times 10^{16}$ W cm $^{-2}$. The spectral width of the K- α_1 component for the smaller laser fluence of 3.5×10^3 J cm $^{-2}$ is ~ 4.2 eV, which is much smaller in comparison to the spectral width of ~ 9.1 eV observed for the higher laser fluence of 4.2×10^4 J cm $^{-2}$. These observations indicate that the spectral width of the K- α radiation is closely linked to the laser fluence rather than the laser intensity.

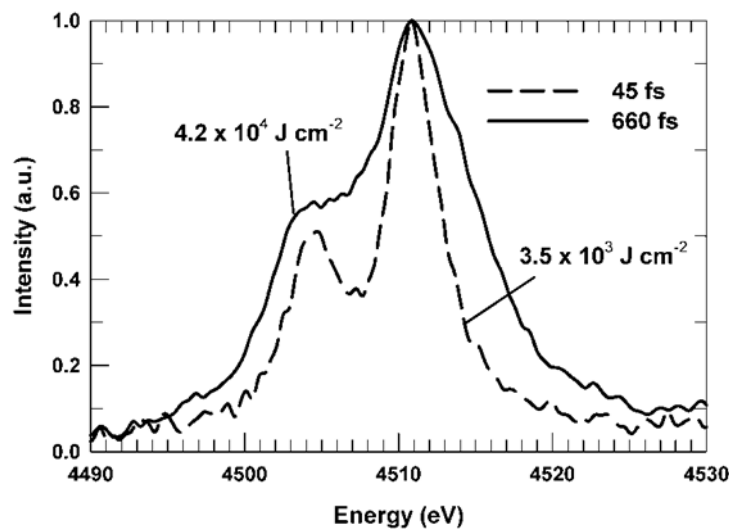


Fig. 7.13: Normalized K- α line radiation profile at two different laser fluences of 3.5×10^3 J cm $^{-2}$ (45 fs) and 4.2×10^4 J cm $^{-2}$ (600 fs), at a fixed laser intensity of $\sim 7.4 \times 10^{16}$ W cm $^{-2}$.

The change in laser parameters also changes the pre-pulse characteristics which in turn affects the onset and temperature of the pre-plasma. The pre-pulse intensity increases with increasing laser intensity (for a fixed pulse duration), resulting in increasingly higher ionic species in the pre-plasma. K- α emission due to hot electrons propagating through this plasma resulting in an increase in spectral broadening of the K- α line seen in Fig.7.10. However, when the experiment was performed at constant fluence at different pulse durations, no change was observed in the spectral width of the K- α line radiation (Fig.7.11). Since the change in pulse duration of the ultra-short pulse was accomplished by adjustment of the separation between compressor gratings, the ns pre-pulse characteristics is largely unaffected. Therefore, at a fixed laser fluence, for different laser pulse durations, there is no change in nanosecond pre-pulse intensity and correspondingly in the characteristics of the pre-plasma formed. This is consistent with no change in the spectral width of the K- α line as seen in Fig.7.11.

Finally, at a fixed laser intensity, the spectral width was higher for the larger fluence at longer laser pulse duration in comparison to the smaller fluence at shorter pulse duration (Fig.7.13). This is because, to get the same intensity at longer pulse duration, the laser pulse has to be amplified to a higher energy, resulting in a corresponding increase in the pre-pulse energy (i.e. higher pre-pulse intensity). So a target irradiated at higher pre-pulse intensity (for the larger fluence) results in an increased creation of higher ionic species which contribute higher frequency components to the K- α radiation line profile.

It is noted that the spectral profile is largely determined by the pre-pulse and direct laser heating of bulk solid. Therefore, the laser irradiation parameters has to be chosen to minimize both pre-pulse and direct laser heating to achieve to achieve minimum spectral width of the K- α radiation. This can be accomplished simply by depositing a thin film of suitable material on the target [201, 204]. However, if thick enough, it will affect the x-ray conversion

efficiency as reported by Kritcher *et al* [209]. This may be due to the fact that the hot electrons must travel further into the target before they can cause K-shell ionization, and a significant fraction may get absorbed with the increasing coating thickness [209].

To summarize the chapter, the spectral width of the K- α radiation has been studied as a function of the laser intensity, laser fluence, and pulse duration. It is observed to increase with increase in the laser intensity. At constant fluence, there is no significant difference in their spectral profiles with increasing laser pulse duration. The optical spectrum is also measured for the above laser intensity and pulse duration parameters. The spectrum has well defined peaks at wavelengths corresponding to 2ω and $3/2\omega$ radiation. The spectral features vary with the laser intensity and show increasing blue shift with increasing laser intensity. At constant laser fluence, there is no significant difference in the $3/2\omega$ radiation with increase in the laser pulse duration. This shows that the spectral broadening of K- α x-ray line is strongly correlated with the optical spectrum of the light scattered from a solid surface irradiated by laser pulses. The K- α radiation has smallest line width when interaction conditions are such that only 2ω emission can be seen. On the other hand, maximum broadening corresponds to presence of only $3/2\omega$. The generation of 2ω and $3/2\omega$ radiation depends mainly on the density scale length of plasma created by pre-pulse. A comparison of line shape of K- α x-ray radiation with optical measurements indicates that inner-shell transitions in the multiply charged titanium ions in the low temperature plasma produced by the pre-pulse, have a strong contribution in the observed spectral broadening. The study brings out the role of pre-pulse in spectral broadening K- α line emission and suggests a simple method for controlling the source properties.

Chapter 8

Time resolved x-ray diffraction studies using K- α radiation

Time resolved x-ray diffraction (TXRD) measurements for studying the dynamics in solids have evoked considerable interest in the recent years [10, 72-77, 210]. In particular, this technique has been used for studying the lattice response of shocked crystals for a variety of research investigations such as phase transition [6,211], strain propagation [210, 212-213] etc. This technique provides the time resolved information on the lattice level, which is important for understanding the mechanisms governing the lattice response and the structural changes under shock propagation [213-215] which cannot be retrieved from conventional measurements. The origin of the shock wave is the ablation of the solid surface irradiated by focussing a laser pulse of short duration (sub-nanosecond) at intensity $\geq 10^9$ W cm⁻² on the sample. The absorption of the laser energy at the sample surface generates plasma, which while expanding outwards drives a shock wave into the sample. Many theoretical and experimental investigations have indicated that the induced shock pressure is related to the laser and target parameters [216].

The generated shock wave has a profile which changes rapidly with propagation distance [217]. The propagation of the shock wave inside the crystal changes the inter-planar spacing, leading to shift or broadening of the diffracted Bragg peak [215,218-220]. Thus, time resolved monitoring of the rocking curve evolution provides direct insight of the lattice response to the external / transient strain propagation inside the bulk material.

TXRD experiments are usually carried out utilizing pump-probe setup, wherein an ultra-short duration optical pump laser synchronized with an x-ray probe is used to perturb the sample. The x-ray probe pulse can be synchrotron radiation [9, 11] or high brightness x-ray free electron laser [9] from a large scale central facility. On the other hand, a small scale

laboratory based laser plasma x-ray source offers jitter free (between the laser pump and the x-ray probe) x-ray pulses of sub-picosecond duration, with moderate brightness. In a typical TXRD setup using laser plasma x-ray source, a major part of the laser beam energy is focussed on to a solid target to generate an efficient, high brightness, sub-picosecond x-ray source of K- α radiation. The K- α line radiation is used as a monochromatic x-ray probe for probing the transient structural modifications in a crystalline sample, induced by the remaining fraction of the laser beam (referred to as the pump laser). The rocking curve widths of the sample are recorded for different time delays between the pump and the probe pulse. Mostly, the experiment is performed in Bragg geometry and the dynamics of the lattice deformation is studied from the shift / broadening of the diffracted x-ray peak and the change in the reflectivity of the sample.

The recorded high resolution x-ray diffraction spectrum in such a setup is the integral of the diffraction from the lattice planes along the x-ray penetration depth in the sample, having contribution of both shocked and unshocked lattices. The studies reported earlier for strain - depth analysis utilizing TXRD setup observed the x-ray diffraction pattern for a particular photon energy. However, this method only gives information about the characteristics of the sample averaged over the penetration depth for that photon energy. For instance, the studies published in refs 215, 219 have used TXRD to investigate the strain – depth profile induced in silicon crystal under pulsed-laser irradiation, using characteristic K- α lines of Cu and Fe respectively as the probe x-ray pulse. In this work, the use of x-ray probe of different photon energies (6 – 8 keV) is shown to yield information about the strain over a greater crystal depth for similar shock wave propagation. The simplest approach of depth analysis is to record the x-ray diffraction pattern using the probing x-rays of different photon energies. The earlier studies [215, 219] have been extended here to bring out the role of depth of penetration of the probe x-rays by using characteristic K- α x-ray lines of three different target materials (titanium, iron, and copper) as the probe, whereas the irradiation parameters

of the laser used to compress the sample are same. The use of x-ray probe of different photon energies yields information about the strain over a greater crystal depth for similar shock wave propagation. Such measurements are also of interest for shock wave propagation studies, where the x-rays are interacting with the shocked as well as the undistorted crystal (at longer depth). It is useful for better understanding of the x-ray diffraction and for refining analytical approach for modelling the data.

The work presented in this chapter is focussed on the lattice modification by shock wave propagation in silicon crystal under laser excitation. The origin of the shock wave and x-ray diffraction are described in section 8.1. The description of the experiment is given in section 8.2. Section 8.3 describes the studies on shock wave propagation in silicon crystal under laser excitation, probing of strain propagation in laser shocked crystal with K- α x-ray probe of different photon energies and measurements on deformation in laser irradiated silicon crystal.

8.1 X-ray diffraction from compressed sample

Most of our knowledge on the structures of crystal at the atomic length scale originates from x-ray-diffraction experiments. In this method, the periodic structure of crystal causes a beam of x-rays to diffract in specific directions. The angles and intensities of these diffracted beams depend of the density of electrons within the crystal and the angle/s subtended with the crystal plane/s. The measurement gives the interplanar spacing/s as well as information about any disorder present in the crystal structure.

A schematic diagram of the basic concept of Bragg reflection from the crystal planes is shown in the Fig. 8.1. Bragg diffraction occurs when electromagnetic radiation or subatomic particle waves with wavelength comparable to atomic spacing, incident upon a crystalline sample, are scattered in a specular fashion by the atomic planes in the system, and undergo constructive interference in accordance to the Bragg's law. For a crystalline solid, the

waves are scattered from lattice planes separated by the interplanar distance d . Where the scattered waves interfere constructively, they remain in phase since the path length of each wave is equal to an integral multiple of the wavelength. The path difference between two waves undergoing constructive interference is given by $2d\sin\theta$, where θ is the angle between the x-rays and the crystal plane. This leads to Bragg's law $2d(hkl) \sin \theta = n\lambda$, which describes the condition for constructive interference from successive crystallographic planes (h , k , and l , as given in Miller notation) of the crystalline lattice. Here 'd' is the separation between parallel reflecting planes of the crystal, n is the order of reflection ($n=1,2,3\dots$), θ is the Bragg angle. Moreover, the condition that the angle of incidence equals the angle of reflection should also be satisfied.

A diffraction pattern is obtained by measuring the intensity of scattered waves as a function of the scattering angle. Very strong intensities known as Bragg peaks are obtained in the diffraction pattern when scattered waves satisfy the Bragg condition. It should be taken into account that if only two planes of atoms were diffracting, as shown in the pictures, then the transition from constructive to destructive interference would be gradual as the angle is varied. However, since many atomic planes are interfering in real materials, they result in very sharp peaks surrounded by mostly destructive interference.

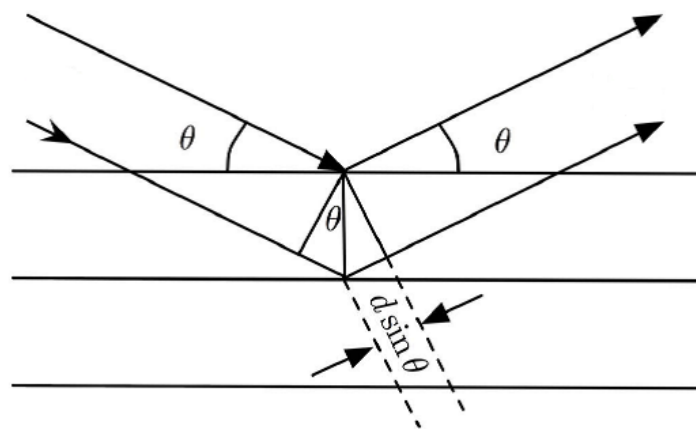


Fig. 8.1: A schematic diagram of the basic concept of Bragg reflection from the crystal planes.

When a polychromatic parallel beam of x-rays is incident on a crystal at an angle θ_0 , x-rays of wavelength $\lambda_0 = 2d \sin \theta_0$ and its sub harmonics i.e. $\lambda_0/2, \lambda_0/3, \dots$ etc. are reflected. On the other hand, when a diverging polychromatic beam is incident on the crystal, subtending a certain range of angles, then the x-rays of different wavelengths, incident at appropriate angles from maximum of θ_1 and θ_2 satisfying the Bragg conditions are reflected as shown in Fig. 8.2. For the latter case, the spectral range and spectral resolution depend upon the crystal used ($2d$ as well as size), the distance between the source and the detector (via crystal), and the orientation of the detector with respect to the x-rays incident on it.

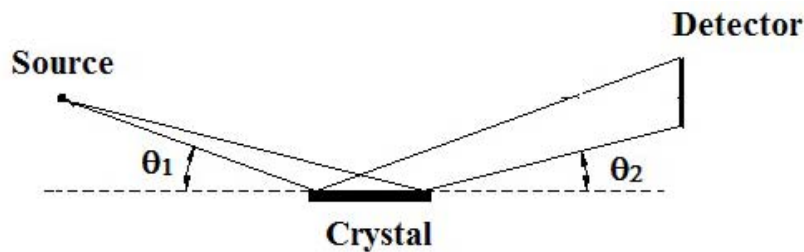


Fig. 8.2: *Diverging polychromatic beam incident on the crystal, subtending a certain range of angles, then the x-rays of different wavelengths satisfying Bragg condition is recorded on detector.*

The origin of the shock wave is the ablation of the solid surface irradiated by focusing a laser pulse of short duration (sub-nanosecond) at intensity $\geq 10^9 \text{ W cm}^{-2}$ on the sample. The absorption of the laser energy at the sample surface generates plasma, which while expanding outwards drives a shock wave into the sample. Many theoretical and experimental investigations have indicated that the induced shock pressure is related to the laser and target parameters [216]. The generated shock wave has a profile which changes rapidly with propagation distance [217]. The propagation of the shock wave inside the crystal changes the inter-planar spacing. This can be probed by simple Bragg or Laue diffraction showing the shift or broadening of the diffracted Bragg peak [215,218-220]. Time resolved x-ray diffraction measurement monitoring of the rocking curve evolution provides direct insight of the lattice response to the external / transient strain propagation inside the bulk material.

The diffraction of the x-rays takes place in a finite volume inside the crystal and the observed diffraction pattern is a weighted sum of the diffraction data from different depths over which the analysis is performed [4]. The schematic diagram shown in Fig. 8.3 shows the basic concept of diffraction from the lattices along the x-ray penetration depth in the sample, having contribution of both shocked and unshocked lattices. When the lattice spacing is such that the Bragg condition is satisfied at a particular angle, the x-ray beam is diffracted from the sample within a thin layer of the crystal. The different layers, strained to different extents under the influence of the compression wave, will diffract at slightly different angles leading to the broadening. On the other hand, if uniform compression is applied than a shift of the Bragg angle will occur. Besides this, thermal wave propagation occurs in a long laser pulse excitation, which leads to the expansion of lattice and diffraction occurs at a lower Bragg angle. The x-rays can penetrate in a given crystal up a distance dependent on the absorption coefficient, which in turn depends on the x-ray photon energy and the degree of crystal perfection [221]. The x-ray penetration depth is much smaller for perfect crystals, the diffraction in this case is usually modelled using dynamical diffraction theory [222, 223]. On the other hand, the kinematical approximation is used for modelling the x-ray diffraction from an imperfect crystal.

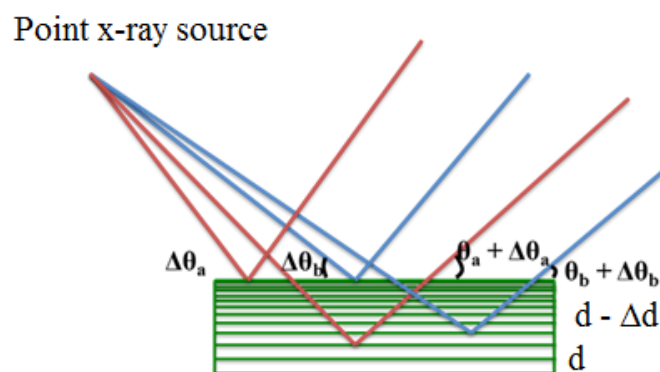


Fig. 8.3: Basic concept of diffraction from the lattices along the x-ray penetration depth in the sample, having contribution of both shocked and unshocked lattices.

In a typical TXRD setup using laser plasma x-ray source, a major part of the laser beam energy is focussed on to a solid target to generate an efficient, high brightness, sub-

picosecond x-ray source of K- α radiation. The K- α line radiation is used as a monochromatic x-ray probe for probing the transient structural modifications in a crystalline sample, induced by the remaining fraction of the laser beam (referred to as the pump laser). The rocking curves of the sample are recorded for different time delays between the pump and the probe pulse. Mostly, the experiment is performed in Bragg geometry and the dynamics of the lattice deformation is studied from the shift / broadening of the diffracted x-ray peak and the change in reflectivity of the sample.

8.2 Description of the experiment

The experiments were conducted using the 10 TW Ti:sapphire laser system. This system (described in Chapter 2) delivers laser pulses at a wavelength of 800 nm. A schematic of the experimental setup is shown in Fig.8.4. The K- α x-ray probe was generated by focusing the 45 fs laser pulses onto a solid target (titanium, iron or copper). The x-ray emission was optimized for its monochromaticity and conversion efficiency by optimizing the laser irradiation parameters [159]. It has been observed that the pre-pulse is a crucial parameter determining both, the conversion efficiency and the monochromaticity [159]. The intensity contrast ratio of the pre-pulses present on nanosecond time scale was measured using a fast photodiode and a digital storage oscilloscope (500 MHz bandwidth). The contrast ratio of the pre-pulse arising due to amplified spontaneous emission (ASE) was about 10^6 . The temporal width of the x-ray pulse from the plasma generated under similar laser irradiation is expected to be of several hundred femtoseconds [74]. The laser irradiation conditions such as energy and angular fluctuations were monitored rigorously to achieve monochromatic and high brightness K- α x-ray radiation. The x-ray conversion i.e. the number of x-ray photons produced versus the number of incoming laser photons are given in Chapter 6.

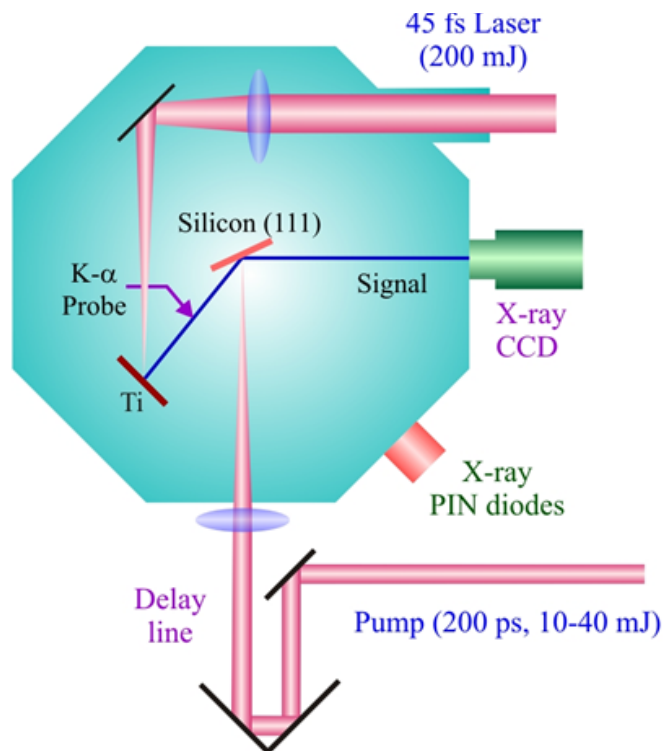


Fig. 8.4: A schematic diagram of the experimental setup.

A part of the stretched (800 nm, 200 ps) pulse was used to irradiate a 500 μm thick flat Si (111) crystal sample ($2d = 6.271 \text{ \AA}$) at an intensity of 6 GW/cm^2 . The laser beam illuminating the surface of the sample had a spot size of 2 mm diameter. The ablation depth in the crystal is expected to be $< 200 \text{ nm}$. The width of the sample participating in the Bragg reflection is $\sim 90 \mu\text{m}$ (in the direction of dispersion). The laser spot size on the sample was approximately twenty two times larger than the x-ray spot size, to ensure probing of a homogeneously excited area. The time delay between the 200 ps pump laser pulse and the probing x-ray pulse was adjusted by an optical delay line. A positive delay here means the pump laser pulse is leading the probe x-ray pulse in time. The zero time was taken as the point where the diffraction signal starts to change. The diffracted x-ray spectrum was recorded on an x-ray CCD camera with an angular resolution better than 0.02° . The pulse

width of the probe x-ray was expected to be sub-ps and the time resolution was about 200 ps, determined by considering the duration of pump pulse.

This is an experiment that involves a challenging task of having spatial overlap between the x-ray beam and the pump beam and temporal synchronization between the x-ray pulse and the laser pulse. Firstly a mechanical alignment of the target, sample and c-ray CCD port was done. We used three He-Ne laser beams from x-ray probe, pump laser and x-ray CCD directions to find the approximate overlap on the crystal. The 800 nm laser beams were ensured to follow the He-Ne beam path during the actual run. To confirm that the overlapped part of the sample is indeed seen by the x-ray CCD, the sample surface was partially blocked with a thin metallic foil strip. This was reflected on the Bragg diffraction pattern as a null region. Once this portion was located by suitably moving the crystal, the pump laser focus was optimized to get maximum deformation of the diffraction at a fixed time delay. The temporal overlap of the beams (identification of “ $t=0$ ”) was ensured first by monitoring the scattered laser radiation from both the laser beams (pump and probe) from the sample with a photo-diode and fast oscilloscope to locate the temporal overlap. Since the pump pulse duration was 200 ps as compared to 45 fs probe laser pulse, even at the time “ $t=0$ ”, a deformation of the rocking curve is expected because of the rising edge of the pump pulse. The overlap between the probe x-ray beam and pump beam was optimized by slightly scanning the pump beam over the surface, and looking for the strongest signal change (i.e. largest shift of the Bragg peak), corresponding to the optimal overlap.

The point x-ray source allowed a direct imaging of a part of the crystal surface onto the x-ray CCD camera [87]. This enables simultaneous recording of the diffracted x-ray spectrum from the pristine (un-irradiated) and the laser irradiated area of the crystal. Figure 8.5a shows the space resolved CCD image of the diffracted iron K- α x-rays from laser

irradiated Si (111) surface, at a delay of +600 ps. The lower part of the same picture shows the pristine sample where the two components of the K- α lines (K- α_1 and K- α_2) are clearly identified. The upper part of the picture shows broadening of the K- α lines induced by non-uniform lattice compression attributed to the cumulative effects of the laser induced compression wave and the associated thermal broadening of the lattice.

A computer routine has been developed for reading and analysing of the data files. It includes all required data analysis routines. A user interface has been provided to choose the region of interest. The line profile on the maximally broadened region is taken for analysis. Variation in the width of the rocking curve for the pristine sample at different locations defines the error in measurement. Figure 8.5b shows the fitted line profile of the pristine sample. The line profiles, best fit parameters are saved separately for further analysis.

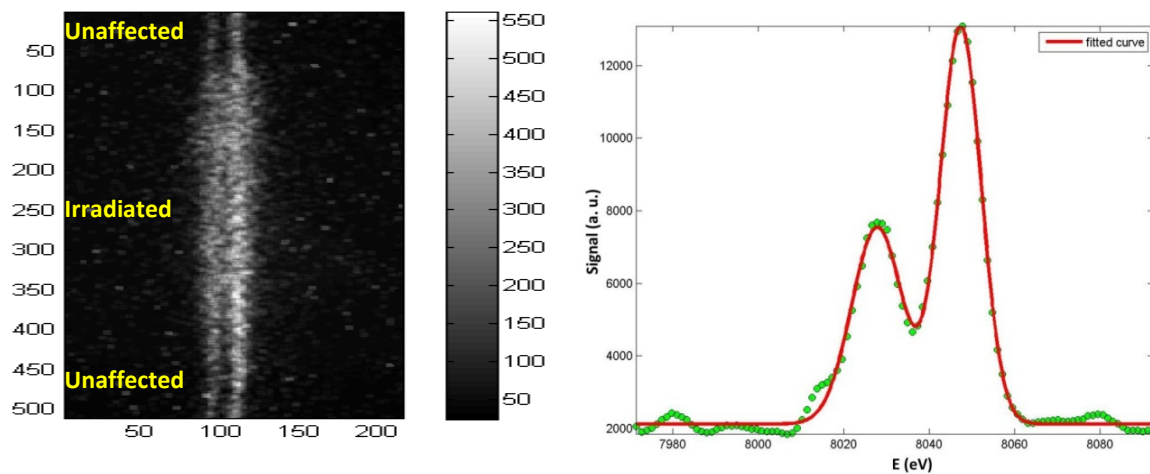


Fig. 8.5: a) Space resolved CCD image of the diffracted iron K- α x-rays from laser irradiated Si (111) surface at a delay of +600 ps, b) fitted line profile of the pristine sample

8.3 Measurement of shock-wave profiles

The x-ray source was used for measurement of shock-wave profiles in a silicon crystal by time resolved x-ray diffraction using Ti K- α x-ray line radiation as the probe pulse. A part of the stretched (800 nm, 200 ps) pulse was used as pump to irradiate a 500 μm thick

flat Si (111) crystal sample at an intensity of 6 GW cm^{-2} determined by considering the duration of pump pulse. The lattice change occurring in the crystal due to shock wave propagation or thermal disordering got manifested as a modification in x-ray diffraction profile integrated over the penetration depth for that photon energy. The broadening of the diffracted signals predominantly towards higher angles indicates shock wave compression of the lattice, whereas the thermal disordering for time delay $> 1 \text{ ns}$ gives rise to broadening towards the lower angle side [224]. Figure 8.6 shows the broadening of the Ti K- α line with the time delay between pump and probe pulse. The typical observed diffraction signal gives signature of expansion and compression through the spread in opposite directions resulting in overall broadening. It is observed that the diffraction pattern broadens with increasing delay to reach a maximum. Thereafter, the K- α_1 width decreases and comes close to the pristine value. It can be seen that maximum broadening occurs at 650 ps. It occurs at the time when the shock wave propagating through the sample reaches the x-ray penetration depth. The reduction in the broadening of the K- α peak is either due to the reduction in compression wave pressure within the penetration depth of probe x-rays in the sample, or due to the passing of the shock wave beyond the maximum probe depth inside the crystal.

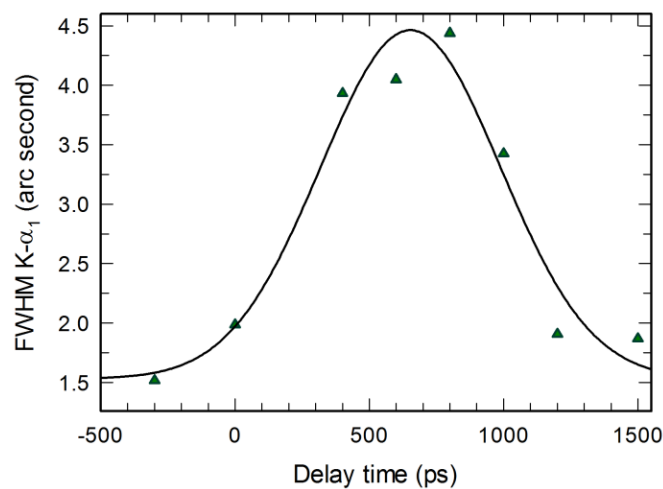


Fig. 8.6: Broadening of the FWHM of Ti K- α line with the time delay between pump and probe pulse.

8.4 Probing of strain propagation in laser shocked crystal with K- α x-ray probe of different photon energies

The irradiation by the pump laser causes formation of plasma and the expansion of this plasma drives a shock wave into the underlying silicon crystal [218, 219]. Probing of the lattice compression as a consequence of the shock wave propagation in a material on a time scale faster than the three dimensional relaxation time scales [225] (few hundreds of picoseconds) can give the information about the shock velocity. The measured rocking curves of Si (111) irradiated by the 200 ps laser pulses at a fluence of 2.3 J cm^{-2} , for various delay times between -300 ps and +1800 ps, are shown in Fig.8.7. The diffraction profiles of Fe K $_{\alpha 1}$ (6403.8 eV) and K $_{\alpha 2}$ (6390.8 eV) are well resolved for zero (and negative) delays. It is observed that the diffraction pattern broadens with increasing the time delay up to +1200 ps. After that, the broadening reduces and finally comes back to the original state for delays larger than +1500 ps. It may be noted that the broadening of the diffracted signals is predominantly towards higher angles, which indicates lattice compression induced by the pump laser beam. The small spreads towards lower angles also appear after 300 ps implying lattice expansion. It is the signature of thermal disordering effect due to heating, indicating a larger role of a thermal wave [224]. The modification of the lattice is either due to the laser ablation of very thin surface of the silicon or due to the stress caused at the front of thermal expansion due to the surface energy deposition. The ablation occurs when the laser fluence is above the threshold of ionization of the ablation vapour and rate of ablation depends on the laser fluence [226]. The pressure wave intensity would decrease monotonically as it propagates in the sample. The lattice change observed is manifested as a modification in x-ray diffraction profile integrated over the penetration depth for that photon energy. By the time the rocking curve is first recorded (the zero time) the shock wave would have penetrated

by about 2 μm . However, this will not affect the measurements because the penetration depth of the Fe K- α x-rays in Si (111) is 11.3 μm , which is much larger 2 μm .

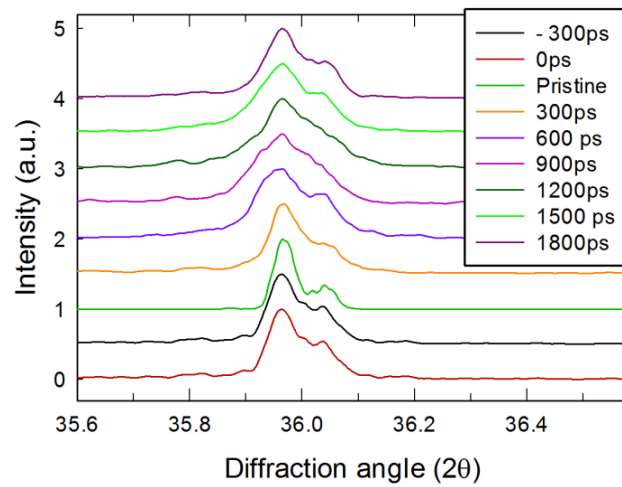


Fig. 8.7: Evolution of Si (111) rocking curve for various time delays, at a fixed fluence of 2.3 J cm^{-2}

We have analysed the dependence of the time evolution of the rocking curves as a function of the pump laser fluence. The laser fluence was varied by changing the laser energy using neutral density filters. Fig. 8.8 shows the evolution of the FWHM of the K- α_1 line as a function of the delay between the pump and the probe pulse, for two different pump laser fluences. It is observed that maximum broadening occurs at a time delay of 1050 ps for a lower laser fluence of 1.2 J cm^{-2} , compared to that at 1160 ps delay observed at a higher fluence of 2.3 J cm^{-2} . The maximum broadening occur at the time when the shock wave propagating through the sample reaches the x-ray penetration depth. The shock pressure is expected to be lower at a lower irradiance and the compression wave will attenuate before reaching a distance equal to the penetration depth. The reduction in the broadening of the K- α peak is either due to the reduction in compression wave pressure within the penetration depth of probe x-rays in the sample, or due to the passing of the shock wave beyond the maximum probe depth inside the crystal. It may be noted that the broadening reduces rapidly for larger

laser fluence indicating a larger thermal expansion and onset of large amplitude rarefaction wave [213, 219], compared to that for the case of smaller laser fluence.

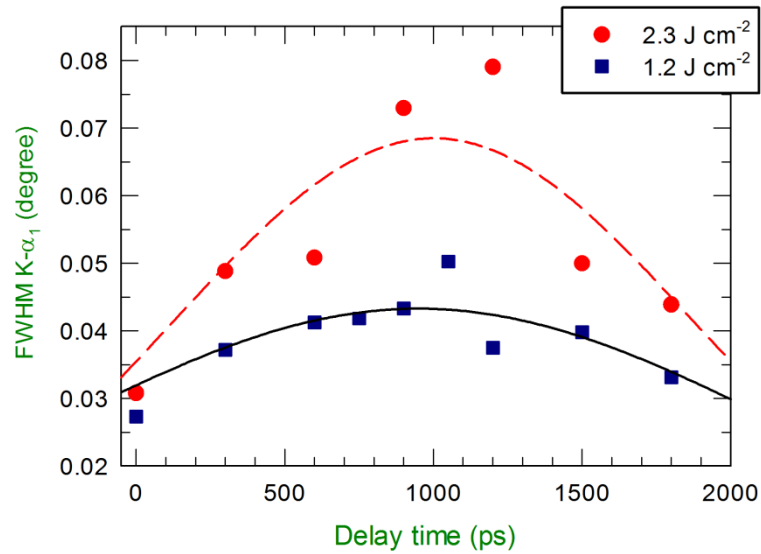


Fig. 8.8: Variation of the FWHM of the $K-\alpha_1$ line of Fe as a function of the delay between the pump and the probe pulse for two different fluences of 2.3 J cm^{-2} (solid squares) and 1.2 J cm^{-2} (hollow circles). The curve is to drawn to guide the eye.

The propagation of the thermal wave and the shock wave is manifested through the spread of diffraction signal in opposite sense. The thermal wave propagates typically with a velocity [227] of few times 10^4 cm/s . The thermal diffusion expected to occur on a time scale of tens of ns after the laser irradiation of the sample. The heating induced by it leads to the lattice expansion and the spread of diffraction signal towards lower angles, and appears when a few micron thick layer of the crystal is heated to a high temperature [218, 224]. On the other hand, the shock wave is launched due to material ablation and its propagation is not limited by the sound velocity. The lattice planes parallel to the shock front propagating into the crystal are compressed. The shift of the diffraction signal towards higher angle side on a time scale of about a ns is observed when the shock wave propagating through the sample reaches the x-ray penetration depth. The typical observed diffraction signal will give signature of expansion and compression through the spread in opposite directions resulting in

overall broadening. Therefore, the differentiation of the shock and thermal waves is not seen clearly.

To bring out the role of probe x-ray region inside the sample on the shock wave profile, the rocking curve of the silicon crystal irradiated at the same laser parameters (200 ps, 2.3 J cm^{-2}) was also measured with Cu K- α (8.05 keV, $\theta_B : 14.2^\circ$) having larger penetration depth compared to Fe K- α at 6.4 keV and Ti K- α (4.5 keV, $\theta_B : 26.7^\circ$). The profiles of the rocking curves are similar to those measured with Fe K- α (4.5 keV, $\theta_B : 18^\circ$). Fig. 8.9 shows the FWHM of the K- α_1 line radiation as function of the delay between the pump and the probe pulse, for Fe and Cu. It is observed that the diffraction pattern broadens with increasing delay to reach a maximum. Thereafter, the K- α_1 width decreases and comes close to the pristine value. Maximum broadening occurs at 790 ps, 1160 ps, and 1870 ps for Ti, Fe and Cu respectively. The FWHM of the rocking curve of the irradiated sample shows broadening of 3.2 ± 0.3 times, compared to that of the rocking curves of the pristine sample, for both the probe x-ray lines. The changes in diffracted x-ray profile shape are the result of lattice imperfection and results in strain broadening. The strain can be calculated from the width of the diffracted line taking the measured width of the pristine sample as the reference width. This gives a measurement of the strain since the lattice spacing is measured for planes parallel to the shock front [218]. The elastic component of calculated strain profile of the sample is shown in Fig. 8.10. The variation of the FWHM of the rocking curve for the two probes is of similar nature. However, it can be noted from the figure that when sample irradiated at same fluence of 2.3 J cm^{-2} is probed with Fe K- α shows maximum strain at 1160 ps whereas it maximum strain at 1870 ps with Cu K- α . Further, the observed maximum strain is $\sim 0.26\%$, $\sim 0.4\%$ and $\sim 0.3\%$ for Ti K- α , Fe K- α and Cu K- α respectively. Nevertheless, it is noted that the measurement of evolving shock profile through the sample is carried out using x-ray diffraction with different energy probe pulse can give the depth profiling of the strain.

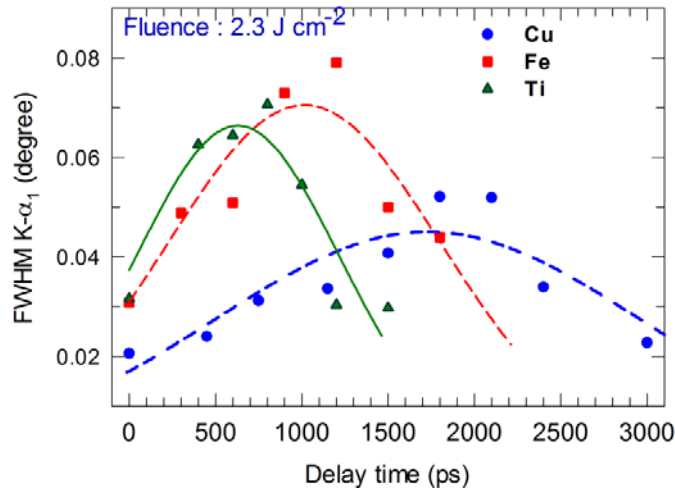


Fig. 8.9: Variation of the FWHM of the $K\text{-}\alpha_1$ line radiation as function of the delay between the pump and the probe pulse, for Ti, Fe and Cu. The curve is to drawn to guide the eye.

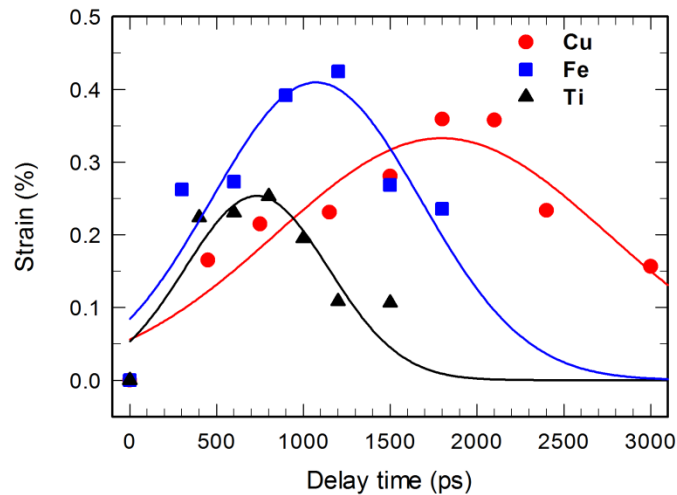


Fig. 8.10: Strain variation as a function of the delay between the pump and the probe pulse, for Fe (hollow circles) and Cu (solid squares).

The diffraction of the x-rays used for recording the rocking curve takes place in a finite volume inside the crystal and the observed diffraction pattern is a weighted sum of the diffraction data from different depths over which the analysis is performed [4]. When the lattice spacing is such that the Bragg condition is satisfied at a particular angle, the x-ray beam is diffracted from the sample within a thin layer of the crystal. The different layers, strained to different extents under the influence of the compression wave, will diffract at slightly different angles leading to the broadening. The x-ray can penetrate in a given crystal

up a distance dependent on the absorption coefficient, which in turn depends on the x-ray photon energy and the degree of crystal perfection [221]. When the crystal is perfect, only the primary extinction (losing intensity as far as diffracted photons will come in) is responsible for the penetration. Primary extinction length is of the order of a few microns [221] e.g., 18 μm and 15 μm for Si (111) and (220) at 8 keV, respectively. Conventionally, the attenuation length is defined as the depth into the material measured along the surface normal where the intensity of x-rays falls to $1/e$ of its value at the surface. Since the x-ray penetration depth is much smaller for perfect crystal, the diffraction in this case is usually modelled using dynamical diffraction theory [222, 223]. On the other hand, the kinematical approximation is used for modelling the x-ray diffraction from an imperfect crystal. However, for the practical case of crystal under moderate shock compression below the Hugoniot elastic limit, x-ray diffraction spectra can be precisely modelled based on the knowledge of x-ray penetration depth [222, 228].

The shock wave propagation [228] in material has been investigated to infer the shock – solid interaction, shock attenuation, variation of shock velocity etc. The shock waves propagate in a material medium in a manner different from that of ordinary acoustic waves. As the shock compression changes the density and temperature of the medium, the shock velocity is normally higher than the sound velocity in the medium in which it propagates. However, at low shocks, due to lower compression, the shock velocity is expected to close to the sound velocity. A study of the time evolution of the rocking curve can be an effective way to understand the propagation of the shock waves inside the crystal. As noted from the Fig. 8.8, maximum broadening occurs for a lower laser fluence of 1.2 J cm^{-2} , at a time delay of 1050 ps compared to 1160 ps observed at higher fluence of 2.3 J cm^{-2} . Ideally, the maximum broadening will occur when all lattice planes within the x-ray probe length are

compressed and contributing in diffracted x-ray spectrum along the x-ray penetration depth. The penetration depth of Fe K- α at 6.4 keV in Si (111) is 11.3 μm [223]. From the above data, it can be calculated that the shock wave propagates with a speed of 11×10^5 cm/s at lower irradiance, and 9.7×10^5 cm/s at higher irradiance. This difference in shock speeds can be either due to the attenuation of the shock wave inside the sample or due to the variation in shock speed in the strained material. From Fig. 4, one can note that the maximum broadening for Cu K- α at 8.05 keV occurs at 1870 ps. The penetration depth of Cu K- α at 8.05 keV in Si (111) is 17.4 μm [229]. The derived shock speed is 9.3×10^5 cm/s. Similarly, the penetration depth of Ti K- α at 4.5 keV in Si (111) is 6.1 μm . The maximum broadening for Ti K- α occurs at 720 ps and the derived shock speed is 8.5×10^5 cm/s. The average derived shock speed is $(9.6 \pm 1) \times 10^5$ cm/s. The measured shock speed represents the average speed and there is ~ 10 % variation in the shock speed derived with three different photon energy x-ray probe. It can be assigned to the fact that the shock waves are attenuated as they propagate and the onset of the rarefaction wave in the sample makes analysis more complex. Nevertheless, the derived shock wave speed is very close to the sound velocity of $\sim 9.4 \times 10^5$ cm/s in Si [230]. The derived shock speed values are also in broad agreement with those obtained under similar irradiation conditions.

The experimentally obtained diffraction profile is useful to derive some quantitative knowledge about the non-uniform variation of the inter planar spacing due to the propagating compression front. For this, one requires to carry out computer simulations based on the dynamical x-ray diffraction theory applied to strained and laser-shocked crystals [231]. Nevertheless, some important information such as interaction of the propagating compression front with the solid, which is a function of the penetration depth, can be obtained from the delay time at which maximum broadening occurs in the diffraction profile. As stated earlier,

in the case of Bragg reflection, a large number of layers participate in the process and the diffraction pattern is a cumulative contribution of all the participating layers. From the Bragg's law, the change in the angle of diffraction is related to the change in the inter-planar spacing. The lattice strain can be estimated using the relation

$$\Delta d/d = -\cot \theta_B \Delta \theta$$

where d is the inter-planar spacing, and θ is the Bragg angle. The maximum change in the Bragg angle ($\theta - \theta_B$) up to which diffraction signal appears is 0.064° . The lattice strain estimated from the shift in Bragg angle, corresponds to a compression of 0.4 %. Hironaka *et al* [219] have reported a maximum lattice strain of 1.05 % in Si, corresponding to the maximum pressure of 2.18 GPa. The maximum lattice strain of 0.4 % in the present experiment corresponds to a pressure of 0.8 GPa.

Many recent studies have used TXRD technique to investigate the strain generated in fs laser excited semiconductor materials. The initial events [227] after fs pulse excitation include the carrier–carrier interaction processes leading to a quasi-equilibrium situation among the electrons on a time scale of few fs. The exchange of energy between the electrons and the phonons takes place in hundreds of fs after the laser excitation peak. The phonon-phonon thermalization time is a few ps after the deposition of the laser energy. Lastly, the thermal diffusion leading to melting (provided sufficient amount of energy has been deposited in the material) can take place on a time scale of the order of tens of ps. Finally, the ablation starts leading to pressure wave generation and propagation on a time scales of hundreds of ps. In the present experimental setup, the time resolution is not sufficient to detect and resolve the initial events after fs pulse excitation. However, using a fs laser as the

probe, phenomena such as photon-electron interaction, electron-phonon coupling, and pressure wave generation and its propagation in the bulk of the crystal can be observed.

8.5 Deformation in laser irradiated silicon crystal

The irreversible structural modification in the recovered sample, after the propagation of shock wave, was examined using iron K- α x-ray radiation. Figure 8.11 shows the XRD pattern obtained from a pristine and irradiated part of the sample. The diffracted K- α_1 and K- α_2 lines from the pristine sample are clearly distinguishable. Laser irradiation at a fluence of 2.3 Jcm^{-2} results in a clear broadening of the spectrum. The FWHMs of the rocking curves for the irradiated sample is $(0.047 \pm 0.006)^\circ$ compared to the 0.021° for pristine sample.

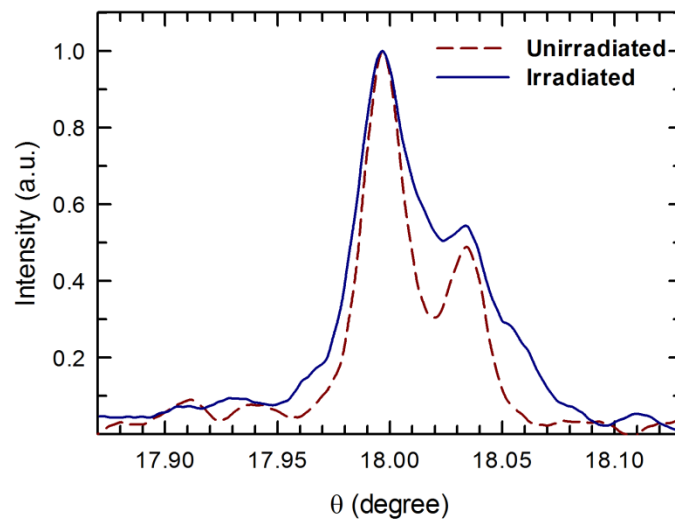


Fig. 8.11: XRD pattern obtained from a pristine and irradiated part of the sample.

It is to be noted that this irreversible broadening can be attributed to the cumulative effect of laser induced lattice compression and associated thermal effects resulting in non-uniform dilation. The extent of irreversible broadening of the rocking curve of Si (111) sample for different laser irradiances is shown in Fig. 8.12. A monotonic increase in the residual broadening clearly implies the role of the laser irradiation in modifying the surface patterns of the irradiated sample.

In order to investigate the effect of laser irradiation in near surface region, we have carried out Raman spectroscopy measurements. The results are presented in Fig. 8.13. As can be seen that in the pristine sample Raman peak appears around 520 cm^{-1} , while for the irradiated sample it is found to be shifted towards lower wave numbers and gets broadened. It appears that the short pulse laser irradiation causes anomalous surface transformations in Si crystal, resulting in the formation of localized surface variations during the process of re-crystallization.

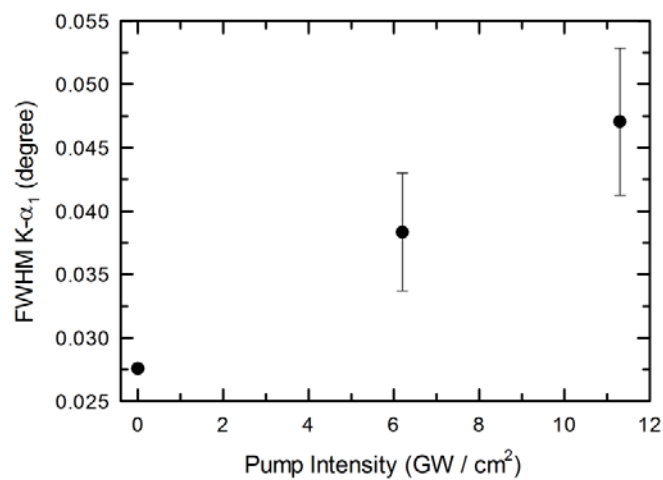


Fig. 8.12: The extent of irreversible broadening of the rocking curve of Si (111) sample for different laser irradiances.

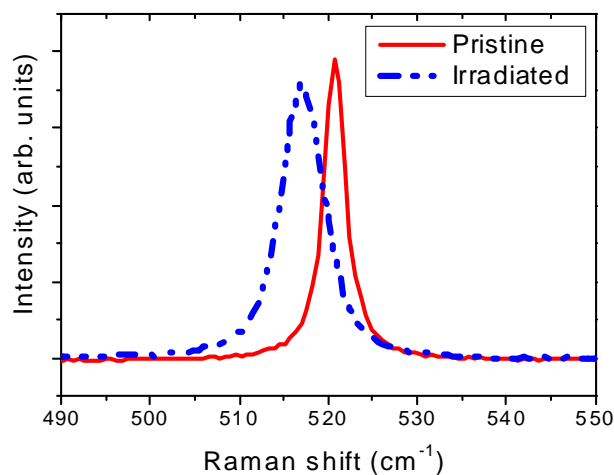


Fig. 8.13: Raman spectroscopy measurements to investigate the effect of laser irradiation in near surface region.

The peak broadening observed in time resolved x-ray diffraction occurs after 1160 ps after the irradiation with laser. The FWHM of K- α_1 was 0.074° reduces to value of 0.047° in the recovered sample primarily due to recrystallization of sample after the propagation of shock or thermal effects. Kishimura *et al* [215] has shown that such deformation of the lattice structure is mainly the formation of mosaic blocks with inclined orientations due to propagation of compression wave in laser ablated samples. The tilting is due to the pressure release after the compression wave is over.

To summarize this chapter, time resolved x-ray diffraction has been carried out to measure the rocking curve of a laser irradiated silicon crystal. The K- α x-ray line emissions from high-intensity ultra-short laser pulse produced plasmas of two different target materials (Fe, and Cu) are used as probe. The dynamics of the strain propagation is studied by measuring the rocking curve of the shocked sample as a function of delay between the pump and the probe pulse. The shock velocity deduced from these measurements is consistent with the predicted velocities. The observed maximum compression is 0.4%, which corresponds to a pressure of 0.8 GPa (8 kbar). The study can be of interest in view of the probing by x-ray pulses of widely different photon energies that can directly give information of the shock penetration depth. This makes this technique promising one for studying the temporal and spatial strain profiles of shocked samples. Such a study is helpful to understand the laser ablation for variety of application such as laser shock treatment and fracture stresses induced during welding etc.

Chapter 9

Conclusion

9.1 Summary of the research work

The thesis deals with experimental study of the x-ray emission from plasma produced by laser pulses from nanosecond to femtosecond duration. The study was aimed at to develop conditions for high conversion efficiency of laser energy into monochromatic x-ray line radiation for its application as an x-ray probe for time resolved measurements. The x-ray line radiations are produced in two relatively distinct processes, namely inner-shell electronic transitions and ionic resonance line transitions. The ionic line emission is due to the electronic transitions in the highly charged ionic species (H-like, He-like) present in the plasma heated to a high temperature and its duration can be less than a picosecond governed by the heating laser pulse duration, hydrodynamical parameters, and ionization dynamics. The plasma produced by long pulse laser is efficient source of ionic line transitions. On the other hand, the short duration laser pulses are more suitable to generate inner-shell characteristic line radiation. The duration of this emission is very short, close to the laser pulse duration, since it is generated through the hot electrons produced during the interaction of the ultra-short, ultra-intense laser pulses with the target. The conversion of both line radiations strongly depends on the irradiating laser parameters. Hence investigation of x-ray emission from laser plasma x-ray source is important for fundamental plasma studies as well as using it for practical application of time resolved studies remains a major area of research in this field.

The subject research area of the thesis *i.e.* X-ray spectroscopic studies of plasma produced by intense laser beam has been extensively reviewed. The spectral feature of x-ray emission has been understood in terms of absorption mechanisms of laser energy into plasma and ionization equilibrium in plasma. A detailed x-ray spectroscopic study of the plasmas generated from nanosecond and picosecond laser pulses has been carried out to investigate the dynamics of x-ray emission. It has been shown that x-ray emission from the plasma depends on the ionization equilibrium linked with the laser irradiation parameters. A comparative study of the keV x-ray emission from gold-copper mix-Z targets of different atomic compositions has been carried out. The keV x-ray yield was observed to decrease even for a small fraction of gold in the mix-Z target. The results have been explained in terms of the enhanced absorption due to free-bound opacity, followed by down-conversion of the absorbed radiation.

The x-ray emission from plasmas produced by the interaction of 45 fs Ti: sapphire laser pulses have been investigated. In this study, both ionic line radiation and inner-shell line radiation were simultaneously measured, changing the laser intensity, pulse duration, and focusing conditions, to understand the partition of energy between the thermal and non-thermal plasma. The plasma conditions prevalent during the emission of x-ray spectrum have been identified by comparing the experimental spectra with the synthetic spectra generated using a spectroscopic code.

The K- α line emissions between 1–8 keV, from Mg, Ti, Fe and Cu solid targets, has been studied using ultra-high intensity 45 fs laser pulses. The absolute yield of the K- α x-rays was measured as a function of the laser pulse duration and irradiation intensity. The results of optimal laser pulse duration for the maximization of K- α x-ray intensity have been explained

in terms of efficient generation of optimal energy hot electrons due to trade-off between the electron energy and re-absorption of the emitted radiation in coming out of the target.

A study on the 2ω and $3/2\omega$ harmonic generation in ultra-short high-intensity laser plasma interaction as a diagnostics for pre-formed plasma has been carried out. The results and analysis of the dependence of the 2ω and $3/2\omega$ intensity on the laser intensity and on the chirp of the laser pulse have been presented. A correlation of the K- α x-ray line shape with the 2ω and $3/2\omega$ emission is also shown. The K- α_1 line (4510 eV) is observed to be broadened (up to ~ 9 eV), predominantly towards the higher energy side and strongly depends on the laser fluence rather than on laser intensity. The reason for the spectral broadening is attributed to the inner-shell transitions in multiply-charged titanium ions in the pre-plasma. The appropriate laser irradiation parameters to achieve high conversion efficiency and minimum spectral width of the K- α radiation are identified.

A study on the time resolved x-ray diffraction from a laser shocked silicon crystal, has been carried out using the 45 fs Ti: sapphire laser. The use of K- α x-ray probe of different photon energies is shown to yield information about the strain over a greater crystal depth. The dynamics of the strain propagation has been inferred by monitoring the evolution of the rocking curve width of the shocked sample at different time delays between the pump and the probe pulse.

For carrying out the above x-ray spectroscopy work, the required x-ray spectroscopes were made by the candidate himself. An x-ray crystal spectrograph was made for high resolution measurements of the x-ray emission from the plasma. It was made on-line by coupling it with the x-ray CCD camera and used for recording x-ray emission spectrum in the range of 1- 8 keV, described in the thesis. A dispersion-less spectrograph based on the x-ray

CCD camera operation in single photon counting technique was designed, set up, characterized, and used in a variety of laser plasma experiment described in the thesis.

9.2 Outlook and Perspective

The results presented in this thesis on the development of x-ray source are an important basis for future research relevant to inertial confinement fusion and material science. There are various problems to be addressed for more effective utilization of the developed x-ray source for the above application. X-ray probe of energy ≥ 10 keV is required for probing density (10^{26} cm⁻³) of the compressed matter. More data on x-ray scaling of x-ray photon yield with laser energy at higher photon energies are required with more powerful lasers (> 100 TW) such as recently installed 150 TW laser facilities at RRCAT.

There is upsurge in interest for the investigation of warm dense matter state isochroically heated by proton beams with a pump probe technique. The spectrally narrow high energy x-ray probes are desirable in an x-ray scattering or diffraction technique. Such experiment requires the x-ray source with high photon flux and high sensitivity x-ray detectors. Optimization of ultra-short x-ray source produced by the irradiation of high contrast laser pulses on nanostructured target should be investigated. In particular, the results presented in present thesis have shown that the pre-pulse intensity contrast ratio plays a detrimental role in controlling the K- α x-ray probe parameters. To solve this problem a plasma mirror configuration to improve the temporal pulse contrast should be investigated.

The x-ray emission measurement has shown that the conversion efficiency of K- α is rather low. Recently it is proposed by Sefkow *et al* [177] by simulation that beam of proton generated by the interaction of intense laser foil interaction can be efficiently used to produce K- α from the second foil placed close to it. Such a design concept can be optimized for

higher x-ray flux. Next, the high resolution spectral measurement can be used for the quantitative estimation of the heating induced by the proton beam in the target.

This thesis presents a study of strain and lattice dynamics in laser shocked silicon crystal using the time resolved x-ray diffraction with the time resolution of sub nanosecond. Future work will seek to achieve the sub-picosecond temporal resolution to investigate the strain and lattice dynamics in photo-excited samples. The x-ray source generated by a kHz laser system and use of suitable x-ray optics will allow obtaining high quality data.

Bibliography

1. C. Rischel, A. Rousse, I. Uschmann, P. A. Albouy, J. P. Geindre, P. Audebert, J. C. Gauthier, E. Förster, J. L. Martin, and A. Antonetti, “Femtosecond time-resolved x-ray diffraction from laser heated organic films”, *Nature* **390**, 490 (1997).
2. C. Rose-Petruck, R. Jimenez, T. Guo, A. Cavalleri, C. W. Siders, F. Raksi, J. A. Squier, B. C. Walker, K. R. Wilson, and C. P. J. Barty, “Picosecond-milliangström lattice dynamics measured by ultra-fast x-ray diffraction”, *Nature* **398**, 310 (1999).
3. A. Rousse, C. Rischel, S. Fourmaux, I. Uschmann, S. Sebban, G. Grillon, P. Balcou, E. Förster, J. P. Geindre, P. Audebert, J. C. Gauthier, and D. Hulin, “Non-thermal melting in semiconductors measured at femtosecond resolution”, *Nature* **410**, 65 (2001).
4. K. Sokolowski-Tinten, C. Blome, C. Dietrich, A. Tarasevitch, M. Horn-von Hoegen, D. von der Linde, A. Cavalleri, J. Squier, and M. Kammler, “Femtosecond X-ray measurement of ultra-fast melting and large acoustic transients”, *Phys. Rev. Lett.* **87**, 225701 (2001).
5. E. Collet, M. H. Lemée-Cailleau, M. Buron-Le Cointe, H. Cailleau, M. Wulff, T. Luty, S. Y. Koshihara, M. Meyer, Loic Toupet, Philippe Rabiller, Simone Techert, “Laser induced ferroelectric structural order in an organic charge transfer crystal”, *Science* **300**, 612 (2003).
6. A. M. Lindenberg *et al*, “Atomic scale visualization of inertial dynamics”, *Science* **308**, 392 (2005).
7. T. Pfeifer, C. Spielmann and G. Gerber, “Femtosecond x-ray science”, *Rep. Prog. Phys.* **96**, 443 (2006).
8. M. Bargheer, N. Zhavoronkon, M. Woerner, and T. Elsaesser, “Recent progress in ultra-fast X-ray diffraction”, *Chem. Phys. Chem.* **7**, 783 (2006).
9. M. Nicoul, “Time-resolved x-ray diffraction with accelerator- and laser-plasma-based x-ray sources”, Dissertation University Duisburg-Essen (2010).
10. A. O. Er, J. Chen, and P. M. Rentzepis, “Ultra-fast time resolved x-ray diffraction, extended x-ray absorption fine structure and x-ray absorption near edge structure”, *J. Appl. Phys.* **112**, 031101 (2012).
11. D. H Bilderback, P. Elleaume and E. Weckert, “Review of third and next generation synchrotron light sources”, *J. Phys. B: At. Mol. Opt. Phys.* **38**, S773 (2005).

12. I. C. E. Turcu and J. B. Dance, "X-Rays from Laser Plasmas: Generation and Applications" (Wiley, New York, 1999).
13. J D. Lindl, "Development of the indirect-drive approach to inertial confinement fusion and the target physics basis for ignition and gain", *Phys. Plasmas*. **2**, 3933 (1995).
14. J D. Lindl *et al*, "The physics basis for ignition using indirect-drive targets on the National Ignition Facility", *Phys. Plasmas* **11**, 339 (2004).
15. R. C. Elton, "X-ray lasers" (Academic Press, 2000)
16. M. Lewenstein, Ph. Balcou, M. Yu. Ivanov, Anne L'Huillier, and P. B. Corkum, "Theory of high-harmonic generation by low-frequency laser fields", *Phys. Rev. A* **49**, 2117 (1994).
17. H. Singhal, V. Arora, B. S. Rao, P. A. Naik, U. Chakravarty, R. A. Khan, and P. D. Gupta, "Dependence of high-order harmonic intensity on the length of pre-formed plasma plumes", *Phys. Rev. A* **79**, 023807 (2009).
18. Y. Shimada *et al*, "Characterization of extreme ultra-violet emission from laser-produced spherical tin plasma generated with multiple laser beams", *Appl. Phys. Lett.* **86**, 051501 (2005).
19. J. A. Chakera, A. Ali, Y. Y. Tsui, and R. Fedosejevs, "A continuous kilohertz Cu K α source produced by submillijoule femtosecond laser pulses for phase contrast imaging", *Appl. Phys. Lett.* **93**, 261501 (2008).
20. J. A. Chakera, P. D. Gupta, Yu. Geondgian, V. V. Sorokin, V. Yu. Korol, and V. P. Avtonomov, "X-ray contact microscopic imaging in keV spectral region using laser-produced plasmas", *Curr. Sci.* **74**, 54 (1998).
21. H. S. Park *et al*, "High-energy K α radiography using high-intensity, short-pulse lasers", *Phys. Plasmas* **13**, 056309 (2006).
22. J. A. Cobble, T. E. Tierney, and J. Abdallah, Jr, "Kilovolt radiation from a laser-produced Al plasma." *J. Appl. Phys.* **102**, 023303 (2007).
23. V.A. Boiko *et al*, "X-ray spectroscopy of laser produced plasma", *Journal of Soviet Laser Research*, **6**, 85 (1985).
24. H.R. Griem, "Principles of Plasma Spectroscopy", Cambridge University Press, Cambridge (1997).
25. B.S. Rao, J.A. Chakera, P.A. Naik, M. Kumar, and P.D. Gupta, "Laser wake-field acceleration in pre-formed plasma channel created by pre-pulse pedestal of terawatt laser pulse", *Phys. Plasmas* **18**, 093104 (2011).

26. A. Macchi, M. Borghesi, M. Passoni, "Ion acceleration by super intense laser-plasma interaction", *Rev. Mod. Phys.* **85**, 751 (2013).
27. J. J. Carroll, D. G. Richmond, T. W. Sinor, K. N. Taylor, C. Hong, J. D. Standifird, C. B. Collins, N. Huxel, P. von Neumann-Cosel, and A. Richter, "Absolute measurement of spatial and spectral characteristics of bremsstrahlung using the photoexcitation of nuclear isomers", *Rev. Sci. Instrum.* **64**, 2298 (1993).
28. F. Ewald H Schwoerer, S Dusterer, R Sauerbrey, J Magill, J Galy, R Schenkel, S Karsch, D Habs and K Witte, "Application of relativistic laser plasmas for the study of nuclear reactions", *Plasma Phys. Control. Fusion*, **45**, A 83 (2003).
29. W. L. Kruer, "The Physics of Laser Plasma Interactions", Addison-Wesley, New York (1988).
30. S. Eliezer, "Interaction of High-Power Lasers with Plasmas", Institute of Physics Publishing Bristol and Philadelphia, Bristol (2002).
31. F.F. Chen, "Introduction to Plasma Physics", Second edition, Plenum Press (1984).
32. L. Tonks, and I. Langmuir, *Phys. Rev.* **33**, 195 (1929).
33. D. Bohm, and E. P. Gross. "Theory of plasma oscillations. A. Origin of medium-like behaviour", *Phys. Rev.* **75**, 1851 (1949).
34. T. Tajima, and J. M. Dawson, "Laser electron accelerator", *Phys. Rev. Lett.* **43**, 267 (1979).
35. D. Giulietti, and L.A. Gizzi, "X-ray emission from laser-produced plasmas", *Riv. Nuovo Cimento* **21**, 10 (1998).
36. B.N. Chichkov, C. Momma, S Nolte, F. V. Alvensleben, A. Tünnermann, "Femtosecond, picosecond and nanosecond laser ablation of solids", *Appl. Phys. A*, **63**, 109 (1996).
37. P. Mora, "Theoretical model of absorption of laser light by a plasma", *Phys. Fluids* **25**, 1051 (1982).
38. V Arora, J. A. Chakera, S. R. Kumbhare, P. A. Naik, N. K. Gupta, P. D. Gupta, "Angular distribution of X-ray line radiation from laser-irradiated planar targets", *Laser and Particle Beams* **19**, 253 (2001).
39. T. W. Johnston, and J. M. Dawson, "Correct values for high-frequency power absorption by inverse bremsstrahlung in plasmas", *Phys. Fluids* **16** 722 (1973).
40. A. A. Andreev, J. Limpouch, A. B. Iskakov, and H. Nakano, "Enhancement of x-ray line emission from plasmas produced by short high-intensity laser double pulses", *Phys. Rev. E* **65**, 026403 (2002).

- 41 C. S. Liu, and M. N. Rosenbluth, "Parametric decay of electromagnetic waves into two plasmons and its consequences", *Phys. Fluids* **19**, 967 (1976).
- 42 L. Veisz, "Investigation of parametric instabilities in femtosecond laser-produced plasmas" Dissertation Friedrich-Schiller-University Jena (2003).
- 43 J. C. Gauthier, "Progress in Ultra-fast Intense Laser Science I", Springer Series in Chemical Physics, Yamanouchi, K.; Chin, S.L.; Agostini, P.; Ferrante, G. (Ed.)) **122** (2006).
- 44 A. J. McAlister and E. A. Stern, "Plasma resonance absorption in thin metal films", *Phys. Rev.* **22**, 1599 (1963).
- 45 L. D. Landau, E. M. Lifshitz, and L. P. Pitaevskii, "Course of theoretical physics: physical kinetics", vol. X (Pergamon Press, 1981).
- 46 F. Brunel. "Not-so-resonant, resonant absorption", *Phys. Rev. Lett.*, **59**, 52 (1987).
- 47 W. L. Kruer, and K. Estabrook "JxB heating by very intense laser light", *Physics of Fluids*, **28**, 430 (1985).
- 48 P. Gibbon, 'Short Pulse Laser Interactions with Matter', Imperial College Press, London (2007).
- 49 C. A. Quarles, "Semi empirical analysis of electron-induced K-shell ionization," *Phys. Rev. A* **13**, 1278 (1976).
- 50 L.A. Gizzi, A. Giulietti, O. Willi, D. Riley, "Soft X-ray emission dynamics in picosecond laser-produced plasmas", *Phys. Rev. E* **62**, 2721 (2000).
- 51 P A Naik, P.D. Nandwana, P.D. Gupta, and S.R. Kumbhare, "X-ray spectroscopy in high temperature plasmas", BARC / I – 911 (1987).
- 52 A. Moorti, "Experimental study of laser driven pulsed electron and keV x-ray generation and its applications", Ph.D dissertation, DAVV, Indore (2007).
- 53 A. Chowdhury, G. P. Gupta, P. A. Naik, and P. D. Gupta, "Effect of dielectronic recombination on the charge-state distribution and soft x-ray line intensity of laser-produced carbon plasma", *Pramana* **64**, 141 (2005).
- 54 C. De. Michelis, and M. Mattioli, "Soft-x-ray spectroscopic diagnostics of laboratory plasmas", *Nuclear Fusion* **21**, 677 (1981).
- 55 G. P. Gupta, and B. K. Sinha, "Effect of ionization and recombination coefficients on the charge-state distribution of ions in laser-produced aluminum plasmas", *Phys. Rev. E* **56**, 2104 (1997)
- 56 H. R. Griem, "Validity of local thermodynamic equilibrium in plasma spectroscopy", *Phys. Rev.*, **131**, 1170 (1963).

- 57 T. Fujimoto and R. W. P. McWhirter, "Validity criteria for thermodynamic equilibrium in plasma spectroscopy", *Phys. Rev. A*, **42**, 6588 (1990).
- 58 D. R. Bates, A. E. Kingston, and R. W. P. McWhirter, "Recombination between electrons and atomic ions in optically thin plasmas", *Proc. Royal Soc.*, **267**, 297 (1962).
- 59 H. Nishimura, "X-Ray Sources", Series in Plasma Physics Applications of Laser-Plasma Interactions edited by S. Eliezer, K. Mima CRC press, Taylor and Francis Group (2008).
- 60 I. J. Feng , M. Lamoureux, and R. H. Pratt, H. K. Tseng," Calculation of free-free Gaunt factors in hot dense plasmas", *Phys. Rev. A*, **27**, 3209 (1983).
- 61 L. Gremillet *et al*, "Time-resolved observation of ultrahigh intensity laser-produced electron jets propagating through transparent solid targets", *Phys. Rev. Lett.* **83**, 5015 (1999).
- 62 P.A. Naik, "X-ray spectroscopy, theory" Encyclopedia of spectroscopy and spectrometry. (Ed: J.C. Lindon, G.E. Tranter, and J.L. Holmes), Academic Press (1999).
- 63 F. B. Rosmej, "Hot electron x-ray diagnostics" *J. Phys. B* **30**, L819 (1997).
- 64 S. B. Hansen *et al*, "Hot-electron influence on L-shell spectra of multicharged Kr ions generated in clusters irradiated by femtosecond laser pulses", *Phys. Rev. E* **66**, 046412 (2002)
- 65 E. A Galtier, Moinard, F. Y. Khattak, O. Renner, T. Robert, J. J. Santos, C. Beaucourt, P. Angelo, V. Tikhonchuk, and F. B. Rosmej, "High-resolution x-ray imaging of $K\alpha$ volume radiation induced by high-intensity laser pulse interaction with a copper target", *Journal of Physics B: Atomic, Molecular and Optical Physics* **45**, 20570 (2012).
- 66 T. Feurer, A. Morak, I. Uschmann, Ch. Ziener, H. Schworer, E. Forster, and R. Sauerbrey, "An incoherent sub-picosecond X-ray source for time-resolved X-ray-diffraction experiments", *Appl. Phys. B* **72**, 15 (2001).
- 67 Ch. Reich, I. Uschmann, F. Ewald, S. Düsterer, A. Lübcke, H. Schwoerer, R. Sauerbrey, E. Förster, and P. Gibbon, "Spatial characteristics of $K\alpha$ x-ray emission from relativistic femtosecond laser plasmas", *Phys. Rev. E* **68**, 056408 (2003).
- 68 R.Toth, S. Fourmaux, T. Ozaki, M. Servol, J. C. Kieffer, R. E. Kincaid Jr, and A. Krol, "Evaluation of ultra-fast laser-based hard x-ray sources for phase-contrast imaging", *Phys. Plasmas* **14** 053506 (2007).
- 69 H. Nakano, A.A. Andreev, J. Limpouch, "Femtosecond X-ray line emission from multilayer targets irradiated by short laser pulses", *Appl. Phys. B* **79**, 469 (2004).

- 70 Ch. Reich, P. Gibbon, I. Uschmann, and E. Forster, "Yield optimization and time structure of femtosecond laser plasma K α sources", *Phys. Rev.Lett.* **84**, 4846 (2000).
- 71 D. Salzmann, Ch. Reich, I. Uschmann, and E. Forster, "Theory of K α generation by femtosecond laser-produced hot electrons in thin foils" *Phys. Rev. E* **65**, 036402 (2002).
- 72 M. Trigo *et al.*, "Probing unfolded acoustic phonons with x rays", *Phys. Rev. Lett.* **101**, 025505 (2008).
- 73 I. Uschmann, T. Kampf, F. Zamponi, A. Lubcke, U. Zastra, R. Loetzsch, S. Hofer, A. Morak, and E. Forster, "Investigation of fast processes in condensed matter by time-resolved x-ray diffraction" *Appl. Phys. A* **96**, 91 (2009).
- 74 F. Zamponi, Z. Ansari, M. Woerner, and T. Elsaesser, "Femtosecond powder diffraction with a laser-driven hard X-ray source", *Opt. Express* **18**, 947 (2010).
- 75 A. Lubcke *et al.*, "Ultra-fast structural changes in SrTiO₃ due to a superconducting phase transition in a YBa₂Cu₃O₇ top layer" *New J. Phys.* **12**, 83043 (2010).
- 76 M. Nicoul, U. Shymanovich, A. Tarasevitch, D. V. Linde, and K. Sokolowski-Tinten, "Picosecond acoustic response of a laser-heated gold-film studied with time-resolved x-ray diffraction" *Appl. Phys. Lett.* **98**, 191902 (2011).
- 77 A. Rouse, C. Rischel, and J.C. Gauthier, "Femtosecond x-ray crystallography", *Review of Modern Physics*, **73**, 17 (2001).
- 78 P. D. Gupta, P. A. Naik, S. R. Kumbhare, A. Chowdhury, C. P. Navathe, B. S. Narayan, J. A. Chakera, and R. A. Joshi, Proc. National Laser Symposium, I.I.T, Madras pp. 296 (1993).
- 79 P. D. Gupta, P. A. Naik, C. P. Navathe, A. K. Sharma, M. Raghuramaiah, J. Upadhyay, H. R. Bundel, S. R. Kumbhare, and M. S. Ansari, Proc. National Laser Symposium, University of Hyderabad, Hyderabad pp. 31 (1999).
- 80 J. A. Chakera, S. R. Kumbhare, V. Arora, P. D. Gupta, V. A. Podvyaznikov, and V. K. Chevokin, Proc. National Laser Symposium, BARC, Mumbai pp. C-9 (1996).
- 81 G. Cheriaux, P. Rousseau, F. Salin, and J. P. Chambaret, "Aberration-free stretcher design for ultra-short-pulse amplification", *Opt. Lett.* **21**, 414 (1996).
- 82 G. Vaillancourt, T. B. Norris, J. S. Coe, P. Bado, and G. A. Mourou, "Operation of a 1-kHz pulse-pumped Ti:sapphire regenerative amplifier", *Opt. Lett.* **15**, 317 (1990).
- 83 E. Treacy, "Optical pulse compression with diffraction gratings", *IEEE J. Quant. Electr.* **5**, 454 (1969).
- 84 A. E. Siegman, "Lasers", University Science books USA p 359 (1986).

- 85 A. Brun, P. Georges, G. Le Saux and F. Sain, "Single-shot characterization of ultra-short light pulses", *J. Phys. D: Appl. Phys.* **24**, 1225 (1991).
- 86 J. Geindre, P. Audebert, A. Rousse, J. C. Gauthier, A. Ya Faenov, T. A. Pikuz, S. A. Pikuz, and T. A. Shelkovenko, "FSSR mica spherical crystal spectrometer with CCD detector for high-resolution x-ray spectroscopy of femtosecond laser produced plasma", *Physica Scripta* **53**, 645 (1996).
- 87 V. Arora, S. R. Kumbhare, P. A. Naik, and P. D. Gupta, "A simple high-resolution on-line x-ray imaging crystal spectrograph for laser-plasma interaction studies" *Rev. Sci. Instrum.* **71**, 2644 (2000).
- 88 Q. Yang, Y. G. Chen, Z. Li, L. Yang, Q. Peng, X. Huang, H. Cai, and Jing Li, "Focusing X-ray spectrograph with spatial resolution and uniform dispersion", *Nuclear Instruments and Methods in Physics Research A*, **634**, 52 (2011).
- 89 K. W. Hill, M. Bitter, L. Delgado-Aparacio, N. A. Pablant, P. Beiersdorfer, M. Schneider, K. Widmann, M. Sanchez del Rio, and L. Zhang, "Application of spatially resolved high resolution crystal spectrometry to inertial confinement fusion plasmas" *Rev. Sci. Instrum.* **83**, 10E125 (2012).
- 90 <http://www.reflex-co.cz/>
- 91 V. Arora, J. A. Chakera, P. A. Naik, S. R. Kumbhare, P. D. Gupta, and N. K. Gupta, "Effect of gold on keV x-ray emission yield from laser produced plasma of gold-copper mix- Z targets", *J. Appl. Phys.* **100**, 033306 (2006).
- 92 L. Labate *et al*, "Novel x-ray multispectral imaging of ultra-intense laser plasmas by a single-photon charge coupled device based pinhole camera" *Rev. Sci. Instrum.* **78**, 103506 (2007).
- 93 C. Stoeckl, W. Theobald, T. C. Sangster, M. H. Key, P. Patel, B. B. Zhang, R. Clarke, S. Karsch, and P. Norreys, "Operation of a single-photon-counting x-ray charge-coupled device camera spectrometer in a petawatt environment", *Rev. Sci. Instrum.* **75**, 3705 (2004).
- 94 C. Tillman, S. A. Johansson, B. Erlandsson, M. Grätz, B. Hemdal, A. Almén, S. Mattsson, and S. Svanberg, "High-resolution spectroscopy of laser-produced plasmas in the photon energy range above 10 keV" *Nuclear Instruments and Methods in Physics Research A* **394**, 387 (1997).
- 95 L. M. Chen, P. Forget, R. Toth, J. C. Kieffer, A. Krol, C. C. Chamberlain, B. X. Hou, J. Nees, and G. Mourou, "High resolution hard x-ray spectroscopy of femtosecond laser-produced plasmas with a CZT detector" *Rev. Sci. Instrum.* **74**, 5035 (2003).

- 96 W. Fullagar, M. Harbst, S. Canton, J. Uhlig, M. Walczak, C. Wahlstrom, and V. Sundstrom, "A broadband laser plasma x-ray source for application in ultra-fast chemical structure dynamics", *Rev. Sci. Instrum.* **78**, 115105 (2007).
- 97 R. Jenkins, R.W. Gould, and D. Gedcke, "Quantitative x-ray spectrometry", Marcel Dekker Inc. NewYork 1995.
- 98 L. Labate, M. Galimberti, A. Giulietti, D. Giulietti, L. A. Gizzi, P. Tomassini, and G. Di Cocco, "A laser-plasma source for CCD calibration in the soft X-ray range" *Nuclear Instruments and Methods in Physics Research Section A* **495**, 148 (2002).
- 99 S. Banerjee, G. R. Kumar, A. K. Saha, and L. C. Tribedi, "Absolute keV X-ray yields from intense, ultra-short laser driven solid plasmas", *Optics communications* **158**, 72 (1998).
- 100 B. R. Maddox, H. S. Park, B. A. Remington, and M. McKernan, "Calibration and characterization of single photon counting cameras for short-pulse laser experiments", *Rev. Sci. Instrum.* **79**, 10E924 (2008).
- 101 C. Fourment, C., N. Arazam, C. Bonte, T. Caillaud, D. Descamps, F. Dorchies, M. Harmand, S. Hulin, S. Petit, and J. J. Santos, "Broadband, high dynamics and high resolution charge coupled device-based spectrometer in dynamic mode for multi-keV repetitive x-ray sources", *Rev. Sci. Instrum.* **80**, 083505 (2009).
- 102 F. Zamponi, Tino Kampf, Andreas Morak, Ingo Uschmann, and Eckhart Forster, "Characterization of a deep depletion, back-illuminated charge-coupled device in the x-ray range", *Rev. Sci. Instrum.* **76**, 116101 (2005).
- 103 A. C. Thompson and D. Vaughan, "X-ray data booklet", Centre for x-ray optics and advanced light source, LBNL, University of California, 2001.
- 104 P. M. Nilson, W. Theobald, J. Myatt, C. Stoeckl, M. Storm, O. V. Gotchev, J. D. Zuegel, R. Betti, D. D. Meyerhofer, and T. C. Sangster, "High-intensity laser-plasma interactions in the refluxing limit" *Phys. Plasmas* **15** 056308 (2008).
- 105 G. C. Idzorek, and R. J. Bartlett, "Silicon photodiode characterization from 1 eV to 10 keV", *SPIE*, **3114**, 349 (1997).
- 106 S. H Glenzer, and R. Redmer, "X-ray Thomson scattering in high energy density plasmas", *Reviews of Modern Physics* **81**, 1625 (2009).
- 107 M. K.Urry, G. Gregori, O. L. Landen, A. Pak, and S. H. Glenzer, "X-ray probe development for collective scattering measurements in dense plasmas", *J. Quant. Spectrosc. Radiat. Transf.* **99**, 636 (2006).

- 108 T. Döppner, O. L. Landen, H. J. Lee, P. Neumayer, S. P. Regan, and S. H. Glenzer, "Temperature measurement through detailed balance in x-ray Thomson scattering" *High Energy Density Physics* **5**, 182 (2009).
- 109 P. Gallents, Z. Jiang, C.Y. Chien, P. Forget, F. Dorchies, J.C. Kieffer, H. Pepin, O. Peyrusse, G. Mourou, A. Krol, "Spectroscopy of solid density plasmas generated by irradiation of thin foils by a fs laser", *J. Quant. Spectrosc. Radiat. Transfer* **65**, 243 (2000).
- 110 H. M. Milchberg, I. Lyubomirsky, and C. G. Durfee, "Factors controlling the x-ray pulse emission from an intense femtosecond laser-heated solid", *Phys.Rev.Lett.* **67**, 2654 (1991).
- 111 A. Djaoui, and S.J. Rose, "Calculation of the time-dependent excitation and ionization in a laser-produced plasma", *J. Phys. B* **25**, 2745 (1992).
- 112 W. Theobald *et al*, "Hot surface ionic line emission and cold K-inner-shell emission from petawatt-laser-irradiated Cu foil targets", *Phys. Plasma* **13**, 043102 (2006).
- 113 L. A. Gizzi, C. A. Cecchetti, M. Galimberti, A. Giulietti, D. Giulietti, L. Labate, S. Laville, P. Tomassini, "Transient ionization in plasmas produced by point-like irradiation of solid Al targets", *Phys. Plasma* **10**, 4601 (2003).
- 114 L. Labate, C. A. Cecchetti, M. Galimberti, A. Giulietti, D. Giulietti, and L. A. Gizzi, "Detailed characterization of the early x-ray emission of a plasma produced by point-like laser irradiation of solid Al targets", *Phys. Plasma* **12**, 83101 (2005).
- 115 J. N. Broughton, and R. Fedosejeves, "keV x-ray production using 50 mJ KrF laser produced plasmas at 1 and 100 ps", *J. Appl. Phys.* **74**, 3712 (1993).
- 116 R. Popil, P. D. Gupta, R. Fedosejevs, and A. A. Offenberger, "Measurement of KrF-laser-plasma x-ray radiation from targets with various atomic numbers" *Phys. Rev. A* **35**, 3874 (1987).
- 117 D. Altenbernd, U. Teubner, P. Gibbon, E. Förster, P. Audebert, J. P. Geindre, J. C. Gauthier, G. Grillon, and A. Antonetti, "Soft x-ray brilliance of femtosecond and picosecond laser-plasmas" *J. Phys. B: At. Mol. Opt. Phys.* **30**, 3969 (1997).
- 118 F. N. Beg, S. D. Moustazis, M. Tatarakis, P. Lee, A. Dyson and A. E. Dangor, "X-ray emission from plasmas formed using an excimer laser with various pulse lengths", *J. Phys. D: Appl. Phys.* **31**, 2777 (1998).
- 119 J. Limpouch, O. Renner, E. Krousky, I. Uschmann, E. Foerster, M. P. Kalachnikov, and P. V. Nickles, "Line X-ray emission from Al targets irradiated by high-intensity, variable-length laser pulses", *Laser Part. Beam* **20**, 43 (2002).

- 120 L. M. Chen, P. Forget, S. Fourmaux, J. C. Kieffer, A. Krol, C. C. Chamberlain, B. X. Hou, J. Nees, and G. Mourou, "Study of hard x-ray emission from intense femtosecond Ti: sapphire laser–solid target interactions", *Phys. Plasma* **11**, 4439 (2004).
- 121 U. Teubner, W. Theobald and C. Wulker, "Mechanisms and origin of continuum and line emission from carbon plasmas produced by ultra-short laser pulses", *J. Phys. B: At. Mol. Opt. Phys.* **29** 4333 (1996).
- 122 P. Gibbon, and E. Forster, "Short-pulse laser-plasma interactions", *Plasma Phys. Control. Fusion*, **38**, 769 (1996).
- 123 B. S. Rao, P. A. Naik, V. Arora, R. A. Khan and P. D. Gupta, "Angular distribution and dose measurements of hard x-ray emission from intense laser-plasma interaction", *J. Appl. Phys.* **102**, 63307 (2007).
- 124 H. Chen, *et al*, "Fast-electron-relaxation measurement for laser-solid interaction at relativistic laser intensities" *Phys. Rev. E* **76**, 056402 (2007).
- 125 A. Zhidkov, and A. Sasaki, "Effect of field ionization on interaction of an intense subpicosecond laser pulse with foils", *Phys. Plasmas* **7**, 1341 (2000).
- 126 R W Lee and J T Larsen, "A time-dependent model for plasma spectroscopy of K-shell emitters", *J. Quant. Spectrosc. Radiat. Transfer* **56**, 535 (1996).
- 127 H. Nishimura, T. Endo, H. Shiraga, Y. Kato, and S. Nakai, "X-ray emission from high-Z mixture plasmas generated with intense blue laser light" *Appl. Phys. Lett.* **62**, 1344 (1993).
- 128 T.J. Orzechowski, M.D. Rosen, H.N. Kornblum, J.L. Porter, L.J. Suter, A.R. Theiessen, and R.J. Wallace, "The Rosseland mean opacity of a mixture of gold and gadolinium at high temperatures" *Phys. Rev. Lett.* **77**, 3545 (1996).
- 129 D. Colombant, M. Klapisch, and A. Bar-Shalom, "Increase in Rosseland mean opacity for inertial fusion hohlraum walls" *Phys. Rev. E.* **57**, 3411 (1998).
- 130 J. Yan and Y. Qiu, "Theoretical investigation of the increase in the Rosseland mean opacity for hot dense mixtures", *Phys. Rev. E.* **64**, 056401 (2001).
- 131 N.K. Gupta, and B.K. Godwal, "Effects of various parameters on numerical simulations of inertial confinement fusion hohlraum and radiation hydrodynamics" *Laser Particle Beams* **19**, 259 (2001).
- 132 J.A. Chakera, V. Arora, S. Sailaja, N.K. Gupta, S.R. Kumbhare, P.A. Naik, P.D. Gupta, and B.K. Godwal, "Dependence of soft x-ray conversion on atomic composition in laser produced plasma of gold–copper mix-Z targets", *Appl. Phys. Lett.* **83**, 27 (2003).

- 133 A. Rickert and J. Meyer-ter-vehn, "Frequency-dependent opacity calculations for high-Z plasma including L-splitting", *Laser Particle Beams* **8**, 715, (1990).
- 134 I.C.E. Turcu and I.N. Ross, "1 W plasma x-ray source for lithography at 1 nm wavelength", *Rev. Sci. Instrum.* **67**, 3245 (1996).
- 135 J.A. Chakera, V. Arora, S.R. Kumbhare, P.A. Naik, V. Ganesan, and P.D. Gupta, "Single shot twin x-ray microscopic imaging using simultaneously produced laser-plasma x-ray sources", *Rev. Sci. Instrum.* **72**, 1421 (2002)
- 136 B. Yaakobi, C. Stoeckl, T. Boehly, D.D. Mayerhofer, and W. Seka, "Measurement of preheat due to fast electrons in laser implosions", *Phys. Plasmas* **7**, 3714 (2000).
- 137 D.H. Kalanter, S.W. Haan, B.A. Hammel, C.J. Keane, O.L. Landen, and D.H. Munro, "X-ray backlit imaging measurement of in-flight pusher density for an indirect drive capsule implosion", *Rev. Sci. Instrum.* **68**, 814 (1997).
- 138 S. Sailaja, V. Arora, S. R. Kumbhare, P. A. Naik, P. D. Gupta, D. A. Fedin, A. A. Rupasov, and A. S. Shikanov, "A simple XUV transmission grating spectrograph with sub-ångström resolution for laser-plasma interaction studies", *Measurement Science and Technology* **9**, 1462 (1998).
- 139 Yu. M. Alexandrov *et al*, "Investigation of sensitometric characteristics of x-ray photoemulsions in the spectral range of 15–80 Å", *Nucl. Instrum. Methods Phys. Res. A* **308**, 343 (1991).
- 140 K.B. Fournier *et al*, "Observations of high-n transitions in the spectra of near-neon-like copper ions from laser-produced plasmas", *J. Phys. B: At. Mol. Opt. Phys.* **35**, 3347 (2002).
- 141 P.A. Naik, P.D. Gupta, and S.R. Kumbhare, "Spectral distribution of x-ray yield of the M-shell emission from laser produced gold plasma", *IEEE Trans. Plasma Sci.* **22**, 53 (1994).
- 142 G. D. Tsakiris, and K. Eidmann, "An approximate method for calculating Planck and Rosseland mean opacities in hot, dense plasmas", *J. Quant. Spectrosc. Radiat. Transfer* **38**, 353 (1987).
- 143 R. Sigel, K. Eidmann, F. Lavarenne, and R. F. Schmalz, "Conversion of laser light into soft x rays. Part I: Dimensional analysis", *Phys. Fluids B* **2**, 199 (1990)
- 144 P.D. Gupta, Y.Y. Tsui, R. Popil, R. Fedosejevs, and A.A. Offenberger, "Experimental study of KrF-laser-high-Z-plasma interaction dominated by radiation transport", *Phy. Rev. A* **34**, 4103 (1986).

- 145 S.J. Rose, "Calculations of the radiative opacity of laser-produced plasmas", *J. Phys. B: At. Mol. Opt. Phys.* **25**, 1667 (1992).
- 146 E. Minguez, and M.L. Gomez, "Analysis of the atomic physics models for the multigroup opacities calculation", *Laser and Particle Beams*. **8**, 103 (1990).
- 147 G. Winhart, K. Eidmann, C.A. Iglesias, A. Bar-Shalom, E. Minguez, A. Richert, and S.J. Rose, "XUV opacity measurements and comparison with models", *J. Quant. Spectrosc. Radiat. Transfer* **54**, 437 (1995).
- 148 S. Bastiani-Ceccotti, P. Renaudin, F. Dorchies, M. Harmand, O. Peyrusse, P. Audebert, S. Jacquemot, A. Calisti, and D. Benredjem, "Temporal and spectral behavior of sub-picosecond laser-created X-ray sources from low-to moderate-Z elements", *High Energy Density Physics* **6**, 99 (2010).
- 149 V. Arora, P. A. Naik, B. S. Rao, and P. D. Gupta, "A comparative study of the ionic keV X-ray line emission from plasma produced by the femtosecond, picosecond and nanosecond duration laser pulses", *Pramana J. Phys.* **78**, 277 (2012).
- 150 S. Le Pape, P. Neumayer, C. Fortmann, T. Döppner, P. Davis, A. L. Kritcher, O. Landen, and S. Glenzer, "X-ray radiography and scattering diagnosis of dense shock-compressed matter", *Phys. Plasmas* **17**, 056309 (2010).
- 151 U. Chakravarty, V. Arora, P. A. Naik, J. A. Chakera, H. Srivastava, A. Srivastava, G. D. Varma, S. R. Kumbhare, and P. D. Gupta, "Enhancement of K α emission through efficient hot electron generation in carbon nanotubes on intense laser pulse irradiation" *J. Appl. Phys.* **112**, 053301 (2012).
- 152 S. J. Pestehe, G. J. Tallents, I. C. E. Turcu, Y. A. Ali, G. Hirst, M. Powers and W. Shaikh, "Efficiency of 1.5-4.5 keV x-ray production from 2 ps duration KrF laser pulses incident onto solid targets" *J. Phys. D: Appl. Phys.* **35**, 1117 (2002).
- 153 B. Hou, J. A. Nees, W. Theobald, G. A. Mourou, L. M. Chen, J. C. Kieffer, A. Krol and C. C. Chamberlain, "Dependence of hard x-ray yield on laser pulse parameters in the wavelength-cubed regime", *Appl. Phys. Lett.* **84**, 2259 (2004).
- 154 A. Rousse, P. Audebert, J. P. Geindre, F. Fallies, J. C. Gauthier, A. Mysyrowicz, G. Grillon, and A. Antonetti, "Efficient K α x-ray source from femtosecond laser-produced plasma", *Phys. Rev. E* **50**, 2200 (1994).
- 155 N. D. Quart, A. S. Safronova, A. Ya. Faenov, T. A. Pikuz, S. V. Gasilov, F. Calegari, M. Nisoli, S. De Silvestri, S. Stagira, L. Poletto and P. Villoresi, "Analysis of the simultaneous measurements of iron K- and L-shell radiation from ultra-short laser produced plasmas", *J. Phys. B: At. Mol. Opt. Phys.* **44**, 065602 (2011).

- 156 J. A. Cobble, G. A. Kyrala, A. A. Hauer, A. J. Taylor, C. C. Gomez, N. D. Delamater, and G. T. Schappert, "Kilovolt x-ray spectroscopy of a subpicosecond-laser-excited source." *Phys. Rev. A* **39**, 454 (1989).
- 157 D. Duston, J. E. Rogerson, J. Davis, and M. Blaha, "Dense plasma effects on K-shell dielectronic satellite lines", *Phys. Rev. A* **28**, 2968 (1983).
- 158 J. Yang, Z. Hu, J. Zhang, T. Zhu, Y. Zhao, T. Wen, Z. Wang, Y. Ding, M. Wei, G. Yang, and B. Zhang, "High intensity x-ray line emission from aluminum plasmas generated by a 120 TW, 30 fs laser pulse", *Phys. Plasmas* **15**, 112704 (2008).
- 159 V. Arora, H. Singhal, P. A. Naik, and P. D Gupta, "Conversion efficiency and spectral broadening of the K- α line emitted from planar titanium targets irradiated with ultra-short laser pulses of high intensity", *J. App. Phys.* **110**, 083305 (2011).
- 160 F. N. Beg, A. Bell, A. Dangor, C. Danson, A. Fewes, M. Glinsky, B. Hammel, P. Lee, P. Norreys, and M. Tatarakis, "A study of picosecond laser–solid interactions up to 10^{19} W cm⁻²", *Phys. Plasmas* **4**, 447 (1997).
- 161 U. Teubner, T. Missalla, I. Uschmann, E. Forster, W. Theobald, and C. Wulker, "X-ray spectra from highly ionized dense plasmas produced by ultra-short laser pulses", *Appl. Phys. B* **62**, 213 (1996).
- 162 Z. Jiang, J. C. Kieffer, J. P. Matte, M. Chaker, O. Peyrusse, D. Gilles, G. Korn, A. Maksimchuk, S. Coe, and G. Mourou, "X-ray spectroscopy of hot solid density plasmas produced by subpicosecond and high contrast laser pulses at 10^{18} - 10^{19} W/cm²", *Phys. Plasmas* **2**, 1702 (1995).
- 163 P. D. Gupta, R. Popil, R. Fedosejevs, A. A. Offenberger, D. Salzmann, and C. E. Capjack, "Temperature and x-ray intensity scaling in KrF laser plasma interaction", *Appl. Phys. Lett.* **48**, 103 (1986).
- 164 D. C. Eder, G. Pretzler, E. Fill, K. Eidmann, and A. Seimann, "Spatial characteristics of K- α radiation from weakly relativistic laser plasmas", *Appl. Phys. B: Lasers Opt.* **70**, 211 (2000).
- 165 F. Y. Khattak, E. Garcia Saiz, T. Dzelzainis, D. Riley, and Z. Zhai, "Scale-length optimizing of short pulse Cu K α laser-plasma sources", *Appl. Phys. Lett.* **90**, 081502 (2007).
- 166 D. Riley, J. J. Angulo-Gareta, F. Y. Khattak, M. J. Lamb, P. S. Foster, E. J. Divall, C. J. Hooker, A. J. Langley, R. J. Clarke, and D. Neely, "K- α yields from Ti foils irradiated with ultra-short laser pulses", *Phys. Rev. E* **71**, 016406 (2005).

- 167 Y. Okano, K. Oguri, T. Nishikawa, and H. Nakano, "Spatial distribution of soft x-ray line emissions from aluminum plasma excited by a pair of femtosecond-laser pulses", *J. Appl. Phys.* **99**, 063302 (2006).
- 168 G. Y. Hu, J. Y. Zhang, J. Zheng, B. F. Shen, S. Y. Liu, J. M. Yang, Y. K. Ding, X. Hu, Y.X. Huang, H. B. Du, R. Q. Yi, A. L. Lei, and Z. Z. Xu, "Angular distribution and conversion of multi-keV L-shell X-ray sources produced from nanosecond laser irradiated thick-foil targets", *Laser & Particle Beams* **26**, 661 (2008).
- 169 C. M. Huntington, C. C. Kuranz, G. Malamud, R. P. Drake, H.S. Park, and B. R. Maddox, "Spectral analysis of x-ray emission created by intense laser irradiation of copper materials", *Rev. Sci. Instrum.* **83**, 10E114 (2012).
- 170 K. Eidmann, J. Meyer-ter-Vehn, Th Schlegel, and S. Hüller, "Hydrodynamic simulation of subpicosecond laser interaction with solid-density matter", *Phys. Rev. E* **62**, 1202 (2000).
- 171 Ch. Ziener, I. Uschmann, G. Stobrawa, Ch. Reich, P. Gibbon, T. Feurer, A. Morak, S. Dusterer, H. Schwoerer, E. Forster, and R. Sauerbrey, "Optimization of $K\alpha$ bursts for photon energies between 1.7 and 7 keV produced by femtosecond-laser-produced plasmas of different scale length", *Phys. Rev. E* **65**, 66411 (2002).
- 172 J. MacFarlane, Prism Computational Sciences, Madison, WI 53711, U.S.A.
- 173 V. Arora, P. A. Naik, J. A. Chakera, R. A. Khan, and P. D. Gupta, "Study of 2ω and $3/2\omega$ harmonics in ultra-short high-intensity laser plasma interaction", *Pramana J. Phys.* **75**, 1175 (2010).
- 174 J. A. Cobble, G. T. Schappert, L. A. Jones, A. J. Taylor, G. A. Kyrala, and R. D. Fulton, "The interaction of a high irradiance, subpicosecond laser pulse with aluminum: The effects of the pre-pulse on x-ray production", *J. Appl. Phys.* **69**, 3369 (1991).
- 175 M. Nishikino, K. Sato, N. Hasegawa, M. Ishino, S. Ohshima, Y. Okano, T. Kawachi, H. Numasaki, T. Teshima, and H. Nishimura, "Note: Application of laser produced plasma $K\alpha$ x-ray probe in radiation biology" *Rev. Sci. Instrum.* **81**, 026107 (2010).
- 176 K. Vaughan, A. Moore, V. Smalyuk, K. Wallace, D. Gate, S.G. Glendinning, S. McAlpin, H.S. Park, C. Sorce, R.M. Stevenson, "High-resolution 22–52 keV backlighter sources and application to x-ray radiography", *High Energy Density Physics* **9**, 635 (2013).

- 177 A. B. Sefkow, G. R. Bennett, M. Geissel, M. Schollmeier, B. C. Franke, and B. W. Atherton, "Efficiency enhancement for K- α x-Ray yields from laser-driven relativistic electrons in solids", *Phys. Rev. Lett.* **106**, 235002 (2011).
- 178 U. Chakravarty, V. Arora, J. A. Chakera, P. A. Naik, H. Srivastava, P. Tiwari, A. Srivastava, and P. D. Gupta, "X-ray enhancement in a nanohole target irradiated by intense ultra-short laser pulses", *J. Appl. Phys.* **109**, 053301 (2011).
- 179 U. Chakravarty, P. A. Naik, and P. D. Gupta, "Electric field enhancement at multiple densities in laser-irradiated nanotube plasma" *Pramana* **79**, 443 (2012).
- 180 E. Stambulchik *et al*, "Progress in line-shape modeling of K-shell transitions in warm dense titanium plasmas", *J. Phys. A: Math. Gen.* **42**, 214056 (2009).
- 181 V. Arora, H.S. Vora, J.A. Chakera, M. Tayyab, P.A. Naik and P.D. Gupta, "Dispersionless spectrograph for absolute measurement of multi keV x-ray flux from high intensity laser produced plasmas", *J. Instrum.* **8**, 01010 (2013).
- 182 A. Brun. P. Georges, G. Le Saux and F. Satin, "Single-shot characterization of ultra-short light pulses", *J. Phys. D: Appl. Phys.* **24**, 1225 (1991).
- 183 K. Eidmann, U. Andiel, F. Pisani, P. Hakel, R. C. Mancini, G. C. Jumkel Vives, J. Abdallah, and K. Witte "K-shell spectra from hot dense aluminum layers buried in carbon and heated by ultra-short laser pulses", *J. Quant. Spectrosc. Radiat. Transf.* **81**, 133 (2003).
- 184 K. Hatanaka, T. Ida, H. Ono, S. Matsushima, H. Fukumura, S. Juodkazis, and H. Misawa "Chirp effect in hard X-ray generation from liquid target when irradiated by femtosecond pulses.", *Opt. Exp.* **16**, 12650 (2008).
- 185 L. M. Chen, M. Kando, M. H. Xu, Y. T. Li, J. Koga, M. Chen, H. Xu, X. H. Yuan, Q. L. Dong, Z. M. Sheng, S.V. Bulanov, Y. Kato, J. Zhang, and T. Tajima, "Study of X-ray emission enhancement via a high-contrast femtosecond laser interacting with a solid foil", *Phys. Rev. Lett.* **100**, 045004 (2008).
- 186 F. Ewald, H. Schwoerer, and R. Sauerbrey, "K α -radiation from relativistic laser-produced plasmas", *Europhysics Letters* **60**, 710 (2002).
- 187 F. Pisani, U. Andiel, K. Eidmann, and K. Witte, I. Uschmann, A. Morak, E. Forster, and R. Sauerbrey, "Influence of the density gradient on the duration of Si-K α pulses generated by a double femtosecond-laser pulse", *Appl. Phys. Lett.* **84**, 2772 (2005).
- 188 A. Compant La Fontaine, C. Courtois, and E. Lefebvre, "Production of multi-MeV Bremsstrahlung x-ray sources by petawatt laser pulses on various targets", *Phys. Plasmas* **19** 023104 (2012).

- 189 R. Ramis, K. Eidmann, J. Meyer-ter-Vehn, and S. Hüller, "MULTI-fs—A computer code for laser–plasma interaction in the femtosecond regime", *Computer Physics Communications* **183**, 637 (2012).
- 190 A. G. MacPhee *et al*, "Diagnostics for fast ignition science", *Rev. Sci. Instrum.* **79**, 10F302 (2008).
- 191 Sebastien Le Pape *et al*, "Characterization of the pre-formed plasma for high-intensity laser-plasma interaction", *Optics letters* **34**, 2997 (2009).
- 192 J.L. Bobin, M. Decroisette, B. Meyer, Y. Vitel "Harmonic generation and parametric excitation of waves in a laser-created plasma", *Phys. Rev. Lett.* **30**, 594 (1973).
- 193 L. Veisz, W. Theobald, T. Feurer, H. Schillinger, P. Gibbon, R. Sauerbrey, "Three-halves harmonic emission from femtosecond laser produced plasmas" *Phys. Plasmas* **9**, 3197 (2002).
- 194 A. Tarasevitch, C. Dietrich, C. Blome, K. Sokolowski-Tinten, and D. von der Linde, "3/2 harmonic generation by femtosecond laser pulses in steep-gradient plasmas" *Phys. Rev. E* **68**, 026410 (2003).
- 195 L. Veisz, W. Theobald, T. Feurer, H. Schillinger, P. Gibbon, R. Sauerbrey, "Three-halves harmonic emission from femtosecond laser produced plasmas with steep density gradients", *Phys. Plasmas* **11**, 3311 (2004).
- 196 R. Lichters, J. Meyer-ter-Vehn, and A. Pukhov, "Short-pulse laser harmonics from oscillating plasma surfaces driven at relativistic intensity", *Phys. Plasmas* **3**, 3425 (1996).
- 197 F. Quéré, C. Thauray, P. Monot, S. Dobosz, Ph. Martin, J.-P. Geindre and P. Audebert, "Coherent Wake Emission of High-Order Harmonics from Overdense Plasmas", *Phys. Rev. Lett.* **96**, 125004 (2006).
- 198 R.A. Ganeev, M. Suzuki, M. Baba, M. Turu, H. Kuroda, "Generation of backscattered 2ω and $3\omega/2$ harmonics of femtosecond radiation from targets with different atomic numbers.", *Appl. Phys. B* **78**, 79 (2004).
- 199 R.A. Ganeev, J.A. Chakera, M. Raghuramaiah, A. K. Sharma, P.A. Naik, and P.D. Gupta, "Experimental study of harmonic generation from solid surfaces irradiated by multipicosecond laser pulses", *Phys. Rev. E* **63**, 264021 (2001).
- 200 A. Sengebusch, S. H. Glenzer, A. L. Kritcher, H. Reinholz, and G. Ropke, "Shift of Cl $K\alpha$ and $K\beta$ Lines in Laser Produced Dense Plasmas", *Contrib. Plasma Phys.* **47**, 309 (2007).

- 201 S. B. Hansen *et al*, Temperature determination using $K\alpha$ spectra from M-shell Ti ions", *Phys. Rev. E* **72**, 036408 (2005).
- 202 H. Chen *et al*, "Fast-electron-relaxation measurement for laser-solid interaction at relativistic laser intensities", *Phys. Plasmas* **14**, 102701 (2007).
- 203 D. Jung, L. A. Gizzi, L. Labate, D. Neely, M. M. Notley, P. P. Rajeev, M. Rothmand G. Gregori, "Experimental characterization of picosecond laser interaction with solid targets", *Phys. Rev. E* **77**, 56403 (2008).
- 204 U. Zastra *et al*, "Temperature and $K\alpha$ -yield radial distributions in laser-produced solid-density plasmas imaged with ultra-high-resolution x-ray spectroscopy", *Phys. Rev. E* **81**, 026406 (2010).
- 205 B. Soom, H. Chen, Y. Fisher, and D. D. Meyerhofer, J Strong, "K α emission in picosecond laser-plasma interactions", *J. Appl. Phys.* **74**, 5372 (1993).
- 206 S. N Chen *et al*, "Creation of hot dense matter in short-pulse laser-plasma interaction with tamped titanium foils", *Phys. Plasmas* **14**, 102701 (2007).
- 207 P. Neumayer, H. J. Lee, D. Offerman, E. Shipton, A. Kemp, A. L. Kritcher, T. Doppner, C. A. Back, S. H. Glenzer, "Isochoric heating of reduced mass targets by ultra-intense laser produced relativistic electrons", *High Energy Density Phys.* **5**, 244 (2009).
- 208 N. L. Kugland *et al*, High $K\alpha$ x-ray conversion efficiency from extended source gas jet targets irradiated by ultra- short laser pulses", *Appl. Phys. Lett.* **92**, 241504 (2008).
- 209 A. L. Kritcher *et al*, "K-alpha conversion efficiency measurements for X-ray scattering in inertial confinement fusion plasmas", *High Energy Density Phys.* **3**, 156 (2007).
- 210 H. J. Lee *et al*, "Optically induced lattice dynamics probed with ultra-fast x-ray diffraction", *Phys. Rev. B* **77**, 132301 (2008).
- 211 J. Hawreliak *et al*, "Analysis of the x-ray diffraction signal for the α - ϵ transition in shock-compressed iron: Simulation and experiment", *Phys. Rev. B* **74**, 184107 (2006).
- 212 D.A. Reis *et al*, "Probing impulsive strain propagation with X-ray pulses", *Phys. Rev. Lett.* **86**, 3072 (2001).
- 213 S.J. Turneare, and Y. M. Gupta, "Real-time x-ray diffraction at the impact surface of shocked crystals" *J. Appl. Phys.* **111**, 026101 (2012)
- 214 T. d'Almeida, M. D. Michiel, M. Kaiser, T. Buslaps, and A. Fanget, "Time-resolved x-ray diffraction measurements on CdS shocked along the c axis", *J. Appl. Phys.* **92**, 1715 (2002).

- 215 H. Kishimura, H. Morishita, Y. H. Okano, Y. Hironaka, K. Kondo, and K. G. Nakamura, and T. Atou, "Micromosaic formation in laser-irradiated Si probed by picosecond time-resolved x-ray diffraction", *Phys. Rev. B* **74**, 224301 (2006)
- 216 D. Batani *et al*, "Ablation pressure scaling at short laser wavelength", *Phys. Rev. E* **68**, 067403 (2003).
- 217 K. D. Liss, T. d'Almeida, M. Kaiser, R. Hock, A. Magerl, and J. F. Eloy, "Time-resolved x-ray diffraction study of laser-induced shock and acoustic waves in single crystalline silicon", *J. Appl. Phys.* **106**, 44914 (2009).
- 218 J. S. Wark, R. R. Whitlock, A. A. Hauer, J. E. Swain, and P. J. Solone, "Subnanosecond x-ray diffraction from laser-shocked crystals", *Phys. Rev. B* **40**, 5705 (1989).
- 219 Y. Hironaka, A. Yazaki, F. Saito, K. G. Nakamura, K. Kondo, H. Takenaka, and M. Yoshida, "Evolving shock-wave profiles measured in a silicon crystal by picosecond time-resolved x-ray diffraction", *Appl. Phys. Lett.* **77**, 1967 (2000).
- 220 D. H. Kalantar *et al*, "High-pressure, high-strain-rate lattice response of shocked materials", *Phys. Plasmas* **10**, 1569 (2003).
- 221 M. S. del Rio, L. Alianelli, T. A. Pikuz, and A. Ya. Faenov, "A novel imaging x-ray microscope based on a spherical crystal", *Rev. Sci. Instrum.* **72**, 3291 (2001).
- 222 S. Takagi, "Dynamical theory of diffraction applicable to crystals with any kind of small distortion" *Acta Crystallogr.* **15**, 1311 (1962).
- 223 D. Milathianaki *et al*, "A Seeman–Bohlin geometry for high-resolution nanosecond x-ray diffraction measurements from shocked polycrystalline and amorphous materials", *Rev. Sci. Instrum.* **80**, 093904 (2009).
- 224 L. G. Lunney, D. J. Dobson, J. D. Hares, S. D. Tabatabaei, and R. W. Eason, "Time resolved x-ray diffraction from silicon during pulsed laser annealing", *Opt. Commun.* **58**, 269 (1986)
- 225 B.A. Remington *et al*, "Material dynamics under extreme conditions of pressure and strain rate", *Mat. Sci. Tech.* **22**, 474 (2006)
- 226 M. Stafe, C. Negutu, N. N. Puscas, and I. M. Popescu, "Pulsed laser ablation of solids", *Romanian Reports in Physics* **62**, 758 (2010).
- 227 D. von der Linde, K. Sokolowski-Tinten, J. Bialkowski, "Laser–solid interaction in the femtosecond time regime", *Applied Surface Science* **109**, 1 (1997)
- 228 Y. Fan, Y. Wang, S. Vukelic, and Y. L. Yao, "Wave-solid interactions in laser-shock-induced deformation processes", *J. Appl. Phys.* **98**, 104904 (2012).

- 229 For x-ray attenuation length of material see http://henke.lbl.gov/optical_constants/atten2.html.
- 230 S. F. Wang , Y .F. Hsu, J. C. Pu, J.C. Sung, L.G. Hwa, "Determination of acoustic wave velocities and elastic properties for diamond and other hard materials", *Materials Chemistry and Physics* **85**, 432 (2004).
- 231 K.G. Nakamura *et al*, "Picosecond time-resolved x-ray diffraction from laser-shocked semiconductors", *Laser and Particle Beams* **22**, 285 (2004).